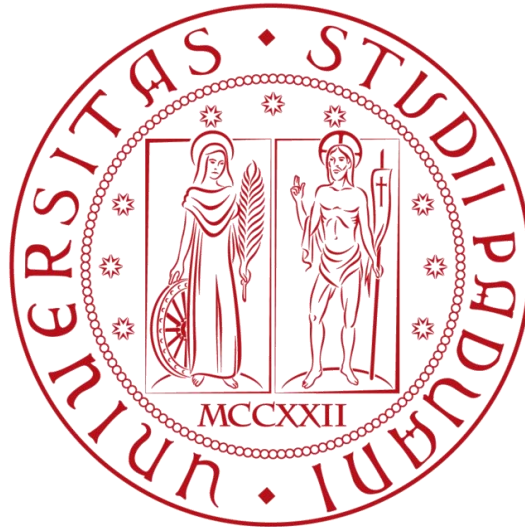


UNIVERSITA' DEGLI STUDI DI PADOVA



DIPARTIMENTO DI INGEGNERIA CIVILE, EDILE ED AMBIENTALE
DIPARTIMENTO DI INGEGNERIA INDUSTRIALE
LAUREA MAGISTRALE IN INGEGNERIA MECCANICA

TESI DI LAUREA

**Nuova metodologia basata sull'elaborazione di immagini
da Ultrasound® per la modellazione e la simulazione
numerica della fistola artero-venosa.**

RELATORE: Prof.ssa Francesca Maria Susin

LAUREANDO: Francesco Curtolo

Matricola: 1106696

ANNO ACCADEMICO 2016 – 2017

A novel protocol based on Ultrasound[®] imaging for patient specific AVF modelling and numerical simulation.

"If a man will begin with certainties, he shall end in doubts; but if he will be content to begin with doubts, he shall end in certainties"

FRANCIS BACON

Acknowledgements

Il più grande ringraziamento va senza dubbio ai miei genitori: grazie per avermi supportato fin qui, per la fiducia sempre data ma anche per aver saputo dire di no nei momenti opportuni. Questo mio traguardo è senz'altro una delle tante dimostrazioni di quanto bene abbiate fatto il vostro lavoro.

Un grosso ringraziamento spetta anche alle mie sorelle Sara ed Alessia: grazie per avermi sempre stimolato, supportato e sopportato.

Grazie poi a tutti gli amici che con pazienza mi sono vicini, in particolare Andrea, Luca, Enrico, Nicolò, Alberto e Tommaso: difficilmente sarei arrivato in fondo senza tutte le minchiate dette e fatte insieme.

Un altro grande ringraziamento spetta al *Race UP Team*, per tutta la fatica e l'esperienza fatta assieme nella fantastica stagione passata. Grazie infine a Stefano e al Prof. Meneghetti che rendono possibile per noi studenti questa impegnativa e affascinante lezione di ingegneria.

Ringrazio anche il professor Andrea Bucchi per l'ospitalità l'aiuto e amicizia riservatimi nel mio periodo di permanenza presso la sua università.

Un ultimo pensiero è per mio nonno Giovanni, per tutto quello che mi ha insegnato e tramandato: le passioni, la simpatia, la generosità, la forza con cui ha affrontato le prove più difficili della sua vita e sarà sempre per me d'esempio.

Abstract

AVF (artero-venous fistula) is one of the most used and studied applications for dialysis access worldwide. It consists of an artificial connection between artery and vein to achieve an acceptable flow rate to provide to the dialysis machine (≥ 0.3 ml/min).

Many studies for both the medical and engineering related topics have been done regarding success and good practice parameters to allow a successful maturation of this application, but nowadays this technique suffers from a success rate about 50-60% for long-term applications.

The aim of this study is to develop a new procedure to study the engineering point of view of this problem. This procedure starts from the necessity to obtain data in an easy, economic and practical way from the standard hospital instruments available, which could be at the same time relevant to the engineering point of view.

The choice came down to Image Editing based on Ultrasound Color-Doppler scans, which allows vessels geometry and paths extraction, in addition to blood pulsewave and velocity data.

Starting by this data a 3D model of the vessels is created before and after the AVF operation and then, with the blood information extracted, a CFD simulation is operated to study the main factors of interest regarding the influence of blood flow on the AVF modification and maturation.

From the results of these simulations, the main factors studied are WSS – TAWSS - GWSS TAGWSS - OSI in their magnitudes and locations looking for correspondences between the results and previous studies and theories.

Sommario

L'AVF (fistola artero-venosa) è una delle applicazioni più utilizzate e studiate per l'accesso di dialisi in tutto il mondo. Consiste in una connessione artificiale tra l'arteria e la vena per ottenere una portata accettabile da fornire alla macchina di dialisi ($\geq 0,3$ ml/min).

Molti studi sono stati fatti, riguardanti sia l'ambito medico che quello ingegneristico, sul successo e i parametri di buona pratica per consentire la maturazione di questa applicazione, ma ad oggi questa tecnica ha un tasso di successo di circa il 50-60% per applicazioni a lungo termine.

Lo scopo di questo studio è quello di sviluppare una nuova procedura per studiare il problema dal punto di vista ingegneristico. Questa nuova procedura inizia dalla necessità di ottenere dati in modo semplice e pratico dagli strumenti ospedalieri comunemente disponibili, che possano essere allo stesso tempo rilevanti sotto il punto di vista ingegneristico.

La scelta cade sull' Image Editing a partire da scansioni Color-Doppler con Ultrasound, che permettono di estrarre geometria e percorsi dei vasi, oltre alla curva di velocità e portata del sangue.

A partire da questi dati è stato creato un modello 3D dei vasi sanguigni prima e dopo l'operazione AVF e quindi, con le informazioni relative al campo di moto fluido estratte precedentemente, viene eseguita una simulazione CFD per studiare i principali fattori di interesse riguardanti l'influenza del flusso sanguigno sulla modifica AVF e maturazione.

Dai risultati di queste simulazioni i fattori principali studiati sono WSS – TAWSS - GWSS TAGWSS - OSI nella loro magnitudine e posizioni, cercando correlazione tra risultati e gli studi e le teorie precedenti.

Table of Contents:

1	INTRODUCTION.....	- 1 -
1.1	The Kidneys (1) (2)	- 2 -
1.2	Kidney Diseases.....	- 4 -
1.2.1	Chronic Kidney Disease (CKD) (3)	- 4 -
1.2.2	Kidney Failure	- 5 -
1.3	Treatment Options	- 6 -
1.3.1	Kidney Transplant (5).....	- 6 -
1.3.2	Dialysis (6).....	- 7 -
1.4	Peritoneal Dialysis and How it Works	- 10 -
1.5	Hemodialysis	- 11 -
1.5.1	Mechanism and Technique.....	- 12 -
1.5.2	Dialyzable Substances.....	- 13 -
1.5.3	Dialysis Equipment	- 14 -
1.5.4	Dialysis Types.....	- 16 -
1.5.5	Dialysis Disadvantages	- 17 -
1.6	Hemodialysis Access Options (13)	- 18 -
2	THE MEDICAL PROBLEM	- 21 -
2.1	The Arteriovenous Fistula (AVF) (13)	- 23 -
2.1.1	Benefits of AV Fistula for Dialysis	- 24 -
2.2	Types of AV Fistula for Dialysis (16)	- 24 -
2.2.1	The Radial Cephalic Fistula	- 26 -
2.2.2	The Brachial Cephalic Fistula	- 26 -

2.2.3	The Brachial Basilic Fistula	- 26 -
2.3	Creation of an AVF.....	- 27 -
2.3.1	Surgical Technique (18)	- 28 -
2.3.2	Technical Points Determining Success (17)	- 33 -
2.4	Pre-Evaluation and Post-Monitoring the AVF	- 35 -
2.5	Physiology and Pathophysiology of Fistula Maturation	- 37 -
2.5.1	Vascular Remodelling and Adaptation to High Flow (17)	- 37 -
2.5.2	Remodelling and Wall Shear Stress	- 41 -
2.5.3	Remodelling and Circumferential Pressure	- 42 -
2.5.4	Intimal Hyperplasia (14)	- 42 -
2.5.5	Outward Remodelling (14)	- 43 -
2.5.6	Impaired Outward Remodelling and Intimal Hyperplasia (IH) (14)	- 44 -
2.5.7	Experimental and Clinical Studies.....	- 46 -
2.6	Pathogenesis of the AV Fistula Failure	- 47 -
2.6.1	Demographic and Clinical Factors (25) (14)	- 47 -
2.6.2	Abnormal Hemodynamic Shear Stress Profiles (25)	- 48 -
2.6.3	Pre-Existing Vascular Abnormalities (25).....	- 49 -
2.7	Complications Related to AVF	- 49 -
2.7.1	First-Use Syndrome (10)	- 50 -
2.7.2	Fluid Shifts	- 50 -
2.7.3	Access-Related Problems.....	- 51 -
2.7.4	Stenosis of Central Veins (27).....	- 51 -
2.7.5	Thrombosis (27).....	- 51 -
2.7.6	Anticoagulation-Related	- 52 -
2.7.7	Steal Phenomenon (27) (17)	- 52 -
2.7.8	Cardiovascular (Heart and Vessels) Diseases (26) (17)	- 53 -
2.8	Main Ways to Fix it (25).....	- 55 -
2.8.1	Cell-Based Therapies	- 56 -
2.8.2	Drug-Based Therapies	- 56 -
2.8.3	Gene-Based Therapies.....	- 56 -
2.8.4	Ligature	- 57 -
2.8.5	Balloon Dilatation (26)	- 57 -

2.8.6	Thrombectomy (27)	- 57 -
2.9	The Medical Problem Conclusion.....	- 58 -
3	THE ENGINEERING PROBLEM.....	- 59 -
3.1	The Case	- 60 -
3.1.1	Wall Shear Stress (WSS)	- 60 -
3.1.2	Spatial Wall Shear Stress Gradient (SWSSG)	- 61 -
3.1.3	Time Average Wall Shear Stress (TAWSS)	- 62 -
3.1.4	Time Averaged Wall Shear Stress Gradient (TAWSSG)	- 63 -
3.1.5	Temporal Wall Shear Stress Gradient (TWSSG)	- 63 -
3.1.6	Oscillatory Shear Index (OSI)	- 64 -
3.1.7	Relative Residence Time (RRT)	- 65 -
3.2	The Patient Specific Aim	- 66 -
3.3	Blood Flow and Rheology	- 69 -
3.3.1	Blood Characteristics	- 70 -
3.3.2	Blood Rheological Models (45) (46)	- 74 -
3.3.3	Blood Flow	- 80 -
3.3.4	Blood Rheological Model Choice	- 87 -
3.4	Structure of Vessels (62)	- 91 -
3.5	The 3D Model	- 94 -
3.5.1	How to create it	- 95 -
3.5.2	How to Collect Data Required	- 95 -
3.6	Fluid Dynamics Study	- 101 -
3.7	Lumped Mathematical Models (68)	- 103 -
3.7.1	Electrical Analog Model of Flow in a Tube (69)	- 105 -
3.7.2	Nodes and the Equations at Each Node (69)	- 106 -
3.7.3	Terminal Load (69)	- 108 -
3.7.4	Windkessel Models (68)	- 110 -
3.7.5	Specific Application to AVF (70)	- 115 -
3.7.6	Possible Applications	- 117 -

3.8	Computational Fluid Dynamics (CFD) (71)	- 118 -
3.8.1	Fluid Characteristics.....	- 120 -
3.8.2	Methodology (73)	- 121 -
3.8.3	Discretization Processes (73)	- 122 -
3.8.4	Solution Algorithms (71)	- 123 -
3.8.5	CFD Simulations (73).....	- 124 -
3.8.6	Post-Processing and Analysis (73)	- 125 -
3.8.7	Uncertainty and Error (73).....	- 125 -
3.8.8	Verification (73)	- 126 -
3.8.9	CFD Advantages and Limitations	- 127 -
3.8.10	Available CFD Software	- 128 -
3.8.11	CFD in Biomedical Engineering Application	- 129 -
3.9	Fluid–Structure Interaction (FSI)	- 130 -
3.9.1	Application of FSI	- 134 -
3.9.2	Approaches for Fluid Structure Interaction Simulation	- 135 -
3.9.3	Classification of FSI Coupled System	- 136 -
3.9.4	FSI Mesh	- 136 -
3.9.5	Numerical Simulation	- 137 -
3.9.6	FSI in Biomedical Engineering Application (79)	- 138 -
3.10	Conclusions	- 140 -
3.11	Procedure Established	- 141 -
4	ULTRASOUND IMAGING	- 145 -
4.1	Medical Ultrasound (87) (88)	- 147 -
4.2	Modes of Sonography	- 150 -
4.3	Doppler Ultrasonography	- 151 -
4.4	How it Works: From Sound to Image	- 153 -
4.4.1	The Transducer	- 153 -
4.4.2	Producing a Sound Wave.....	- 154 -
4.4.3	Receiving the Echoes	- 155 -
4.4.4	Forming the Image.....	- 155 -
4.4.5	Colour Doppler Technique (88)	- 156 -

4.4.6	Image Resolution (88).....	- 157 -
4.4.7	Imaging Artefacts (88)	- 160 -
4.5	Ultrasound Imaging Properties (87)	- 163 -
4.5.1	Medical Ultrasound Strengths	- 163 -
4.5.2	Medical Ultrasound Weaknesses	- 164 -
4.6	Applications in our Case Study: Vascular Mapping prior to Hemodialysis Access Placement	- 164 -
4.7	Protocol Established with the Hospital	- 166 -
4.7.1	The Image Capturing Protocol	- 167 -
4.8	Data Obtained	- 175 -
5	IMAGE PROCESSING.....	- 177 -
5.1	The Case	- 178 -
5.2	Image Analysis (91)	- 179 -
5.3	The DICOM Imaging Standard (93)	- 182 -
5.3.1	Images Format	- 183 -
5.3.2	Services (93).....	- 184 -
5.3.3	Compatibility (93)	- 185 -
5.4	MATLAB Programming Software	- 186 -
5.4.1	Digital Image Processing: MATLAB Image Processing Toolbox™ (97)	- 187 -
5.5	Image Processing Conclusions	- 195 -
5.6	Edges Points Extraction	- 196 -
5.6.1	The Sobel Filtering Technique (100)	- 197 -
5.6.2	Otsu's Thresholding Method (101)	- 199 -
5.6.3	Principal Commands Used (102)	- 200 -
5.6.4	Procedures\Algorithms.....	- 203 -
5.6.5	Edges Points Extraction Results	- 204 -
5.7	Edges Points Generator	- 213 -
5.7.1	The Savitzky–Golay Filter (104).....	- 214 -
5.7.2	Principal Commands Used (102).....	- 215 -

5.7.3	Procedures\Algorithms.....	- 216 -
5.7.4	Edges Points Generator Results.....	- 217 -
5.8	Velocity PulseWave Extraction	- 224 -
5.8.1	The Least Squares Fitting (107).....	- 225 -
5.8.2	Principal Commands Used (102).....	- 228 -
5.8.3	Procedures\Algorithms.....	- 230 -
5.8.4	Velocity PulseWave Extraction Results.....	- 231 -
5.9	Uncertainties and Errors.....	- 241 -
5.9.1	Procedure and measures uncertainty	- 241 -
5.9.2	Edges Points Extraction Measured Errors.....	- 245 -
5.9.3	Edges Points Generator Measured Errors	- 245 -
5.9.4	Velocity PulseWave Extractor Measured Errors.....	- 247 -
5.9.5	Errors Measurement.....	- 249 -
5.10	Other Programs	- 254 -
6	3D MODELLING	- 257 -
6.1	The Case	- 258 -
6.2	Where to Start.....	- 259 -
6.3	Software.....	- 259 -
6.3.1	Autocad® (112).....	- 260 -
6.3.2	Inventor® (113).....	- 261 -
6.4	Procedure.....	- 262 -
6.4.1	The Grid	- 262 -
6.4.2	The 3D Model	- 264 -
6.5	Precedents and Possibilities	- 280 -
6.5.1	First Models	- 280 -
6.5.2	First Real Vessels Procedure	- 281 -
6.5.3	A Virtual Model of AVF Based on Separated Vessels.....	- 282 -
6.5.4	An Additional Step: Inlets/Outlets Extensions.....	- 283 -
6.6	Uncertainties and Errors.....	- 284 -

6.6.1	Template Arm	- 285 -
6.6.2	Probe Positioning on the Real Grid	- 287 -
6.6.3	Grid Re-Positioning on the Template Arm	- 288 -
6.6.4	Cross-Sectional Alignment and Positioning	- 289 -
6.7	3D Modelling Results	- 290 -
6.7.1	First Models	- 290 -
6.7.2	Virtual Reconstruction of an AVF	- 291 -
6.7.3	AVF Real Case	- 292 -
7	THE NUMERICAL MODEL	- 295 -
7.1	The Software: COMSOL Multiphysics (117) (118)	- 296 -
7.2	CFD Simulation of the AVF	- 300 -
7.2.1	Pre-Operative Operations	- 300 -
7.2.2	Pre-Processing	- 314 -
7.2.3	Simulation	- 324 -
7.2.4	Post-Processing	- 328 -
7.3	Validation	- 330 -
7.4	Results	- 331 -
7.4.1	Pressure	- 332 -
7.4.2	Reynolds Number	- 335 -
7.4.3	Velocity Profile	- 337 -
7.4.4	Wall Shear Stress	- 346 -
7.4.5	Wall Shear Stress Gradient	- 350 -
7.4.6	Time Averaged WSS	- 352 -
7.4.7	Oscillatory Shear Index	- 355 -
7.4.8	Relative Residence Time	- 356 -
7.5	Precedent Studies	- 358 -
7.5.1	Single Vessel Simulation	- 358 -
7.5.2	Virtual AVF Simulation	- 360 -
7.6	Solutions Errors Evaluation	- 368 -
7.6.1	Errors Calculations	- 369 -

8	DISCUSSION AND CONCLUSIONS	- 373 -
8.1	Ultrasound Imaging & Hospital Protocol	- 374 -
8.2	Matlab Image Analysis Editing.....	- 375 -
8.3	3D Model.....	- 377 -
8.4	CFD Simulations.....	- 378 -
8.5	FSI Simulations	- 380 -
8.6	General Conclusions	- 381 -
9	APPENDIX.....	- 383 -
9.1	Matlab Codes	- 384 -
9.1.1	DicomREAD	- 384 -
9.1.2	Edge Extraction: "EDGEpointsEXTRACTION"	- 386 -
9.1.3	Points Conversion: "EDGEpointsGENERATOR"	- 424 -
9.1.4	Velocity Profile Generation: "PulseWaveExtractor"	- 442 -
10	BIBLIOGRAPHY & REFERENCES.....	- 465 -

1 INTRODUCTION¹

¹ Eventual references on the chapter or paragraph titles are to be intended to be the main sources of the informations provided on that chapter or paragraph.

1.1 The Kidneys ⁽¹⁾ ⁽²⁾

The kidneys are two bean-shaped organs of the human body placed on the left and right sides of the abdominal cavity.

In the human's body, kidneys position is at each side of the spine in the abdominal cavity. Because of the liver encumbrances, they present an asymmetric location, with the right kidney being lower and smaller than the left one.

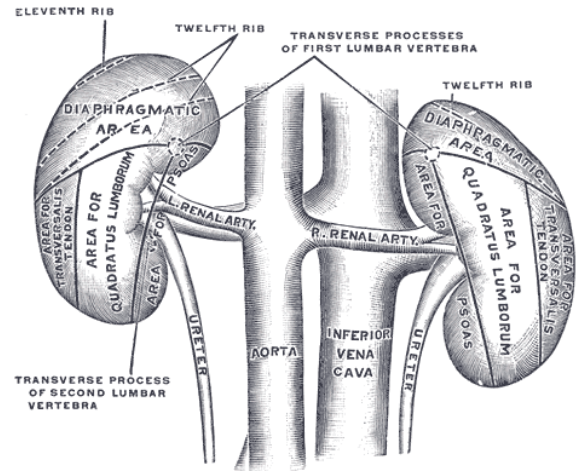


Figure 1 Human kidneys viewed from behind with spine removed. (2)

The kidney structure resembles a bean with a convex and a concave border, with the adrenal gland positioned at the very top of each one.

The weights of these organs can vary from person to person, but on average for male men is around 125 -170 grams, with an average length of 11.2 cm (left side kidney) and 10.9 cm (right side kidney), resulting respectively in a volume of 134 cm³ and 146 cm³.

Their primary role is to clean blood, producing urine, controlling also the blood pressure and balancing the fluids and mineral concentration in the body. A non-secondary activity related to the kidneys is the regulation of red blood cells, controlled by the adrenal glands on the top of them.

The basic unit of the kidney is the nephron, the very small filtering structure that filtrates blood. A nephron is made up of a glomerulus and tubules and their number in a single kidney exceeds the million. When nephrons get any damage, the kidney consequently loses efficiency.

Simple mechanisms are at the basis of every kidney function: filtration, reabsorption, and secretion, are the principal and took place in the nephrons. Filtration is operated by renal corpuscles, where blood is cleared from cells and large proteins that eventually becomes urine. The kidneys are able to manage 180 litres of filtrate a day reabsorbing a large percentage of that quantity and producing only approximately 2 litres of urine. Reabsorption is fundamental to achieve that, enabling the extraction of molecules from this ultra-filtrate and give back fluids into the blood. Secretion works in a reverse way, transporting molecules from blood into the urine.

The physiological operations of the kidneys can be summarised on:

- **Excretion of wastes**

As said, the kidneys work is to excrete waste products produced by metabolism into the urine. This is due to how the human body works, requiring energy to feed cells. The cells then produce waste products that must be expelled from the body, for this reason kidneys are so important. When the body can not remove adequately all these waste products, it starts to suffer, causing a sickness called "uremia". The amount of waste products present in the blood is called "azotemia."

- **Reabsorption of nutrients**

Kidneys are responsible for reabsorption of important nutritive like glucose, amino acids, bicarbonate, Na^+ , Cl^- , K^+ , Cl^- , Mg^{2+} , Ca^{2+} , phosphate and H_2O regained from the excreted materials.

- **Acid-Base balancing**

The kidneys then have also a primary role in maintaining the acid-base balance reabsorbing and regenerating bicarbonate from urine, and excreting hydrogen ions and fixed acids into urine.

- **Osmolality regulation**

Any significant rise in plasma osmolality is detected by the hypothalamus causing water reabsorption by the kidney and an increase in urine concentration, maintaining the right water and salt level of the body.

- **Blood pressure control**

Although the kidney cannot directly sense blood, long-term regulation of blood pressure predominantly depends upon the kidneys which release renin, an enzyme that regulates blood pressure

1.2 Kidney Diseases

Kidneys are subjected to a variable quantity of pathologies, the principal are: nephritic and nephrotic syndromes, renal cysts, acute kidney injury, chronic kidney disease, urinary tract infection, kidney stones, and urinary tract obstruction.

Various cancers affecting the kidney exist; the most common adult renal cancer is renal cell carcinoma. Cancers, cysts, and some other renal conditions can be managed with removal of the kidney.

When the renal function, measured by the glomerular filtration rate, is persistently poor, dialysis and kidney transplantation may be treatment options.

1.2.1 Chronic Kidney Disease (CKD) (3)

Chronic kidney disease occurs when the kidney nephrons are irreparably damaged. Each kidney has about a million of them, and when they get damaged, kidneys lose efficiency not being able, over time, to keep the body healthy. Once kidney function declines under a certain level, the waste products and excess fluid build-up in the blood causing sickness.

Some people are more prone to getting chronic kidney disease: people with diabetes or high blood pressure have a higher risk of developing kidney disease, as these are the top causes of CKD. Several studies have shown then that there is a correlation between obesity and chronic kidney disease too.

Those with a family history of kidney disease are also at increased risk of developing chronic kidney disease. For example, the polycystic kidney disease (PKD) is a hereditary kidney disease called which is transmitted from one or both parents to their children.

Glomerular diseases are the third leading cause of kidney disease, causing damage to the glomeruli in the nephrons. The most common glomerular diseases are glomerulonephritis (an inflammation of the glomeruli), and glomerulosclerosis (the glomeruli hardening). When the glomeruli become inflamed or harden, they are no longer able to conduct their work.

“Once enough of the glomeruli in the nephrons are destroyed, the chronic kidney disease develops to end-stage renal disease (ESRD) or kidney failure. At this point that either dialysis or a transplant is needed.” (4)

Sometimes however, kidneys loss of function does not happen slowly, this is the case of genetic birth defects, injuries, infections and some medical treatments. Luckily, even a single kidney can provide enough filtration to allow humans to survive with only one of them. For this reason, only when both kidneys are greatly compromised CKD develops.

1.2.2 Kidney Failure

Worth to underline that usually kidney failure is permanent, though some kinds of kidney diseases can get better after treatment. In some cases of non-acute kidney failure, the sole dialysis treatment can allow the kidneys get better, helping them to recover.

In chronic or end stage kidney failure anyway, kidneys do not get better and patients will need dialysis for the rest of their life.

“The National Kidney Foundation has classified five stages to help doctors better treat their patients based on how much kidney function the patient has left. Measuring a person’s Glomerular Filtration Rate (GFR) indicates how much blood is being filtered through the kidneys. The five stages of chronic kidney disease are defined as followed:

- *Stage 1: GFR > 90 millilitre/minute is CKD with normal or high GFR;*
 - *Stage 2: GFR = 60-89 ml/min is mild CKD;*
 - *Stage 3: GFR = 30-59 ml/min is moderate CKD;*
 - *Stage 4: GFR = 15-29 ml/min is severe CKD;*
- *Stage 5: GFR <15 ml/min is the end-stage renal disease (ESRD) or kidney failure.” (4)*

1.3 Treatment Options

“During the first two stages of kidney disease, a doctor may recommend diets, controlling blood sugar and blood pressure levels, stopping smoking, exercising and practising overall healthy habits.” (4)

Eventually, the kidneys function decreases to the point that they can no longer sustain the body. The subsequent treatment options for kidney failure can be dialysis, transplantation or palliative care (end of life management).

1.3.1 Kidney Transplant⁽⁵⁾

A kidney transplant can be an option if kidneys start to fail. Getting a transplant is not a cure for the end-stage renal disease (ESRD), but a well-matched and taken care of organ should last many years.

A kidney transplant is a surgery that takes a healthy kidney from a donor and replaces a failing kidney in another person. Kidneys can come from a living donor or a deceased organ donor: family members or others who are a good match may be able to donate one of their kidneys.

The waiting list for a kidney transplant can take several years and need nephrologist evaluations for applying for. If the tests determine the patient is a good candidate for a kidney transplant, he/she will be placed on the list. Then he/she will be called when a donor is found. Because cadaver kidneys are from the only people who donate their organs after their death, and there are more people who need kidneys than donate, the procedure is long.

1.3.2 Dialysis ⁽⁶⁾

“Dialysis is a process for removing waste and excess water from the blood and is used primarily as an artificial replacement for lost kidney function in people with kidney failure.” (6)

Dialysis helps the body by performing the functions of failed kidneys: it works to keep chemicals level and waste of the blood under safe limits exploiting the principles of the diffusion of solutes and ultrafiltration of fluid across a semi-permeable membrane, helping to control blood pressure.

During dialysis, the blood is removed from the body, passed through a filter and returned to the body.

Dialysis is a long process requiring 3-5 hours, 3 times a week. Gaining safe and easy access to the blood system is necessary for dialysis, and is obtained by one of three methods: catheter, arteriovenous (AV) graft and arteriovenous (AV) fistula.

Inside the dialysis machine, blood flows on one side of it, and a dialysate (a special dialysis fluid) flows on the other. To separate the two sides there is the semi-permeable membrane allowing smaller solutes and fluid passing through, but the blocking larger substances like the red blood cells and large proteins.

Dialysis can be done in a hospital, in external structures, or at home. Patient and doctor will decide which place is best, based on patient medical condition and wishes.

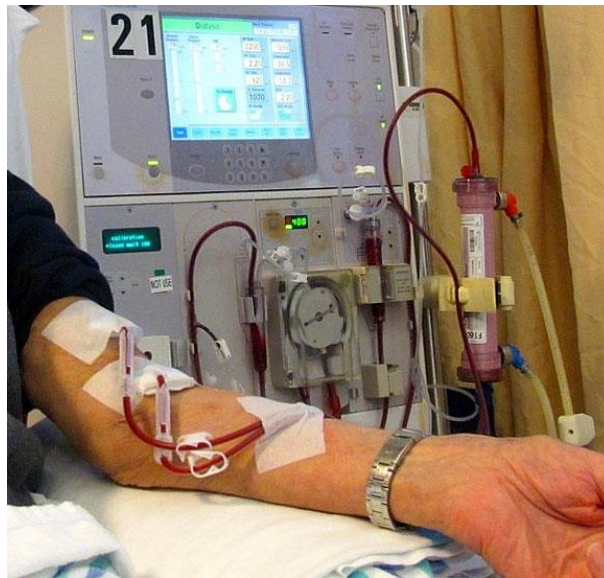


Figure 2 Patient receiving hemodialysis.

1.1.1.1 When Patients Require Dialysis

Once kidney function goes below 10-15% of normal function, the blood fills with toxins and fluids, endangering the life of the patient. The level of the waste products usually builds up slowly. (7)

Creatinine level and the blood urea nitrogen (BUN) level are the two chemicals measured as kidney health indicators. When these two levels rise, it means that kidneys are starting to lose the ability to cleanse the body from waste products. (7)

Life expectancy on dialysis can vary depending on general medical conditions and body treatment acceptance: the average life expectancy is 5-10 years, but in many cases 20 or even 30 years were exceeded. (8)

1.1.1.2 Types of Dialysis

There are two main types of dialysis: "hemodialysis" and "peritoneal dialysis."

Hemodialysis uses a special type of filter external to the body to remove excess waste products and water from the blood.

Peritoneal dialysis uses a fluid placed into the patient's abdominal cavity through a special plastic tube to remove excess waste products and fluid from the body. (7)

It is up to the patient and their kidney doctor to decide which of these procedures is best by considering lifestyle, other medical conditions, support systems, and how much responsibility and participation in the treatment program is desired.

1.4 Peritoneal Dialysis and How it Works

Peritoneal dialysis uses the patient's own body tissues inside of the belly (abdominal cavity) to act as the filter. The abdominal cavity is lined with a special membrane, the peritoneal membrane (7). A plastic tube called "peritoneal dialysis catheter" is placed into the abdominal cavity, while a special dialysate is then flushed into the abdominal cavity and washes around the intestines. The peritoneal membrane acts as a filter between this fluid and the blood stream. By using different types of solutions, waste products and excess water can be removed from the body.

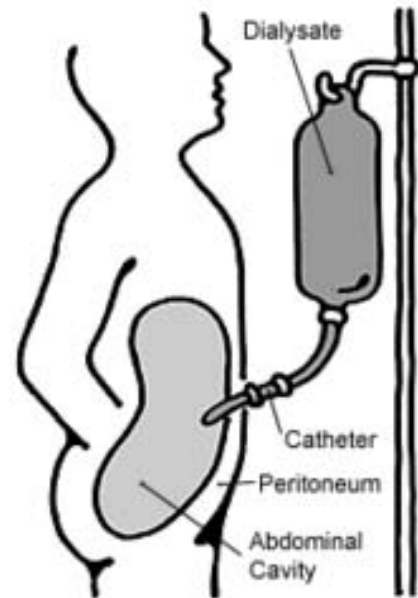


Figure 3 Schematic diagram of peritoneal dialysis. (6)

This process has to be repeated 4–5 times per day, and usually automatic systems can run more frequent exchange cycles overnight. Peritoneal dialysis though being less efficient than hemodialysis is able to provide the necessary filtration thanks to the longer application period of this. (6)

For those patients preferring more independence, peritoneal dialysis allows for more flexible scheduling and can be performed at home by the patient, often without help and no specialised equipment. This frees patients from the routine of having to go to a dialysis clinic multiple times per week but dialysis requires the patient to play a more active role in their dialysis treatment.

The major problem with peritoneal dialysis is infection because of the plastic tube going from the peritoneal cavity to the outside of the body, increasing the risks of bacterial infections. For this reason, of primary importance is the patient's responsibility for maintaining clean the catheter area where treatment is administered. (9)

1.5 Hemodialysis

Hemodialysis is the most popular method of treatment for patient, so that dialysis and hemodialysis are usually confused.

Hemodialysis provides excellent, rapid clearance of solutes and wastes and water removal by circulating blood outside the body through an external filter, called a dialyzer that contains the semipermeable membrane. The dialyzer is composed of thousands of tiny hollow synthetic fibres which act as a semipermeable membrane.

(6)

To have access to this procedure the patient needs a specialised plastic tube placed between an artery and a vein in the arm or leg ("Gore-Tex graft"), or a direct connection made between an artery and a vein in the arm ("Arteriovenous fistula").

For many patients, the major advantage of hemodialysis is minimal participation in the treatment, in exchange for undergoing to a specific schedule and travel to the dialysis unit three times a week. Hemodialysis also requires stricter diet control and fluid control than peritoneal dialysis. (9)



Figure 4 Hemodialysis machine. (10)

Patients generally need to go to the dialysis unit three times a week for treatments, which last from 2 ½ to 4 ½ hours. During this time, the dialysis staff checks the patient's blood pressure and adjusts the dialysis machine to ensure that the proper blood filtration. On occasion, patients who are very motivated may be able to perform dialysis themselves at home in a process called home hemodialysis. For larger patients more sessions are prescribed, as well as patients who have trouble with fluid overload. (7)

Moreover, there is growing interest in short daily home hemodialysis, which is 1.5 - 4 hr sessions given 5-7 times per week, usually at home. There is also interest in nocturnal dialysis, which involves dialysing a patient, usually at home, for 8–10 hours per night, 3-6 nights per week. (10)

1.5.1 Mechanism and Technique

Two needles are placed in the graft or fistula, and blood passes through the filter into the dialysis machine and returns to the patient. The blood flows in one direction and the dialysate flows in the opposite inside the dialysis machine: the counter-current flow maximises the concentration gradient of solutes between the blood and dialysate, helping to remove more urea and creatinine from the blood. (6)

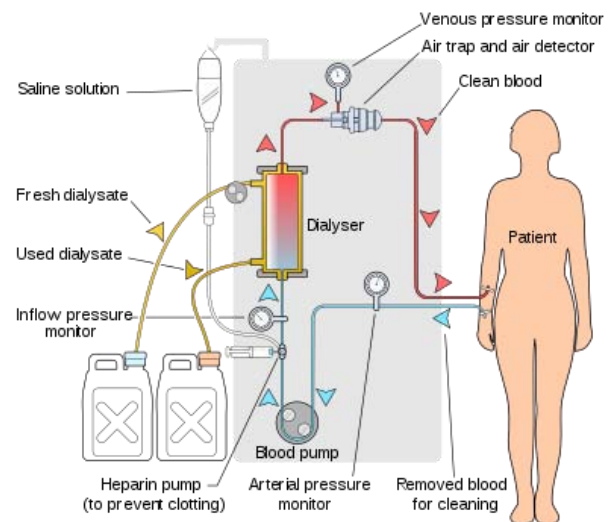


Figure 5 Schematic of a hemodialysis circuit. (10)

The fluid removal (ultrafiltration) is achieved by increasing the hydrostatic pressure across the dialyzer membrane (usually a negative pressure to the dialysate is applied).

This pressure gradient causes water to pass from blood to dialysate, allowing the required fluid removal. (6)

Urea and other waste products diffuse into the dialysis solution, which increases in their concentration; for this reason, a constant replacement of the dialysate ensures that the concentration of undesired solutes is kept under control. (6)

Potassium and calcium dialysate concentrations are kept similar to their natural levels in healthy blood, as for the bicarbonate, which level is set at a slightly higher to encourage its diffusion into the blood to stabilise pH and neutralise the metabolic acidosis that is often present in patients. (6)

A nephrologist, according to the needs of the individual patient, typically prescribes the levels of the components of dialysate. (6)

1.5.2 Dialyzable Substances

Dialyzable substances, substances that can be removed using dialysis, have following properties:

- low molecular mass
- high water solubility
- low protein binding capacity
- prolonged elimination (long half-life)
- small volume of distribution.

Substances being dialysed are Ethylene glycol - Procainamide - Methanol - Isopropyl alcohol - Barbiturates - Lithium - Bromide - Sotalol - Chloral hydrate - Ethanol - Acetone - Atenolol - Theophylline - Salicylates.

1.5.3 Dialysis Equipment

1.1.1.3 Water System ⁽¹⁰⁾

An extensive water purification system is critical for hemodialysis: being the patient blood at direct contact with external water, even a little trace of contaminants or bacteria can filter into the patient's blood. For this reason, water used in hemodialysis is carefully purified before use. Initially, water is filtered and its pH is corrected, then it is run through a tank to adsorb organic contaminants. Final removal of leftover electrolytes is done, leaving ultrapure water.

Once purified water is mixed with dialysate concentrate and its conductivity. During dialysis, the conductivity is the indicator monitored to control chemicals concentration and filtration.

1.1.1.4 Dialyzer ⁽¹⁰⁾

The dialyzer is the part of the equipment that actually filters the blood. It is a cylindrical bundle of hollow fibres, whose walls are composed of a semi-permeable membrane. This assembly stays into a clear plastic cylindrical shell with four openings. One opening at each end of the cylinder communicates with each end of the bundle of hollow fibres, forming the "blood compartment" of the dialyzer.

Blood is pumped through this bundle of very thin capillary-like tubes, while the dialysate is pumped through the space surrounding the fibres. A pressure gradient is applied when fluid removal from blood is necessary.

Dialyzers come in many different sizes: larger dialyzer with a larger membrane area usually removes more solutes, especially at high blood flow rates. Most dialyzers have values of efficiency (membrane area x permeability) between 500 to 1500 mL/min.

The dialyzers either may be disposable or be reused, but reuse requires an extensive procedure of high-level disinfection. The consensus today is that reuse of dialyzers, if done carefully and properly, produces similar outcomes to a single use of dialyzers.

1.1.1.5 Membranes ⁽¹⁰⁾

Dialyzer membranes come with different pore sizes. So called "low-flux" membranes have smaller pore size and "high-flux" membranes have larger pore sizes. Pore size is related to different size molecules removal: "low-flux" dialyzers cannot filtrate large molecules, explaining the need for high-flux dialyzers. However, such dialyzers require newer dialysis machines and high-quality dialysis solutions to control the entire dialysis process properly.

First dialyzer membranes were made of cellulose, but they were not very biocompatible. New generation membranes are made from synthetic materials, and can be made in either low- or high-flux configuration, but most are high-flux. Nanotechnology is being used in some of the most recent high-flux membranes to create a uniform pore size.

1.5.4 Dialysis Types

1.1.1.6 In-Centre Conventional Hemodialysis (11)

With in-centre hemodialysis, a patient goes to a dialysis centre where the staff of nurses and technicians undertake the treatment. Conventional hemodialysis is usually done three times per week, for about 3–4 hours for each treatment, during which the patient's blood is drawn at a rate of 200-400 mL/min. The machine is connected through two tubes and needles inserted in the dialysis fistula or graft, or connected to one port of a dialysis catheter. During the procedure, the patient's conditions (blood pressure) are closely monitored to guarantee a safe and comfortable performing dialysis. During the treatment, the patient's entire blood volume (about 5000 ccs) circulates through the machine every 15 minutes. During this process, the dialysis patient is exposed to a week's worth of water for the average person. (10)

1.1.1.7 Home Hemodialysis(12)

There are three types of home hemodialysis (standard, short daily and nocturnal), all of them requiring a home hemodialysis machine available from multiple companies.

Short daily home hemodialysis has a shorter treatment time but requires more frequent sessions about five to seven days each week for two and a half to three hours. This treatment is more convenient for people who want to be independent or likes to travel, and it is less stressful even if requires more frequent access. This type of dialysis application is simple with catheters but more problematic with fistulas or grafts. (6)

Studies have demonstrated the clinical benefits of dialysing frequently and for shorter periods for up to 6-8 hours, especially if undertaken by night. This type of hemodialysis, called "nocturnal daily hemodialysis", has shown a significant improvement in both small and large molecular weight clearance. These frequent long treatments are often undertaken at home while sleeping but are flexible to schedules changes. (6)

1.5.5 Dialysis Disadvantages

The disadvantages in the dialysis treatments are several, as:

- restricts independence, as people undergoing this procedure cannot travel around because of supplies availability
- requires more supplies such as high water quality and electricity
- requires reliable technology like dialysis machines
- the procedure is complicated and requires that caregivers have more knowledge
- requires time to set up and clean dialysis machines, and expense with machines and associated staff.

1.6 Hemodialysis Access Options ⁽¹³⁾

A vascular access is the patient predisposed connection, which makes hemodialysis treatments possible. This is a surgically created connection for the needles used to remove and return blood during hemodialysis. The vascular access should be in place weeks or months before the first hemodialysis treatment to ensure a correct function.

Two types of vascular access designed for long-term use include the arteriovenous (AV) fistula and the AV graft. The third type of vascular access, the venous catheter, is for short-term use.

The type of access is influenced by factors such as the expected time course of a patient's renal failure and the condition of his or her vasculature.

1.1.1.8 Arteriovenous Fistula (AVF)

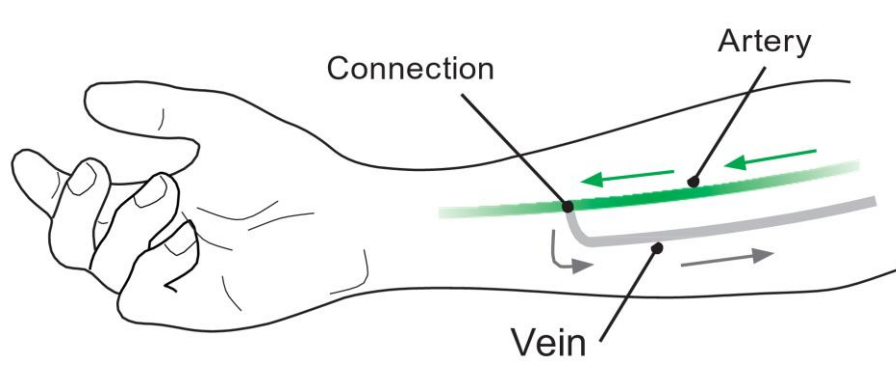


Figure 6 ArterioVenous Fistula in the forearm.

The arteriovenous fistula (AVF) is the preferred type of access for dialysis. It consists on the sewing of a superficial vein to an artery, resulting in the vein enlargement over a period of about six weeks until the fistula thickens and matures enough to be ready for dialysis.

This is the best type of access in terms of best duration and the least complications (less likely to form blood clots or become infected). Unfortunately, not everyone's veins are good enough to have an AV fistula. (13)

1.1.1.9 Arteriovenous Graft (AVG)

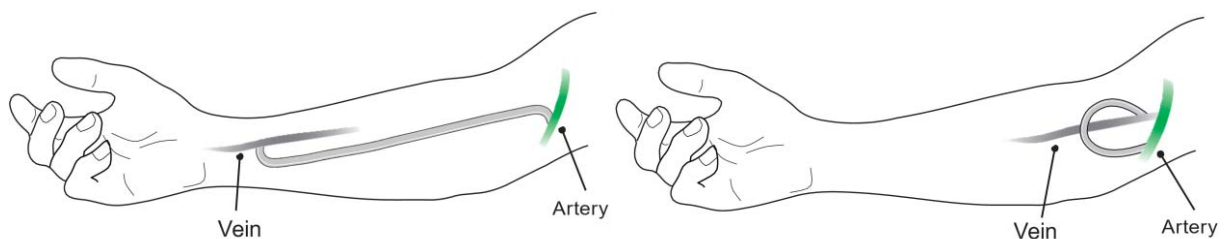


Figure 7 Straight and Loop Graft in the forearm.

The second strategy to Hemodialysis access is the arteriovenous graft (AVG), where a special Teflon tube bridges between an artery and vein under the skin. This can be used for dialysis in about two to three weeks or less, but may not continue working as long as a fistula (can be prone to blood clots due to the vessels narrowing over time).

AV graft is the second choice for a long-lasting vascular access. (13)

1.1.1.10 Catheter

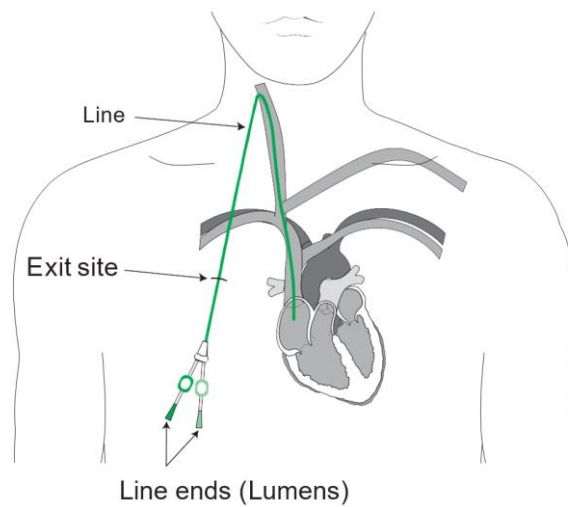


Figure 8 Tunnelled venous catheter.

Sometimes a patient requires immediate dialysis care. In these situations, a catheter is placed in one of the large veins of the neck, chest or groin. Tubes from the dialyzer are attached to the catheter, one to take blood from the body and another to put the blood back in.

Catheters are recommended to be used only for a short period of time or in emergency cases where dialysis needs to be administered right away, because they cause more infections, and should be avoided unless absolutely necessary.

Usually happens that patients may have multiple access procedures, usually because an AV fistula or graft is maturing and a catheter is still being used.

The placement of a catheter is usually done under light sedation, while fistulas and grafts require an operation. (13)

2 THE MEDICAL PROBLEM²

² Eventual references on the chapter or paragraph titles are to be intended to be the main sources of the informations provided on that chapter or paragraph.

Patients with end-stage renal disease are largely dependent on the dialysis as renal replacement therapy. Chronic hemodialysis requires adequate vascular access. Arteriovenous Fistulas (AVFs) are the preferred solution considering the higher patency rates and lower complications than other solutions. However, AVF durability is far from optimal, with one-year primary patency rates ranging from 60% to 65% (not considering fistulas that have not matured). Maturation failure contributes significantly to the poor AVFs patency rates, 60% of which is not suitable for dialysis between 4 and 5 months after surgery although these numbers vary between different types of AVF.

According to KDOQI (Kidney Disease Outcomes Quality Initiative) guidelines, AVFs maturation is considered clinically effective if 6 weeks after surgery the fistula supports a flow of 600 ml/min is at a maximum of 6 mm from the surface and has a diameter of > 6 mm. (14)

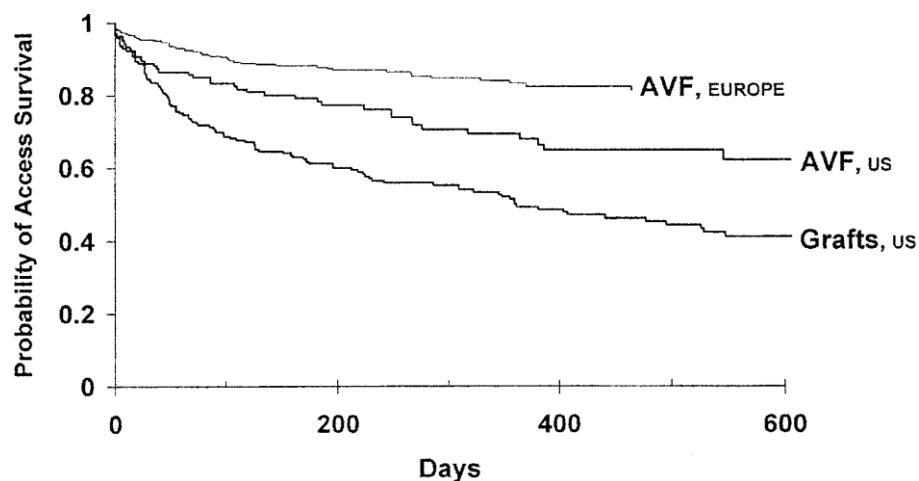


Figure 9 Fistula versus graft survival in patients starting hemodialysis. (17)

2.1 The Arteriovenous Fistula (AVF) ⁽¹³⁾

An AV fistula is a connection, made by a vascular surgeon, of an artery to a vein. Arteries carry blood from the heart to the body, while veins carry blood from the body back to the heart. The surgeon usually places an AV fistula in the forearm or upper arm, which causes extra pressure and extra blood to flow into the vein, making it grow large and strong. In this way, the enlarged vein provides easy, reliable access to blood vessels. (13)



Figure 10 Example of an ArterioVenous Fistula Established in a forearm.

This kind of operation is made because untreated veins cannot withstand repeated needle insertions collapsing under the strong suction of the dialysis machine.

AV fistula is recommended over the other types of access because it provides good blood flow for dialysis, it lasts longer and it is less likely to get infected or cause blood clots than other types of access.

As previously described, AVF is used to provide an access to the dialysis machine through two needles: one needle to carry blood out of the body to the dialyzer, the other to carry filtered blood back into the body.

2.1.1 Benefits of AV Fistula for Dialysis

The use of the arteriovenous fistula AVF for dialysis is considered the best option because, in comparison to other types of access, it has lower complication rates, is less prone to infection or blood clotting and allows for a greater blood flow. Moreover, AV fistula has demonstrated to be less expensive to maintain, and with a longer lifespan. To date, over 66% of continued patients and more than 50% of all new patients on dialysis use a fistula. (15)

2.2 Types of AV Fistula for Dialysis (16)

There are three basic types of AVF dialysis:

- Radial Cephalic fistula;
- Brachial Cephalic;
- Brachial Basilic Transposition.

All of them are created from native vessels, with no use of synthetic materials in the body. The surgical process is relatively simple and relatively quick and at the end requires a maturation time in order to obtain the better condition of vessels and blood flow. (15)

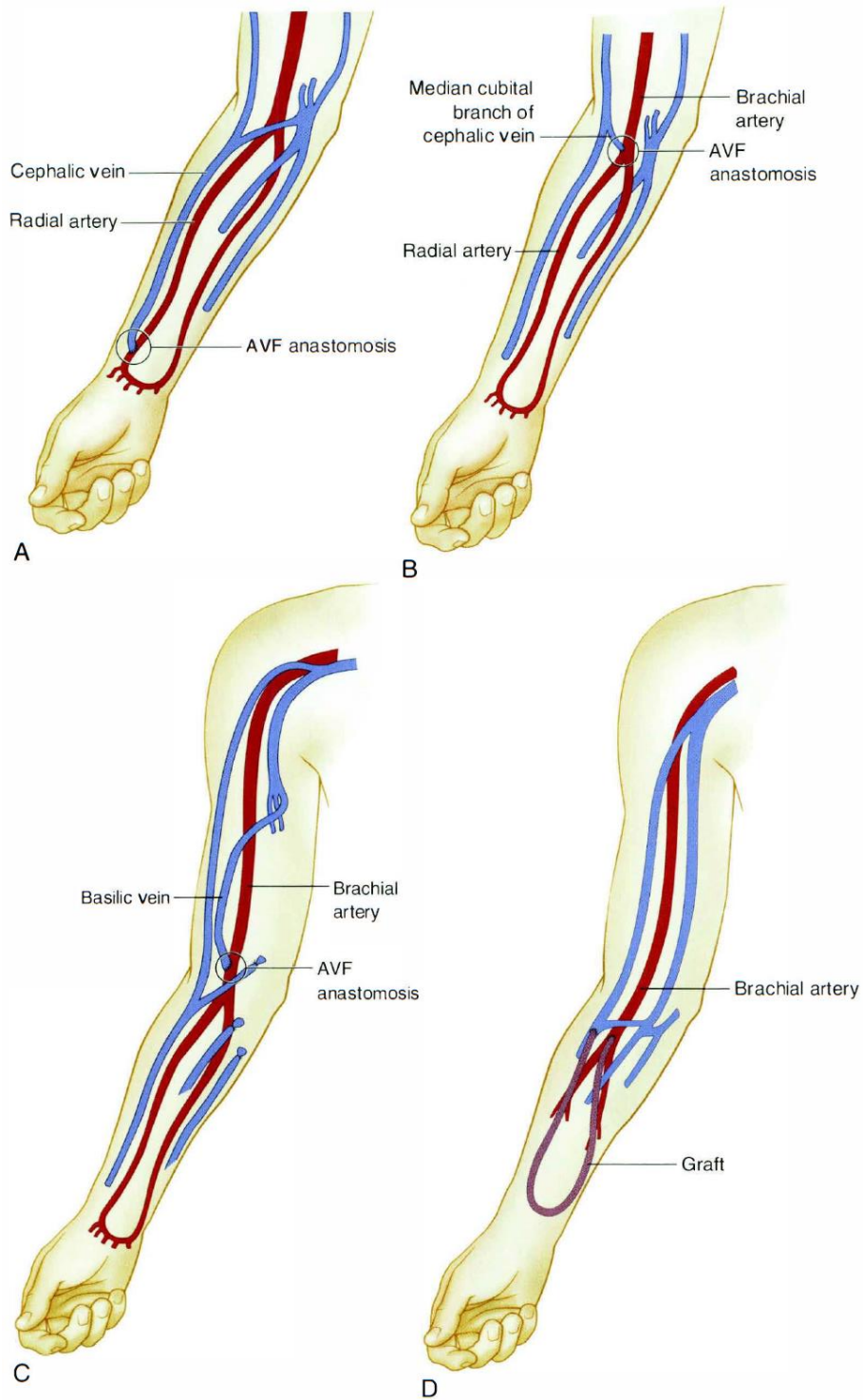


Figure 11 Anatomic drawings of the most common hemodialysis accesses: radio-cephalic fistula (A), brachio-cephalic fistula (B), brachio-basilic vein fistula (C), and the most common ArterioVenous Graft (D).

2.2.1 The Radial Cephalic Fistula

Radial Cephalic Fistula is quite hard to create. The surgical operation consists on the cephalic vein to radial artery anastomosis, establishing a connection through them. The radial cephalic anastomosis provides a lower blood flow than the other two types, but preserves upper arm vessels for later attempts, if needed. The radial cephalic arteriovenous at the wrist is the recommended first choice for hemodialysis access. (16)

2.2.2 The Brachial Cephalic Fistula

Brachial Cephalic Fistula is created by using the larger upper arm cephalic vein and connecting it to the brachial artery. Due to the bigger size of these vessels, it is the easiest fistula to create, requiring less dissection and being easier to cannulate. The brachial-cephalic fistula allows for higher blood flow, but also has a slightly higher incidence of steal syndrome. (16)

2.2.3 The Brachial Basilic Fistula

Brachial Basilic Fistula is more complex to create, requiring the vein to be elevated and transposed in order to become usable. The brachial-basilic fistula is associated with more patient morbidity, but also tends to be better preserved. The shorter length makes the brachial-basilic fistula more difficult to cannulate, and has a higher incidence of steal syndrome. This form of access is used as a last chance in patients whose previous fistulas had failed. (16)

2.3 Creation of an AVF

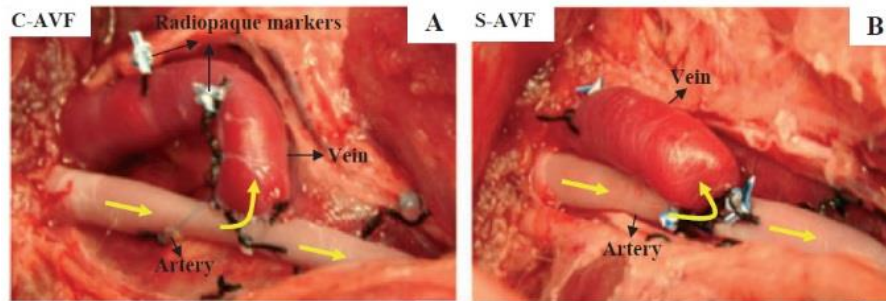


Figure 12 Surgical configurations of (A) Curved-AVF and (B) Straight-AVF during surgery. Arrows show the flow direction.

Creation of an AV fistula is an interdisciplinary task, which in many countries is delegated to a “fistula manager” who is responsible for both nephrology, surgery, and radiology fields. The creation of fistulae should be delegated to a restricted number of dedicated surgeons because nowadays only surgeons with considerable expertise only achieve good results. (17)

For the operation, the patient does not need full anaesthesia.

Before AV fistula surgery, the surgeon performs a mapping test of the vessels using Doppler ultrasound, and then the radiologist interprets the images. Ultrasound uses a device, called a transducer that bounces safe, painless sound waves off organs to create an image of their structure. A Doppler ultrasound shows how much and how quickly blood flows through arteries and veins so the surgeon can select the best blood vessels to use.

An AV fistula frequently requires 2 to 3 months to develop, or mature, before the patient can undergo to hemodialysis. When a fistula fails, a surgeon must repeat the procedure. (13)

2.3.1 Surgical Technique ⁽¹⁸⁾

Nowadays, the most used technique of anastomosis is the (artery-) side to (vein-) end technique, even if the first anastomoses used were side-to-side; another strategy, the end-to-end technique was introduced, but today the side-to-end technique remains the most commonly used approach. All three techniques have advantages and disadvantages. (17)

The general surgical operation is described just below:

- 1) After the skin incision in the distal arm, diathermy and scissors are used to dissect around the fat tissue. The vein is located, and isolated. Care is taken to avoid direct contact with the vein to avoid thermal damage. Surgical clips are used for significant feeding vessels and ligation for vein branches. The vein is thus dissected, but not yet ligated. (18)*



Figure 13 Skin incision medial to the vein marked pre-operatively. (18)

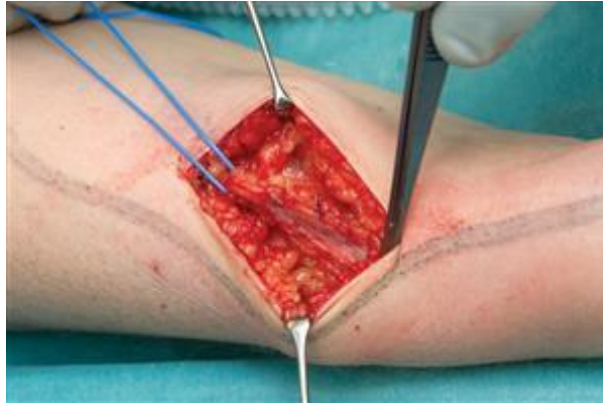


Figure 14 Dissection of the vein with its surrounding tissue. (18)

- 2) The radial artery is dissected on the medial and lateral side until a pedicle of the artery with its satellite veins is isolated by vessel loops for proximal and distal control. (18)*



Figure 15 Vein (blue vessel loop) and artery (red vessel loop) dissected by No Touch Technique. (18)

- 3) The artery is opened and a 6-8 mm longitudinal anterior arterotomy is performed. Both vessels are prepared for the anastomosis while preserving the pedicle around it. (18)*



Figure 16 The vein is prepared for end-to-side anastomosis. (18)

4) Vein to artery anastomosis (end-to side) is created with a continuous suture.



Figure 17 Anastomosis by parachute technique. (18)



Figure 18 The radiocephalic fistula completed. (18)

5) Back flow and then in-flow is restored.

6) The wound is closed using subcutaneous and intra-cutis absorbable separate sutures. The fistula is then examined for thrill both by palpation and auscultation. (18)

2.3.1.1 Side-to-Side Anastomosis⁽¹⁷⁾

The side-to-side is the vessels configuration presenting the most technical simplicity, allowing a practical testing of the venous distensibility, especially before it is ligated and after the creation of the anastomosis.

This type of anastomosis however, presents several problems related to the risk of venous hypertension causing swelling of the hand (particularly for anastomoses in the elbow area). The solution to that is achieved by ligation of the distal run-off vein, practically changing the side-to-side configuration into a side-to-end configuration. This requires additive surgical operations and complications.

2.3.1.2 End-to-End Anastomosis⁽¹⁷⁾

The end-to-end anastomosis is a particular configuration rarely used. It has the advantage to avoid hyper-circulation, having a relatively limited flow compared to the other solutions. However, its surgical complication is significant, presenting very great difficulties in case of large vessels dimension discrepancy. Moreover, the directly closed

junction of the vein and the artery frequently causes the ischemia of the hand, especially in elder and diabetic patients. An additional problem that this technique causes is related to thrombosis, which if eventually occurs, it is prone to extend into both arterial and venous limbs. Finally is to underline that even the major advantage relative to the good flow provided is not always achieved: especially in sclerosed vessels, the anastomosis is obtained with an acute angle between the vessels, causing disturbed un-physiological blood flow affecting the AVF success.

2.3.1.3 Side-to-End Anastomosis ⁽¹⁷⁾

Although all these techniques for anastomosis are available, the side-to-end anastomosis has become the preferred choice for the vascular access creation. Even when the vein and the artery are far from each other, this technique is anyhow the most used to operate the vessels anastomosis. The main reason of that is to ascribe to a common prevention of an acute angle configuration between the vein and the artery, helping to achieve a good blood flow. Eventual thrombosis usually affects only the distal venous limb, allowing an easier treatment of this pathology and permitting to create a more proximal anastomosis in case of major problems.

However, this type of anastomosis still presents some problems, which probably are the cause of the high primary malfunction rates reported in practice and studies.

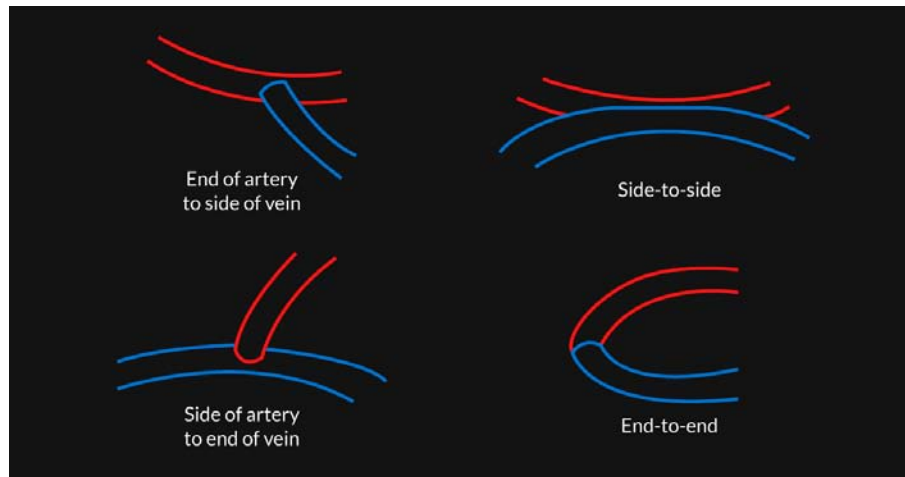


Figure 19 Principal strategies in the anastomosis creation.

2.3.2 Technical Points Determining Success ⁽¹⁷⁾

An AV fistula causes an un-physiological high-flow into the vein, so that every obstacle to blood flow can cause turbulence, damaging endothelial cells, and increasing the risk of stenosis related to that. For this reason kinking, acute angles, torque etc. must be avoided.

The AVF angle between the vessels is the factor determining the length of the. As said the primary intention is to keep the angle the less acute possible.

Even clamping the thin-walled veins during the operation should be avoided to prevent late stenoses, preferring to that a digital compression, which is sufficient to locally interrupt the blood flow. For the same reason, veins torque is not welcome (the principal strategy to avoid it is with a preventive rotation before the vessels junction).

Veins ligation is discouraged at the time of first fistula surgery because usually it is impossible to predict the future function of the fistula, especially because venous tissue may be useful later on. If venous hypertension develops, there can be a targeted ligation then.

Sometimes veins have to be mobilised to be more easily adapted to the artery, but this manoeuvre predisposes to sclerosis and stenosis, so this should not be done at the time of the first surgical intervention because veins are still thin-walled. When veins have matured and remodelled, they can be used. For this purpose, it is possible to create a temporary AV anastomosis, not to obtain a fistula for puncturing, but to create a vein suitable for later transposition or superficialization.

Wrist anastomosis is sensible only in case both artery and vein are able to dilate so as to accommodate an increase in blood flow (the increase is of a factor between 20-100). Only the surgeon is able to determine the quality of the vessels using an ultrasonographer. This is an important operation particularly in case of elderly and diabetic patients, who usually presents sclerosed or calcified radial arteries. Worth to note that the radial artery rarely develops atherosclerotic plaques.

Also relevant is that at the level of the wrist, the cephalic vein divides into two branches, with the smaller closer to the radial artery and the larger running across the dorsum of the hand. The smaller branch usually has problems to be used, because of the presence of a valve impeding venous run-off, and being the lumen of the vessel usually unable to accommodate the needed flow rates. In this case, it is often preferred a more proximal site for anastomosis.

Like in chess, in a fistula establishment one must always anticipate the next two or three moves and must consider what possibilities remain after the fistula has potentially failed. However, the creation of an AVF does not preclude future corrective surgery.

Related to the anastomosis site and length there is blood flow: the higher the site of anastomosis, the higher the future blood flow, and the smaller should the anastomosis consequently be.

It is important to consider that the uremic patients, particularly the diabetic uremic patients, have a higher risk of infection. It is to stress that an increasing number of patients requires new approaches respect the classical wrist fistula, because of the inability to

achieve high flow rates in diabetic and elderly patients. The solution may be anastomosis at a more proximal level.

2.4 Pre-Evaluation and Post-Monitoring the AVF

It has recently been recognised that Ultrasonography and Duplex sonography are valuable for preoperative assessment that will provide useful information to the surgeon. The primary aim is the indication to the surgeon whether an anastomosis at the usual site above the wrist will be successful and whether a steal phenomenon is a likely outcome. (17)

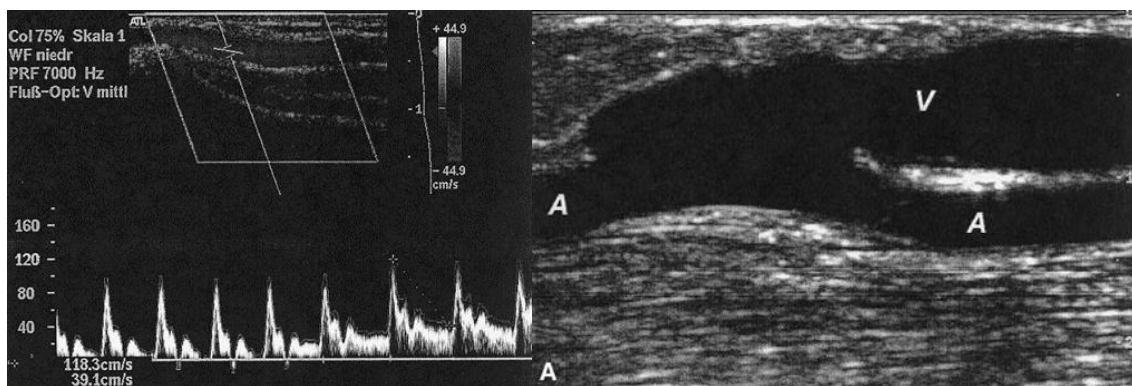


Figure 20 Pre-operative Ultrasound-Doppler blood velocity assessment (left); B-mode sonogram showing a longitudinal section of an AVF: vein (V) and artery (A) are detected (right). (17)

The lumens of the radial artery and the vein are a meaningful parameter to assess. Poor AV-Fistulas outcome could be predicted by these vessels diameters:

- Arterial diameter < 1.5 mm (internal diameter)
- Venous diameter < 2.5 mm (using a tourniquet)
- Resistance index > 0.8 (after fist clenching). (17)

After AVF establishment, periodic controls are made by nurses, trained to check the progressive increase of venous inflow pressure and post-puncture bleeding time, and by the doctors, to detect development and progression of stenoses in time to prevent eventual thrombosis. Normal controls happen every few weeks.

The critical flow rate in all thrombosed fistulae is < 200 ml/min, which is of far less than what is required to enable a good dialysis: low blood flow cause dialysis to be ineffective and recirculation will occur.

Several procedures help recognition of critically low blood flow rates and impending stenoses at the bedside:

- Auscultation (high frequency bruits at the site of stenosis);
- Hand elevation test (collapse of the post-stenotic venous segment and persisting congestion of the pre-stenotic segment);
- Prolonged bleeding after removal of the needle from the puncture site;
- Elevated venous inflow pressure during hemodialysis sessions, particularly progressively increasing venous inflow pressures during consecutive dialysis sessions;
- Once a critically low fistula flow and stenosis have been documented, one has two alternatives: interventional radiology or corrective surgery.

2.5 Physiology and Pathophysiology of Fistula Maturation



Figure 21 An established fistula with a sensitive venous enlargement.

2.5.1 Vascular Remodelling and Adaptation to High Flow ⁽¹⁷⁾

In the study of Wedgewood et al. measuring the flow rates in the radial artery before and immediately subsequent to the creation of an end-to-side fistula, the flow increased from 21.6 ± 20.8 ml/min to 208 ± 175 ml/min immediately after the operation. In well-developed fistulae, flow rates may ultimately reach values of 600 to 1200 ml/min. (19)

This flow increase is to attribute to both vasodilation and vascular remodelling. It was found that the intima media thickness remained practically unchanged while the diameter of the vein increased. Moreover, the venous dilation causes an average shear stress reduction, with a return to normal values by 3 months. At the same time, the venous limb of the AV fistula undergoes to eccentric hypertrophy, despite a remodelling of the radial artery characterised by an increase in diameter and blood flow, without arterial hypertrophy. (20) (21)

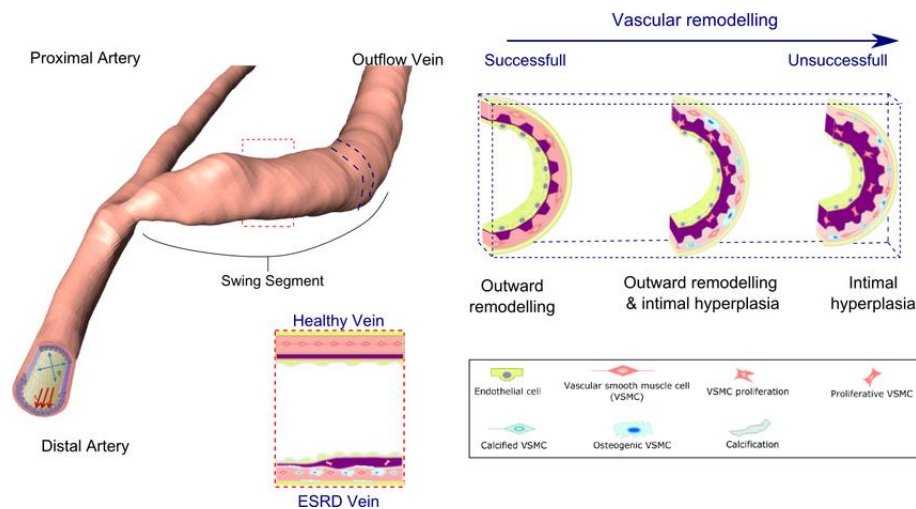


Figure 22 Typical geometry of an arteriovenous fistula illustrated with the various vascular remodelling responses. (22)

The changes in blood flow after the creation of an AV fistula initiate compensatory responses that are still to be deepened. Apart from primarily NO (nitric oxide) mediated vasodilation, reorganisation of cellular and extracellular components induces an adaptive remodelling of the vessel wall, altering wall geometry and enlarging the arterial diameter. This response usually occurs rapidly, especially at high-induced shear stress. (23) Endothelial cells play a central role in adaptive remodelling because shear stress acts on them, deforming them in the direction of blood flow and causing rapid cytoskeletal remodelling with a signalling cascade which leads to the release of nitric oxide (NO).

The crucial importance of endothelial cells is because the de-endothelialisation eliminates the dilation resulting from an increase of flow. The acute flow-induced endothelial release of nitric oxide (NO) have been documented. (17)

"The first step of remodelling involves controlled removal of pre-existent vessel wall constituents. The arterial wall of an early AV fistula exhibits fragmentation of the internal elastic lamina increasing arterial distensibility." (17)

Worth to note is that uremics generate a reduced amount of NO, causing abnormalities in endothelial cells, increase in intimal thickness and intimal cell proliferation in their arteries when exposed to low-flow conditions.

"It is thought that the changes provoking delayed stenoses are initiated during surgery and consist of denudation of the surface endothelial cells and with deposition of fibrin and thrombi. " (17)

Another factor influencing the evolution of the AV fistula is the effect of the continuous punctures on the AV fistula: puncture displacing tissue causes an endothelial defect and a scar. After healing, the edges of the puncture hole stay apart, resulting in a continuous local enlargement of the AVF mediated by the punctures frequency.

Because of that, three different options for cannulation have been developed: (a) the rope ladder pattern, (b) the area puncture pattern, and (c) the buttonhole pattern.

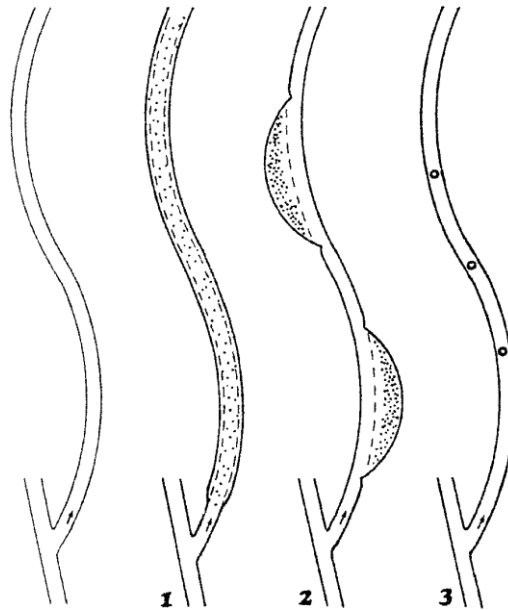


Figure 23 The three different types of cannulation techniques. 1, rope-ladder puncture; 2, area puncture; 3, buttonhole puncture. (17)

In the rope ladder pattern is the most used technique, with the punctures regularly distributed along the entire length of the vein, inducing a distributed dilatation all along the vein.

In contrast, with the area puncture technique, they are restricted to a small area.

With the buttonhole technique, punctures are always performed through the exactly identical spot.

These last two techniques are most prone to circumscribed dilatation, disruption of wall texture, and aneurysm formation. Thinning of the wall of the vein causes progressive enlargement of an aneurysm. (17)

2.5.2 Remodelling and Wall Shear Stress

In 1983, the study of Zarins et al. on the carotid blood flow demonstrated that intimal thickening and atherosclerosis occurred in regions of low wall shear stress with flow separation and non-unidirectional flow. (24) Numerous studies in different vascular models have confirmed this correlation between low flow, low wall shear stress and intimal thickening.

For example, Roy-Chaudhury et al. state that:

“The increase in shear stress usually results in endothelial quiescence and survival, the orientation of endothelial cells in the direction of flow and the secretion of anti-inflammatory and anticoagulant mediators. At a physiological level, this generally results in a dilatation of the vessel with a reduction in neointimal hyperplasia (beneficial vascular remodelling). These vascular responses also tend to return shear stress levels back toward their baseline.

In contrast, a reduction in blood flow and shear stress is associated with endothelial cell activation and proliferation, cellular shape change and the release of inflammatory and pro-coagulant substances. At a physiological level, this manifests as vascular constriction and increased neointimal hyperplasia. Moreover, the specific pattern of shear stress also appears to play an important role in the vascular response, with physiological (laminar) shear stress resulting in endothelial stability and appropriate dilatation, while oscillatory shear stress (of which we will talk later) often results in a pro-inflammatory state with increased cellular proliferation.” (25)

2.5.3 Remodelling and Circumferential Pressure

Transmural (i.e. circumferential) pressure is the second major hemodynamic parameter that is presumed to influence the AV fistula behaviour. Numerous studies demonstrated that an increase in pressure leads to wall thickening, with a reduction of transmural pressure back toward the basal level. Basing on these result, the hypothesis is that neointimal hyperplasia in the AV fistula maturation is caused by an abnormal wall shear stress profile, while medial hypertrophy is due to the increase in transmural pressure. (25)

2.5.4 Intimal Hyperplasia ⁽¹⁴⁾

Intimal Hyperplasia (IH) is a pathologic lesion in AVFs that may result in stenosis and thrombosis.

Usually, blood physiological conditions are related to high laminar shear stress triggering endothelial quiescence, endothelial alignment in parallel with the flow and secretion of anti-inflammatory and anti-coagulant substances, thus preventing IH.

The opposite condition of low flow and WSS levels, with the presence of oscillating flow patterns, is more prone to endothelial cell activation with increased expression of pro-coagulant and pro-inflammatory mediators that predispose to IH, as said by Rothuizen et al:

“Although AVFs generally express high-flow profiles, the presence of few spots with low and oscillating flow and WSS levels in the venous part of the AVF has been correlated to intimal hyperplasia prone regions.” (14)

Alterations in anastomosis angle could affect the flow rates and patterns, potentially influencing IH formation, with angles around 30° generating the most favourable outcomes.

Nevertheless, abnormal WSS profile is not the only promoter of IH, being IH observed also in veins prior to AVF establishment. As you will see below, outward remodelling is also involved in the process of IH, with the impaired result of both contributing to the fistula failure.

2.5.5 Outward Remodelling ⁽¹⁴⁾

After the AVF is established, the rapid increase in flow causes vascular distension and nitric oxide (NO) synthesis by endothelial cells, acting on Vascular Smooth Muscle Cell (VSMC) relaxation and leading to vasodilation. Together with these events, the haemodynamic changes promote the structural vascular remodelling resulting in an arterial and venous calibre increase and thickening, especially for the venous wall.

The driving forces of all these events are the wall shear stress (WSS) and wall tension, which provoke a diameter increase response of the vessel in an attempt to reduce WSS to pre-AVF levels (0.5-2 Pa).

Furthermore, the pressure increase in the venous side of the fistula stimulates the medial thickening, an another vessels adaptive response.

Rothuizen et al. noted that:

“Within the first week after fistula formation, the flow increased accompanied by the increase in WSS resulting in a progressive increment in venous luminal calibre. Then, following vessels distension, WSS gradually returns to a physiological range.” (14)

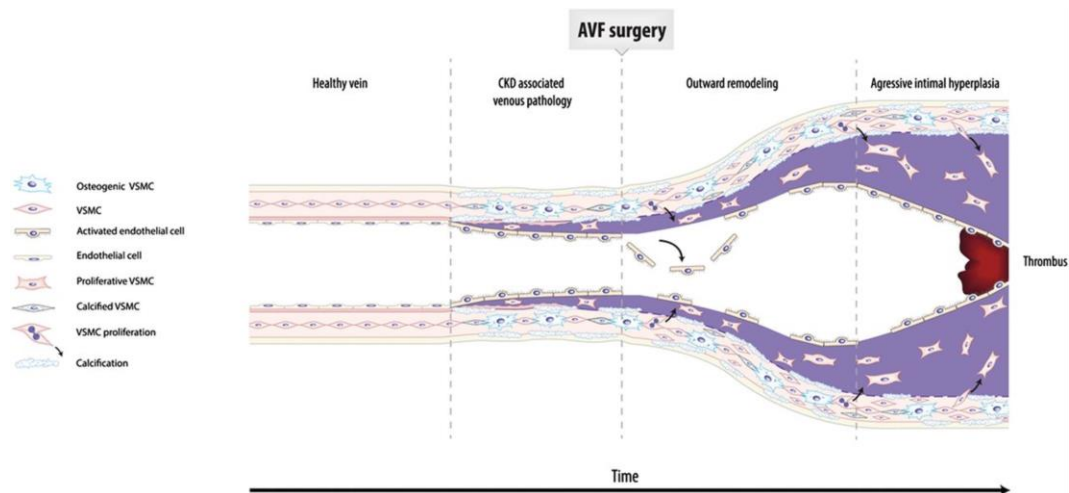


Figure 24 Potential mechanisms of the remodelling response upon fistula creation. (14)

In addition, both the vessels internal and external diameters increase, with an increase of cross-sectional wall area.

On a biological level, endothelial cells function as mechanosensors, responding to the WSS stimuli, converting them into biochemical signals. With an increased circumference of the vessel wall, it seems logical that some VSMC reorganisation should occur as well to keep pace with the expansion.

2.5.6 Impaired Outward Remodelling and Intimal Hyperplasia (IH) (14)

It is to stress how the majority of the stenotic lesions in fistulas failures are located in the juxta-anastomotic venous tract. This could suggest that venous luminal expansion, together with IH, may control the luminal calibre, allowing the fistula to mature. The adequate outward remodelling could preserve luminal calibre and may, therefore, be valuable for successful fistula maturation.

The hypothesis is that the net result of adaptive outward expansion, vessels narrowing by IH and thrombosis may determine luminal calibre, flow and long-term AVF patency. However, the exact mechanisms underlying maturation failure are still unknown, even if impaired outward remodelling, as well as intimal hyperplasia (IH), are known to contribute.

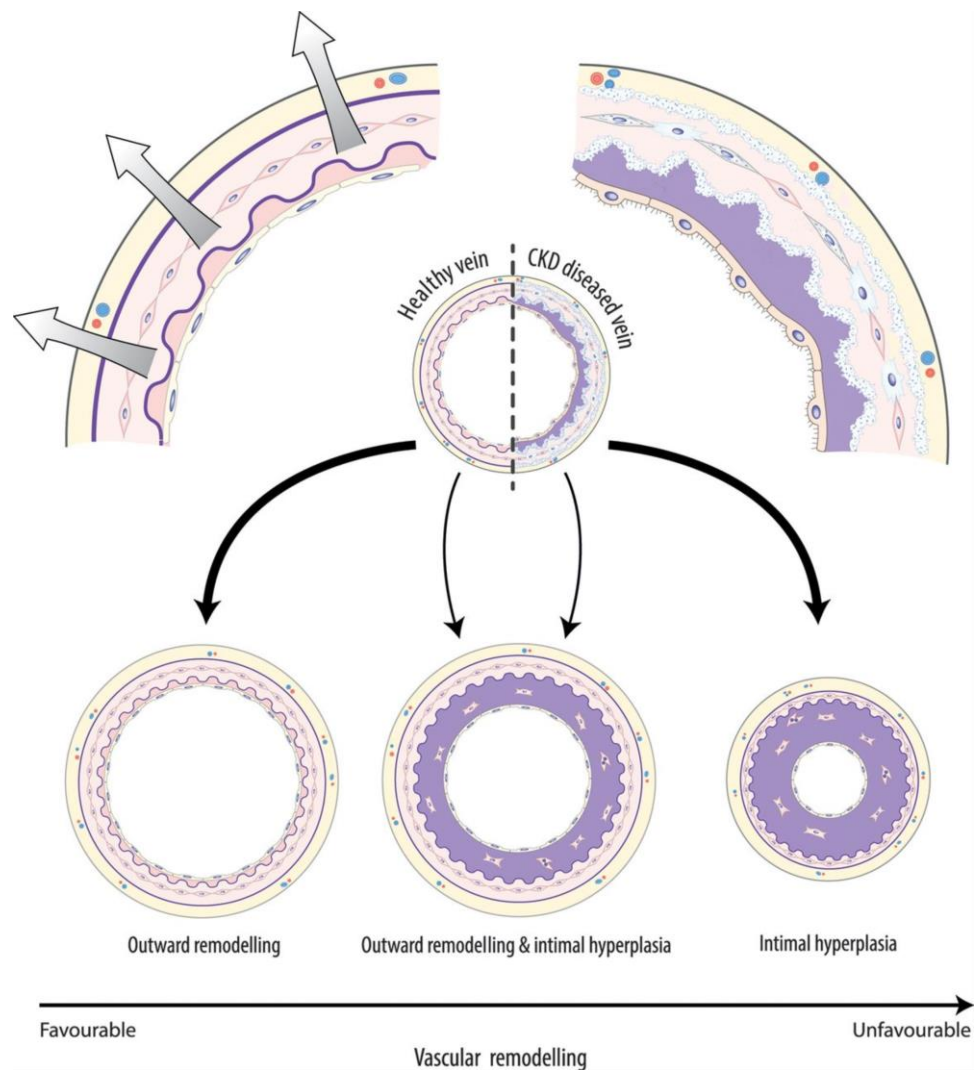


Figure 25 Different modalities of the vascular remodelling response after fistula creation. (14)

2.5.7 Experimental and Clinical Studies

Data from animal experiments demonstrated substantial flow rate and shear stress increase after AVF placement. In particular, the raised wall stress causes arterial dilatation as physiological response, which in turn tends to restore this stress to normal values in one-month period. This vessels behaviour is mediated by the release of nitric oxide (NO), which has been noted to be activated by the blood flow characteristics. In case of inhibition of NO release due to the flow conditions, the vasodilatation is blocked and endothelial denudation occurs. (25)

It is important to emphasise that less information has been found on the role of hemodynamic shear stress, oxidative stress, nitric oxide or endothelial denudation on vascular remodelling and intimal hyperplasia of the venous segment, even if a similar behaviour is presumed.

Corpataux et al. undertook an important study in this regard, deducing how hemodynamic parameters affects vascular remodelling in six AV-Fistula patients. The main strategy consists of Doppler ultrasound testing of vessel diameter, cross-sectional wall thickness, blood pressure and blood flow after fistula placement and in a period of 1 and 3 months. (21) (25)

It was noted an increase in blood flow with a consequent increase in the wall shear stress from a physiological 0.5-1.5 Pa to 2.45 Pa. At the same time, the vein diameter increased around 100% the first week and 50% at fourth causing a reduction in wall shear stress within normal range. Wall cross-sectional area accompanied these changes. The balance between inner diameter increase and wall cross-sectional area did not cause any stenosis. Throughout the study, the blood pressure in the AVF remained almost unchanged. (23)

Based on the above physiological, experimental and clinical data, the sequence of events that results in the rapid maturation of an AV fistula appears to be as follows:

- increased arterial and venous wall stresses induced by the increased blood flow;
- arterial and venous dilatation mediated by the nitric oxide and reactive oxygen species release by the endothelial cells, which are activated by vessels wall shear stresses;
- medial hypertrophy of the venous tract caused by the pressure increase.

It is to underline that only a 23%-46% incidence of maturation failure and a primary patency at 1 year of only 60%-65% within the study samples occurred. (25)

2.6 Pathogenesis of the AV Fistula Failure

2.6.1 Demographic and Clinical Factors ⁽²⁵⁾ ⁽¹⁴⁾

A number of clinical studies have attempted to identify risk factors for AV fistula failure. Miller et al. and Lok et al. studies describe the diabetes mellitus, race, older age, peripheral vascular disease and female sex to be principal risk factors. The specific surgeon skills in AV fistula creation, vessel handling, torsion, kinking and the degree of endothelial injury caused are other important factors affecting operation success. Van der Linden et al. have recently demonstrated that also genetic predisposition to flow-mediated dilatation plays a significant role in fistula maturation, with the venous distensibility providing better chances of a successful operation.

The conclusion is that principal clinical AVF success factor is related to the capability of vessels to dilate, rather than the mere initial vessels size. Confirmation of that comes from

studies which besides associating small vessels size to a poor success rate, didn't find a direct correlation between larger vessels and a better AVF survival.

2.6.2 Abnormal Hemodynamic Shear Stress Profiles ⁽²⁵⁾

The entire process leading to positive vessels remodelling has been shown strongly related to shear stresses. If high laminar shear stress is associated with good vascular dilatation and low neointimal hyperplasia, its opposite, the low oscillatory shear stress shows a strong correlation with insufficient vascular dilatation and an increase in neointimal hyperplasia.

The respective physiology under this vascular behaviour is endothelial quiescence, high levels of nitric oxide release and low levels of inflammatory cytokines for the positive remodelling, and their opposite for the failure in the remodelling.

Nevertheless pilot studies on shear stress presented different stresses in different experimental and clinical settings, generally it has been concluded that in AV fistulae failure a "bad" hemodynamic profile following access surgery is one of the governing factors. In fact, this bad hemodynamic profile related to regions of low flow and oscillatory shear stress within the venous segment results not only in aggressive venous neointimal hyperplasia but also in the dilatation failure.

However, the final amount of neointimal hyperplasia and medial hypertrophy will not result in luminal stenosis if an adequate dilatation occurs.

As result of the balance between the vascular dilatation on one side, and the neointimal hyperplasia and medial thickening on the other, it is possible to determine the final amount of luminal stenosis in an AV fistula.

Parallel to fluid flow and stress parameters, medical factors as surgical injury and insertion of dialysis needles (needle infiltrations), are also likely to play a role. It is reasonable to believe that dialysis needles can affect blood flow, increasing turbulence up to 4 cm downstream of the site of puncture (results from experimental studies).

2.6.3 Pre-Existing Vascular Abnormalities ⁽²⁵⁾

Especially for uremic patients, who tend to have increased vascular stiffness caused by calcifications, growing consideration is now taken to pre-existing arterial and venous abnormalities.

Respectively Kim et al. and Wali et al. undertook studies on arterial and venous thickening and hyperplasia, concluding that the pre-existence of these vascular abnormalities is strongly correlated to poor fistula survival, suggesting where to concentrate the attention to improve vascular health and consequent success.

However, also local therapies to reduce vessels stiffness have been developed, increasing the maturation rates and AVF success.

2.7 Complications Related to AVF

Problems with dialysis access are a leading cause of complications and hospitalisations of patients with kidney disease. The more patients understand about their access, the more they are empowered, which leads to an improved quality of life by staying out of the hospital and having efficient dialysis. It is also important for patients not yet on dialysis to understand the types of dialysis access available so they can be prepared and make

informed choices about dialysis access when they are not in crisis. This also helps to prevent starting on dialysis with a catheter as an emergency procedure.

2.7.1 First-Use Syndrome (10)

“First-use syndrome is an anaphylactic reaction to the artificial kidney. Its symptoms include sneezing, wheezing, shortness of breath, back pain, chest pain, or sudden death. It can be caused by residual sterilant in the artificial kidney or the material of the membrane itself. In recent years, the incidence of first-use Syndrome has decreased, due to an increased use of different sterilisation instead of chemical sterilants, and the development of new membranes of higher biocompatibility.”
(10)

2.7.2 Fluid Shifts

Side effects of hemodialysis caused by removing too much fluid and/or removing fluid too rapidly include low blood pressure, fatigue, chest pains, leg cramps, nausea and headaches. These symptoms can occur during the treatment and can persist. These side effects can be avoided and lessened by limiting fluid intake between treatments or increasing the dose of dialysis more often or longer. (10)

2.7.3 Access-Related Problems

Since hemodialysis requires access to the circulatory system, patients undergoing hemodialysis may expose their circulatory system to microbes, which can lead to infections affecting vascular system or bones. The risk of infection varies depending on the type of access used. Bleeding may also occur. (10) Infections can be minimised by strictly adhering to infection control best practices. (26)

2.7.4 Stenosis of Central Veins (27)

A central venous stenosis may be clinically asymptomatic before creating the vascular access and become symptomatic only when flow is increased. If a critical stenosis is unable to accommodate increased flow rates, the result will be swelling of the arm and cyanosis. Central stenoses are usually the result of past subclavian catheters, primary thrombosis, compression by tumours, etc. the preferred intervention is to correct the stenosis, either by dilation with stenting or by surgical correction. The latter involves major surgery and carries a considerable surgical risk and because of this is the less desirable option. (26)

2.7.5 Thrombosis (27)

“Thrombosis is a critical reduction of fistula blood flow. Sometimes thrombosis occurs as result of an inflow or outflow stenosis.” (27)

Early fistula thrombosis usually is caused by inflow problems, while late thrombosis generates by outflow stenosis. The previous problems, if neglected, result in thrombosis

of the fistula correlated to neointimal hyperplasia, which causes stenosis, consequent decrease in access flow and finally thrombosis. Hypotension, higher haemoglobin target, and hypercoagulability are the major systemic factors leading to higher access thrombosis risks.

Already discussed aspects in thrombosis and local stenosis incidence are sex (female), diabetes, uraemia and needling techniques. Hematoma and needle complications such infection and inflammation cause a 25% increased risk of thrombosis and access related problems. (27) (26)

2.7.6 Anticoagulation-Related

“Allergy to heparin, the most commonly used anticoagulant in hemodialysis, can infrequently be a problem. In such patients, alternative anticoagulants can be used. In patients at high risk of bleeding, dialysis can be operated without anticoagulation.” (10)

2.7.7 Steal Phenomenon (27) (17)

Steal Phenomenon is a frequent affection of AVF patients leading to ischemic lesions. Age and diabetes, together with vascular diseases, are aggravating factors. About this complication, there are two varieties: high-flow steal, when low resistance fistulas “suck-off” blood from the hand causing fingers ischemia, and low-flow steal resulting from arterial stenosis causing critical ischemia even in working fistulas. (26)

If the first steal type is easily corrected by limiting the fistula flow with an additional fistula ligation, the second type is more difficult to solve, requiring specific

angioplasty operations. Worth to note that, according to Poiseuille law the resistance goes with the 4th power of the radius, so only drastic reduction of the anastomosis lumen will be effective. In conclusion, the achievement of a safe and effective fistula lumen is tricky and risky, exposing to thrombosis or ischemia risks. (17)

2.7.8 Cardiovascular (Heart and Vessels) Diseases (26) (17)

Long-term hemodialysis-associated forms of heart and vascular disease occur when frequency and length of treatments increase causing pathologies like enlargement of the heart. (10)

Patients with fistula hyper-circulation problems have been noted to increase the risk of left ventricular hypertrophy (LVH).

“LVH is an adaptive response to increased cardiac workload that has short-term beneficial effects on cardiac function but long-term detrimental. The mechanisms of hemodynamic compensation in hemodialysis patients are very complex and involve, among other things, reduced vascular resistance and arterial dilatation as a result of increased blood flow and the formation of collaterals.” (26)

To obviate to this pathology no guidelines are still present, even if cardiovascular complications are the leading cause of death for hemodialysis patients, with LVH being the major responsible factor.

In AV fistulas Aneurysms are related to vessels wall damage and destruction of the normal endothelial and muscular layers, with their replacement with stiffer collagenous tissue.

Aneurysm has a degenerative progress: once formed it has the tendency to spontaneously enlarge, being the wall stresses increasing together with the aneurysm diameter increase.

Scar tissue generated by the several punctures of the fistulas is a breeding ground for aneurysm development. Major complications are rupture, infection and embolism are the related complications to this pathology.

The surgical correction includes partial or complete resection, correction of accompanying stenoses, and reconstruction of an adequate lumen as illustrated in. (27) (17)

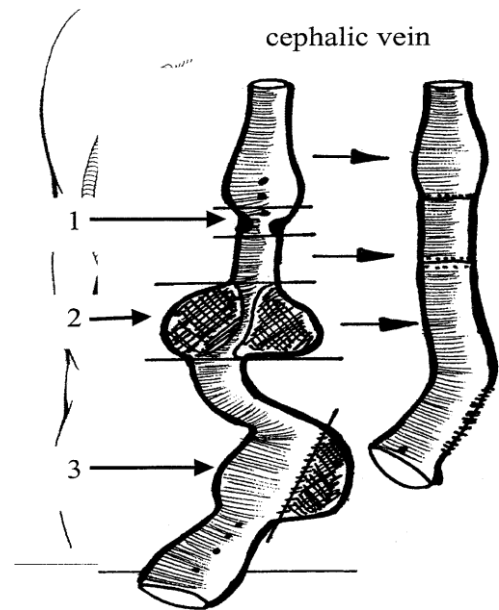


*Figure 26 Example of two aneurysms and a short stenosis along the cephalic vein and their removal.
(17)*

2.8 Main Ways to Fix it⁽²⁵⁾

First of all, it has to be underlined as:

“Before the intervention, adequate imaging using ultrasonography is absolutely indispensable for identification of thrombi, assessment of the degree of outflow stenosis, and evaluation of the surrounding tissue.” (17)

And that:

“A potential disadvantage of using a single agent to attenuate a complex process such as AV fistula stenosis is that biological systems tend to be redundant.” (25)

Angioplasty is the principal treatment for AVF stenoses, although the actual strategies are prone to cause important vessels walls damage which can even worsen the previous condition, exacerbating the stenosis.

Nowadays the efforts are focused on preventing the different types of pathologies and injuries related to a fistula placement and maturation, In this regard, new therapies are concentrated to:

- identification of the optimal anatomical configuration and location for the AV fistula in order to achieve the best hemodynamic profile;
- the design of new dialysis needles causing less injury and turbulence;
- new evidence-based guidelines for performing angioplasty;
- attenuation of angioplasty and surgical damages exploiting anti-proliferative or pro-dilatory agents.

2.8.1 Cell-Based Therapies

Wraps loaded with endothelial cells can be placed around the arteriovenous anastomosis of AV fistulae at the time of surgery with the aim to mimic the main functions of endothelial cells, promoting vascular dilatation and inhibiting neointimal hyperplasia. (25)

2.8.2 Drug-Based Therapies

Perivascular wraps loaded with specific anti-proliferative agents can attenuate the venous neointimal hyperplasia, as shown in the study of Roy-Chaudhury et al. (25)

2.8.3 Gene-Based Therapies

This could become an effective means of local therapy for neointimal hyperplasia in AV fistulae, especially if improvements continue to be made in the safety and efficacy of delivery techniques. Currently, the gene transfer of endothelial and inducible nitric oxide synthase has achieved inhibition of neointimal hyperplasia in experimental angioplasty models. (25)

2.8.4 Ligature

The ligature is a suture that ties around the blood vessel to limit the blood flow. To operate it, the surgeon will clamp the vessel perpendicular to the axis of the artery or vein, and then secure it by ligating it. This technique is used if the fistula is causing problems such as steal phenomenon and ischemia.

2.8.5 Balloon Dilatation (26)

Balloon angioplasty (percutaneous transluminal angioplasty) is a minimally invasive, endovascular procedure to widen narrowed or obstructed arteries or veins, to treat vessels sclerosis and stenosis. In the treatment of vascular access stenosis improves fistula function and prolongs fistula survival in patients with shorter lesions (~1 cm), but restenosis remains the major problem. Although percutaneous interventions are less invasive than surgical revision for preserving vascular access, long-lasting PTA outcomes have not been demonstrated to be useful. (26)

2.8.6 Thrombectomy (27)

Surgery is an established technique for salvage of a thrombosed access. The surgical technique involves the use of a thrombectomy combined with retrograde manual removal of the clot.

Thrombectomy

Catheter aspiration thrombectomy



Blood clot is removed using suction

Mechanical thrombectomy



Blood clot is broken up into small pieces and removed

Figure 27 Illustration of the thrombectomy techniques.

2.9 The Medical Problem Conclusion

In the end, it is possible to conclude that there is not a univocal and single approach in the evaluation of the ArterioVenous Fistula creation and maturation, as well as for the medical and surgical management of it.

A useful strategy comprehends the early referral and establishment of the vascular access, preceded by an accurate assessment through ultrasonography to select the best configuration, location and vessels to join. Moreover, a periodical monitoring of the fistula condition is strongly suggested to control maturation and the occurrence of new complications and pathologies, in order to prevent their degeneration. (27)

It is the author belief that the simple following of the new strategies developed in the recent years, a proper monitoring can lead the success rate, and effectiveness of the operation of a new AV fistula to more than today's 60%.

In order to have some landmarks to evaluate future developments of an AVF, studies reported the influence of blood flow characteristics in the positive vascular remodelling leading to maturation. (17)

Finally, it can be stated that blood flow and related stresses behaviour, patterns and magnitude should be the meaningful factor on which concentrate the study of the very patient specific fistula creation and maturation, as many studies show.

3 THE ENGINEERING PROBLEM³

³ Eventual references on the chapter or paragraph titles are to be intended to be the main sources of the informations provided on that chapter or paragraph.

3.1 The Case

Regarding AVF, what is resulted a leading factor for the assessment of a good fistula quality and maturation is the blood flow behaviour and the hemodynamic stresses on the vessels surface generating from those. As said, for example, disturbed blood flow or oscillatory WSS, activate mechano-transduction pathways that lead to decreased release of nitric oxide and up-regulated expression of pro-inflammatory, pro-proliferative, and pro-thrombotic genes.

Considering the studies and analysis already done, what is now to deal with is the engineering transposition of the parameters and subjects resulted significant and sensible, to deepen the evaluation the blood flow in the anastomosis area of the fistula.

For this reason blood flow lines, Reynolds and Womersley numbers, Wall Shear Stress, Spatial and Temporal Wall Shear Stress Gradients, Oscillatory Shear Index, Time Averaged Wall Shear Stress and Time Averaged Wall Shear Stress Gradient have been the objects to which focus the attention.

The main aim from the engineering point of view is to find a correlation and good practice values and distribution for the parameters just mentioned. What is desired in addition to that is to become able to evaluate a pre-existing AVF status/possibility of maturation, and try to have the same information starting from the vessels characteristics before the AVF surgery operation.

3.1.1 Wall Shear Stress (WSS)

Wall Shear Stress is the flow induced stress in the layer of fluid next to the wall of a pipe, which generates between a moving fluid and borders themselves.

It is defined as:

$$WSS = \tau = \mu \left(\frac{\partial \vec{u}}{\partial y} \right) \Big|_{y=0}$$

Where μ is the dynamic viscosity, u the flow velocity parallel to the wall and y is the distance to the wall.

Acting directly to vessels layers it has been shown that there is a strong correlation between wall shear stress and neointimal formation, thrombosis, re-endothelialization, and restenosis. (28) Thus, arterial regions where unidirectional, laminar WSS exists are relatively free of the formation of atherosclerosis or arterial NH (neointimal hyperplasia). (29) (30)

3.1.2 Spatial Wall Shear Stress Gradient (SWSSG)

In complex geometries, high WSS is often accompanied by significant spatial WSS gradient (WSSG), the spatial derivative of WSS along the flow direction with respect to the stream-wise distance.

Wall Shear Stress Gradient is indeed the gradient of the WSS:

$$GWSS = |\nabla \tau| = \sqrt{\left(\frac{\partial \tau_w}{\partial x} \right)^2 + \left(\frac{\partial \tau_w}{\partial y} \right)^2 + \left(\frac{\partial \tau_w}{\partial z} \right)^2}$$

It describes how the stresses spatially change along vessels surfaces, being able to see hot spots, where there is minimum WSSG, and where maximum increases are located. The latter is useful to detect the causes of acute changes in flow behaviour, which suggests flow separation and un-physiological flow patterns, revealing the locations where attention should be paid on. (29) (22)

It has been found in vivo that cerebral aneurysms initiate in the acceleration zone characterized by both high WSS and positive WSSG. Furthermore, computational fluid dynamic (CFD) analyses indicated that WSSG combined with high WSS is significant at the throats of stenoses and affects endothelial cells function with subsequent vessel remodelling. Positive WSSG creates a net stretching force along the endothelium surface, instead, negative WSSG causes net cell compression, high shear stress and gradients in vascular remodelling along the luminal surface. In vitro evidence confirmed this results: positive WSSG appears to amplify the response of the endothelial cells to high WSS, while negative WSSG seems to placate them. (31) (32)

3.1.3 Time Average Wall Shear Stress (TAWSS)

The total shear stress exerted on the wall throughout an entire cardiac cycle can be evaluated using the time-averaged WSS (TAWSS) that can be expressed as:

$$TAWSS = \frac{1}{T} \times \int_{\alpha}^T |W\vec{SS}| dt$$

Where T is the temporal period (cardiac cycle).

Low AWSS develops at the concave parts of the curved flow regions and is a marker of low average WSS. Its capability to describe the cumulative stresses acting on every side of the vessels can provide a generalised view of where the zones at high and low WSS are located. (33) (34)

3.1.4 Time Averaged Wall Shear Stress Gradient (TAWSSG)

The Time Averaged Wall Shear Stress Gradient defined as:

$$TAWSSG = \frac{1}{T} \times \int_{\alpha}^T |WSSG| dt$$

Is the analogue of TAWSS for the WSSG. It enables to evaluate where the mean Wall Shear Stress Gradient has its biggest and lowest hot spots. No applications of this parameter have been found in the literature.

3.1.5 Temporal Wall Shear Stress Gradient (TWSSG)

“The study by Kharboutly et al. reported a strong association with high temporal wall shear stress gradient (TWSSG) and locations of calcified plaque compared to low WSS and OSI and concluded that this parameter may be an important determinant of endothelial cell function and plaque formation.” (22)

Temporal wall shear stress gradient is defined as:

$$|TWSSG| = \frac{\partial \tau_w}{\partial t} = \frac{1}{T} \int_0^T |TWSSG| dt \quad (35) \quad (36)$$

3.1.6 Oscillatory Shear Index (OSI)

The Oscillatory Shear Index is esteeming how much the WSS deviate from its main axial direction over time, thus characterizes flow separation from the vessels wall. Its values widen between 0 to 0.5: lower OSI values indicate the WSS is oriented predominately in the primary direction of the blood flow while a value of 0.5 means that the instantaneous vector is never aligned with the time-averaged vector, which indicates a very oscillatory behaviour. (28) (34)

OSI expression is:

$$OSI = \frac{1}{2} \times \left(1 - \frac{\left| \int_0^T \vec{WSS} dt \right|}{\int_0^T |\vec{WSS}| dt} \right)$$

Oscillatory shear stress is a weaker inducer of eNOS (endothelial nitric oxide synthase) than steady state shear stress and creates greater endothelial cell proliferation similarly the turbulent shear stress. This is due to the strong correlation between eNOS promotion and WSS magnitude, which is not noticed by OSI. (37)

Therefore,

“the combination of low and oscillatory shear stress could be a better indicator of disturbed flow within AVFs. The low shear stress results were paired against intimal medial thickening. IMT was also observed at a location downstream, in a region of higher shear and low OSI.” (22)

OSI is insensitive to shear stress magnitude and must, therefore, be used with caution; a large OSI value can indicate a disturbed flow region with high or low WSS magnitudes.

This suggests that multiple aspects of shear stress may stimulate intima-media thickening or that multi-directional characteristic of the disturbed flow might be described more accurately with metrics such as Relative Residence Time (RRT) rather than OSI alone. (38)

3.1.7 Relative Residence Time (RRT)

Relative Residence Time indicates the time of residence the molecules spent at endothelium:

$$RRT = [(1 - 2 \times OSI) \times TAWSS]^{-1}$$

It is emerging as appropriate tools for atherosclerosis localization. (33)

Himburg et al. introduced this indicator of the ‘disturbed’ shear environment, being the RRT inversely proportional to the distance the particles travel during a cardiac cycle, which may be expressed as a combination of OSI and time-averaged WSS (TAWSS) over the cardiac cycle. (38)

In this formulation, OSI acts to scale the effect of TAWSS on the relative residence of particles near the wall and thus RRT incorporates information on both low and oscillating shear.

3.2 The Patient Specific Aim

The purpose of this research is to deepen knowledge in this particular surgery operation, which is the AVF anastomosis. Because of the variety and particular complexity of the subject, it has been intended to develop a patient specific procedure to study it.

Patient specific means that the most of the specific patient details and data possible are taken into account to provide the most accurate representation of what is really happening inside the AVF.

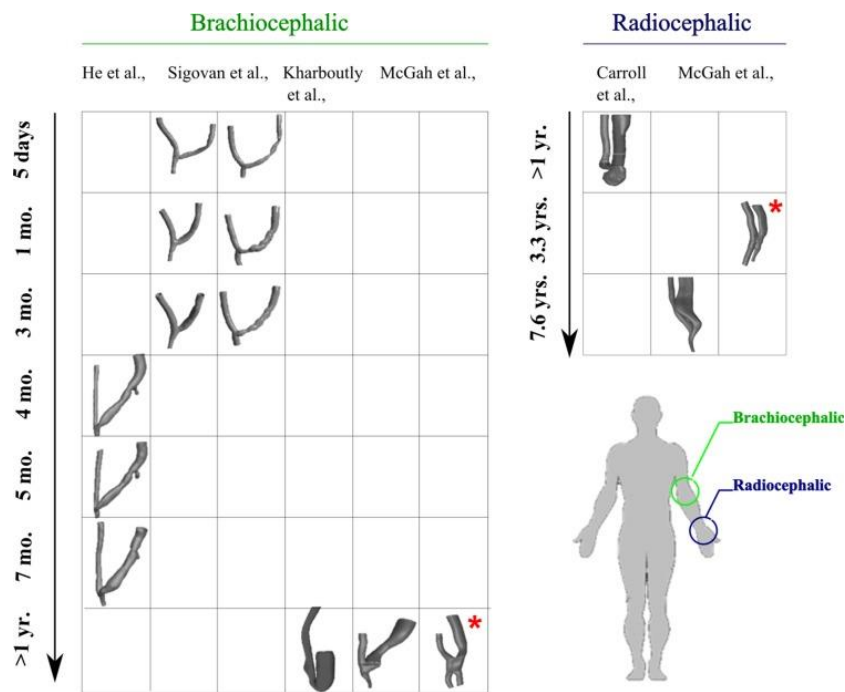


Figure 28 Different reconstructed 3D models of brachiocephalic & radiocephalic AVFs. * indicates a side to side configuration, all the other AVFs were configured end to side. (22)

Many studies had revealed that the principal factors involved are:

- Blood flow
- Vessels properties.

Therefore, basing on the previous speculations, what we are intended to achieve is the study of the blood flow inside the specific ArterioVenous Fistula of every patient, paying attention to the stresses generating on the walls.

Several mathematical models have been developed to study the flow of blood in vessels, and some of them are even very complex and precise. Main characteristic and problem of this kind of models is that they tend to generalise and discretize real characteristics trying to fit them to a standard behaviour, attributing the same behaviour to different conditions.

An important role in this field plays the number of variables considered and the precision of their discretization compared to reality. Thus, if these models are good in predicting, for example, the dynamic pressure drops and flows in branched vessels structures, they are not as good in analysing the same variables in critic spot regions or geometries.

For this reason, the focus of the study is to develop a patient specific model for the study of the AVF maturation and prediction of its development.

However, many factors are involved in the physiology of the AVF maturation, the most important are vessels size and geometry, vessels mechanical properties (i.e. elastic modulus, density), blood rheology and its flow conditions proximal and distal the AVF.

All these variables are very different from person to person, and even considering good practice values, the geometry of the AVF is very variable depending on the precise conditions and anatomy of the patient. This condition is affecting consistently the flow in the anastomosis, making difficult or even impossible to analyse the AVF conditions excluding it.

Therefore, the intention is to build a solid procedure based on the previous parameters which could be consistent with the data and physiology obtained from every patient and very precise too.

Computational Fluid Dynamics comes to help, permitting a very high flexibility and precision on studying how complex fluid behaves in different and complex geometries.

An interesting development that can be done is to include vessels distensibility into account, performing a Fluid Structure Interaction simulation. We did not perform it because of the lack of time and data for an accurate acquisition of additional vessels geometrical (thicknesses) and mechanical properties and the subsequent analysis. Moreover, the need to achieve a good synchronisation between velocity pulse wave and pressure pulse on the different boundary conditions of the models resulted the most intriguing and challenging problem, due to the fact that FSI is very sensitive to even small discrepancies in boundary data. Thus, Fluid Structure Interaction simulation is the logical development of this research and, for this reason, is intended and recommended to deepen in next studies.

Now remains to establish what is needed to perform this kind of study.

First in order is to obtain a 3D geometrical model of the anastomosis, with a sufficient distance from that to permit the blood flow analysis.

Then blood rheological properties are required to describe the better possible how it flows inside the vessels.

To complete the numerical model then, a series of boundary conditions about how is the blood status at every entrance and exit of the vessels is required, among which there are: inlet velocity pulse wave (magnitude and time evolution), outlet velocity pulse wave and blood pressure pulse wave.

If what we want to perform is an FSI simulation then, in addition to this data we will need also vessels thickness and mechanical properties information.

3.3 Blood Flow and Rheology

One of the main peculiarities in studying blood flow in vessels is that this biological fluid has not a Newtonian behaviour, besides other characteristics that will be deepened further. This means that blood viscosity does not remain constant at different shear rates, resulting in a nonlinear correlation between shear stress and shear rate.

Many studies have been undertaken to analyse the sensitivity of the results that the blood shear thinning behaviour generates. The results of those are that, especially in small vessels at small shear rates, the difference between the Newtonian model of blood and real behaviour is such important to motivate the shift to a more complex non-linear model to describe blood behaviour.

In this field, different models have been proposed trying to fit the real behaviour the better with the lesser number of variables, among those, there are: power law, Casson model, Carreau model, Walburn-Shneck model, Quemada model, Cross model, etc.

Another very characteristic property of the blood flow is its pulsatility, due to the heart work, which operates as an intermittent pump.

3.3.1 Blood Characteristics

3.3.1.1 Physical Properties of Blood ⁽³⁹⁾ ⁽⁴⁰⁾

Blood is about 7% of the human body weight, with a normal adult having around 5 litres of blood in its body. Its density is approximately $1054 \sim 1056 \text{ kg/m}^3$.

Blood is a complex liquid tissue consisting of a solution of several elements (corpuscles or cells; about 45% by volume) in a fluid known as plasma (about 55% by volume).

The plasma is a dilute electrolyte solution in which about 8% are proteins. Plasma proteins are large molecules with high molecular weight and do not pass through the capillary wall.

The formed elements of blood are red blood cells (95%), white blood cells (0.13%) and platelets (4.9%).

In humans, mature red blood cells lack a nucleus and organelles. They are produced in the bone marrow, and their life span is about 125 days. The red blood cell is biconcave in shape.

The diameter of red blood cell is about $8.5 \text{ }\mu\text{m}$ at the thickest portion and about $1 \text{ }\mu\text{m}$ at the thinnest portion. Its membrane is flexible and the cell can pass through capillaries of diameter as small as $5 \text{ }\mu\text{m}$ assuming a bent shape. It consists of a concentrated solution of haemoglobin, an oxygen-carrying protein.



Figure 29 Blood red cell.

The percentage of blood volume made up by red blood cells is referred to as the hematocrit (H). Hematocrit ranges from 42 to 45 in normal blood and plays a major role in determining the rheological properties of blood.

3.3.1.2 Viscosity of Blood⁽⁴⁰⁾ (41)

The viscosity of blood and plasma varies from person to person because of the different concentrations of various constituents like protein and red blood cells.

The viscosity of blood is also strongly dependent upon its temperature, increasing of about 2% for each °C. (39)

Human plasma has a viscosity range between 1.1 and 1.6×10^{-3} Pa·s, resulting higher than water because of the presence of proteins.

While plasma is nearly Newtonian, whole blood exhibits marked Non-Newtonian pseudo-plastic in its behaviour, particularly at low shear rates. From experimental measurements, it has been determined that blood behaves as a Newtonian fluid only at high shear rates ($\gamma = \partial v / \partial y \geq 100 \text{ s}^{-1}$). (42)

Blood viscosity depends on the viscosity of the plasma, its protein content, the hematocrit, the temperature, the shear, and the narrowness of the vessel in which it is flowing). The presence of white cells and platelets does not significantly affect the viscosity since they are such a small fraction of the formed elements.

A secondary effect called the Fahraeus-Lindqvist effect affects viscosity in dependence on the narrowness of the vessel diameter.

The viscosity of whole blood at a physiological hematocrit of 45% is about 3.2×10^{-3} Pa·s. Higher hematocrit results in higher viscosity, for example at a hematocrit of 60%, the relative viscosity of blood is about 6.4×10^{-3} Pa·s. (42)

For whole blood, the relationship between shear stress and shear strain is complicated for the following reasons.

If a blood sample is at rest, above a minimum hematocrit of about 5-8%, blood cells form a continuous structure. A yield stress τ_y is required to break this continuous structure into a suspension of aggregates in the plasma. Even yield stress also depends on the concentration of plasma proteins, in particular, fibrinogen. (43)

For 45% hematocrit blood, the yield stress is in the range $0.001 < \tau_y < 0.006 \text{ N/m}^2$.

Beyond the yield stress, when sheared in the bulk, up to about $\dot{\gamma} < 50 \text{ s}^{-1}$, the aggregates in blood break into smaller units called rouleaux formations. For shear rates up to about 200 s^{-1} , the rouleaux progressively break into individual cells. For whole blood, at low shear rates, $\dot{\gamma} < 200 \text{ sec}^{-1}$, the variation of τ with $\dot{\gamma}$ is noted to be nonlinear, so non-Newtonian.

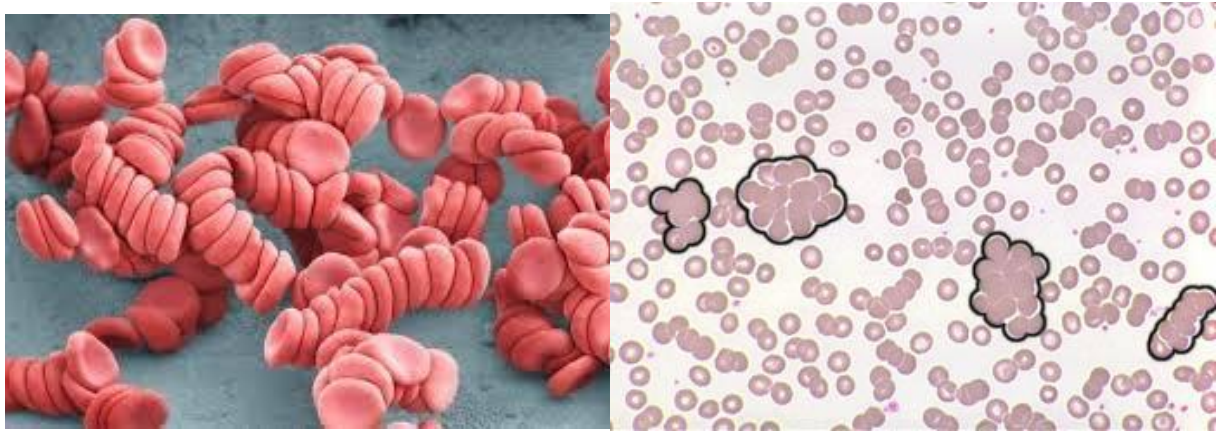


Figure 30 Images describing the rouleaux formations

Low $\dot{\gamma}$ values are associated with flows in small arteries and capillaries (microcirculation). At higher shear rates, $\dot{\gamma} > 200 \text{ sec}^{-1}$, the relationship between τ and $\dot{\gamma}$ is linear, and the viscosity approaches an asymptotic value of about $3.5 \times 10^{-3} \text{ Pa}\cdot\text{s}$.

Blood flow in large arteries has quite high shear rates, and the viscosity in such cases may be assumed as constant. Since whole blood behaves like a Non-Newtonian, the slope of the shear stress rate of strain characteristic at any given point on the curve depends on the prevailing $\dot{\gamma}$ at that point.

There are a number of constitutive equations available in the literature that attempt to model the relationship between the shear stress and shear rate of flowing blood.

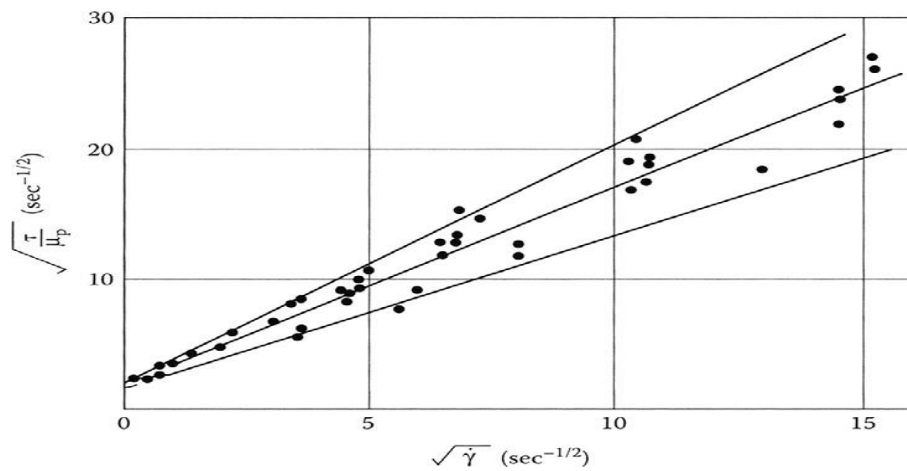


Figure 31 Shear stress versus shear rate for blood flow.

3.3.1.3 Fahraeus-Lindqvist Effect ⁽⁴⁰⁾ ⁽⁴⁴⁾

It was observed that in very small diameter tubes the apparent viscosity of blood has a very low value. The viscosity increases with the increase in tube diameter and approaches an asymptotic value at tube diameters larger than about 0.5 mm. This is a second non-Newtonian characteristic of blood and is called the Fahraeus-Lindqvist effect. This is because the hematocrit in the small vessel decreases as the tube diameter decreases. While the discharge hematocrit value may be 45%, the corresponding dynamic hematocrit in a narrow-sized vessel such as an arteriole may be just 20%. Consequently, the apparent viscosity decreases.

As the blood flows through a tube, the blood cells tend to rotate and move towards the centre of a tube. Hence, a cell-free layer exists near the wall leaving a layer of plasma, whose width increases with increasing shear rate. In tubes with a small diameter, the area of the cell-free zone is comparable to the central core. The cell-free plasma layer reduces the tube hematocrit. As the size of the vessel gets smaller, the fraction of the volume occupied by the cell-free layer increases, and the tube hematocrit is further lowered.

The net effect of the cell-free zone with a lower viscosity (viscosity of plasma alone) is to reduce the apparent viscosity of flow through the tube.

The reduced viscosity in narrow tubes is beneficial to the pumping action of the heart.

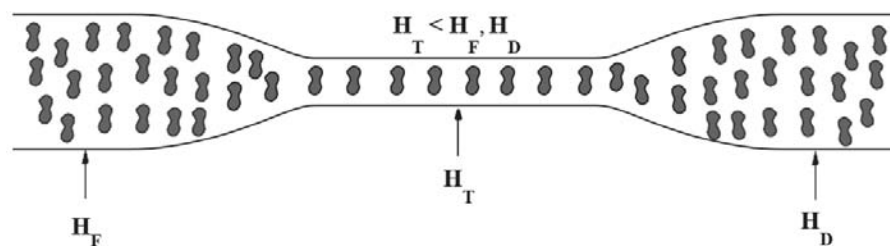


Figure 32 The Fahraeus effect: the hematocrit falls in the smaller vessels because of non-Newtonian and particulate nature of blood cells.

3.3.2 Blood Rheological Models (45) (46)

The choice of the correct rheological models is very important because, thanks by that, it is possible to model the very particular and complex behaviour of such complex biological fluid which is the blood.

Many mathematical models have been developed by the years to reproduce the behaviour of fluid and materials of every gender and property. Usually nowadays, when is intended to model a new material property, the best choice made is trying to work with already

existent models, looking for the one which is providing the best fit at the minimum complication costs.

When it is clear that a new model is necessary to reproduce faithfully its characteristics, only then a new mathematical expression is developed looking for the right expression which could encompass all the sensitive variables, with the right mathematical formulation which is related to the physics law which there is behind.

Here it is a list of principal rheological models to mimic blood behaviour.

3.3.2.1 Newtonian Model

The simplest model to describe blood flow is the Newtonian. Blood Newtonian viscosity is usually considered to be $\eta=0.00345$ Pa·s.

Limitations of this model are that under-estimates WSS at low inlet velocities leading to very wrong results in zones affected by low flow velocities (the ones of major interest), its strength is the simplicity.

3.3.2.2 Power Law Model

The first non-Newtonian model developed is the Power law model:

$$\eta = \eta_0 \dot{\gamma}^{n-1}$$

where $\eta_0 = 0.035$ Pa·s and $n = 0.6$.

The strength of this model is that it predicts shear-thinning effects and it is possible to obtain numerous analytical solutions to the governing equations. (34)

The main limits to this model are that it overstates non-Newtonian behaviour, creating viscosities far from Newtonian viscosity at both low and high shear rates and so it is not a proper model. For this reason, it over-estimates WSS at low inlet velocities and underestimates it at high inlet velocities.

Moreover, the power law model shows that, in the shear thinning case, the zero shear rate viscosity is unbounded and the asymptotic limit as $\dot{\gamma} \rightarrow \infty$ is zero. Both these behaviours are unphysical and limit the range of shear rates over which the power-law model is reasonable for blood. (47) (48)

3.3.2.3 *Casson Model*

The Casson model correlates directly shear stress and shear rate as:

$$\eta = \left[\left(\eta^2 J_2^{\frac{1}{4}} \right) + 2^{-\frac{1}{2}} \tau_y^{\frac{1}{2}} \right] J_2^{-\frac{1}{2}}$$

where $|\dot{\gamma}| = 2\sqrt{J_2}$, $\tau_y = 0.1(0.625H)^3$, $\eta = \eta_0(1 - H)^{-2.5}$, $\eta_0 = 0.012 \text{ Pa}\cdot\text{s}$ and $H=0.37$.

The Casson model as a special case, closely agrees with the Carreau model for low to mid-range shear and is effectively Newtonian at mid-range to high shear.

Many studies have demonstrated the Casson model to be very reliable to mimic blood viscosity (it exhibits the yield stress, tends to Newtonian behaviour at high shear rates

and interpolate well experimental data), enabling to include in the blood flow characterization also the hematocrit H.

The main drawback is the difficulty to find all the data to set the model, besides a more complicated formulation. (34) (47) (48)

3.3.2.4 Carreau Model

Carreau model formula for μ is:

$$\eta = \eta_{\infty} + (\eta_0 - \eta_{\infty}) \cdot [1 + (\lambda\dot{\gamma})]^{\frac{n-1}{2}}$$

where the viscosity at high shear rate η_{∞} equals the value for the Newtonian model 0.0035 Pa·s while the value at zero-shear is $\eta_0=0.056$ Pa·s. Moreover, $\lambda = 3.313$ s and $n = 0.3568$.

In favour of Carreau (and Carreau–Yasuda) model, there is that it has a simple formulation, it predicts the shear-thinning effects, and it represents moderate IG values (non-Newtonian importance factor) and fits quite well the experimental data, if compared to the Casson model.

The main weakness is its worst accuracy at low shear rates, if compared to the Casson model, but still fitting quite well the data. (34) (47) (48) (49)

3.3.2.5 Quemada Model

The Quemada model is described by the equation:

$$\mu = \mu_F \cdot \left(1 - \frac{1}{2} \frac{k_0 + k_\infty \sqrt{\dot{\gamma} / \dot{\gamma}_c}}{1 + \sqrt{\dot{\gamma} / \dot{\gamma}_c}} H \right)^{-2}$$

where $\mu_F=1.2$ mPa·s, $k_\infty=2.07$, $k_0=4.33$, $\dot{\gamma}_c=1.88$ s⁻¹ and the haematocrit $H=0.45$.

Its formulation takes account of Hematocrit, and it is quite complex. About this model, there's not much to say, except that it predicts the shear-thinning effects, and in all the studies analysed it has not been used a lot. (49) (50)

3.3.2.6 Cross Model

In the Cross model μ is defined as:

$$\mu = \mu_\infty + \frac{\mu_0 - \mu_\infty}{1 + (C\dot{\lambda})^m}$$

where $\lambda=1.007$ s and $m=1.028$.

Its strength is that it predicts shear-thinning effects, but like the Quemada model, it is usually discarded in favour of other models. (34) (49) (50)

3.3.2.7 Walburn–Schneck Model

The Walburn-Shneck model defines μ as:

$$\eta = C_1 e^{C_2 H} \cdot e^{C_2 \cdot TPMA / H^2} \cdot \dot{\gamma}^{C_3 H}$$

where $C_1 = 0.00797$, $C_2 = 0.0608$, $C_3 = 0.00499$, $C_4 = 14.585 \text{ g}^{-1}$, $H = 40\%$

and $TPMA = 25.9 \text{ g/l}$.

This model under-estimates WSS at high inlet velocities and was seen to give markedly different results from the other models in pulsatile conditions. It was mainly developed for low shear rates, and was not valid for certain shear rate regimes seen in the pulsatile flow simulations. In the end, this model is only a modification of the general power law model, and shares with it its pros and cons. (48) (46) (51)

3.3.3 Blood Flow

3.3.3.1 Reynolds Number ⁽⁵²⁾

The Reynolds number (Re) is a dimensionless factor helping to qualify flow patterns (transition from laminar to turbulent flow).

“This is defined as the ratio of inertial forces to viscous forces within a fluid which is subjected to relative internal movement due to different fluid velocities.” (53)

High flow movement tends to generate disturbances and confusion amplifying with the velocity, leading to turbulent flow. The viscosity of the fluid, on the other hand, is opposing to this effect, absorbing the more kinetic energy, the more viscous is the fluid. The Reynolds number assess the impact of these two different forces on a specific flow condition, determining when laminar or turbulent flow occur. (54)

Laminar flow is the particular fluid behaviour at very low Reynolds numbers, when viscous forces are dominant, causing a smooth and constant fluid motion.

Turbulent flow, on the other hand, occurs at high Reynolds numbers, resulting in an inertial forces flow dominated tending to produce chaotic eddies, vortices and other flow instabilities.

For flow in a pipe or tube, the Reynolds number is generally defined as:

$$\text{Re} = \frac{\text{inertial forces}}{\text{viscous forces}} = \frac{\rho v D}{\mu} = \frac{v D}{\nu}$$

where:

- D is the hydraulic diameter of the pipe
- v is the velocity of the fluid
- μ is the dynamic viscosity of the fluid
- ν is the kinematic viscosity ($\nu = \mu / \rho$)
- ρ is the density of the fluid

For complex shapes the hydraulic diameter, D, is defined as:

$$D = \frac{4A}{p}$$

where A is the cross-sectional area and P is the wetted perimeter

For flow in a pipe of diameter D, experimental observations show that for "fully developed" flow, laminar flow occurs when $Re < 1000$ and turbulent flow occurs when $Re > 2000$.

Between 1000 and 2000, both laminar and turbulent flows can be detected. This interval is called transitional flow, and it is dependent on other factors, such as pipe roughness and flow uniformity. This result is generalized to non-circular channels using the hydraulic diameter, allowing a transition Reynolds number to be calculated for other shapes of the channel.

These transition Reynolds numbers are also called critical Reynolds numbers and are different for every geometry.

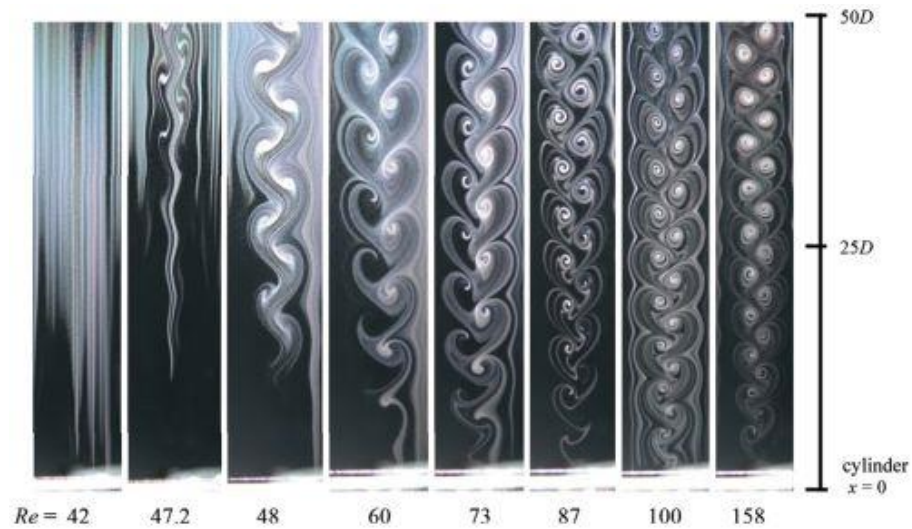


Figure 33 Eddies formation and laminar-to-turbulent changing Reynolds Number values.

Typical values of Reynolds number in human physiology are $\sim 1 \times 10^2$ for blood flow in brain vessels and $\sim 1 \times 10^3$ for blood flow in the aorta.

Rapid changes in vessel diameter may lead to turbulent flow, for instance when a narrower vessel widens to a larger one.

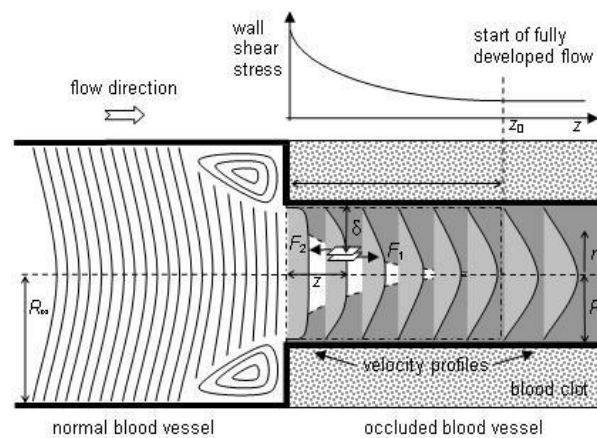


Figure 34 Description of Blood Entrance Length Velocity Profiles development. (41)

Related to the Reynolds number value is the entrance length.

“Entrance length refers to the area following the pipe entrance where effects originating from the interior wall of the pipe propagate into the flow as an expanding boundary layer. When the boundary layer expands to fill the entire pipe, the developing flow becomes a fully developed flow, where flow characteristics no longer change with increased distance along the pipe.” (55)

The wall shear stress (τ_w) is the highest in this hydrodynamic entrance region, where the boundary layer thickness is the smallest, then decreasing along the flow direction.

The length of the hydrodynamic entry region along the pipe is called the hydrodynamic entry length and it is a function of Reynolds number of the flow. In case of laminar flow, this length is given by:

$$L_{\text{laminar}} = 0.05 \times \text{Re} \cdot D$$

where Re is the Reynolds number and D is the diameter of the pipe.

In the case of turbulent flow, entrance length is shorter, being:

$$L_{\text{turbulent}} = 1.359 \times D \cdot \text{Re}^{\frac{1}{4}}$$

Generally, in practice, the entrance effects are considered expired after a pipe length of 10 times the diameter. Therefore, approximating:

$$L_{\text{turbulent}} \sim 10D$$

For this reason, one of the main parameter considered in the next chapters regarding the vessels 3D modelling, is that anastomotic area would be more than 10D far from every entrance. (52)

3.3.3.2 Womersley Number ⁽⁵⁶⁾

“The Womersley number (α) is a dimensionless expression of the pulsatile flow frequency in relation to viscous effects. The Womersley number is important to prove if parabolic profile of the steady state Poiseuille hypothesis is acceptable or not and in determining the thickness of the boundary layer to see if entrance effects can be ignored.” (56)

$$\alpha^2 = \frac{\text{transient inertial forces}}{\text{viscous forces}} = \frac{\omega R^2}{\nu} \quad \alpha = R \sqrt{\frac{\omega \rho}{\mu}}$$

This parameter, very important for biofluid mechanics, provides a comparison between unsteady inertial forces and viscous forces and has a significance similar to that of Reynolds number in the steady flow.

In the human circulatory system, α ranges from 10–3 in capillaries to 18 in the aorta in rest.

Vessel	Diameter (m)	α
Aorta	0.025	13.83
Artery	0.004	2.21
Arteriole	$3 \cdot 10^{-5}$	0.0166
Capillary	$8 \cdot 10^{-6}$	$4.43 \cdot 10^{-3}$
Venule	$2 \cdot 10^{-5}$	0.011
Veins	0.005	2.77
Vena cava	0.03	16.6

Table 1 Principal vessels diameters and relative Womersley number.

When $\alpha \leq 1$, viscous forces dominate in every region in the tube (known as quasi-steady flow) and Poiseuille parabolic velocity profile is accepted.

An increasing α means that the inertial forces are becoming more important, making feel their effects starting by the centre of the conduit. The result is a delay in the bulk flow respect to the driving pressure gradient, with a flattered velocity profile in the central region of the tube.

The velocity profile created by a pressure that oscillates sinusoidally at different frequencies is shown below, where is possible to notice how a true parabolic profile is not formed at any time even at the lowest frequency.

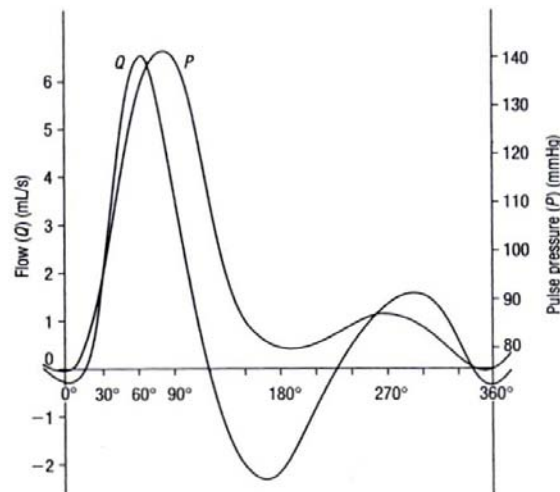


Figure 35 A flow velocity pulse (Q) and the arterial pressure pulse (P) recorded simultaneously. (41)

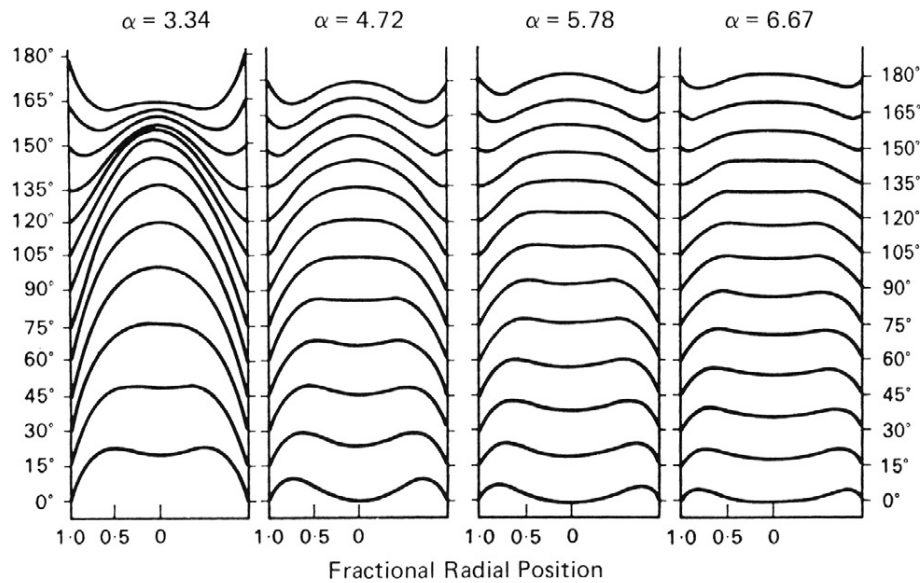


Figure 36 The velocity profiles of the flow resulting from a sinusoidal pressure for the first four harmonics of the flow curve at different Womersley numbers (α : 3.34, 4.72, 5.78 and 6.67), for different frequencies. (41)

As illustrated, there is a phase lag between the applied pressure and the movement of the liquid. The laminae that move first are those nearest the wall: since they always have a low velocity because of the effect of viscosity, they can reverse easily. Moving towards the axis of the tube there is a greater lag between the pressure gradient and the movement of the liquid, being the momentum becoming higher respect to the viscous drag. In this situation, the liquid begins to behave rather like a solid mass sliding inside a thin layer of viscous liquid surrounding it. (56)

As the frequency increases, α increases and the velocity profile becomes very flattened in the central region, with a reduction of amplitude of the flow and the rate of reversal of flow increases close to the wall. The same kind of behaviour is obtained increasing the diameter.

Thus, the velocity profiles in an artery can be seen as the sum of many profiles of the main harmonic components, with their appropriate amplitudes and phases, and the parabolic profile deriving from the steady-flow component. (41)

3.3.4 Blood Rheological Model Choice

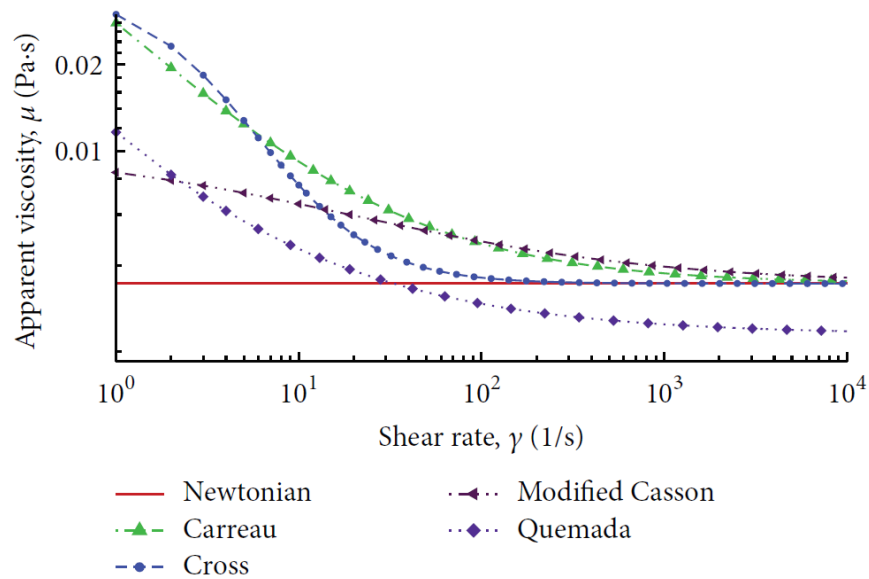


Figure 37 Apparent viscosity compared between the various rheological models in the study of Rabby et al. (57)

Comparisons made by different studies revealed interesting results.

The study from Rabby et al. shows how the point of separation for a stenosis model with the Cross and the Quemada models is exactly the same. Separation occurs a bit later by the Carreau model, with only the Newtonian and the Modified Casson models causing flow separation in more than one place. Comparing all the reattachment points, the Carreau model underpredicts the regime of the post-stenosis recirculation of blood, while the Newtonian model has an overall maximum prediction of the recirculation regime in case of critical stenosis. The streamlines analysis demonstrated the Newtonian fluid recirculation zones to be the largest, with the smallest recirculation region caused by the Carreau model. Limitations of this investigation include the consideration of rigid wall and simple sinusoidal pulsatile inlet profile instead of the compliant arterial wall and physiological realistic inlet profile. (45)

It is to underline that these results are useful to investigate the different models response in a physiological situation, but the study condition here is quite different from our problem. If in a stenosis there is a strong occlusion of a quasi-straight vessel, in an AVF we have a bifurcation of the vessel with a concurrent enlargement of the cross-sectional area and a consequent large difference in velocity magnitude and distribution.

For these reasons, there have been some researches to find a reasonable model that describes the behaviour of the blood in an established AVF more accurately. Gijssen et al. (1998) concluded that wall shear stresses, induced by the red blood cell suspension, could be modelled accurately by employing a Carreau model. (57) (58)

They employed a Carreau model successfully described the behaviour of a macroscopic blood analog fluid in various geometries under physiologically relevant flow conditions. The study found a good agreement between numerical and experimental results, indicating that the macroscopic blood analog fluid behaves like an inelastic shear thinning fluid. (58)

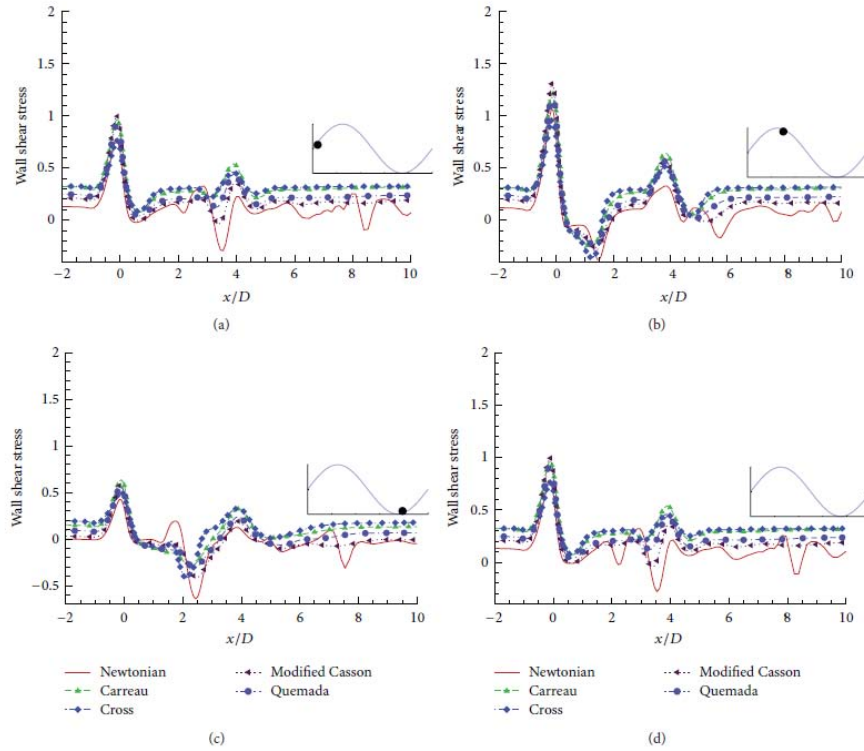


Figure 38 Wall shear stresses for different rheological models, at different pulsatile phases obtained by the study of Rabby et al. (57)

It has been concluded that the non-Newtonian aspect of blood flow in vessels is significant for low velocities. (58) Indeed, there are times in a cardiac cycle where the flow rate is near zero. Therefore, it is clear that is worth performing transient simulations with a physiological flow profile, and then studying the resultant WSS distributions, if precise results are needed.

Considering studies already done about the best rheological modelling of blood made by Hong Sun Ryou and F.J.H. Gijssen show that one of the best choices are the Casson or the Carreau models.

From the comparisons, Casson model resulted in the most accurate, with some disadvantages of the Carreau model in describing the correct viscosity at very low shear rates.

But, in the end, referring the good results achieved by the studies of AVF blood flow done by Giuseppe Remuzzi and Bogdan Ene-Iordache using Carreau model, and considering that the CFD software that we're going to exploit (Comsol Multiphysics) has a particular tool specifically developed to process Carreau model, the choice fell on the latter. (38) (59)

Other information gathered to have confirmation to this choice come from Noreen Sher Akbar et al., Joshua Boyd et al. and Johnston B.M. et al. (60) (61) (48)

For what regards the type of flow expected inside the vessels, starting by physiological blood velocity on radial artery (80 cm/s at the systolic peak) and vessel tighter diameter (4mm), a Newtonian viscosity of 0.0035 Pa·s and a blood density of 1056, the Reynolds Number estimated is 965. This value is at the very edge of the transitional flow but, considering that the rest of the cycle presents velocities very lower, the decision was to consider the study in the laminar flow condition.

About Womersley number, as for the Reynolds number, with a physiological heart rate of 93 bpm ($\sim 1.5 \text{ Hz} = 9.739 \text{ rad/s}$), it results to be around 1.1, so the velocity profile can be considered parabolic.

3.4 Structure of Vessels (62)

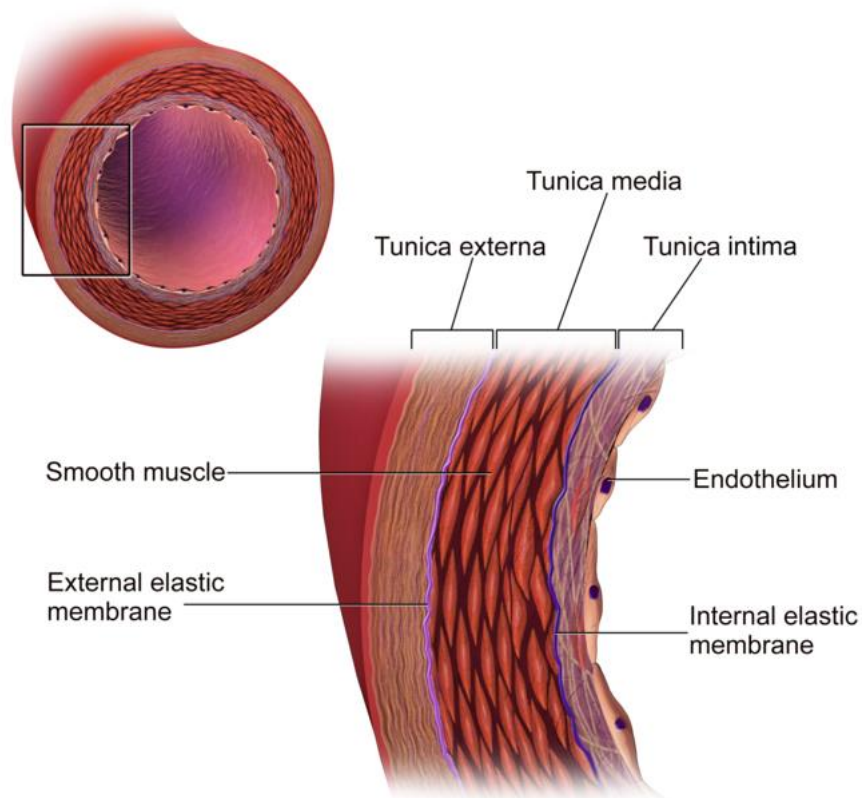


Figure 39 A section of an artery wall shows the endothelial cells structure: the intima, media and adventitia layers. (62)

All blood vessels other than capillaries are usually composed of three layers: the tunica intima, tunica media, and tunica adventitia.

At any given time, about 13% of the total blood volume resides in the arteries and about 7% resides in the capillaries, the rest is divided into veins and venules.

The tunica intima consists of a layer of endothelial cells lining the lumen of the vessel (the hollow internal cavity in which the blood flows), as well as a sub-endothelial layer made

up of mostly loose connective tissue. (63) The endothelial cells are in direct contact with the blood flow. An internal elastic lamina often separates the tunica intima from the tunica media.

“The tunica media is composed chiefly of circumferentially arranged smooth muscle cells. Again, an external elastic lamina often separates the tunica media from the tunica adventitia. The tunica adventitia is primarily composed of loose connective tissue made up of fibroblasts and associated collagen fibres. In the largest arteries, such as the aorta, the amount of elastic tissue is considerable. Veins have the same three layers as arteries, but boundaries are indistinct, walls are thinner, and elastic components are not as well developed.” (40)

Where blood flows under high pressure (like in the aorta), vessels have stronger walls. During left ventricular systole, the aorta stretches providing the potential energy that will help maintain blood pressure during diastole, and during the diastole, the aorta contracts passively. Medium arteries are about 4 mm in diameter with a wall thickness of about 1 mm and arterioles are about 50 μm in diameter. (64)

Their vascular tone is controlled by regulatory mechanisms, and they constrict or relax as needed to maintain blood pressure.

“The veins are a low-pressure type of vessels: they are thin-walled, distensible, and collapsible tubes: some of them may collapse in normal function. They are about 5 mm in diameter and the wall thickness is about 500 μm , and transport blood at a lower pressure than the arteries. Veins are surrounded by helical bands of smooth muscles which help maintain blood flow to the right atrium. Most veins have one-way flaps called venous valves. These valves prevent gravity from causing blood to flow back and collect in the lower extremities. Veins more distal to the heart have more valves.” (40)

In the venous system, a large increase in the blood volume results in a relatively small increase in pressure compared to the arterial system. The veins act as the main reservoir for blood in the circulatory system and the total capacity of the veins is more than sufficient to hold the entire blood volume of the body.

Venous and arterial mechanical properties are a fundamental data to have if a Fluid Structure Interaction FSI simulation is intended to be undertaken. This is because, as explained, arteries and veins are quite difficult in their composition and structures, and because they are biological tissues, and by their nature, they are subject to significant variability. (64)

3.5 The 3D Model

To study a patient specific behaviour of an AVF, a geometrical model of the latter is required to study how blood flows inside of it. Given the variability in the human anatomy and in the surgery operation possibilities, a specific model of the fistula is required to mimic the better the conditions that the blood flow meets in reality.

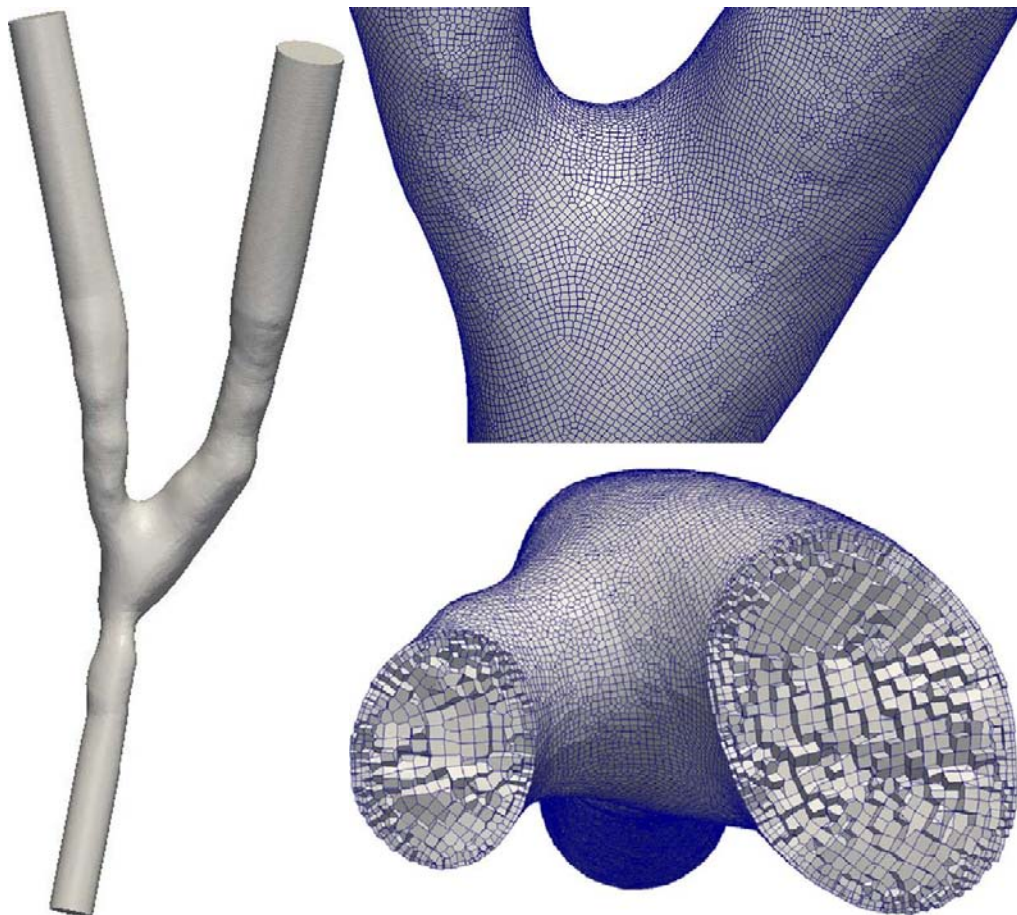


Figure 40 3D model of a patient specific AVF and its geometrical discretization (39)

3.5.1 How to create it

Common procedures detected to recreate the geometrical model of the AVF are:

- Follow average physiological features, building artificially a general “representative” AVF using a CAD software;
- Extract data from clinical analyses and use/convert this data into a compatible format for the simulation software.

If the first solution has the benefit of being quite cost-effective, on the other hand it is clear that we cannot truly believe in the results, considering them at least only as a reference for deeper studies: the real cases and critical hot spots determining flow problems in the anastomosis area are not possible to detect with this procedure.

With the second solution, we have a solid basis to entrust with, to have very precise results from subsequent simulations. So even this solution is the most expensive (clinically for the patient and economically for the hospital), this is the most adequate to achieve the best results.

3.5.2 How to Collect Data Required

Considering the intention to approach this study patient specifically, the first concern is to gain sufficient data to ensure a good modelling to get valuable results. The major issue when we have to face with the patient specific theme is that every patient is unique, so its anatomy is, and even its vessels shapes, dimensions and position. For this reason, surgery operations are different one from another, even for a relatively simple operation like the ArterioVenous Fistula. Aware of that, it is not conceivable to study patient AVF ignoring

AVF geometry, and for this reason, the necessity of a precise geometrical model of the fistula is essential.

Now the question to solve is how to collect the data required to obtain the 3D model we want and we need with the minimum effort and costs.

The fact is that patient specific studies in this field has already been done, but following an expensive procedure involving MRI and/or MRA application.

In the medical and engineering practice, the best solution found for this problem is MRI, and precisely MRA.

Looking at these solutions is evident that the best engineering solution should be a middle point between the two (standard physiology reconstruction and MRI geometry extraction) already exposed: the better solution should be cost effective and patient specific correspondent.

Considering this, an alternative way consists in the employment of Ultrasound Echo-Doppler machine. The main idea is to mimic the MRI operation using the data provided by ultrasound scans: collecting different cross-sectional areas of the vessels involved and their relative positions we could be able to merge them into a solid model of the AVF.

3.5.2.1 MRI⁽⁶⁵⁾

Magnetic resonance imaging (MRI) is a medical diagnostic and imaging technique developed in the 1970s used in radiology. The MRI scanners use strong magnetic fields and radio waves, to provide anatomical images of the organs and the physiological processes in the body.

MRI is based on the science of nuclear magnetic resonance (NMR), exploiting the magnetic field of the hydrogen atoms to generate a detectable radio-frequency signal: *“pulses of radio waves excite the nuclear spin energy transition, and magnetic field gradients localise the signal in space.”*⁽⁶⁵⁾ In this way, most MRI scans essentially map the location of water and fat in the body through locating the hydrogen, being the hydrogen atoms at the basis of both water and fats.

Usually, the MRI images are 2-dimensional, presented as sliced of the internal anatomy of the body. However, with the help of the new computer calculation power new strategies has been developed to join together several scans with a technique called “tomography”, enabling the creation of 3-dimensional models of the area of interest. This application is called 3D MRI.

To take a scan, MRI machines typically require a great time, with the patient going into a narrow, confined tube. Moreover, they are louder and present some limitations for people with medical implants or other non-removable metal inside the body.



Figure 41 A GE Signa HDxt 1.5T MRI machine.

However, during years, MRI has proven to be a highly versatile and effective imaging technique, being widely used in hospitals and clinics for medical diagnosis. The main issue with MRI is the sustained increase in demand for this technology, leading to concerns about cost effectiveness and over-diagnosis.

3.5.2.2 MRA⁽⁶⁶⁾

Magnetic Resonance Angiography (MRA) is a particular type of magnetic resonance image (MRI) scan focused in the analysis of blood vessels.

With an MRA, both the blood flow and the condition of the blood vessel walls can be seen in order to detect problems with a person's arteries and veins, such as an aneurysm, a blocked blood vessel, or the torn lining of a blood vessel (dissection). The test is often used to check the blood vessels leading to the brain, kidneys, and the legs.

As for MRI, during MRA, the area of the body to scan is put inside an MRI machine, often using a dye (contrast material) to make blood easier to detect and study. Much like an MRI, information from an MRA scan can be saved and stored on a computer for more study. Photographs of selected MRA views can also be made.

3.5.2.3 *Medical Ultrasound*⁽⁶⁷⁾

Medical ultrasound (also known as diagnostic sonography or ultrasonography) is another frequently used diagnostic and imaging technique. It uses high-frequency sound waves ($>20,000$ Hz) emitted in pulses from a transducer (probe) to render images of the internal body structures such as tendons, muscles, joints, vessels and internal organs. It is one of the most frequent tools used to make accurate and fast diagnoses in many branches of medicine.

The images are reconstructed exploiting sound echoes off the tissue, with different tissues reflecting varying degrees of sound. Particular types of ultrasound imaging can display blood location and flow, the motion of tissues over time, the presence of specific molecules, the stiffness of tissue, or the anatomy of a three-dimensional region.

Compared to other prominent methods of medical imaging, like the ones cited above, ultrasound benefits of several advantages. It provides images in real-time, it is portable and flexible, it has lower in cost for scans and maintenance, and it does not use radiation. Main drawbacks of ultrasonography concern its limits in its field of, the difficulty to operate imaging of structures behind bone and air, and its dependence on a skilled operator.

A deeper analysis of this imaging technology is available in Chapter 4.



Figure 42 The PHILIPS Epiq® 7G ultrasound imaging system.

3.5.2.4 Scanning Costs

It is well known that MRI scans result very expensive in terms of time and costs.

For an MRI scan costs varies between 300£ - 3000 £ per scan region depending on zones and width, with costs beyond 10000£ for complete accurate scans. It takes between 20 – 90 minutes to have a partial scan. This kind of techniques, though effective and very precise in providing data about geometry, blood flow and vessels condition are very expensive in terms of costs related to the operator, the time required, and the machinery used. Indeed an MRI machine has costs that vary from 300000£ for the older and simpler machines to up to 1200000 £ for the newest.

On the other hand, Ultrasound machines have costs which vary between 5000£ – 100000 £ at most for the better machines, with a time required around 5 - 20 minutes, and with a scan cost which is between 50£ - 300 £ per scan region depending on number and width.

Looking for a cost/benefits ratio improvement a new approach has been detected with the support and willingness of the hospital, based exactly on the utilization of the Ultrasound Echo-Doppler and Colour-Doppler techniques.

3.5.2.5 Solution

Ultrasound has also limitations. These are related to the possibility to achieve a 3D model first. A good solution to Ultrasounds limits is trying to obviate to them elaborating le information which can be extracted by Ultrasound scans.

Comes to help to this purpose the Image Processing Toolbox of MATLAB software. Thanks to this commands toolbox it is possible to analyse, extract and enhance geometry (and not only) information included in Ultrasound scans.

Therefore, the combination of a good Ultrasound scans protocol combined with a MATLAB Image Processing dedicated program, can allow achieving the results we are looking for.

3.6 Fluid Dynamics Study

To study how a fluid flows inside a pipe, a vessel or a container, many strategies during years have been developed. Starting by “simple” mathematical expressions based on Navier Stokes Equations, increasingly complex systems have been developed.

Starting with lumped parameters models, a real revolution has been done with the implementation of the fluid dynamics by numerical methods. With the CFD first and with Multiphysics models now, a large field of possibilities is now available to study very deeply every kind of problem.

At the basis of all these techniques there are, in different formulations and detail, there are the Navier-Stokes equations.

Navier-Stokes main equations are:

- Continuity Equations (conservation of mass):

$$\frac{\partial \rho}{\partial t} + \nabla \cdot (\rho \vec{u}) = 0$$

where ρ is the fluid density and u the fluid velocity.

- Momentum Equations (Cauchy momentum equation):

$$\frac{\partial(\rho u)}{\partial t} + \nabla \cdot (\rho u \times u) = -\nabla \cdot p + \nabla \cdot \vec{\tau} + \rho \vec{g}$$

where p is the fluid pressure, τ the fluid viscous stress and g the gravitational acceleration.

- Energy Equations (conservation of energy):

$$\rho \left[\frac{\partial h}{\partial t} + \nabla \cdot (h \vec{u}) \right] = -\frac{dp}{dt} + \nabla \cdot (k \nabla T) + \phi$$

where k is the thermal conductivity and T is the absolute temperature. Then h is the specific enthalpy which is related to specific internal energy as $h=e+p/\rho$ and Φ is the dissipation function representing the work done against viscous forces, which is irreversibly converted into internal energy.

3.7 Lumped Mathematical Models ⁽⁶⁸⁾

Since the pioneering work of Otto Frank in 1899, there have been many types of mathematical models of blood flow. The aim of these models is a better understanding of the biofluid mechanics in cardiovascular systems. Moreover, mathematical computer models aim to facilitate the understanding of the cardiovascular system in an inexpensive and non-invasive way.

A common lumped parameter segment is built of three types of elements: resistors representing resistance to blood flow, inductors related to the force that is needed to accelerate blood and capacitors representing the storage capacity of the blood vessel.

Lumped parameter models are in common use for studying the factors that affect pressure and flow waveforms. In a lumped parameter model, a finite number of variables, defined at special points called nodes, represents the continuous variation of the system's state variables in space. The model will be less computationally expensive, with a correspondingly lower spatial resolution, while still providing useful information at important points within the model.

The most used and studied Lumped parameters models to calculate the distribution of pressure and flow throughout the vascular system are the Windkessel models.

Windkessel models are commonly used to represent the load undertaken by the heart during the cardiac cycle. It relates blood pressure and blood flow in the aorta and characterises the arterial compliance, the peripheral resistance of the valves and the inertia of the blood flow.

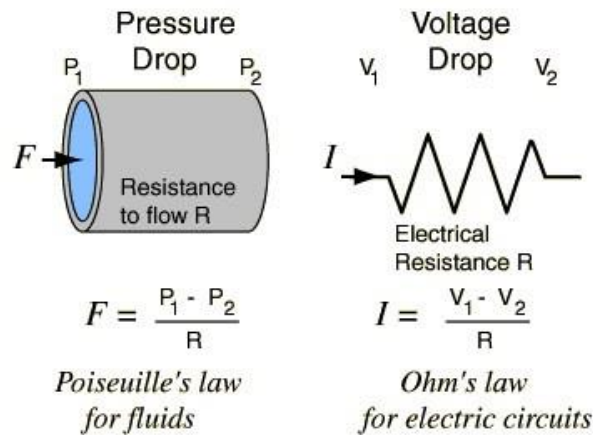


Figure 43 Fluid Dynamics element and its Electrical Circuit Equivalent. (68)

The Windkessel model takes into consideration the following parameters while modelling the cardiac cycle:

- Arterial Compliance:** refers to the elasticity and extensibility of the major artery during the cardiac cycle
- Peripheral Resistance:** refers to the flow resistance encountered by the blood as it flows through the systemic arterial system
- Inertia:** simulates the inertia of the blood as it is cycled through the heart

The Windkessel Model is analogous to the Poiseuille Law for a hydraulic system. It describes the flow of blood through the arteries as the flow of fluid through pipes following the electrical circuit equivalent as shown, calculating the pressure curve determined by the cardiac cycle. As the number of elements in the model increases, a new physiological factor is accounted for and more accurate the results are when related to the original curve.

3.7.1 Electrical Analog Model of Flow in a Tube ⁽⁶⁹⁾

Using the solutions to RLC circuits, it became possible to characterize parameters like the natural frequency and dimensionless damping ratio of the system of interest.

Here it is exposed the development of the modelling of flow through any vessel or tube based on that analogy. The values for resistance, capacitance, and inductance for each component are calculated from the blood vessel properties on a per unit length basis.

The hydrodynamic resistance of a blood vessel depends on its radius and length as well as the viscosity of the fluid flowing in the tube. For this type of discretized model, is derived from Poiseuille law:

$$R_V = lR_{visc} = c_v \frac{8\mu l}{\pi r^4}$$

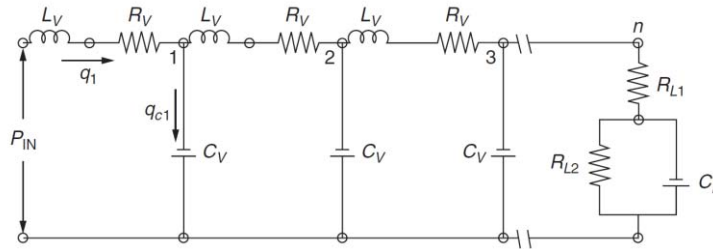


Figure 44 Electrical schematic of a model of blood flowing through a vessel or tube, with the V transcript representing the characteristics of the vessel and L representing the terminal load.

Using the SI system of units, the dimension of R is Ns/m^5 .

The inductance in the vessel for each discrete inductor element becomes:

$$L_V = lL = c_u \frac{\rho l}{\pi r^2}$$

The inductance will have units of Ns^2/m^5 .

The capacitance of the vessel is the compliance of the vessel (dA/dP) depends on the pressure at the point where the capacitor is located:

$$C_v \equiv \frac{q}{dP/dt}$$

Its units in SI are m^5/N .

To keep in mind is that resistance, inductance, and capacitance of each vessel segment can vary in a tapering vessel.

3.7.2 Nodes and the Equations at Each Node ⁽⁶⁹⁾

In the model, the input flow to the first element is labelled q_1 . The input pressure is labelled P_{in} .

Considering node 1, the equation for the pressure drop across the first resistor and inductor is the first-order differential equation:

$$P_{in} - P_1 = q_1 R_{V1} + L_{V1} \cdot \frac{dq_1}{dt}$$

In this equation, P_{in} represents the input pressure to the vessel, P_1 is the pressure at node 1 and q is the flow through the vessel. The change of flow during time is designated dq/dt .

L_{vi} and R_{vi} can vary from node to node, and can even vary with pressure, which would cause our model to be nonlinear.

At node 1 a second differential equation, which is also first order, describes the flow into the capacitor at node 1. The flow q_1 is the vessel compliance at this point C_1 multiplied by dP/dt :

$$q_{c1} = C_{v1} \frac{dP_1}{dt}$$

The pressure at each of the nodes has been considered the independent variables and the flows the dependent variables. Mathematically, the P 's and q 's are dependent on time and location, and time is the only independent variable.

At the end, a system of two first-order ordinary differential equations can be written for each node n . Although the model dimension can be computationally expensive, the equations for each node are relatively straight forward.

The general equations for a general node i , between node 2 and node n , will be

$$P_{(i-1)} - P_i = q_i R_{vi} + L_{vi} \frac{dq_i}{dt}$$

$$q_{c_i} = C_{vi} \frac{dP_i}{dt}$$

3.7.3 Terminal Load ⁽⁶⁹⁾

If we are modelling a vessel, it is possible to divide the vessel into segments and write a set of equations for each finite segment. Continuing to add the downstream details of every branch of the aorta, the model will become larger and more complicated, with a bigger computational cost. Finally, it becomes impractical to individually model each one of the tens of billions of capillaries in the circulatory system. Instead, a more practical solution is to lump together all of the elements downstream of, or distal to, the main vessel that we are trying to understand with our model.

Because the capillaries are primarily resistance vessels it is possible to estimate a load resistance that is based on the pressure at node n , and the flow moving through the entire capillary bed. The total, terminal load resistance, R_T is equal to the pressure at node n divided by the total flow q_n :

$$R_T = \frac{P_n}{q_n}$$

Although R_T would be a good first-order estimate of the terminal load in our model, empirical evidence shows that the capillary bed does not act as a pure resistance element. If the model of the aorta is completed with a single resistance, pressure waves will be reflected proximally because of a mismatch in impedance.

In many cases, the model will predict standing pressure waves where the empirical data show no standing pressure waves. Therefore, the pressure along the vessel will not show a steady pressure gradient as one might expect, but a time-varying pressure gradient that looks like periodic noise. In fact, the vessels downstream the model that make up the terminal load also exhibit a capacitive effect.

It has been suggested that a terminal load for our model could be estimated as a resistor in series with a second resistor parallel to a capacitor as shown in the image below. For steady flow, or at very low frequencies, the total load impedance is equal to the total load resistance, which in this case is the sum of the two resistors. The total terminal resistance R_T is equal to R_{L1} plus R_{L2} , the sum of the values of the two terminal load resistors.

One method of estimating the capacitance of the load C_L is by impedance matching.

For practical, biological systems, we would expect the output impedance of our model to match the input impedance of the terminal load, so that wave reflections are minimized. The ratio of R_{L1} and R_{L2} , as well as the value for capacitance, can be chosen to minimize wave reflections and to match the behaviour of empirical data as closely as possible.

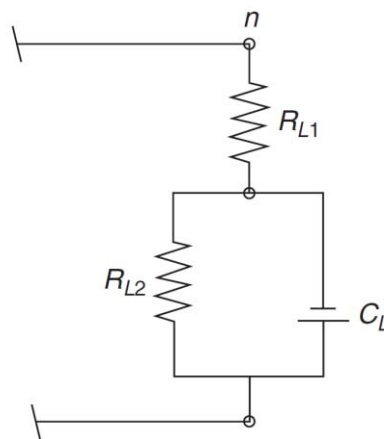


Figure 45 Terminal load of the model described above.

3.7.4 Windkessel Models (68)

About Windkessel models, there have been developed several models with different complexity and configurations. The next models are presented with reference to the modelling of the thoracic aorta, the first and principal artery exiting from the heart.

We have to say that the use of such predictive models is not common in clinical practice yet, even if they might be applied in predictive surgery.

One of the main issue with this modelling technique is that geometric information is lost, and for some physiological aspects this is a top-flight parameter.

3.7.4.1 2-Element Windkessel Model

The simplest of the Windkessel models demonstrating the hemodynamic state is the 2-Element Model. During a cardiac cycle, it takes into account the effect of arterial compliance and total peripheral resistance.

In the electrical analogy, the arterial compliance (C in cm³/mmHg) is represented as a capacitor with electric charge storage properties; the peripheral resistance of the systemic arterial system (R in mmHg x s/cm³) is represented as an energy dissipating resistor.

The theoretical modelling as seen in the electrical analog is given as:

$$i(t) = \frac{P(t)}{R} + C \frac{dP(t)}{dt}$$

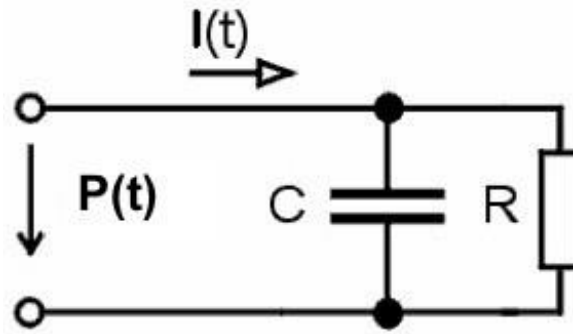


Figure 46 Electrical Analog of the 2-Element Windkessel Model.

3.7.4.2 The 3-Element Windkessel Model

The 3-Element Windkessel Model better simulates the characteristic impedance of the vessels. A resistor is added in series to better fit the blood dynamic behaviour. The already existing parallel combination of resistor-capacitor represents the total peripheral resistance and compliance in the 2-element model as discussed before.

The theoretical modelling as seen in the electrical analog is given as:

$$\left(1 + \frac{r}{R}\right) i(t) + CR \frac{di(t)}{dt} = \frac{P(t)}{R} + C \frac{dP(t)}{dt}$$

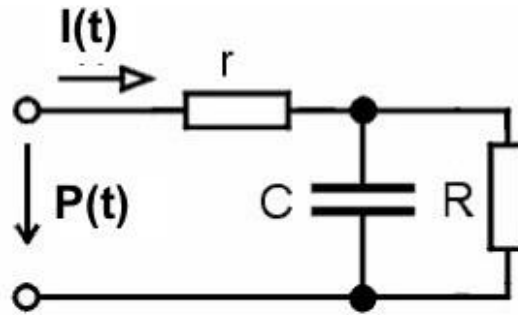


Figure 47 Electrical Analog of the 3-Element Windkessel Model.

3.7.4.3 The 4-Element Windkessel Model

This model includes an inductor in the main branch of the circuit as it accounts for the inertia to blood flow in the hydrodynamic model. The drop in electrical potential across the inductor is given as $L (d i(t)/d t)$. The 4-element model gives a more accurate representation of the blood pressure vs. cardiac cycle time curve when compared to the two and the three element models. The electrical analog is shown here:

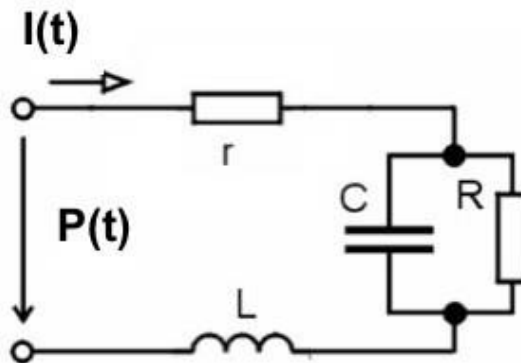


Figure 48 Electrical Analog of the 4-Element Windkessel Model.

Theoretical modelling:

$$\left(rC + \frac{L}{R}\right) \frac{di(t)}{dt} + LC \frac{d^2i(t)}{dt^2} = \frac{P(t)}{R} + C \frac{dP(t)}{dt}$$

3.7.4.4 Model of the Blood Flowing from the Origin (Heart)

The flow of blood into a vessel $i(t)$ is modelled as a sine wave with amplitude i_0 during systole and is zero otherwise, following our learning of the cardiac physiology. During diastole, when the ventricles are relaxed, there is no blood flow into the aorta, and therefore, $i(t) = 0$. During the systole, blood is ejected into the aorta and can be modelled as a sinusoidal wave, therefore:

$$i(t) = i_0 \sin\left(\pi \frac{\text{mod}(t, T_c)}{T_s}\right)$$

where t is time in seconds, T_c is the period of the cardiac cycle in seconds, T_s is the period of systole, in seconds, and $\text{mod}(t, T_c)$ represents the remainder of t divided by T_c . T_s is assumed to be $2/5T_c$, according to the dynamics of the cardiac cycle.

Solving then analytically for the 2-Element Windkessel Model, which given by:

$$C \frac{dP(t)}{dt} + \frac{P(t)}{R} = I(t)$$

In the Systolic phase, an inhomogeneous solution found is:

$$y(t) = c_1 e^{\left(\frac{-t}{RC}\right)} + \frac{e^{\left(\frac{-t}{RC}\right)} T_s I_0 R \left(C \pi R \cos\left(\frac{\pi t}{T_s}\right) \right) - T_s \sin\left(\frac{\pi t}{T_s}\right)}{T_s^2 + C^2 \pi^2 R^2}$$

To solve for the constant c_1 , we consider the initial conditions for $P(t)$ at the start of the systolic cycle.

In the Diastolic phase, a homogeneous solution is found:

$$P_{(t)} = c e^{\left(\frac{-t}{RC}\right)}$$

To determine the constant c , we solve for the initial condition for $P(t)$ at the start of diastole.

The expected value is around 120 mmHg, because the blood pressure for a healthy person is around 120mmHg/80mmHg (Systolic/diastolic).

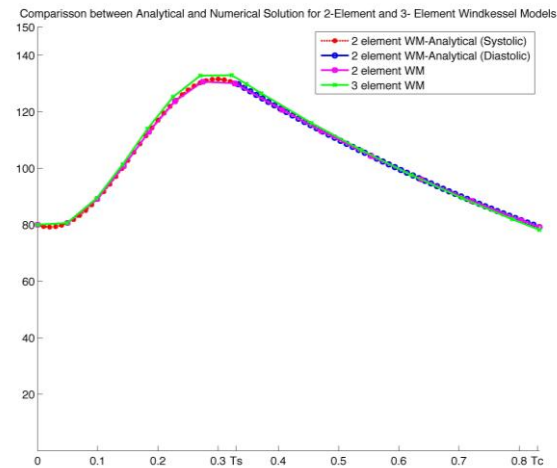


Figure 49 Comparison of 2-Element and 3-Element Windkessel Models for Analytical and Numerical solutions. (68)

3.7.5 Specific Application to AVF (70)

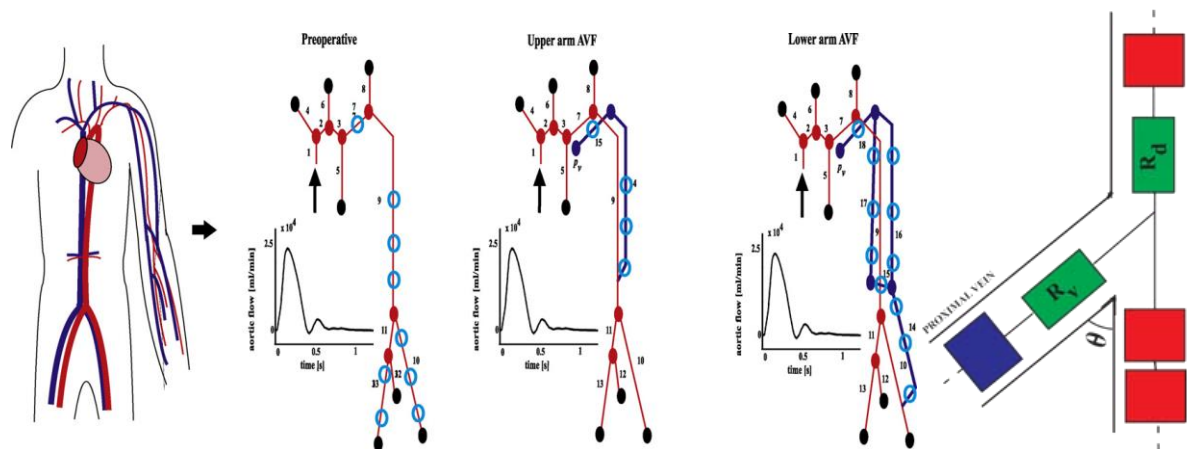


Figure 50 Schematics of the lumped model exploited to model vascular system before and after AVF. (70)

Looking at some recent studies taken on the AVF issue with a lumped mathematical modelling technique, an interesting result has been achieved by W. Huberts et al.

They studied the pulse wave propagation models incorporated with nonlinear equations to describe the relationship between cross-sectional area and pressure, describing additional pressures drops resulting from stenoses, curvature and anastomoses. These pulse wave propagation models include the multi-branched configuration of the arterial system and a description of the distributed nature of arterial properties.

As already described, the vascular system has been divided into segments that represent local blood and vessel wall properties. All segments were serially connected based on the anatomical configuration. For each segment, the relation between pressure and flow was described by the one-dimensional momentum and continuity equations, and a constitutive law is used to describe wall behaviour.

The relation between pressure “ p ” and flow “ i ” for each vascular segment was derived from conservation of mass and the momentum equation by assuming fully developed incompressible Newtonian flow in a straight vessel.

In the momentum equation, approximations for wall shear stress and the convective acceleration term were needed, and the expression for wall shear stress as function of “ p ” and “ i ” is derived from a time and frequency dependent approximated velocity profile which is based on boundary layer theory.

The lumped parameter segment consisted of a Womersley number dependent resistor per unit length R and a Womersley number dependent inductor per unit length L in series representing the momentum equation.

Linear segments could not model the anastomosis because the radial velocity component is no longer infinitesimally small compared to the axial velocity and flow separation can occur in this region. Consequently, a special segment was created to model pressure losses over the anastomosis. The complex flow patterns caused by the anastomosis geometry didn't make possible to apply any classical pressure loss formulation. The reference used was obtained by Steele et al. and Jones et al. have applied pressure loss relations for a T-junction to model the anastomosis

As boundary conditions, arteries were terminated with a three-element Windkessel, with a prescribed pressure. At the end of the venous branch and at the end of the Windkessel model pressures were prescribed.

The results obtained with this technique are very promising.

3.7.6 Possible Applications

Taking into account what is the aim of this study, the main purpose found for the lumped model of the vessels, and eventually of the anastomosis itself, is not to model them to directly study the results provided. Instead, the utility of this kind of models has been detected in the setting up of the subsequent CFD and especially FSI simulations, for what regards the definition of the boundary conditions.

The ability to detect how blood pressure and velocity develop in space and time is very helpful when a good synchronisation of them is required, as in the FSI simulations.

This need is due to the difficulty of collecting simultaneous information at different places with the Ultrasound technique (and with other too). In fact, the strategies used by clinicians to measure blood flow, pressure and velocity are usually different in terms of quality and methods, and they are separated too because of the eventual disturbance of one measurement on the other.

If Ultrasound Colour-Doppler or MRA are the common non-invasive high-resolution techniques to measure blood velocity, for the pressure the only non-invasive pressure measurement is the cuff technique (sphygmomanometer), which occupies a lot of the arm surface (not locally accurate) and allows only the measurement of the systolic and diastolic pressure peaks. On the other hand, a more precise, but complex, solution is the catheter pressure sensor. These sensors are very precise in measurements of pressure in time and space, but they have the flaw to need an invasive operation causing a

complication in the clinical protocol, as well as alter the blood flow inside the vessels of interest.

To overcome this difficulty, helped by researches made and cited above, the idea is to exploit the flexibility and simplicity of the lumped models to achieve the general information at the entrances and exits of the area of our interest, allowing to have a good start point for a more accurate and localized analysis.

3.8 Computational Fluid Dynamics (CFD) ⁽⁷¹⁾

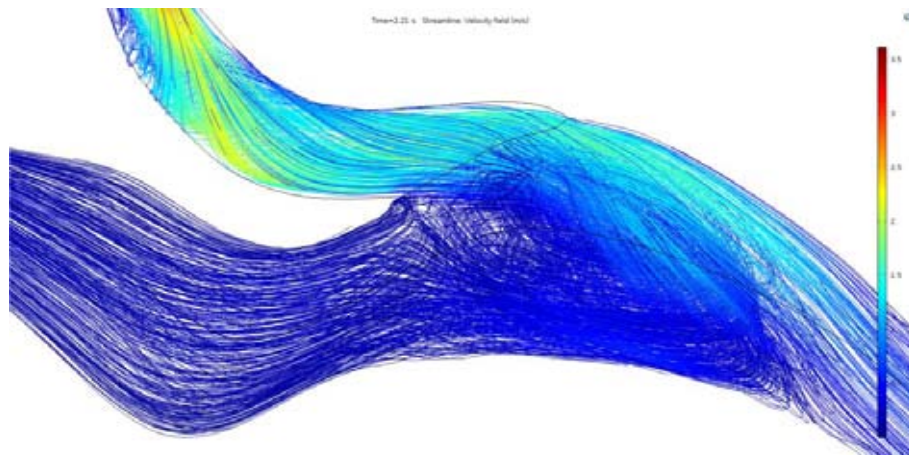


Figure 51 Example of results achievable with CFD simulations.

“Computational fluid dynamics (CFD) is the branch of fluid mechanics that uses numerical analysis to solve and analyse problems that involve fluid flows.” ⁽⁵⁸⁾

Computers are used to perform the calculations required to simulate the interaction of fluids with surfaces defined by boundary conditions.

CFD provides a qualitative and quantitative prediction of fluid flows enabling researchers to perform numerical experiments in a virtual laboratory.

Major means exploited are:

- mathematical modelling (partial differential equations)
- numerical methods (discretization and solution techniques)
- software tools (solvers, pre- and post-processing utilities)

The final focus of all of these is to provide an insight into flow patterns, which could be difficult, expensive or impossible to study otherwise. (72)

At the basis of the CFD theory, there are the Navier-Stokes equations of fluid flow (continuity equations, momentum equations, energy equations). These equations have the power to describe and analyse the fluid flow in every condition, under the appropriate hypotheses and boundary conditions. Nevertheless being quite complex, one of the other strengths of these equations is that they can also be simplified, in circumstances where these simplifications do not affect the final results. The principal simplifications consist on the removing of the viscous terms, leading to the Euler equations. Going further, it is possible to remove the vorticity terms, leading to the full potential equations. The last simplification possible regards the linearization of the full potential equations in case of low disturbed subsonic flows. The first methods developed were the ones solving this very specific problem. (71)

One of the earliest types of calculations resembling modern CFD are those by Lewis Fry Richardson who set the basis for modern CFD and numerical meteorology using finite differences and divided the physical space into cells. First models studied were two-dimensional problems, where several Panel Codes have been developed to study and analyse airfoil. With the improvement of calculation power available, three-dimensional methods developed up to become very spread and exploited in different fields and applications. The Navier-Stokes equations were the ultimate target of development.

Starting by these landmarks different models had been developed trying to fit every different physics branch regarding fluid dynamics.

3.8.1 Fluid Characteristics

The macroscopic properties of the fluid are the first parameters affecting flow behaviour. As already discussed, the main variables to consider in a CFD simulation are the density ρ , the viscosity μ , the pressure p , temperature T and the velocity v .

Basing on these variables, the geometry, the temporal variations, and the number of fluids/phases considered, fluid flow can be classified as:

- viscous or inviscid
- compressible or incompressible
- steady or unsteady
- laminar or turbulent
- single-phase or multiphase.

The reliability of CFD simulations is strictly dependent on the type of fluid flow, with laminar/slow flows more reliable than turbulent/fast ones, as single-phase flows compared to for multiphase flows and chemically inert systems compared to reactive flows. The types of assumptions, simplifications and methods used to solve the flow equations motivate this.

3.8.2 Methodology⁽⁷³⁾

In all of these approaches to solve Navier-Stokes equations, the same basic steps in the procedure are the following:

1) Pre-processing phase

First it is defined the Problem statement to give information about the flow; then the Mathematical model is set: Initial Boundary Value Problem (IBVP) = Partial Differential Equation (PDE) + Initial Conditions (IC) + Boundary Conditions (BC). The geometry and physical bounds of the problem are defined using computer aided design (CAD), and basing on that a Mesh is generated, dividing the volume occupied by the fluid into discrete elements. The physical modelling and the Boundary conditions are defined, specifying the fluid behaviour and properties at all bounding surfaces of the fluid domain. Finally, Direct/Iterative solver is chosen and set up, leading to the CFD software implementation.

2) Simulation phase

The simulation is run and the equations are solved following the equations and the settings imposed.

3) Post-processing phase

Post-processing visualization of the results and data analysis are performed, and the Verification and validation of the model are carried out basing on the collected results.

3.8.3 Discretization Processes ⁽⁷³⁾

The Partial Differential Equations (PDE) system has to be transformed into a set of algebraic equations. In this procedure, discretization involves different aspects in CFD analysis, in particular:

- Mesh generation (decomposition into cells/elements):

In this step, the choice of structured or unstructured elements, with hexahedral, tetrahedral, prismatic, pyramidal or polyhedral geometry is done. Even the mesh size and refinements in 'interesting' flow regions are set up.

- Space discretization (approximation of spatial derivatives):

The best method (finite differences/volumes/elements/...) is selected, so the choice of high- vs. low-order approximations.

- Time discretization (approximation of temporal derivatives):

The explicit or implicit schemes and stability constraints are set up, and the local time-stepping/adaptive time step control are defined.

The stability of the selected discretization is generally established numerically, taking care to ensure that the discretization handles discontinuous solutions gracefully.

Some of the discretization methods being used are: Finite volume method, Finite element method, Finite difference method, Spectral element method, Boundary element method, High-resolution discretization schemes.

3.8.4 Solution Algorithms ⁽⁷¹⁾

The result after the spatial discretization is a system of ordinary differential equations (unsteady problems) or algebraic equations (steady problems) to be integrated using implicit or semi-implicit strategies and giving as output a system of usually non-linear algebraic equations.

To solve these systems, which moreover are often non-symmetric, direct or iterative solvers are exploited, depending on the size of the problem to solve. Iterative solvers work minimising the residual over successive subspaces generated by the preconditioned operator, and are indicated for large problems. Iterative solvers and preconditioners are able to reduce the high-frequency part of the residual, but are limited to do the same for the low-frequency components. To help with that issue is the Multigrid operation, which can reduce all the components, ensuring a mesh-independent number of iteration too. (71)

The main strategies are to iteratively solve the algebraic equations are:

- Outer iterations: the coefficients of the discrete problem are updated using the solution values from the previous iteration
- Inner iterations: the resulting sequence of linear sub-problems is typically solved by an iterative method because direct solvers are too much expensive
- Convergence criteria: it is necessary to check the residuals, relative solution changes and other indicators to make sure that the iterations converge. (73)

3.8.5 CFD Simulations ⁽⁷³⁾

Once ready the solver run the simulation. The main aspect of interest at this time is the computational cost of the numerical problem.

The computing times for a flow simulation depend on:

- The choice of numerical algorithms and data structures
- Linear algebra tools, stopping criteria for iterative solvers
- Discretization parameters (mesh quality, mesh size, time step)
- Programming language
- Many other things (hardware, vectorization, parallelization etc.).

The quality of simulation results depends on:

- The mathematical model and underlying assumptions
- Approximation type, stability of the numerical scheme
- Mesh, time step, error indicators, stopping criteria . . .

3.8.6 Post-Processing and Analysis ⁽⁷³⁾

Post-processing of the simulation results is performed after the conclusion of the solver work, in order to extract the desired information from the computed flow field.

The main actions operated in the post-processing are:

- Calculation of derived quantities (stream function, vorticity, stresses,...)
- Calculation of integral parameters (lift, drag, total mass, averaged velocities and stresses)
- Visualization (representation of numbers as images) of 1D data - 2D data - 3D data, arrow plots, particle tracing, animations . . .
- Systematic data analysis by means of statistical tools
- Debugging, verification, and validation of the CFD model.

3.8.7 Uncertainty and Error ⁽⁷³⁾

Whether or not the results of a CFD simulation can be trusted depends on the degree of uncertainty and on the cumulative effect of various errors.

Acknowledged errors in CFD simulations are related to:

- Physical modelling due to uncertainty and simplifications
- Discretization and approximation of PDEs by algebraic equations
- Iterative convergence which depends on the stopping criteria
- Round-off due to the finite precision of computer arithmetic.

Unacknowledged errors are related to computer programming errors (“bugs”) in coding and logical mistakes, or to usage errors in wrong set up of the simulation.

Awareness of these error sources and the ability to control minimize them are important prerequisites to achieve reliable CFD results.

3.8.8 Verification ⁽⁷³⁾

The verification is the final procedure after a simulation, to look for errors in the implementation of the models, basing on:

- Checking the computer programming
- Examining iterative convergence
- Controlling consistency
- Testing grid convergence
- Comparing the computational results with analytical and numerical solutions.

3.8.9 CFD Advantages and Limitations

Computer Fluid Dynamics best ability is allowing to have an insight into flow patterns which are difficult, expensive or impossible to study exploiting experimental techniques.

Indeed, numerical simulation has its strength in the flexibility and precision achievable in a wide amount of different cases and situations, adapting in an easy practical way to the very specific case. The computing power required to the hardware is proportional to the square of the complexity and refinement desired, being one of the main factor limiting the choice of these methods. In the recent times however, thanks to the continuous improvement of the available technology, even this limit is going to be less influent.

Regarding the numerical modelling, nowadays a deep comprehension of physical laws and equation behind the phenomena studied is necessary not to incur to errors and incoherent results.

A lot of data to set up complex models is still needed, especially regarding the 3D structured models. Due to the high sensibility of the fluids to the geometrical variations, a lot of care has to be committed to the establishment of a precise model, building the most thorough representation of the boundary condition to the problem.

Compared to experimental studies, numerical simulations are advantaged because of the relatively low cost. In fact, experiments are known to be expensive, slow, sequential and single-purpose. Simulations instead are cheaper, faster, parallel and multiple-purpose procedures allowing a sensible cut in experimental times and costs. The flexibility and availability strengths of the CFD consist in being a tool accessible from every part of the world, in every condition, in an easy-access way, not presenting any kind of limitation in specimen or prototype dimensions, transportation and set up of complex laboratories and facilities.

Moreover, CFD can provide a higher resolution in space and time of the virtual studies, because there is no need to introduce instruments to operate measurements, even if it cannot still replace entirely experimental measurements.

Causes of error are dependent on the modelling, the discretization, the iteration and implementation of the entire study. The results of a CFD simulation are never 100% reliable because the input data may involve too much guessing or imprecision or the mathematical model of the problem at hand may be inadequate or even the accuracy of the results is limited by the available computing power. A good strategy is to test and verify results.

3.8.10 Available CFD Software

Since from beginning of CFD era, a lot of strategies and codes have been developed to fit the better the reality. For this purpose, and for economic competition reasons, many software and software houses have been born to supply every customer need. The principal are:

- STAR-CD (<http://www.cd-adapco.com> commercial)
- ANSYS CFX (<http://www.ansys.com> commercial)
- FLUENT <http://www.fluent.com> commercial)
- COMSOL Multiphysics (<http://www.comsol.com> commercial)
- FEATFLOW (<http://www.featflow.de> open-source)
- OPENFOAM (<https://openfoam.org>).

Nowadays the differences between these software are limited (depending on the available solving and meshing algorithms) and resulting mainly on business and

strategies and initial software structure design (i.e. user interface, user friendliness, usability, customization, etc.).

As of now, CFD software is not yet ready to allow a blind usage by designer and analysts without a basic knowledge of the underlying physics and numerics, especially in the new mathematical models require modification of existing / development of new CFD tools.

A basilar strategy is to make some previous experience with numerical solutions of a simplified problem, making it easier to analyse strange looking simulation results and identify the causes irregularities.

3.8.11 CFD in Biomedical Engineering Application

Today CFD investigations are used to clarify the characteristics many clinical issues. Primarily focused on cardiovascular problems, due to a large amount of fluid this biological system has to manage, its usage is focused on detailed studies of blood flow that are otherwise invisible to experimental measurements. The first step in analysing these problems is the creation of a CAD 2D or 3D model (depending on the interests and resources available) of the particular subject, extracted thanks to the most suitable imaging techniques. It is also possible before solving to set the specific blood properties and Non-Newtonian behaviour, over the patient specific boundary conditions. In this way, it is possible to study and optimise every application regarding blood flow in the cardiovascular system.

Principal advantages of these techniques are the possibility to simulate future vessels and flow cases, leading to a better understanding of various pathologies and allowing the surgeons to choose the best solutions for every surgical operation.

CFD software accuracy and flexibility to every problem and condition, with the concurrent recent development in computational power of modern computers, is the reason why nowadays, especially for localized problems, this is the best choice for a thorough study.

3.9 Fluid–Structure Interaction (FSI)

“Fluid-structure interaction (FSI) is a Multiphysics coupling between CFD (fluids) and FEM (mechanics) simulations where fluid flow affects deformation of a solid structure, which in turn changes the boundary condition of the fluid flow.” (74)

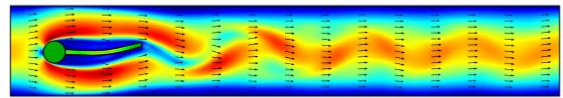


Figure 52 FSI simulation of a vibrating beam in fluid flow.
(74)

The interaction is iterative, because of the coupled effect of one physics on the other. This kind of simulations has been exploited to study interaction movable or deformable structures within a fluid flow.

“When a fluid flow encounters a structure, stresses and strains are exerted on the solid object, forces that can lead to deformations. These deformations can be quite large or very small, depending on the pressure and velocity of the flow and the material properties of the actual structure.” (74)

Two types of FSI simulations occur: the first is referred to a fluid flow little influenced by the structure deformation, the second one is applied when the fluid flow undergoes to significant changes due to the induced deformations. In this second case, the problem has to be studied bi-directionally: the fluid flow and pressure fields will affect the structural deformations, which in turn will affect the flow and pressure.

The governing equations at the basis of the FSI theory are:

- For compressible fluids:

1) Momentum Equation:

$$\begin{aligned}\rho \cdot \frac{\partial u_{fluid}}{\partial t} + \rho(u_{fluid} \cdot \nabla)u_{fluid} = \\ = \nabla \left[-pI + \mu \left(\nabla u_{fluid} + (\nabla u_{fluid})^T \right) - \frac{2}{3} \mu (\nabla \cdot u_{fluid})I \right] + F\end{aligned}$$

2) Continuity Equation:

$$\frac{\partial \rho}{\partial t} + \nabla \cdot (\rho u_{fluid}) = 0$$

3) Newton Second Law Equation:

$$\rho \frac{\partial^2 u_{solid}}{\partial t^2} - \nabla \sigma = F_v$$

- For incompressible fluids:

1) Momentum Equation:

$$\rho \cdot \frac{\partial u_{fluid}}{\partial t} + \rho(u_{fluid} \cdot \nabla)u_{fluid} = \nabla \left[-pI + \mu \left(\nabla u_{fluid} + (\nabla u_{fluid})^T \right) \right] + F$$

2) Continuity Equation:

$$\rho \nabla \cdot u_{fluid} = 0$$

3) Newton Second Law Equation:

$$\rho \frac{\partial^2 u_{solid}}{\partial t^2} - \nabla \sigma = F_V$$

4) The fluid-solid interface boundary conditions:

$$u_{fluid} = u_{wall}$$

$$u_{wall} = \frac{\partial u_{solid}}{\partial t}$$

Where ρ is the fluid density, u_{fluid} the fluid velocity, p the fluid pressure, μ the fluid viscosity, F the body force vector of the fluid medium, σ the solid internal stress, u_{solid} the structure displacement and F_v are the external forces.

The transfer of the boundary conditions between the solid and fluid interfaces is one of the most important operations in an FSI solution. Fluid-Structure coupling occurs in various forms in many fields of engineering, both in natural systems as well as artificial objects.

These problems are usually analysed by numerical simulations, being too much complex to undergo to an analytical study. In cases for which numerical simulations are applied are the ones in which experimental testing and study are not economical, feasible or too much time-consuming.

Thanks to this numerical approach, frequently a better understanding of the problems is achieved, because of the deep level of detail these techniques can provide in studying structures often difficult to analyse physically.

One of the biggest limitation is related to the big computational costs and times related the study of these complex problems, which requires dedicated stable and accurate coupling algorithms to reach convergence. However, during last decades massive developments have been achieved in coupling algorithm optimisation and performance enhancement, together with computer computational power increase. This overcame the past problems, enabling to solve some physical applications that were not accessible in the past.

Understanding how a flexible structure, directly coupled to a fluid flow environment, behaves may present novel engineering insights, improving the general understanding of several biological phenomena.

Specifically, Fluid-Structure Interactions can be stationary or time-dependent: in time-dependent interactions, the strain induced by the flow causes the structure displacement

until when the source of strain is reduced, enabling the structure to return to its more stable configuration. (74) (75)

3.9.1 Application of FSI

Very important FSI applications in man-made objects field are aero-elasticity, hydro-elasticity, flow-induced vibration, thermal deformation etc.

One of the most infamous examples in which FSI played a fundamental role is the large-scale failure of Tacoma Narrows Bridge (1940),

collapsed under the aero-dynamical induced resonance (flutter). Even aircraft wings and turbine blades can break due to the same FSI effects.

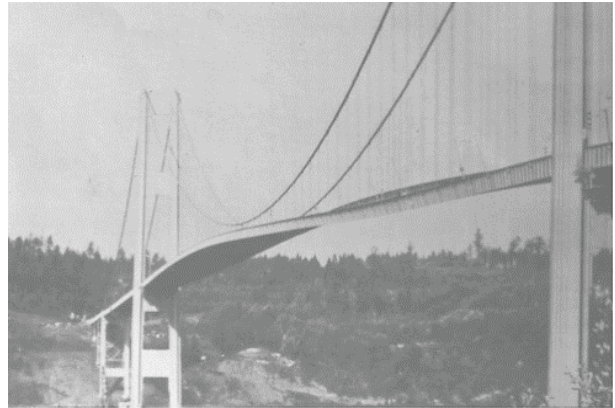


Figure 53 The famous Tacoma Narrows Bridge 1940 collapsed by the effect of resonance induced by wind flow.

Fluid-structure interactions also occur in moving containers, where liquid sloshing causes significant forces and moments to the container structure affecting the stability of the entire container.

This phenomenon has been taken into account also in the analysis of blood flow inside the vessels and through the artificial heart valves. The natural operation principle of the entire cardiovascular system is based on the fluid-structure interaction mechanism, related to pressure generated by the heart and pressure waves along the peripheral vessels.

Thanks to FSI simulations, the studies regarding blood flow inside several different structures of the cardiovascular system has been deepened, also thanks to the new and better imaging, modelling, mesh generation, computation and visualization technologies.

“State-of-the-art vascular modelling involves fully coupled fluid-structure simulations of large portions of the human cardiovascular system.” (76)

The fluid-structure interaction problems in pressured vessels and piping systems involve diverse mechanical failure mechanisms. The major applications are focused on *“the analysis of the stationary structures in a flowing fluid, the moving structures immersed in a flowing or quiescent fluid, the stationary pipes or vessels containing cold or hot flowing fluid, as much as flow-induced vibration, water hammer, thermal deformation and fatigue”.* (75)

3.9.2 Approaches for Fluid Structure Interaction Simulation

Two main approaches exist for the numerical simulation of fluid–structure interaction problems: the Monolithic Approach and the Partitioned Approach.

The first performs the solution of both flow and structure equations simultaneously, in this way requiring substantially more resources and expertise to set a convergent simulation.

The second solves the flow and structure equations separately, with distinct solvers. The challenge here is to coordinate the different algorithms to achieve accurate and efficient solutions with the minimal computational costs. (75)

3.9.3 Classification of FSI Coupled System

As mentioned, at the interfaces between the two physic fields the information are exchanged, “coupling” the problems. The coupling can be weak or strong, depending on the fact if induced reactions on the other physical field are considered or not.

A weakly coupled FSI system is a system in which the structural changes slightly affect the fluid flow, enabling not to consider the feedback of the structural problem on the fluid flow problem.

Vice-versa a strongly coupled problem takes into account the alteration of the flow field due to large deformation or high-amplitude vibrations of the structure which cannot be neglected.

Obviously, this second type of coupling is more complex and requires a deep and accurate set up to allow convergence and good results at the lowest computational cost.

3.9.4 FSI Mesh

Usually, FSI meshes are simple to establish, even if not matching. Anyway, as soon as mesh-morphing is needed, the mesh problem starts to become relevant and difficult to be solved. The key-problems with mesh-morphing are performance and surface quality. To work properly, CFD models requires efficient morphing algorithms, which usually are very requesting for the computational resources.

Moreover, to calculate reliable and convergent solutions, the solving algorithms requires a very good surface discretization otherwise, oscillations and artefacts start to be observed. This is namely a challenge in the case where the mesh providing the

deformation (structural FE-mesh) is significantly coarser than the surface mesh of the CFD-model. (77)

3.9.5 Numerical Simulation

To solve FSI problem, usually the Newton–Raphson method or a different fixed-point iteration are used, for both the monolithic and the partitioned approach. These methods solve the nonlinear flow equations and the structural equations in the entire fluid and solid domain with the Newton–Raphson method.

The FSI solving can even be performed with the fixed-point Gauss-Sidel iterations, computing successively the flow problem and the structural problem. With this technique, the main concern is the convergence, which is slower, especially with strongly coupled problems. However, convergence can be stabilised and accelerated exploiting Aitken relaxation and steepest descendent relaxation. (78)

3.9.6 FSI in Biomedical Engineering Application ⁽⁷⁹⁾

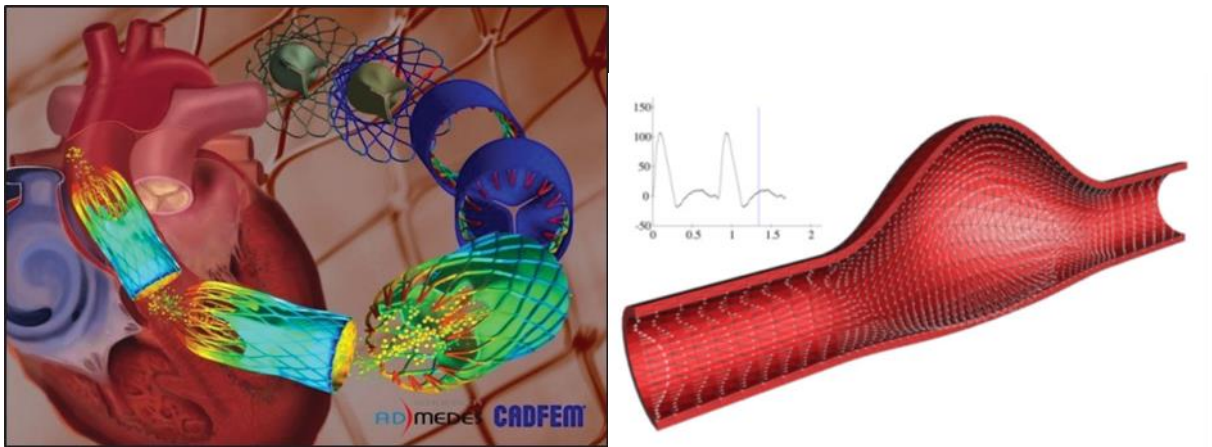


Figure 54 FSI Application in Cardio Vascular System. (126)

Numerical methods for incompressible fluid dynamics have recently received a strong impulse from the applications to the biomedical engineering studies: recent years have seen a strong trend towards modelling and simulation in biomedical engineering, biomechanics, biofluids, and mechano-biology.

Fluid–Structure Interaction methods have been extensively investigated to achieve accurate and possibly fast in-depth analysis of many human systems, not only to understand the physiology and pathology of these systems, but even for prevention and prediction of several diseases and complications.

High tech Imaging may help to elucidate the interplay between blood flow and vessel wall stability by providing patient-specific data on regional blood flow, vessel wall geometry, and vessel wall deformability, but the resolution of these data, in particular of the vessel wall composition, is limited. However, the new possibilities offered by the most recent medical imaging technologies properly processed, open up new frontiers in simulating fluid flow in real patient-specific cases, increasing the potential impact of scientific computing on the clinical practice. (79)

Anyway, “in-silico” experiments are currently extensively used in bioengineering for completing more traditional in vivo and in vitro investigations to get all the necessary data to perform the further numerical analysis. This need of quantitative data for further diagnostic purposes has strongly stimulated the design of new methods and instruments for measurements and imaging. (79)

The final result of these techniques consists in Data Assimilation, which merges the experimental measures and the numerical simulations to provide a sound integration of these diverse sources of information. The outcomes of these processes are the robust and efficient patient-specific measures and mathematical models. The strength of these procedures consists in the possibility to adapt the numerical simulations to the availability of individual data making them more reliable.

Due to its significance, FSI and new measurements techniques have been heavily applied to hemodynamic nevertheless, despite all efforts undertaken so far, a lot of questions and issues related to the representativeness of the results obtained are still open.

The cardiovascular system is a very complex biological system, in which several factors play fundamental roles in determining the sensible interaction between blood flow and the vessels walls. Diseases such as plaque or aneurysm rupture, atherosclerosis, etc. occur when hemodynamic blood dynamic conditions and thus internal stress exceed a threshold that cannot be compensated by vessel wall deformation. Magnetic resonance imaging (MRI) has been detected as the most promising imaging technique to interpret the interaction between blood flow and vessel wall stability by providing patient-specific data on regional blood flow, vessel wall geometry, and vessel wall deformability, but the resolution of these data, in particular of the vessel wall composition, is limited. (79)

Other interesting and promising researches involve the study of lungs expansion during the breath, eyes surgery and physiology, vocal chords vibration, vessels pathologies, etc., for both large displacement and vibrating problems.

(Helpful cases, researches and documents studied to acquire a good comprehension of the application of FSI in biomedical engineering studies, specifically looking for cardiovascular problems, are Topiwala et al. (75) Bertagna et al. (79) Bazilevs et al. (80), Wang et al. (81), Crosetto et al. (82), Scotti et al. (83), Bluestein et al. (84), Malvè et al. (85).)

3.10 Conclusions

Cardiovascular numerical simulations are nowadays a mature discipline not only for understanding and improving basic knowledge of diseases but also for supporting the clinical practice, with an accurate quantitative estimate, prediction, identification of optimal therapies. In particular, the common denominator of this exciting perspective is the presence of inverse problems, where problems related to blood flow and FSI, traditionally per se challenging, need to be solved several times, assimilated to available measures, analysed with probabilistic tools.

This is true also for the identification of the optimal realization of a therapy or, more specifically, of a surgical intervention. For instance, in the identification of the optimal placement of leads for optimizing pace-making action in the heart is addressed, the computation of a personalized patient-specific peritoneal dialysis is addressed in.

This process bringing complex quantitative analyses from the computer to the bedside requires a strong integration with available data, shifting the goal of performing a patient-specific computation to the patient-specific “assimilation”. This is a crucial step for improving the reliability of numerical elaborations, reducing uncertainty and eventually the risks of failure.

This chapter intended to offer a brief introduction with a special emphasis on CFD and FSI problems to some possible methods and to their interplay. Far to be a conclusive and exhaustive presentation.

3.11 Procedure Established

The problem related to the study and prediction of the ArterioVenous Fistula maturation has been demonstrated to be primarily influenced by the blood flow magnitude and distribution in time. More precisely, the stresses generated by this kind of blood flow are the main indicators of endothelial response and AVF maturation.

An approach based on Computational Fluid Dynamics has been chosen to develop these studies because of its flexibility and ability to provide precise results in a condition of large variability in geometry and fluid conditions.

The problem here has been to establish a new technique versatile, easy and cost effective, but in the meantime accurate, to study patient-specific AVF and evaluate significant parameters revealing maturation success.

The data required for a patient-specific study was the AVF geometry, the blood pressure and velocity conditions at inlets and outlets. Obtaining these data has been the most significant milestone of this work: patient pre- and post-AVF vessels condition has been studied in a restricted area around the anastomosis.

Capturing images of these vessels with ultrasound equipment, and exploiting the image analysis and editing through MATLAB Image Processing Toolbox, it has been possible to rebuild the geometric model of vessel configuration.

Image acquisition was the first step for setting up a good model for our case study. Quality of images and precision in their positions were the most relevant parameters to guarantee a good image processing and a good accuracy in the final model.

What we were supposed to do was to create a 3D model of the two vessels of interest (vein and artery) and of the anastomosis operated to obtain the AVF starting with many cross-sectional images obtained through Echo-Doppler Ultrasound.

Subsequently, also thanks to MATLAB and Ultrasound Colour-Doppler, we have been able to extract the data required to set up the boundary conditions and run a CFD simulation.

The data needed was:

- Time-dependent Velocity profile at the inlet/outlet
- Time-dependent Pressure at the inlet/outlet.

From the CFD simulation results, we have been finally able to evaluate the objects of our interest.

To check if the model and simulation results were reliable and correct, additional requirement should be:

- MRI (MRA) scan to check vessels geometry match and real blood flow profile and magnitude in the entire domain of interest
- Ultrasound Colour Doppler blood flow velocity to check real blood flow profile and magnitude in specific positions.

Starting from the equipment available (PHILIPS Epiq® 7G ULTRASOUND SYSTEM® - MATLAB Image Processing Toolbox® - Microsoft Excel® - Autodesk Inventor® - Autodesk AutoCAD® - COMSOL Multiphysics®) the main issues to solve were:

- The need to create 3D geometry starting with 2D images
- The inability to take a picture of the entire area of interest (the inability to capture in the same image both the vessels)
- The lack of knowledge about the relative position of the probe and the arm when the picture was taken
- The inability to detect, separate and extract the vessels geometry of interest, knowing the relative position on the arm
- The difficulty to set up an easy procedure to capture images knowing in the same time the exact position in which each picture was taken

- The need to convert the vessels to real shape and position in a CAD model
- The necessity of information about the blood flow in terms of velocity magnitude and profile and time.

The solution found to design the model was to establish a procedure in which several images of vein and artery were separately taken in precise positions. Each of these positions has a precise reference on the arm of the patient (the better solution is to use a tattoo applied to a cling film specifically designed with a grid coordinate). Once these images were captured, an image processing operation was set up to detect and extract vessel profiles and convert them into segmented points coordinates to import in the CAD software.

In the CAD software, a sample of a human arm (5th percentile correspondent) was used to place in the correct position the different sets of coordinates, with the help of an image of the patient's arm with the grid applied. Using LOFT command in CAD the vein and artery geometry were built through the cross-sectional areas imported.

Once the 3D model was finished, it was imported into COMSOL, in which several CFD analysis were solved using the boundary conditions extracted from the Ultrasound Colour Doppler, and studying the flow related parameters demonstrated to affect the AVF maturation (Wall Shear Stress, Oscillatory Shear Index, etc.).

Further possibilities of this work, with the help of lumped parameters modelling, are to set up even an FSI simulation, trying to extract the pressure pulse wave magnitude and timing needed for the simulation through this mathematical method.

This can open up new strategies in analysing the AVF problem, besides giving results closer to the physiological reality. The major problem in this is to find reliable information about vessels mechanical properties, ensuring the accuracy of the pulse wave synchronization with the blood velocity pulse wave.

4 ULTRASOUND IMAGING⁴

⁴ Eventual references on the chapter or paragraph titles are to be intended to be the main sources of the informations provided on that chapter or paragraph.

Ultrasound is a particular type of sound waves, usually described by its frequency, which is greater than 20 kHz, as defined by the American National Standards Institute. Audible sound waves are in the range of 20 Hz to 20 kHz, whereas ultrasound related devices operate with frequencies from 20 kHz up to several gigahertz, so for human is quite difficult to perceive this type of sound waves.

Different Ultrasound uses and applications are listed below.

- Non-contact sensor
- Motion sensors and flow measurement
- Non-destructive testing
- Ultrasonic range finding
- Ultrasound Identification
- Ultrasonic impact treatment
- Ultrasonic cleaning
- Ultrasonic disintegration
- Ultrasonic humidifier
- Ultrasonic welding
- Wireless communication
- Physical therapy (treating connective tissues)
- Biomedical applications and treatments (non-invasive scans and measures, breaking up stony deposits or tissue, accelerate the effect of drugs).

Regarding our field of interest, Ultrasound imaging or sonography is often used in medicine as a non-invasive inspection tool for many different pathologies. (86)

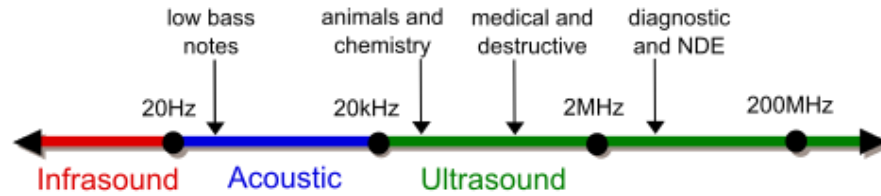


Figure 55 Approximate frequency ranges corresponding to ultrasound, with a rough guide of some applications. (86)

4.1 Medical Ultrasound (87) (88)

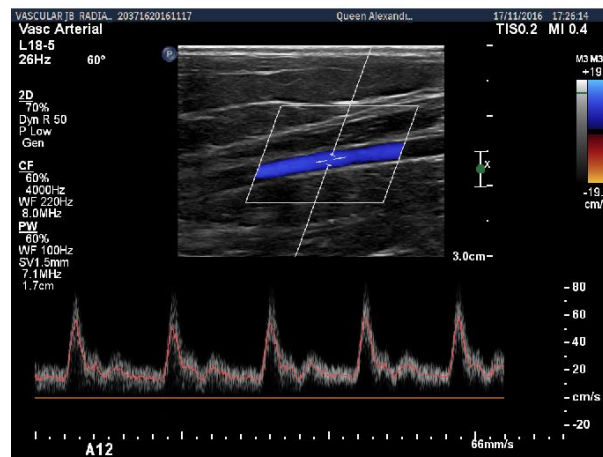


Figure 56 Application of Ultrasound to vascular assessment.

In medical Ultrasonic imaging the frequencies, range widens between 2 mega-Hertz and up to 4 giga-Hertz to provide the best quality medical images: the shorter wavelength allows better resolution of small details.

Diagnostic ultrasonography is an ultrasound-based diagnostic medical imaging technique used to visualize tissues and organs, to control their size, structure and any pathological lesions with real time tomographic images.

Nowadays, it has long been that radiologists have used Ultrasound for medical purposes, so that during the last 50 years it has become one of the most widely used diagnostic tools. Ultrasound technology is relatively inexpensive and has the advantage to be easily portable, especially when compared with other techniques, such as magnetic resonance imaging (MRI) and computed tomography (CT).

Ultrasound can be extremely useful in the evaluation of the many problems facing the hemodialysis patient. Being a non-invasive technique, it can show more vascular detail than physical examination, without any risk of information alteration or patient disturb.

Many different types of images can be obtained exploiting sonographic instruments. The most useful type for our cardiovascular examination purposes displays images of blood flow, motion of tissue over time, the location of blood, the presence of specific molecules, the stiffness of tissue, or the anatomy of a specific region.

With Vascular Ultrasound examinations, the instruments provide a black and white anatomical image that can demonstrate the presence of a disease along the vessels wall. With Colour-Doppler Ultrasound, it allows extracting a colour flow image, which displays the blood flow in arteries and veins. Spectral Doppler analysis then enables recording the Doppler waveforms, allowing the detection of changes in flow patterns and the calculation velocity measurements.



Figure 57 Two different applications of the ultrasound imaging.

Standard sonographic instruments operate in the frequency range that is a trade-off between spatial resolution of the image and imaging depth, resulting in a range of 1 to 18 megahertz.

With the higher frequency sound waves, it is possible to study even smaller structures, with a consequent larger attenuation due to the major absorption by the tissues, limiting the depth of penetration. Superficial structures such as veins are imaged at higher frequencies of 7–18 MHz. The lower frequencies provide less resolution but allow deeper images into the body: internal organs such as liver and kidney are imaged at frequencies of 1–6 MHz.

The typical probes used in medical sonography are hand-held probes called transducers, directly placed and moved on the patient skin. The transducer simply converts the sound energy emitted into the electrical signal and vice-versa. In the case of an ultrasound transducer, this conversion is from electrical energy to mechanical vibration, exploiting the piezoelectric effect.

Medical sonography is used several medical applications, like Anesthesiology - Angiology - Emergency Medicine - Gynecology - Neurology Ophthalmology - Pulmonology - Urology- ...

In Angiology, it is helpful to diagnose arterial and venous disease all over the body, and the same is for Cardiology, where it is used to diagnose dilatation of parts of the heart and function of heart ventricles and valves. Looking at the cardiovascular system, ultrasound imaging is exploited to assess patency and possible obstruction of arteries: arterial sonography diagnoses deep vein thrombosis and determines extent and severity of venous insufficiency.

As currently applied in the medical field, properly performed ultrasound poses no known risks to the patient, although the long-term effects due to ultrasound exposure at diagnostic intensity are still unknown.

4.2 Modes of Sonography

Several modes of ultrasound are used in medical imaging. The relevant types for our purposes are:

- A-mode: this simplest type of ultrasound uses a single transducer to provide 1D scans as a function of depth.
- B-mode or 2D mode: a linear array of transducers simultaneously scans a plane through the body plotting a two-dimensional image on screen.
- C-mode: provide an image in a plane normal to a B-mode image.
- M-mode: it emits pulses in quick succession, enabling to record videos and determine the velocity of specific organ structures.

- Doppler mode: makes use of the Doppler effect in measuring and visualizing blood flow, the principal technique is the “Colour Doppler”, where velocity information is presented as a colour-coded overlay on top of a B-mode image
- Pulse inversion mode: is used to highlight non-linearly responding materials like gases
- Harmonic mode: is used to reduce noise and artefacts due to reverberation and aberration.

4.3 Doppler Ultrasonography

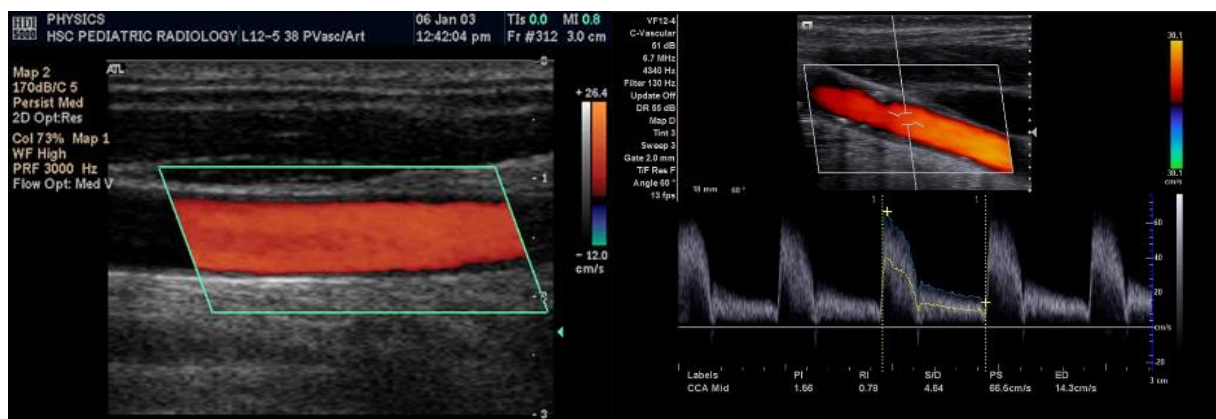


Figure 58 Spectral Doppler scan and Colour Doppler scan of the carotid artery. (152)

Sonography scans can be enhanced in their information with Doppler measurements, which employ the Doppler Effect to assess where and how blood is flowing, and its relative velocity. This is achieved calculating the frequency shift of a sample volume of blood. This application results very helpful in diagnoses and studies in cardiology and angiology. What this technology can provide is data regarding velocity and flow

distribution displayed graphically using spectral Doppler, or as an image using Colour Doppler.

The tool enabling that kind of information to be extracted is a particular type of probe, emitting and receiving series of sound pulses, instead of a single one, and measuring the relative phase changes of these to extract the frequency shift. The major advantages of this pulsed Doppler over continuous wave is that it can also provide the distance information, evaluating the time delay between emitted and received pulses knowing the velocity of sound in the tissues. The major disadvantage of this technique, instead, is that in particular condition the measurements may suffer from aliasing. The terminology "Doppler ultrasound" or "Doppler sonography" is referred to both continuous and pulsed Doppler systems despite the different mechanisms by which the velocity is measured, with a standard about Colour-Doppler images display not still established. (89)

4.4 How it Works: From Sound to Image

The creation of an image from sound is done in three steps: producing a sound wave, receiving the echoes and forming the image.

4.4.1 The Transducer



Figure 59 Linear array transducer (ultrasound probe).

To permit all the imaging procedure to succeed, the probe used is equipped with several electronic transducers, usually 128 piezoelectric elements disposed in line with a total length of about 4 cm, allowing producing many adjacent beams, or scan lines, without the need to move the transducer itself. Consequently, the shape of the ultrasound beam produced by the transducer will depend on the shape of the element(s), on the transmitted frequency and on whether the beam is focused.

To produce a 2D image, the ultrasound beam has to sweep adjacent areas of the tissue. Once this was achieved manually, moving or rotating the probe, but today, the new linear array transducers, can exploit different techniques based on the singular element pulses

control to shape different beams in space and time. In fact, exciting the elements at slightly different times, the resulting wave fronts will interfere differently than they would if they were all generated at the same time, with the waves front propagating with an angle respect to the front of the transducer. This angle will depend directly by the delay imposed on every element: changing the delay it is possible to steer the waves beam, enabling to scan a very wider area. Phased array transducers use a smaller array of elements and electronically steer the beam in this way.

The ultrasound beam can be focused to improve the image quality within the focal zone. This is achieved exploiting the delaying strategy already described.

Furthermore, arranging the elements in a curvilinear array the beam paths will diverge, enabling to capture a larger field at the price of a loss in image quality, especially at the image borders. Curvilinear arrays are mainly used for abdominal imaging.

Obviously, the quality of the image depends on the distance between adjacent beam paths, (line density). Therefore, the frame rate of the images is affected by the number of scan lines and by the width and depth of the region of tissue being imaged: the deeper the tissue being interrogated, the longer it will take for the returning signal.

The range of signal amplitudes used is in decibel scale and reach the 100 dB and it can be compressed using a nonlinear amplifier.

4.4.2 Producing a Sound Wave

The transducer, in direct contact with the body (except for a thin layer of gel improving the transmittance), emits the sound wave. The emission is managed by the several piezoelectric elements, which compose the transducer of the probe. These elements are controlled in timing and voltage by the ultrasound machine.

Then the arc-shaped sound wave spreads inside the body as far as it encounters layers, tissues or structures with different impedance. Facing this different impedance, the sound wave partially reflects, or scatters (if the structures are small), returning back toward the body surface and the probe. The path along which the reflected ultrasound travels will also affect the amplitude of the signal detected by the transducer. During this travel even refraction can occur, causing the change in beam direction and the signal attenuation. Besides that, attenuation of the ultrasound signal is caused by absorption, scattering, reflection and beam divergence.

4.4.3 Receiving the Echoes

The returning sound wave behaves as the initial one, except the fact that comes from the inside of the body. The returned sound wave mechanically excites the piezoelectric elements, which vibrate and in turn generate electrical signal pulses. These pulses are transmitted back to the ultrasound machine, which processes and transform them into the digital image scan.

4.4.4 Forming the Image

Once the signal is received, the ultrasound scanner determines the time delay from the originating signal and its returning echo, and the strength of this one too. Basing on these two information the scanner can track down the pixel position to which allocate the information resulting in a certain bright level. Acting in the same way for the different sound waves emitted by the different elements of the transducer, every pixel of the 2D image is filled with its specific information, providing the resulting scan.

Finally, the images are displayed and then transferred from the ultrasound scanner using the DICOM standard.

4.4.5 Colour Doppler Technique⁽⁸⁸⁾

The Doppler Effect is the change in the observed frequency due to the relative motion of the source and the observer resulting in the so-called Doppler shift. The relative velocities of the source and the observer determine the magnitude of the Doppler shift frequency.

In the case of vascular ultrasound, the Doppler Effect is used to investigate the blood velocity. The strategy consists in the study of the Doppler shift depending on the frequency of the sound wave transmitted by the ultrasound machine and the blood velocity, with the side influence of the angle between the probe and the flow direction. To achieve that, the blood corpuscular property is exploited, being the red blood cells occupying the 36-55% of the entire blood volume. Because of their shape, red blood cells act as scatterers, partially reflecting the sound signal and enabling the probe to detect it.

Ultrasound scanners can also provide a velocity colour map of the blood flow superimposed onto the anatomical map. Duplex ultrasound systems act for this purpose, combining pulse echo imaging with Doppler ultrasound. This kind of map is useful for rapid interrogation of a region of interest (ROI) and enabling the operator to select the best points in which operate the investigations.

4.4.5.1 Extracting the Doppler Signal

The signal received by the probe presents different frequencies and a lower amplitude from the initial signal. The first aspect is to owe to the Doppler Effect, the second one to the attenuation of the signal by the crossed tissues. For this reason, once the Doppler shift frequency has been extracted it is amplified. To generate the 2D colour flow map, hundreds of volumes samples along the scan lines are exploited to detect the back-scattered signal.

4.4.5.2 Analysis of the Doppler Signal

Once amplified, the Doppler signal is also investigated using spectral analysis, allowing waveforms to be displayed and blood velocity to be measured. Spectral Doppler ultrasound uses fast Fourier transform (FFT) achieve that. Modern colour flow imaging scanners use also the phase shift approach, employing a process known as autocorrelation detection to estimate the mean Doppler shift frequency.

4.4.6 Image Resolution⁽⁸⁸⁾

The resolution of an ultrasound image can be distinguished in axial (along the beam), lateral (across the image) and slice thickness.

The main factor affecting resolution is the excitation pulse, which in turn depends on the frequency of the transducer: the higher the frequency, the better the resolution. The final choice of the better frequency of transducer depends on a compromise between the depth of the region of interest and the axial resolution desired: usually it is selected the highest

transducer frequency providing the adequate penetration. Other influencing parameters of the image quality are all the sets of imaging controls, such as gain settings.

The slice thickness affects the region perpendicular to the scan plane providing unwanted echoes. To prevent that, the slice thickness should be as thin as possible, focusing as well as possible the beam with the help of incorporated lens or by electronic focusing using a 2D array of elements.

For what regards the Colour-Doppler imaging, the same three directional resolution should be considered, adding the dynamic parameter related to the temporal resolution.

Here, the length of the individual sample volumes along the scan line affects the axial resolution; the width of the beam and the density of the scan lines instead govern the lateral resolution.

The principal factors affecting the Doppler spectrum are: blood flow profile, non-uniform insonation of the vessel, sample volume size, sources of error in vessel diameter measurement, image resolution, calliper velocity calibration, variable vessel diameter, non-circularity of the vessel lumen, errors in measuring TAV and aliasing.

Also blood flow profile affects the Doppler spectrum of the velocities: being the blood travelling with a parabolic profile, velocities near the walls will be smaller than the velocities in the central part of the vessel, affecting the range of the velocity spectrum extracted by the Doppler scan. Even more, problems related to the Doppler spectrum will occur in zones of complex blood flow or presenting turbulence, being these zones prone to an even more wide range of different velocities that will increase the spectrum broadening. Worth to note that these effects are also influenced by the Doppler instrumentation.

Related to the previous problem there is also the sample volume size. In fact, if a small sample volume is placed in the centre of a large vessel, it may not detect any of the flow near the vessel wall at all. On the other hand, a larger sample volume covering the whole

depth of the vessel would detect the flow only near the walls, all of this resulting again in a spectral broadening.

Being the flow proportional to the cross-sectional area of the vessel, which in turn is directly related to its radius, any error in the diameter will cause an error in the flow measurement. The causes of error in vessel diameter measurement are exposed below.

First of all, the diameter measurements are strictly related to the image resolution. Usually, axial resolution is the best, and the one considered for the measurement operation and it is of the order of the wavelength of the ultrasound (varying between 0.5-0.15 mm for frequencies between 3-10 MHz).

Related to the diameter measurement error there is also the assumption of perfect circularity of the vessels, which is not completely true in the reality.

Moreover, the vessels diameter changes during the cardiac cycle, resulting in a different flow estimation. For this reason, usually, a singular measurement of the diameter is not representative.

Another aspect related the blood flow measurement is the calliper velocity calibration. Having the blood a different velocity of sound respect to the tissues (respectively 1580 m/s vs. 1540 m/s), this causes some problems, being the scanner set to a single velocity of sound, which normally is the tissues one. This led to errors up to 5% in the measurements.

Still related to the velocity evaluation, the mean velocity in vessels can be under- or over-estimated by the non-complete insonation of the vessels, leading to altered velocity spectra and flow estimation.

Aliasing, in the end, can also affect the flow measurement, causing a limitation in the velocities measurability of the equipment. This depends on the depth of the vessels, and the required frequency to reach them with a proper accuracy. Needing the deeper vessels

lower frequencies, these can decrease until to a frequency insufficient to guarantee the Nyquist threshold frequency, providing, in the end, unreliable data.

Worth to say that even ambient noise plays a crucial role in ultrasound imaging resolution.

4.4.7 Imaging Artefacts ⁽⁸⁸⁾

It is usual for ultrasound scans to present some artefacts when the quality achieved through the proper set up of the instrumentations is not optimal.

The assumptions at the basis of the ultrasound equipment are that the ultrasound waves travels straight along their original path, on both going ahead and back, and that the attenuation of tissues is constant. Any factor affecting these assumptions can lead to errors and artefacts indeed.

The main causes are:

- Multiple reflections along the same path, between the transducer and a strongly reflecting boundary or between two parallel, strongly reflecting surfaces
- Refraction that can lead to bending of the path of the ultrasound beam
- Ambiguity of precedent echoes from distant boundaries after the current ultrasound pulse has been transmitted (the scanner will assume that the echo is from the current pulse)
- Grating lobes produced as a function of the multi-element structure of array transducers and resulting in lower intensity ultrasound areas outside the main beam. These can lead to strongly reflecting surfaces outside the main beam being displayed in the image.

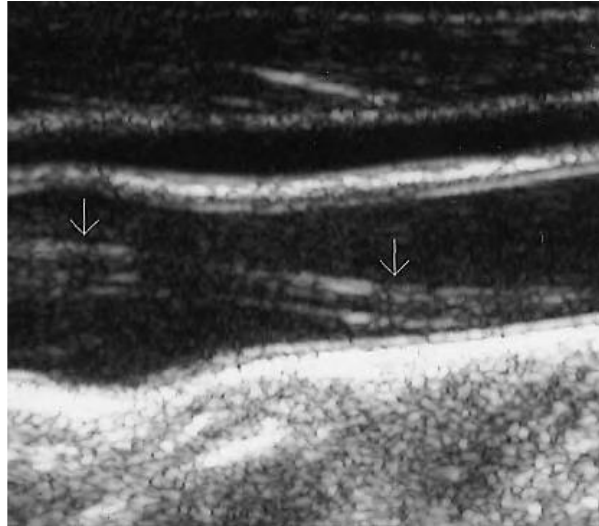


Figure 60 Example of an artefact inside the vessel area. (88)

In addition, Colour-Doppler images suffer from artefacts resulting in the failure to display flow when, in fact, it is present, or in its non-compliant locations. The factor playing a major role here is the colour gain settings. If the gain is too low, then the coloured velocity information could vanish in situations of significant noise, on the other hand with a very high gain there is the possibility of locating coloured pixels out of the vessels region because of reflections and scattering defects, giving the appearance of the colour 'bleeding' out of the vessel.

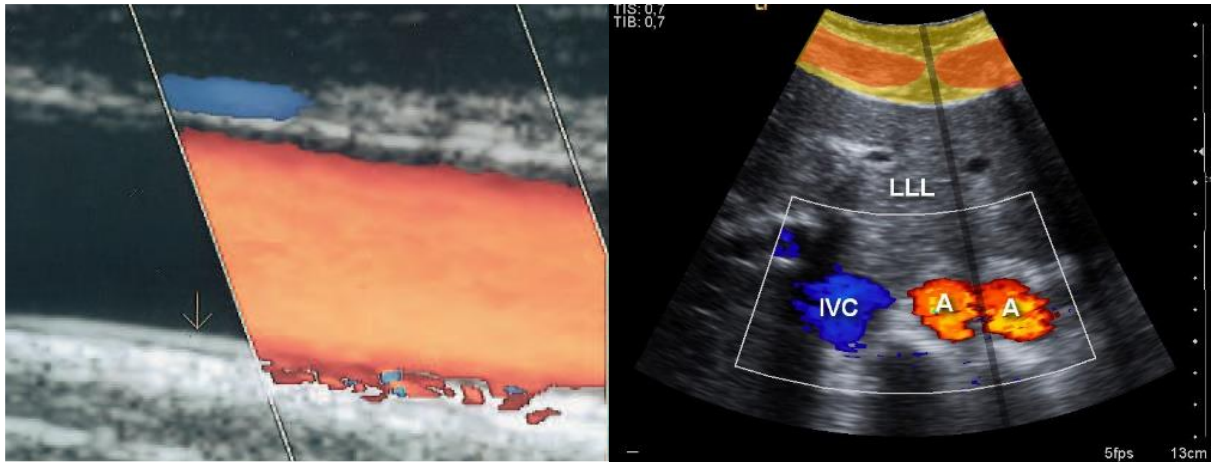


Figure 61 The “bleeding out” of the vessel colour image artefact and the “doubled aorta” artefact in sonography. (88)

Moreover, mirror images can be produced by multiple reflections of the ultrasound signal, with a Doppler shift frequency detected which can not represent the real conditions.

Even the angle of insonation may cause a false representation of the relative blood velocities, because of to changes in vessel direction.

Aliasing artefacts, in the end, will also occur, changing the appearance of the colour image.

4.5 Ultrasound Imaging Properties ⁽⁸⁷⁾

Compared to other prominent methods of medical imaging, ultrasound has several pros and cons, which now will be deepened.

4.5.1 Medical Ultrasound Strengths

- Allows detecting tissues and interfaces between solid and fluid-filled spaces
- Can provide real-time "live" images, where is possible to dynamically select the most useful information to display, enabling rapid diagnoses and ultrasound-guided biopsies or injections
- It shows the structure of organs
- It has no known side effects and rarely causes any discomforts
- Equipment is widely available and flexible
- It is relatively small and easy to carry: the examinations can be performed in every situation and condition
- Relatively inexpensive compared to technologies such as X-ray tomography, DEXA or MRI
- The spatial resolution is better than it is in most other imaging modalities. (87)

4.5.2 Medical Ultrasound Weaknesses

- Has some trouble penetrating bones
- Performs very poorly when gas are involved due to the extreme differences in acoustic impedance
- The depth penetration of ultrasound depends on the frequency of imaging: deep structures may be difficultly captured
- Image quality and accuracy are limited in case of obese patients or high depths, or low frequencies
- The method is operator-dependent, depending on the skills and experience of the operator in capturing good-quality images
- There is no scout image as there is with CT and MRI: once acquired there is not a precise way where the scan was taken. (87)

4.6 Applications in our Case Study: Vascular Mapping prior to Hemodialysis Access Placement

Regarding applications of Ultrasonography to studies similar to ours and related our subject, the book “Peripheral Vascular Ultrasound How,Why and When” by Abigail Thrush and Tim Hartshorne and the work of Aishwarya K.C. et al. can be cited.

In particular:

“ Ultrasound can be used to assess AVF or access grafts, especially when a clinical problem has been found, such as inadequate flow in the graft or fistula to allow adequate hemodialysis. Ultrasound can be used

to measure volume flow in access grafts or in the access segment of AVFs. It can also be used to identify occlusions, stenoses, thrombus formation, aneurysms or false aneurysms in the fistula or graft. Preoperative assessment of the in-flow artery and vein can also be performed with ultrasound. In depth discussion of these scanning techniques is beyond the remit of this book, so we refer the reader to the work published by Landwehr (1995) and Deane & Goss (2001). “
(88)

And also:

“ A high-resolution linear ultrasound transducer is used to evaluate the arm vessels (generally 7 MHz or higher). The transverse plane is used to identify vessels (artery and vein) and evaluate their diameter and wall thickness. Sequential vein compression is used to assess for compressibility. The depth from the skin surface of the anterior wall of the cephalic vein is measured. Colour and spectral Doppler waveforms are obtained in the longitudinal plane of vessels selected for potential vascular access. The forearm veins and arteries are assessed to determine whether the patient is a candidate for a forearm AVF, the most desirable initial type of hemodialysis access. If vascular anatomy suitable for forearm fistula creation is not found, the upper arm vessels should be mapped. Arteries should be assessed for intimal thickening and stenosis. The presence of significant concentric calcification should be noted, as the artery may be too calcified for successful surgical access creation. An important aspect of planning for AVF and graft creation is vessel size assessment.” (90)

Many other sources have been exploited.

4.7 Protocol Established with the Hospital

Starting from what it has been analysed and discussed in Chapter 3, in addition to the presentation of the Medical Ultrasound Imaging just done, it has been planned a specific strategy to achieve the aim proposed, based on the hospital available Ultrasound equipment.

With the precious help provided by hospital operators and the surgeon supervising all this work, it has been possible to arrange a strategy which could fulfil all the hospital requirements in terms of patient annoyance, time requested for the procedure to be carried out and costs directly associated with all the operations done.

In detail, the procedure is determined to mimic the strategies applied to 3D tomographic imaging technologies, scanning several sections of the vessels cross-sectional areas at specific positions, enabling a successive reconstruction of the 3D geometry thanks to the information provided together with the scans, regarding the scan position and number.



Figure 62 The PHILIPS Epiq® 7G ultrasound imaging system and the operator using it.

4.7.1 The Image Capturing Protocol

The image capturing protocol deeply rely on the standard vascular ultrasound diagnostic procedures. The main difference here stands on the number of the scans requested and particular attentions paid on the probe positioning and images labelling. The procedure makes use of some extraordinary equipment in addition to the ultrasound scanner: a cling film to apply on the patient arm with applied a specific grid, enabling the operator to correctly position the probe and detect its location.

The first idea regarding the reference grid was about applying a removable tattoo directly on the patient arm. Then, thinking about patient annoyance related removing the tattoo, the choice fell on the cling film, with the same tattoo applied on it.

A	1	2	3	4	5	6	7	8	9	10	11
B	1	2	3	4	5	6	7	8	9	10	11
C	1	2	3	4	5	6	7	8	9	10	11
D	1	2	3	4	5	6	7	8	9	10	11
E	1	2	3	4	5	6	7	8	9	10	11
F	1	2	3	4	5	6	7	8	9	10	11
G	1	2	3	4	5	6	7	8	9	10	11
H	1	2	3	4	5	6	7	8	9	10	11
I	1	2	3	4	5	6	7	8	9	10	11
J	1	2	3	4	5	6	7	8	9	10	11
K	1	2	3	4	5	6	7	8	9	10	11
L	1	2	3	4	5	6	7	8	9	10	11
M	1	2	3	4	5	6	7	8	9	10	11
N	1	2	3	4	5	6	7	8	9	10	11
O	1	2	3	4	5	6	7	8	9	10	11
P	1	2	3	4	5	6	7	8	9	10	11
Q	1	2	3	4	5	6	7	8	9	10	11
R	1	2	3	4	5	6	7	8	9	10	11
S	1	2	3	4	5	6	7	8	9	10	11
T	1	2	3	4	5	6	7	8	9	10	11



Figure 63 The grid designed and its application on the patient's forearm.

In order to obtain the best results with the equipment available, ensuring a repeatable robust and precise procedure, affordable in terms of cost and complexity, the suggested protocol for the hospital operators is:

- 1) If needed make a first rapid scan to find the main vein and artery paths and borders (if possible take some reference from the initial coarse scan)
- 2) Apply the GRID with the anastomosis (or where anastomosis is thought to be set) halfway and in central position, paying attention to cover the area where the vein and artery are supposed to pass (consider the thickness of the vessels)

- 2.1. The orientation has always to be: “A” proximal – “T” distal
- 3) Take photos of the grid applied to the arm (just before or after the entire procedure – the entire grid and arm have to be well visible and detectable)
- 4) Collect the images of the cross sectional areas of the single vessel at every step:
- 4.1. Centre the probe at the middle of each row
- 4.2. For each step (vein and artery) align the shorter edge of the probe to the nearest left longitudinal line (for left arms, nearest right line for right arms), taking care that this allows in every case to capture completely the vessels profiles
- 4.3. Take the pictures at every step of the grid (if not starting by the first step, indicate the starting step using the naming procedure) aligning the probe to the transversal line
- 5) Name/Label every capture in this way:

«Type of vessel (A//V) – Step Letter (A-B-C...) - n° of the box containing the longitudinal aligning line1-2-3...)»

- 5.1. For the anastomosis reverse N° of steps (A-B-C...) and n° of the box in the naming; align the probe always towards the nearest upper arm edge of the grid (upper side=right side of the image)
- 5.2. (left arm considered by default – specify if right arm is used)
- 6) Proceed in this way along the steps

7) In addition, at anastomosis rotate 90° the probe and capture the anastomosis path

7.1. Name/Label every capture in this way:

«F - n° of the box containing the longitudinal aligning line1-2-3...» - Step Letter (A-B-C...)»

7.2. Reverse N° of steps (A-B-C...) and n° of the box in the naming

7.3. Align the probe always towards the nearest upper arm edge of the grid (upper side=right side of the image)

7.4. (left arm considered by default – specify if right arm is used)

8) Save the images relative a specific patient separately and with the same code (*)

(*) Make possible to ascribe each set of images to the specific patient (to ensure the correct comparison of result before/after the AVF application). To achieve that the suggestion is to use different folders for each patient and a patient specific code, using it every time images of the patient are taken, filing the images of each patient and every date in a specific folder named with the code and the date in which the images are taken.

Additionally:

- Take photos of the grid applied to the arm (just before or after the entire procedure)
- For each patient apply the protocol before the AVF application, 7 days and 28 days later the AVF application
- Take Colour Doppler images of blood flow at the anastomosis to describe the flow patterns with the best precision

- If possible to capture both vein and artery, add an additional capture with both without aligning to a line, but changing the name of the vessels in "B", specifying only the step in this way:

«B - N° of step (A-B-C...) - n° of the box containing the longitudinal aligning line1-2-3...»

- Acquire the pulsewave flow velocity graph for artery and vein at:
 - First and last step of the grid (for each vessel)
 - 10 cm backward and forward (for each vessel)
- For the colour spectrum and pulsewave velocity images name each file in this way:

« Type of vessel (A//V//F) – Position »

(Types of vessel: A=artery; V=vein; F=fistula/anastomosis; Position: Proximal (P); Distal (D); 10 cm proximal (10P); 10 cm distal (10P))

Grid notes:

- The design of the grid is performed in Autodesk AutoCAD: a system of coordinates (letters longitudinally, numbers laterally) allows an easy and precise detection of the probe position
- The grid is Print once designed and nested to the sheet dimensions (2 grid per sheet) to optimise the available space on the tattoo paper
- The grid must be printed on the tattoo paper and then applied to the cling film, which will then be placed on the fistula site. It must be placed on the site of interest such that the centre of the grid is placed in the centre of the fistula and then fixed with some sellotape to the arm.

- The application of the grid to the cling film is done to avoid complications and patient annoyance due to the tattoo application directly on the arm
- After the grid is placed on the site, and prior to the start of the imaging procedure, or after its completion, a photo should be taken from the grid *in situ*.

Figure 64 The imaging and labelling protocol illustration provided to the hospital.

Velocity information:

The black and white velocity waves should be acquired at both ends of the grid, as well as (ideally) 10 cm before and after each end for both the artery and the vein:

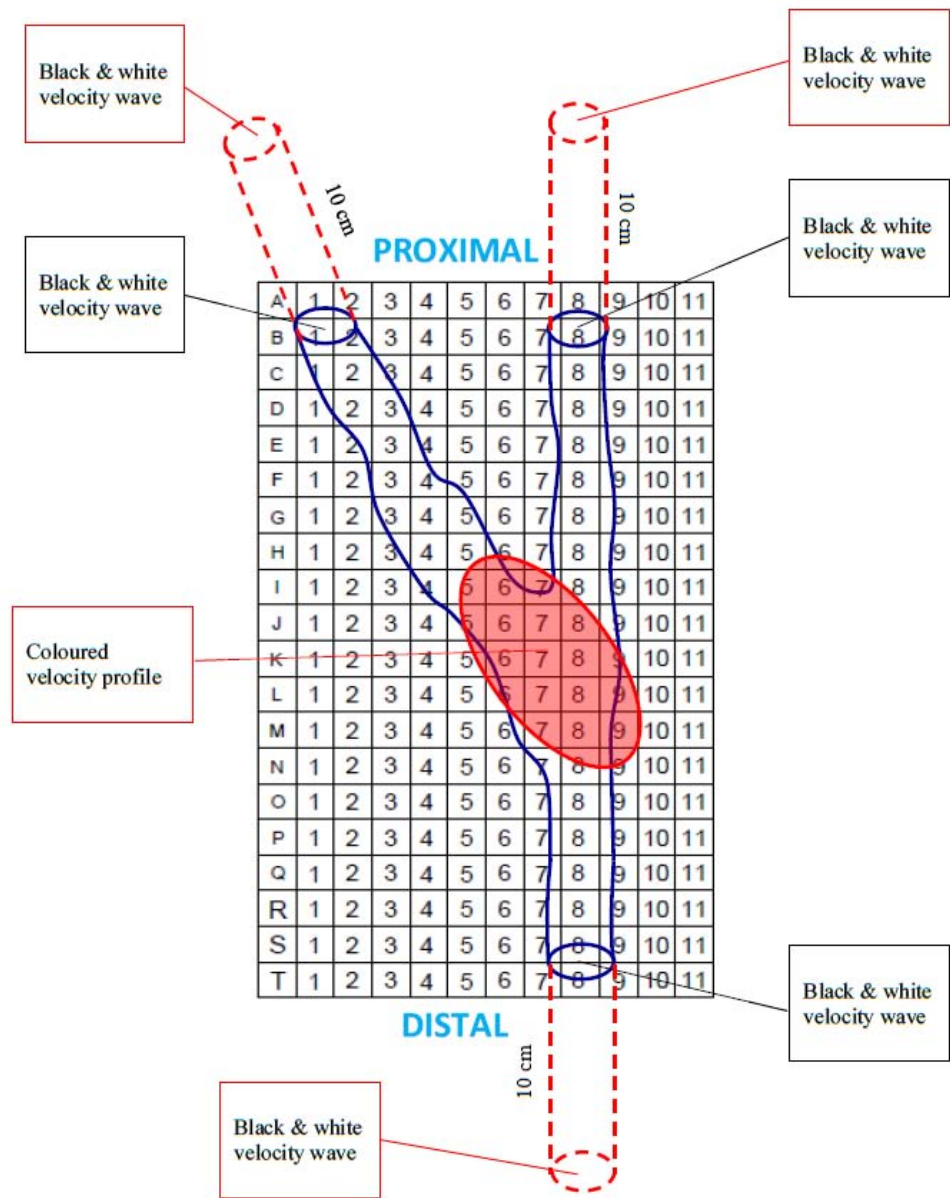


Figure 65 The velocity-measure scanning protocol illustration provided to the hospital.

The images containing the velocity wave (black and white) information in 10cm distal and proximal to the grid should be labelled as follows:

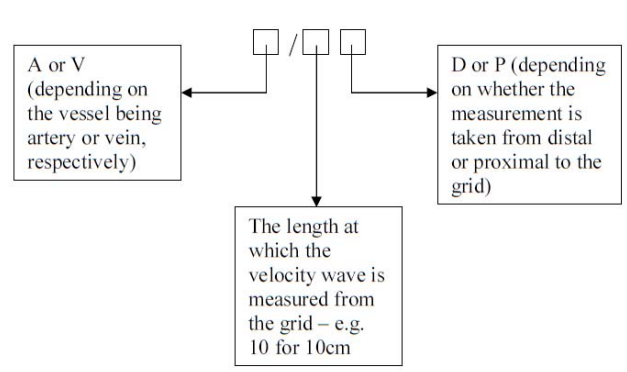


Figure 66 The velocity-measure scanning labelling protocol provided to the hospital.

For example:

- A/10P meaning the velocity measurement was taken from Artery at 10cm proximal to the grid.
- V/5D meaning the velocity measurement was taken from Vein at 5cm distal to the grid.

4.8 Data Obtained

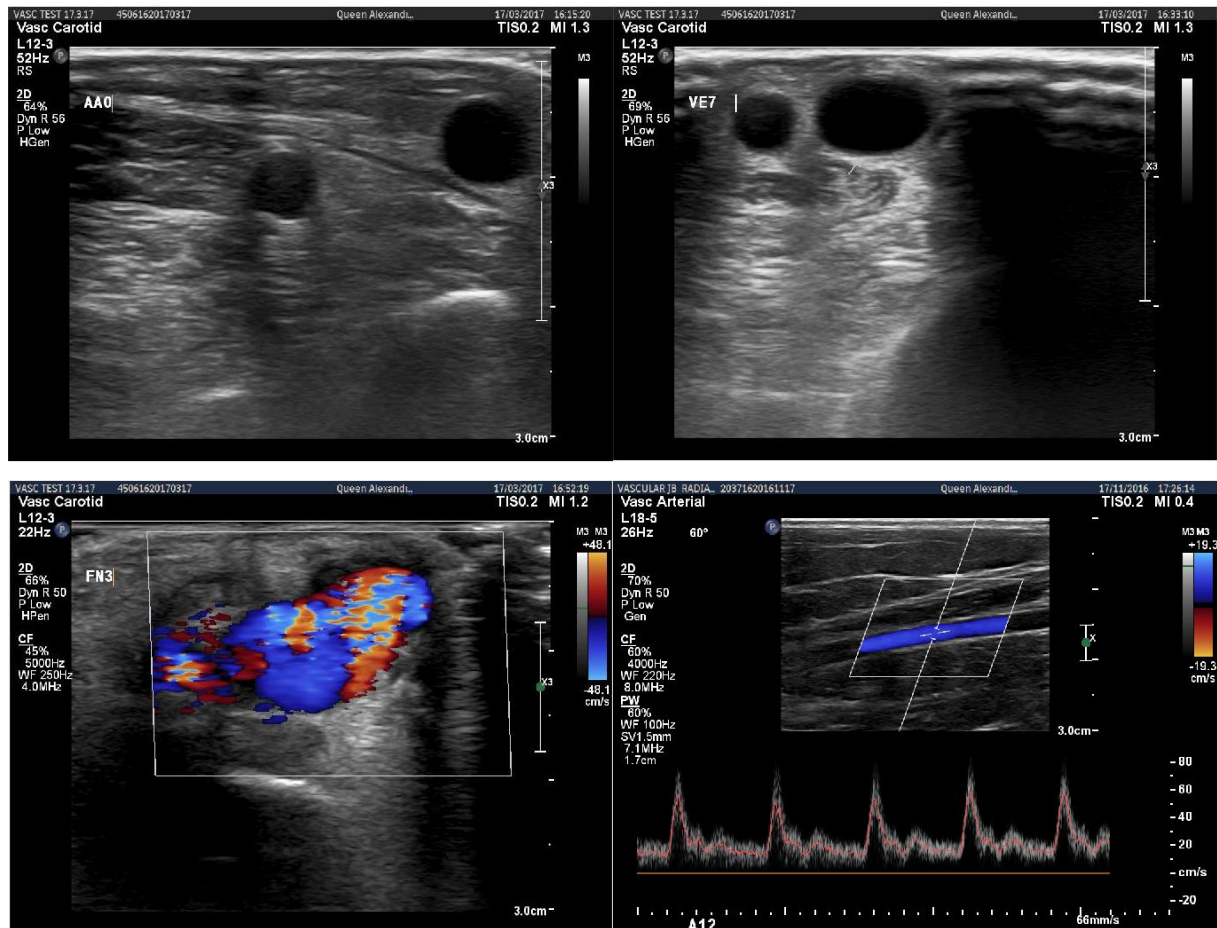


Figure 67 Two Mode-B scans of the vein and artery cross-sectional area (upper left and right); a Colour-Doppler scan at the anastomosis (lower left); a Doppler velocity scan (lower right).

The results obtained are a list of Black & White ultrasound scans of the region of interest, for both artery and vein involved in the study, each of them taken in a very specific position. Every scan provides also information about this position in the labelling on it.

The second type of scans consists in the AVF anastomosis Colour-Doppler scan to be able to compare the results of the next studies in terms of velocity magnitude and patterns.

The last type of scans gathered are the ones providing the Doppler extracted velocities, with a red line representing the averaged Fast Fourier Transform velocity-representative pulse wave, necessary for the subsequent boundary conditions setup of the fluid dynamic simulation.

5 IMAGE PROCESSING⁵

⁵ Eventual references on the chapter or paragraph titles are to be intended to be the main sources of the informations provided on that chapter or paragraph.

5.1 The Case

As explained at the end of Chapter 3, what is needed after the imaging of the vessels through the Ultrasound instrument is the ability to extract useful information from these images for reconstructing the geometric model and setting up the fluid dynamics simulations.

The output of Ultrasound images is a DICOM standard image, inside which it is possible to obtain different information. With Ultrasound B mode, it is easy to get a vision of the internal structure of organs and tissues, such as veins and arteries. With the Ultrasound Colour-Doppler, it is possible to obtain different information about speed distribution within the blood vessels, as well as to have a precise description of how time and velocity profile evolves. All these are useful information to set better CFD simulations and to have a first validation of these.

To achieve this in an accessible way from the various software available, an extraction and conversion operation is required for all images. For this aim, MATLAB comes to the help, which with the Image Processing Tool makes possible a variety of techniques and strategies to achieve our goal.

The extraction procedure is established to identify, separate and extract the edges of the blood vessels from images containing different noises and unnecessary objects. An important aspect of subsequent geometric reconstruction is the ability to maintain a position reference between the image (and in particular the blood vessel) and the position of the arm in which this image was captured.

To do this, an agreement has been established between the author and the hospital doctor and practitioners of the vascular area representing the hospital on a procedure to obtain this kind of information, which was also one of the most characteristic and influential aspects of the entire procedure. A detailed description of the procedure established has just been described in Chapter 4.

This chapter aims to illustrate the techniques and algorithms that have made it possible to achieve this goal.

5.2 Image Analysis ⁽⁹¹⁾

Image analysis consists in the extraction of meaningful information from digital images by means of digital image processing techniques (91). The human visual cortex itself is an excellent image analysis apparatus and for this reason, many important image analysis tools and techniques are inspired by it (i.e. edge detectors and neural networks).



Figure 68 Extracting information from an aerial image. (126)

Computers, on the other hand, are indispensable for the analysis of large amounts of data, for tasks that require complex computation, or for the extraction of quantitative information.

The acquisition of images (producing the input image in the first place) is referred to as imaging and is provided by a lot of different sensors, with several different qualities, standards and formats (91).

Digital Image Analysis is the specific case when a computer automatically studies an image to obtain useful information from it. Computer Image Analysis is at the basis of computer or machine vision, and medical imaging, and exploit techniques such as pattern recognition, digital geometry, and signal processing (91). This field of computer science developed originally as a branch of artificial intelligence and robotics starting by the 1950s at academic institutions such as the MIT A.I. Lab and it consist on the quantitative or qualitative characterization of digital images. The applications of digital image analysis are wide and continuously expanding through all areas of science and industry, including astronomy, defence, filtering, machine vision, materials science, medicine, metallography, microscopy, optical character recognition, remote sensing, robotics and security.

Image analysis can be divided into two main branches:

- Interpretation and analysis
- Crossing Analysis.

Interpretation and analysis of remote sensing imagery involve the identification and/or measurement of various targets in an image in order to extract useful information about them. (92) Targets in remote sensing images may be any feature or object which can be observed in an image: they may be a point, line, or area feature with any form, and they must be distinguishable (they must contrast with other features around them). However, much interpretation and identification of targets in remote sensing imagery are still performed manually or visually, i.e. by a human interpreter.

When remote sensing data are available in digital format, digital processing and analysis may be performed using a computer. Digital processing is more recent and may be used to enhance data as a prelude to visual interpretation. (92) There are many different implementations used in the automated analysis of images. Each technique is specific for a particular task, for this reason there still aren't any known methods of image analysis that are generic enough for wide ranges of tasks, if compared to the image analysing capabilities. (91)

Some examples of image analysis techniques are:

- 2D and 3D object recognition
- image segmentation
- motion detection
- video tracking
- optical flow
- medical scan analysis
- 3D Pose Estimation
- automatic number plate recognition

Nowadays, it is also possible to carry out digital processing and analysis to automatically identify targets and extract information completely without manual intervention. However, rarely is digital processing and analysis carried out as a complete replacement for manual interpretation. Often, it is done to supplement and assist the human analyst.

Both manual and digital techniques for interpretation of remote sensing data have their respective advantages and disadvantages. Generally, manual interpretation requires little, if any, specialized equipment, while digital analysis requires specialized, and often expensive, equipment. Manual interpretation is often limited to analysing only a single channel of data or a single image at a time, while the computing environment is more amenable to handling complex images of several or many channels or from several dates, so it can process large data sets much faster than a human interpreter can. Manual interpretation is a subjective process, meaning that the results will vary with different interpreters, while digital analysis is based on the manipulation of digital numbers in a computer and is thus more objective, generally providing results that are more consistent. However, determining the validity and accuracy of the results from digital processing can be difficult.

In most cases, a mix of both methods is usually employed when analysing imagery. In fact, humans still have to make the ultimate decision about the utility and relevance of the information extracted at the end of the analysis process.

In modern sciences and technologies, images also gain much broader scopes due to the ever-growing importance of scientific visualization, especially in fields like medicine, where non-invasive and accurate methods for diagnoses are fundamental.

5.3 The DICOM Imaging Standard ⁽⁹³⁾

Digital Imaging and Communications in Medicine is the acronym for DICOM, the standard for storing and transmitting medical images. It enables to exchange DICOM images between every equipment able to work with this image format, including a file format definition and a network communications protocol. (93)

The DICOM Standards Committee developed this standard, and today its members are also partly members of the National Electrical Manufacturers Association (NEMA), which holds its copyright. (93)

DICOM enables the integration and interoperability of medical imaging devices, even from different manufacturers. All these devices come with DICOM Conformance Statements which clearly state which DICOM classes they support. DICOM has been widely adopted by hospitals because of its universal application capability and flexibility.

DICOM has its ISO standard too, which is ISO 12052:2006 "Health Informatics -- Digital imaging and communication in medicine (DICOM) including workflow and data management". (93)

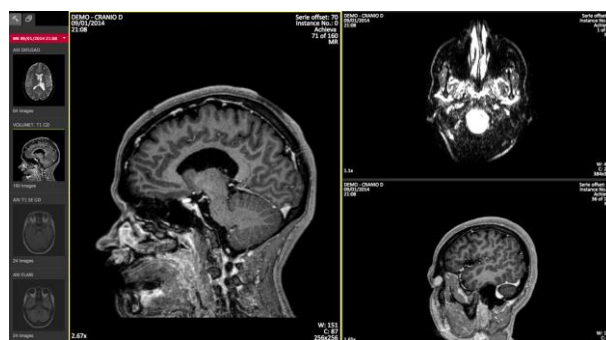


Figure 69 A DICOM MRI scan of a patient head.

5.3.1 Images Format

The most common mistake with DICOM images is made in interpreting the term as assimilated to a compression format (e.g. JPEG, GIF, etc.).

Indeed, the DICOM standard works encapsulating data and defining how these should be encoded or interpreted but does not define any new compression algorithm. The original image is usually stored uncompressed, following the encoding it produces, however there are software that can produce or interpret DICOM files containing compressed data.

Over the simple image, a DICOM also includes a header, where several information are contained: patient name and surname, scan type, location and image size, and so on. The size of this header obviously varies depending on the amount of information stored. "DICOM tags" organise all the information inside a DICOM file to make possible the interpretation of these to every equipment.

Group - Element	Description	Type	Length	Value
0002 0000	Group 0002 Length	UL	4	200
0002 0001	File Meta Information Version	OB	2	(binary data)
0002 0002	Media Storage SOP Class UID	UI	26	1.2.840.10008.5.1.4.1.1.7
0002 0003	Media Storage SOP Instance UID	UI	54	1.2.826.0.1.3680043.2.1208.34948545565201041914916296
0002 0010	Transfer Syntax UID	UI	18	1.2.840.10008.1.2
0002 0012	Implementation Class UID	UI	18	1.2.804.114118.3
0002 0013	Implementation Version Name	SH	6	
0002 0016	Source Application Entity Title	AE	18	
0002 0100	Private Information Creator UID	UI	0	(empty)
0002 0102	Private Information	OB	0	(binary data)
0008 0005	Specific Character Set	CS	12	ISO_IR 100
0008 0008	Image Type	CS	24	ORIGINAL\PRIMARY\OTHER
0008 0012	Instance Creation Date	DA	10	20100419
0008 0013	Instance Creation Time	TM	14	140916.000000
0008 0016	SOP Class UID	UI	26	1.2.840.10008.5.1.4.1.1.7
0008 0018	SOP Instance UID	UI	54	1.2.826.0.1.3680043.2.1208.34948545565201041914916296
0008 0020	Study Date	DA	10	20100419
0008 0021	Series Date	DA	10	20100419
0008 0030	Study Time	TM	14	140916.000000
0008 0031	Series Time	TM	14	140916.000000
0008 0032	Acquisition Time	TM	14	140916.000000
0008 0033	Content Time	TM	14	140916.000000
0008 0050	Accession Number	SH	2	
0008 0060	Modality	CS	4	OT
0008 0064	Conversion Type	CS	4	WSD
0008 0070	Manufacturer	LO	4	IIS
0008 0080	Institution Name	LO	2	
0008 0090	Referring Physician's Name	PN	2	

Figure 70 List of all DICOM tags. (93)

There are many programs that allow DICOM images to be displayed on standard PCs, often also freely downloadable over the Internet. Many of these also allow performing post-processing operations on basic imaging, such as linear and area measurements.

5.3.2 Services ⁽⁹³⁾

DICOM consists of several services, many of which involve data transmission over a network; the following are the main services:

- **STORE:** to send images or other persistent objects to a PACS or a workstation.
- **STORAGE COMMITMENT:** to confirm the permanent storage of an image on a device.
- **QUERY / RETRIEVE:** to find listings of images or other objects and then retrieve them from a PACS.
- **MODALITY WORKLIST:** to get patient details and worklist exams, avoiding manually typing that information.
- **MODALITY PERFORMED PROCEDURE STEP (MPPS):** to send a report of an exam made including all the data acquired during imaging
- **PRINTING:** to send images to a DICOM printer, usually to print an "X-Ray" movie.
- **OFF-LINE MEDIA (DICOM Files):** to store diagnostic information for images on removable media.

DICOM limits the average 8-character DICOM file names. No information should be extracted from these names, in fact it is a possible source of trouble with the media created by developers who have not read the DICOM specifications carefully. This is a key requirement for maintaining compatibility with existing systems, as well as the presence of a media directory, the DICOMDIR file, which provides the index and summary

information for all DICOM files on the media. DICOMDIR information provides detailed information on each file in the media.

5.3.3 Compatibility ⁽⁹³⁾

As said DICOM is not only an industry standard but also an ISO standard (ISO 12052: 2006).

This because in the past the tolerances in the implementation of the specifications for DICOM format of several types of equipment led to the non-compliance between their different formats. In most cases, an equipment was conforming to a part of the standard (such as image storage), while adopting proprietary technologies for other features (such as patient list management).

Today, DICOM compatibility and in general any compatible DICOM device is certified through the Conformance Statement, which lists its functionality. As consequence, the good result of a connection between two DICOM devices is in the first instance linked to the comparison between the two conformance statements, with no errors in documents or omissions in the implementation, other than remote.

5.4 MATLAB Programming Software

MATLAB, short for MATrix LABoratory, is a multi-paradigm numerical computing environment and fourth-generation high-performance programming language specifically designed for quick and easy scientific calculations and I/O of partial differential equations and data analysis. (94) This proprietary programming language is developed by MathWorks.



Figure 71 MATLAB logo.

The software allows several computations, such as matrix manipulations, plotting of functions and data, implementation of algorithms, the creation of user interfaces, and interfacing with programs written in other languages. (95) It has literally hundreds of built-in functions for a wide variety of computations and many toolboxes designed for specific research disciplines, including statistics, optimization, solution

Furthermore, MATLAB is a modern programming language environment: it has sophisticated data structures, contains built-in editing and debugging tools, and supports object-oriented programming. MATLAB features a family of application-specific solutions called toolboxes, comprehending collections of MATLAB functions (M-files) that extend the MATLAB environment to solve particular classes of problems. (96)

The MATLAB system consists of five main parts:

- **The MATLAB language.** This allows both "programming in the small" and "programming in the large" to rapidly create quick throw-away programs and to create complete large and complex application programs.

- **The MATLAB working environment.** This is the set of tools and facilities that are worked with as the MATLAB user or programmer. It works for developing, managing, debugging, and profiling M-files, MATLAB's applications.
- **Handle Graphics.** This is the MATLAB graphics system. It includes high-level commands for two-dimensional and three-dimensional data visualization, image processing, animation, and presentation graphics.
- **The MATLAB mathematical function library.** This is a vast collection of computational algorithms ranging from elementary to more sophisticated functions.
- **The MATLAB Application Program Interface (API).** This is a library that allows writing C and Fortran programs that interact with MATLAB. (96)

Typical MATLAB uses include:

- Math and computation
- Algorithm development
- Modelling, simulation, and prototyping
- Data analysis, exploration, and visualization
- Scientific and engineering graphics
- Application development, including Graphical User Interface building

5.4.1 Digital Image Processing: MATLAB Image Processing Toolbox™ (97)

Image Processing Toolbox™ is the MATLAB application which provides all the techniques, algorithms and workflow apps to operate the image processing, analysis and visualization. With this all the image segmentation, image enhancement, noise reduction,

geometric transformations, image registration, and 3D image processing operations are possible. Image Processing Toolbox™ apps even let automate common image processing workflows. It can be set to interactively segment image data or compare image registration techniques, and batch-process large data sets. The visualization functions and apps let open and explore every kind of images, 3D volumes, and videos.

Key features and possibilities of this toolbox are (98):

- Image analysis, including segmentation, morphology, statistics, and measurement
- Apps for image region analysis, image batch processing, and image registration
- 3D image processing workflows, including visualization and segmentation
- Image enhancement, filtering, geometric transformations, and deblurring algorithms
- Intensity-based and non-rigid image registration methods

In the next pages, principal operations, techniques and commands been useful to this study are shortly described.

5.4.1.1 Import, Export, and Conversion (98)

Image data import and export, conversion of image types and classes is a very powerful tool of Image Processing Toolbox™. Image Processing Toolbox™ supports images and video generated by a wide range of devices, including medical imaging devices, microscopes, telescopes, and other scientific instruments. Therefore, Image Processing

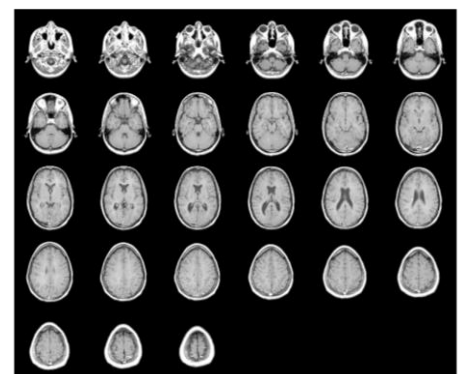


Figure 72 Exploring Slices from an MRI Data Set.

Toolbox™ supports DICOM files, as well as the Analyse 7.5 and Interfile formats. With Image Acquisition Toolbox™, it is possible to acquire live images and video from frame grabbers and several other devices.

5.4.1.2 Display and Exploration ⁽⁹⁸⁾

The toolbox encompasses a suite of image processing apps to apply various algorithmic approaches. Each app enables automatic MATLAB code generation and the ability to capture interactive steps programmatically, which is beneficial in automating multi-image workflows.

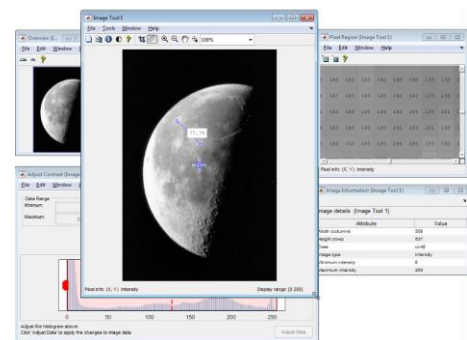


Figure 73 Image Viewer-App. ⁽⁹⁸⁾

5.4.1.3 Geometric Transformation and Image Registration ⁽⁹⁸⁾

All the basic operations like scaling, rotating and aligning images using intensity correlation, performing other N-D transformations, feature matching, or control points mapping are all included as the basic tools of the package.

5.4.1.4 Image Enhancement⁽⁹⁸⁾

Image enhancement is used, according to specific requirements, to point highlight certain information at the same time, to weaken or remove some unwanted information, increasing the signal-to-noise ratio and accentuate image features. The purpose is to make the

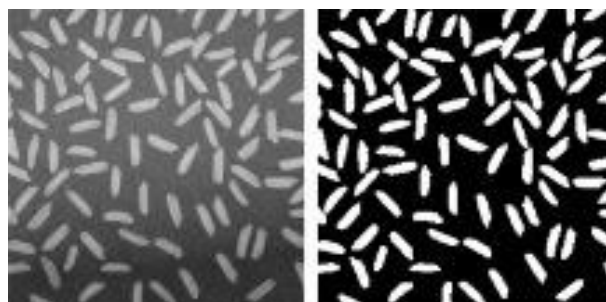


*Figure 74 Removing noise with morphological operations.
(98)*

processed image more effective. It can be divided into two kinds depending if processing is operated by the frequency domain method or space method. Custom or predefined filters and functions can help to remove noise, adjust contrast, and remap the dynamic range. Contrast adjustment, morphological filtering, deblurring, and other are other principal image enhancement tools. The toolbox includes specialized filtering routines and a generalized multi-dimensional filtering function that handles integer image types, offering multiple boundary-padding options, and performing convolution and correlation.

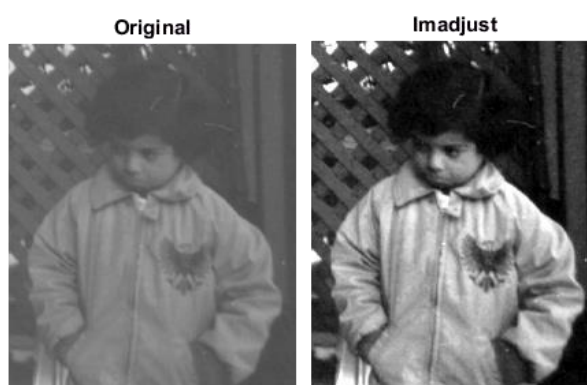


Figure 75 Image Enhancement performing Histogram Equalization. (98)

5.4.1.5 Image Registration Methods⁽⁹⁸⁾

Image Processing Toolbox™ supports *intensity-based image registration*, to enable automatic alignment of the images using their relative intensity patterns. Both multimodal 3D registration and non-rigid registration can be performed. Results can be visually inspected then, by creating composite images that highlight misalignments. Additionally, with Computer Vision System Toolbox™ feature-based image registration is possible, aligning images using feature detection, extraction, and matching, with a successive geometric transformation estimation.

5.4.1.6 Image Segmentation and Edge Detection Techniques⁽⁹⁸⁾

Performing the image segmentation consists on partitioning an image into parts or regions. This division is based on the characteristics of the different images pixels. There are different approaches to image segmentation, like multilevel automatic thresholding, or iterative approaches such as fast marching and active contours, and colour-

based and intensity-based methods. One of the most used techniques is to look for abrupt discontinuities in pixel values, which typically indicate edges, which can define these regions. All of these strategies can be explored interactively in the segmentation apps.

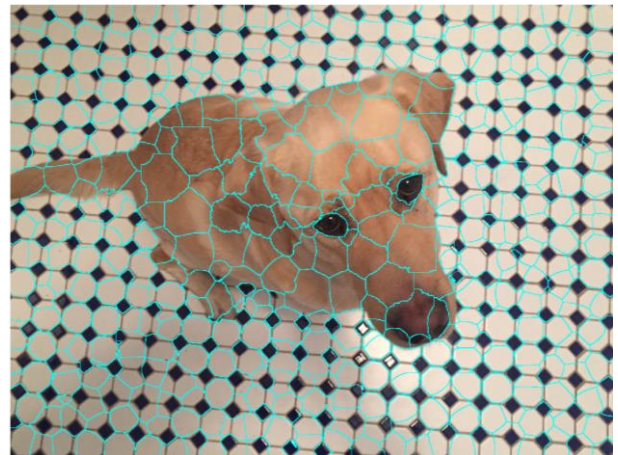


Figure 76 Example of Image Segmentation with Super Pixels. (98)

These morphological operators then enable to detect edges, segment the images into regions, or perform skeletonization on regions. Morphological functions in Image Processing Toolbox™ include:

- Labelling of connected components
- Watershed segmentation
- Reconstruction
- Distance transform



Figure 77 Examples of Marker-Controlled and Colour-Based Segmentation. (98)

Edge detection, as specific application, helps to identify object boundaries in an image. This particular algorithm works by detecting discontinuities within the image (brightness is one focus point and is used for image segmentation and data extraction in areas such as image processing, computer vision, and machine vision.

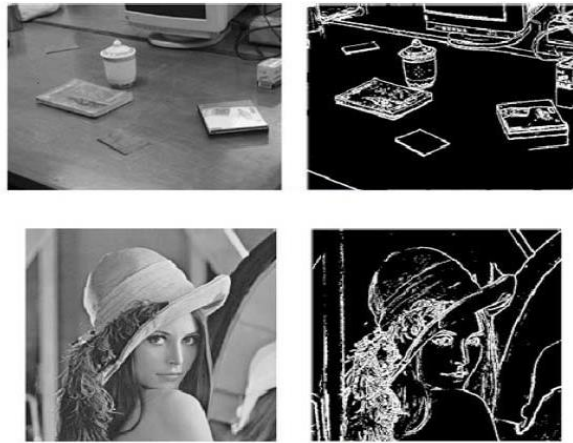


Figure 78 Examples of edges detection.

Common edge detection algorithms include Sobel, Canny, Prewitt, Roberts, and logic methods. The Canny method, for instance, can detect true weak edges without being fooled by noise.

5.4.1.7 Image Deblurring⁽⁹⁸⁾

Image deblurring algorithms in Image Processing Toolbox™ includes functions that help correct blurring caused by several causes (atmospheric conditions, out-of-focus optics, movement by the camera or the subject, short exposure time, etc.). The major algorithms available are Lucy-Richardson, Wiener, and regularized filter deconvolution, as well as conversions between point spread and optical transfer functions.



Figure 79 Deblurring Images Using the Blind Deconvolution Algorithm. (98)

5.4.1.8 Hough Transform⁽⁹⁸⁾

The Hough transform is a feature extraction technique with the purpose to detect particular shapes or objects within a certain class of shapes by a voting procedure (99). This procedure is operated in a parameter space, from which object candidates are obtained as local maxima in a so-called accumulator space specifically constructed by the algorithm for computing the Hough transform. Using the Hough transform is possible to find line segments and endpoints, measure angles, find circles based on size, etc.

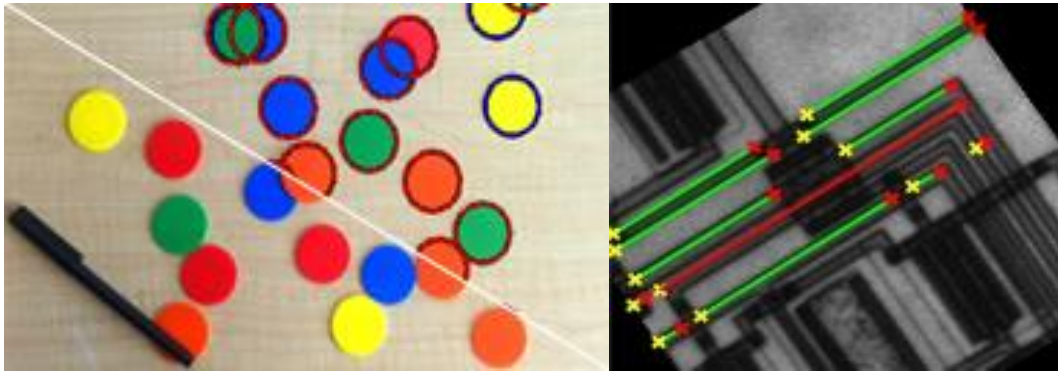


Figure 80 Detection of Circular Objects and Lines in Images Using Hough Transform. (98)

5.4.1.9 Statistical Functions⁽⁹⁸⁾

Finally, Image Processing Toolbox™ statistical functions permit then to analyse the general characteristics of an image by statistical methods like computing the mean or standard deviation, determining the intensity values along a line segment, displaying an image histogram, etc.

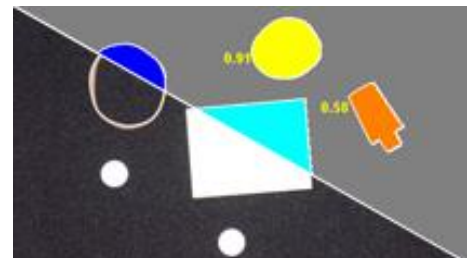


Figure 81 Example of Identifying Round Objects. (98)

5.5 Image Processing Conclusions

It has been showed how image analysis involves processing an image into fundamental components in order to extract statistical data. Image analysis can include such tasks as finding shapes, detecting edges, removing noise, counting objects, and measuring region and image properties of an object.

Image analysis is a broad term that covers a range of techniques that generally fit into these sub-categories:

- Image enhancement to remove noise.
- Image segmentation to isolate regions and objects of interest.
- Morphological filtering to remove more noise.
- Region analysis to extract statistical data.

This analysis is possible in MATLAB thanks to the Image Processing Toolbox™, which provides image processing algorithms, tools, and a comprehensive environment for data analysis, visualization, and algorithm development.

Given this introduction to Image analysis, the exploitation of MATLAB as the best suitable software to operate the information extraction from the images provided by the Ultrasound Imaging seems the logical consequence.

5.6 Edges Points Extraction

Considering our problem, image processing from Ultrasound imaging is necessary to extract useful information.

The main aim, as exposed at the end of Chapter 3, is to extract vessels cross-sectional area and position from every Ultrasound scan.

The problems encountered in such operation are several, related to the image quality and variability, depending on factors as operator skills, scans environment and tools, patient anatomical characteristic, etc. The efforts undertaken in this section are focused on finding a good procedure to extract desired information in the best way achievable, with the lower operator time required, and a code enough flexible to provide good data even when the image quality is not the best.

Objects recognition was intended to be completely automated, but due to the complexity and noisiness of the images, it was not found robust and reliable in detecting the correct shapes. Edges Points Extraction is focused on this purpose, setting up a procedure to encompass many strategies with the aim to find the best result regarding the edges detection and extraction.

After the user manually sets the folder and the number of images to process, the program iteratively analyses all of them one by one. The user is asked to comply with additional requests in order to allow the correct development of the procedure, like the input of the image dimensions and the measurement of the latter on MATLAB, to ensure a precise and correct scaling from images pixels to metric coordinates. Before starting with the procedure, it is also asked to crop the area of interest of the image, to ease the edges detection by the program and lighten the entire calculations and procedure.

The procedure consists of a list of strategies and methods to extract the cross-sectional area borders. The principal techniques and strategies exploited are: morphological

operations (skeletonization and interiors removal), Sobel filtering and thresholding. A frame that surrounds the final image is created, to best accommodate positioning in CAD software. Step by step the user selects whether or not to use a particular strategy and at the end chooses the best result to save it. There are various check points to allow to come back to the previous step.

The program is designed to iterate itself along the number of files the user set at the beginning of the procedure.

5.6.1 The Sobel Filtering Technique ⁽¹⁰⁰⁾



Figure 82 Application of the Sobel filter to a B&W image.

One of the strategies set up to extract cross-sectional areas borders is the Sobel filter. The Sobel filtering operator is used in image processing as edge detection algorithms with the purpose to emphasise images edges.

Sobel filter is a discrete differentiation operator, computing an approximation of the gradient of the image intensity function using two 3×3 kernels convolved with the original image operated in the horizontal and vertical directions to detect both horizontal

and vertical changes. At each point in the image, the result is either the corresponding gradient vector or the norm of this vector. Due to its characteristics, this kind of operator is relatively inexpensive in terms of computations.

Starting with the source image A , it is possible to obtain G_x and G_y which are the two images representing the horizontal and vertical derivatives:

$$G_x = \begin{bmatrix} +1 & 0 & -1 \\ +2 & 0 & -2 \\ +1 & 0 & -1 \end{bmatrix} * A$$

$$G_y = \begin{bmatrix} +1 & +2 & +1 \\ 0 & 0 & 0 \\ -1 & -2 & -1 \end{bmatrix} * A$$

where $*$ here denotes the 2-dimensional signal processing convolution operation.

At each point in the image, the resulting gradient approximations can be combined to give the gradient magnitude, using:

$$G = \sqrt{G_x^2 + G_y^2}$$

Using this information, we can also calculate the gradient's direction:

$$\Theta = \text{atan}\left(\frac{G_y}{G_x}\right)$$

where, for example, Θ is 0 for a vertical edge which is lighter on the right side.

The final result is an image where the pixels with the major changes in their grey values (where the edges are supposed to be) are emphasized.

5.6.2 Otsu's Thresholding Method ⁽¹⁰¹⁾

Otsu's thresholding method is exploited in computer image analysis to perform automatic grey levels thresholding to reduce the grey levels of a binary image. The principle behind this method is the assumption that the initial image could be reduced to a class of only two different types of pixels: the ones being part of the foreground, and the ones being part of the background. Taking into account this initial assumption the algorithm then calculates the optimum threshold to sort and classify each pixel into these two classes in order to minimize the intra-class variance of the black and white pixels (weighted sum of variances of the two classes).

Originally, Otsu's method was one-dimensional, but developments based on this technique led to multi-level thresholding methods.



Figure 83 Application of Otsu's thresholding to a B&W image. (101)

5.6.3 Principal Commands Used ⁽¹⁰²⁾

The list below present the Image Processing Toolbox™ commands which characterised this program:

- **“dir(name)”** lists files and folders that match “name”. When “name” is a folder, “dir” lists the contents of that folder. (103)
- **“dicomread(filename)”** reads the image data from the compliant Digital Imaging and Communications in Medicine (DICOM) file “filename”.
- **“imtool”** opens the Image Viewer app in an empty state. The window opened provides some basic tools like measure and point coordinates displayer.
- **“imcrop”** creates an interactive image-cropping tool associated with the image displayed in the current figure, called the target image. The Crop Image tool is a moveable, resizable rectangle that you can position over the image and perform the crop operation interactively using the mouse. Then, imcrop returns the cropped image. The Crop Image tool blocks the MATLAB® command line until the operation is completed.
- **“rgb2gray(RGB)”** function converts the truecolor RGB image to the greyscale intensity image by eliminating the hue and saturation information while retaining the luminance. The command can perform this conversion on a GPU.
- **“uint32(array)”** converts the elements of an array into unsigned 32-bit (4-byte) integers of class uint32 to be compatible with the following operations.
- **“im2double(I)”** converts the intensity image “I” to double precision, rescaling the data if necessary. “I” can be a greyscale intensity image, a truecolor image, or a binary image.
- **“graythresh(I)”** computes a global threshold, basing on the level, that can be used to convert an intensity image to a binary image. The graythresh function uses

Otsu's method. It returns the Effectiveness Eetric, "EM", as the second output argument which indicates the effectiveness of the thresholding of the input image.

- **"im2bw(I, level)"** converts the greyscale image "I" to a binary image. The output image replaces all pixels in the input image with luminance greater than "level" with the value 1 (white) and replaces all other pixels with the value 0 (black). The specific "level" is in the range [0,1].
- **"imfill(BW,locations)"** performs a flood-fill operation on background pixels of the input binary image "BW", starting from the points specified in locations. If "locations" is a P-by-1 vector, it contains the linear indices of the starting locations. If "locations" is a P-by-ndims(BW) matrix, each row contains the array indices of one of the starting locations.
- **"imfill(BW,'holes')"** fills holes in the input binary image "BW". In this syntax, a hole is a set of background pixels that cannot be reached by filling in the background from the edge of the image.
- **"bwperim(BW)"** returns a binary image that contains only the perimeter pixels of objects in the input image "BW". A pixel is part of the perimeter if it is nonzero and it is connected to at least one zero-valued pixel. The default connectivity is 4 for two dimensions images.
- **"gpuArray(X)"** copies the numeric array "X" to the GPU, and returns a gpuArray object. It is possible to operate on this array by passing its gpuArray to the feval method of a CUDA kernel object, or by using one of the methods defined for gpuArray objects in Establish Arrays on a GPU. The MATLAB array "X" must be numeric or logical, and the GPU device must have sufficient free memory to store the data.
- **"bwmorph(BW,'operation')"** applies a specific morphological "operation" to the binary image "BW". 'remove' removes interior pixels to leave an outline of the shapes. 'skel', with n = Inf, gets the image skeleton of the image removing pixels on the boundaries of objects but does not allow objects to break apart. The pixels remaining make up the image skeleton.

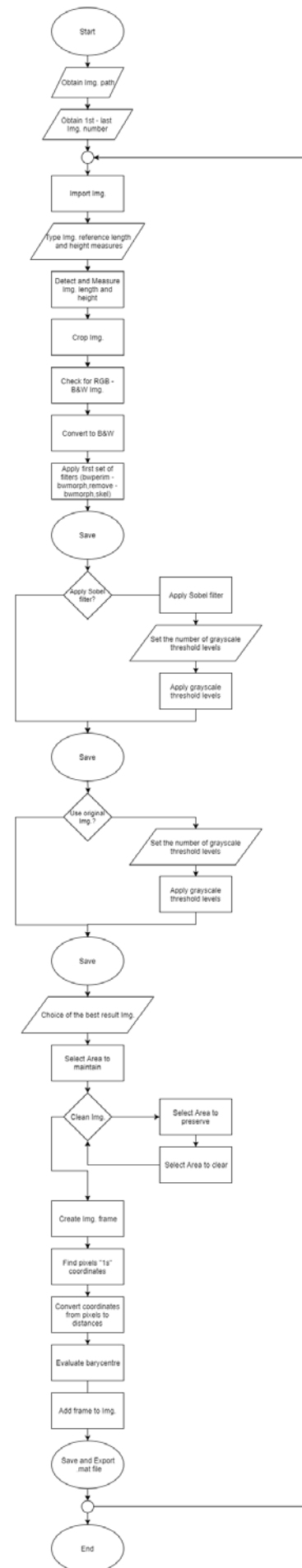
- **“getrect”** lets select a rectangle in the current axes using the mouse to click and drag the desired rectangle. “rect” is a four-element vector with the form [xmin ymin width height].
- **“find(X)”** returns a vector containing the linear indices of each nonzero element in array “X”. If “X” is a vector, then find returns a vector with the same orientation as “X”; if “X” is a multidimensional array, then find returns a column vector of the linear indices of the result; if “X” contains no nonzero elements or is empty, then find returns an empty array.

5.6.4 Procedures\Algorithms

Just below you can find a simplified algorithm of what the MATLAB code does and how is the basic structure of the program.

The main operations conducted by the program are:

- Start
- Obtain Img. path
- Obtain 1st - last Img. number
- Import Img.
- Type Img. reference length and height measures
- Detect and Measure Img. length and height
- Crop Img.
- Check for RGB - B&W Img.
- Convert to B&W
- Apply first set of filters (bwperim - bwmorph,remove - bwmorph,skel)
- Save
- Apply Sobel filter?
- Apply Sobel filter
- Set the number of greyscale threshold levels
- Apply greyscale threshold levels
- Save
- Use original Img.?



- Set the number of greyscale threshold levels
- Apply greyscale threshold levels
- Save
- Choice of the best result Img.
- Select Area to maintain
- Clean Img.
- Select Area to preserve
- Select Area to clear
- Create Img. frame
- Find pixels "1s" coordinates
- Convert coordinates from pixels to distances
- Evaluate barycentre
- Add frame to Img.
- Save and Export .mat file
- End.

The entire MATLAB code can be found in the Appendix.

5.6.5 Edges Points Extraction Results

As result of this first step code, there are some .mat files containing the matrices of the coordinates related the raw points extracted after the image analysis and processing, and a second array containing information about the scaling factors, images length and height and the reference scale measures from the original image.

Being an intermediate step for the points extraction, no errors have been considered or measured at this point, leaving this operation at the end of the Edges Points Generator program.

5.6.5.1 *Procedure*

Principal steps of the procedure the user has to follow during the program running are described below:

- 1) Input the folder path, selecting the images and entering the reference measures:

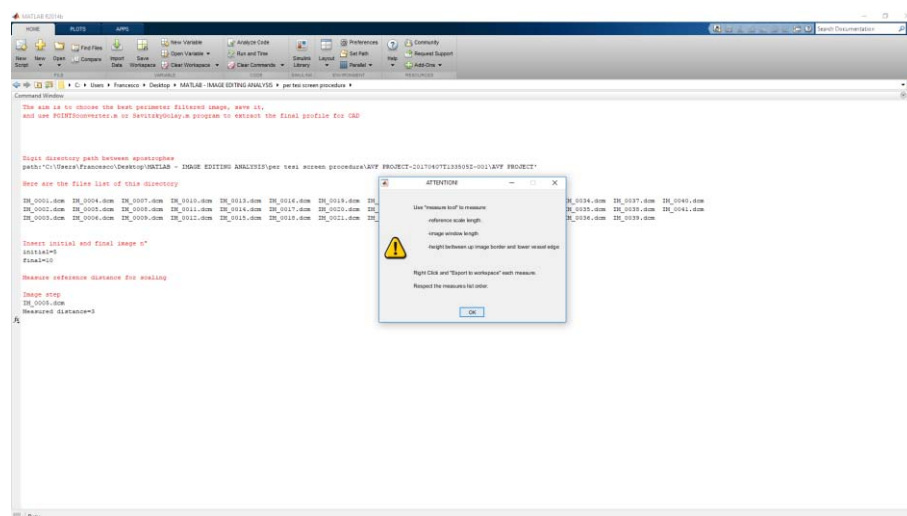


Figure 84 Step 1: images import and selection - reference measure input.

2) Measuring the related measures of interest on the real image:



Figure 85 Step 2: image reference measures measurement.

3) Cropping the area of interest:

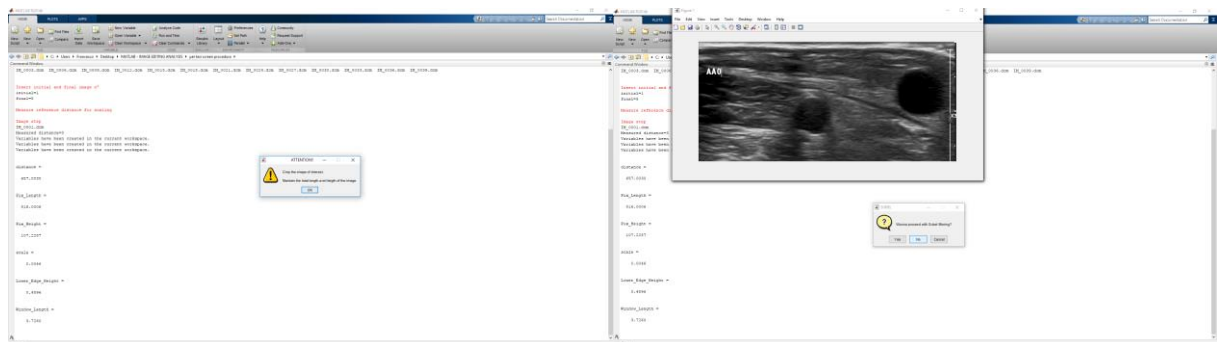


Figure 86 Step 3: image cropping.

4) Sobel filtering and thresholding:

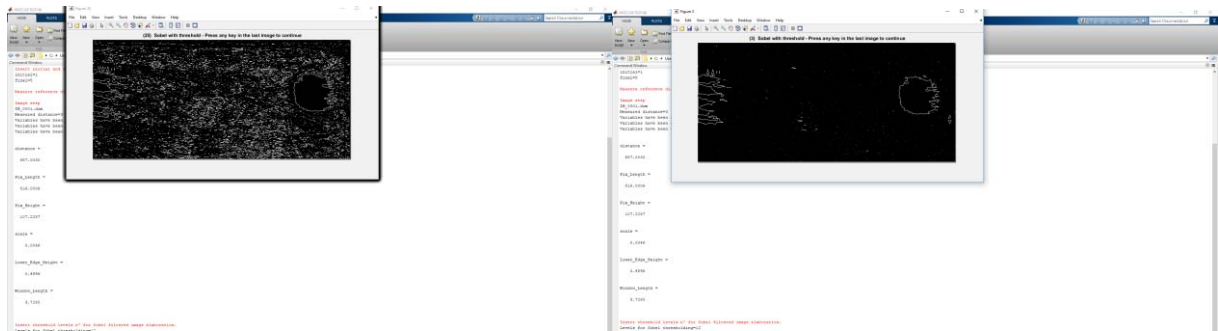


Figure 87 Step 4: Sobel filtering procedure.

5) Original image thresholding:

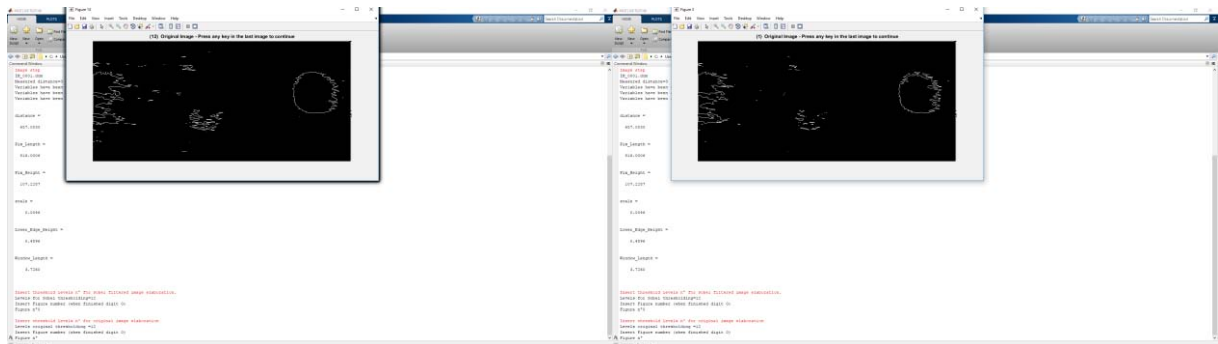


Figure 88 Step 5: original image thresholding procedure.

6) Image cleaning:

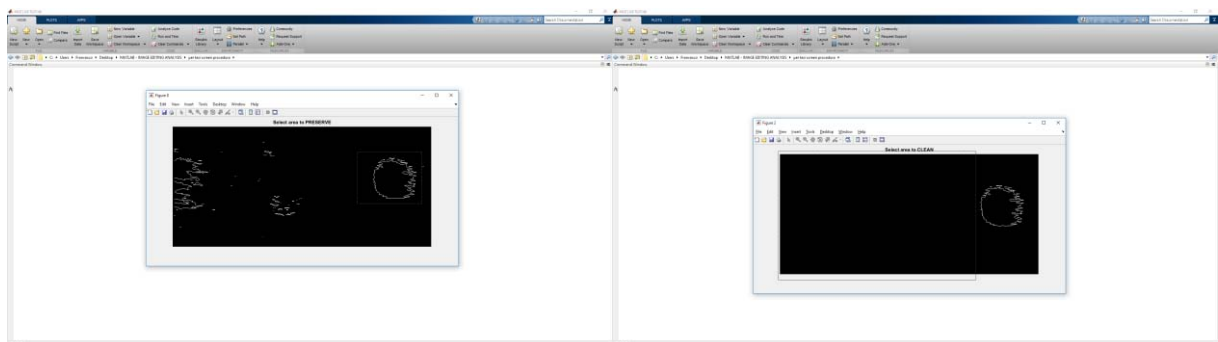


Figure 89 Step 6: image cleaning.

7) Image coordinates conversion and export:

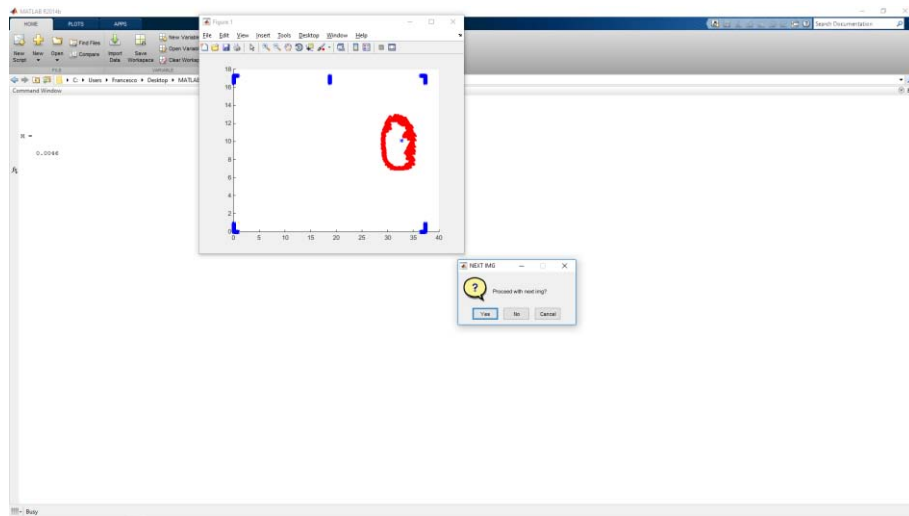


Figure 90 Step 7: edges points coordinate conversion and export.

5.6.5.2 Results

Here below, there can be seen some images processed and edited the program can provide, basing on the different techniques followed:

- Original image:

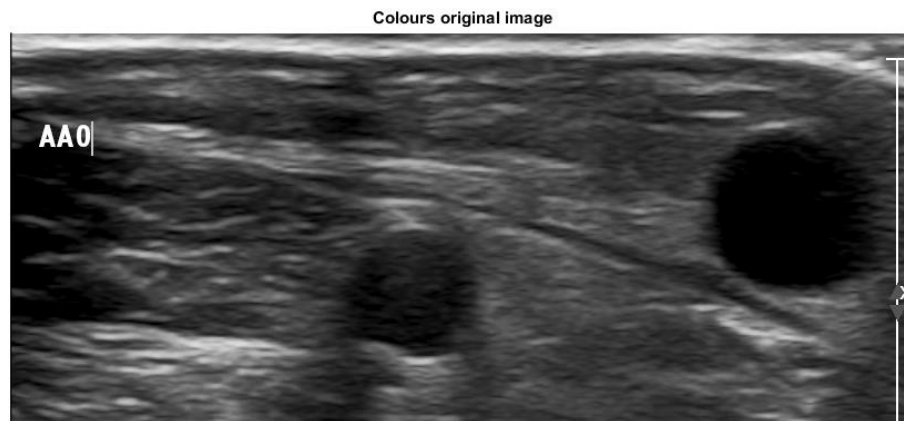


Figure 91 The original imported image.

- Bwmorph (morphological operators):

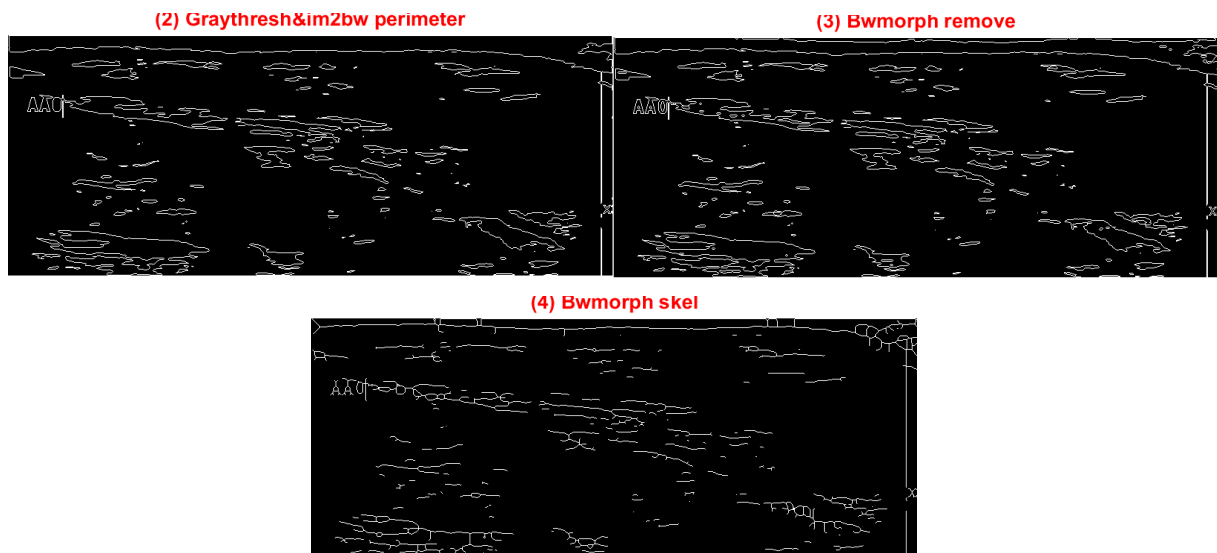


Figure 92 Results of the morphological operators.

- Sobel filtering and thresholding:

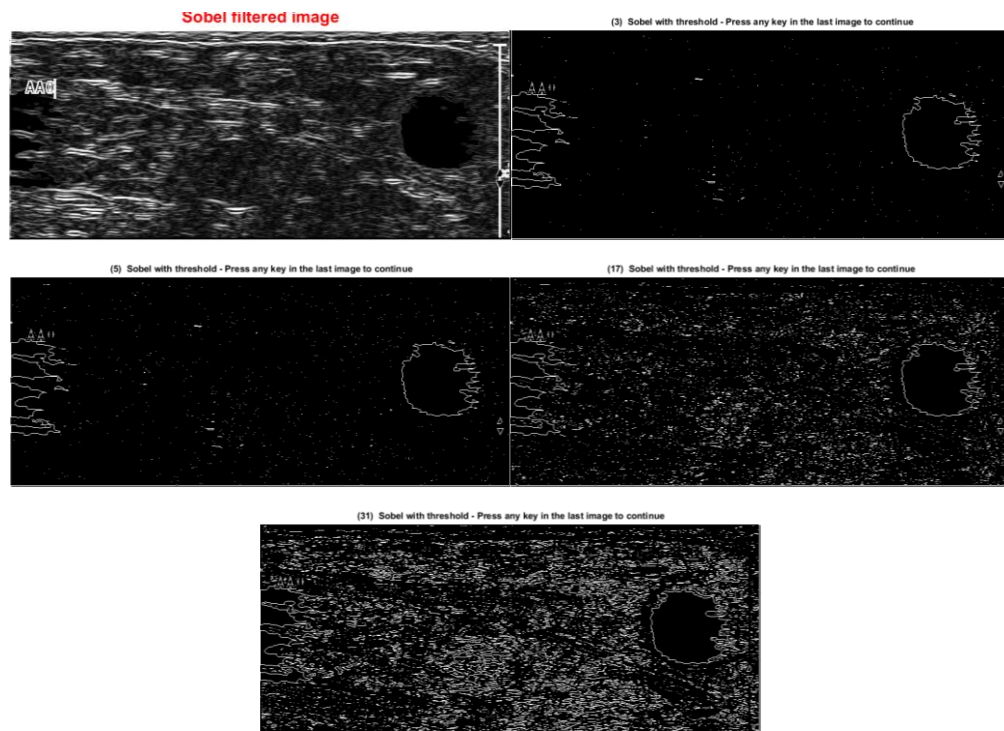


Figure 93 Sobel filtering procedure results (different thresholding levels).

*image numbers go with the threshold different level adopted (intermediate levels have been omitted)

- Original image thresholding:

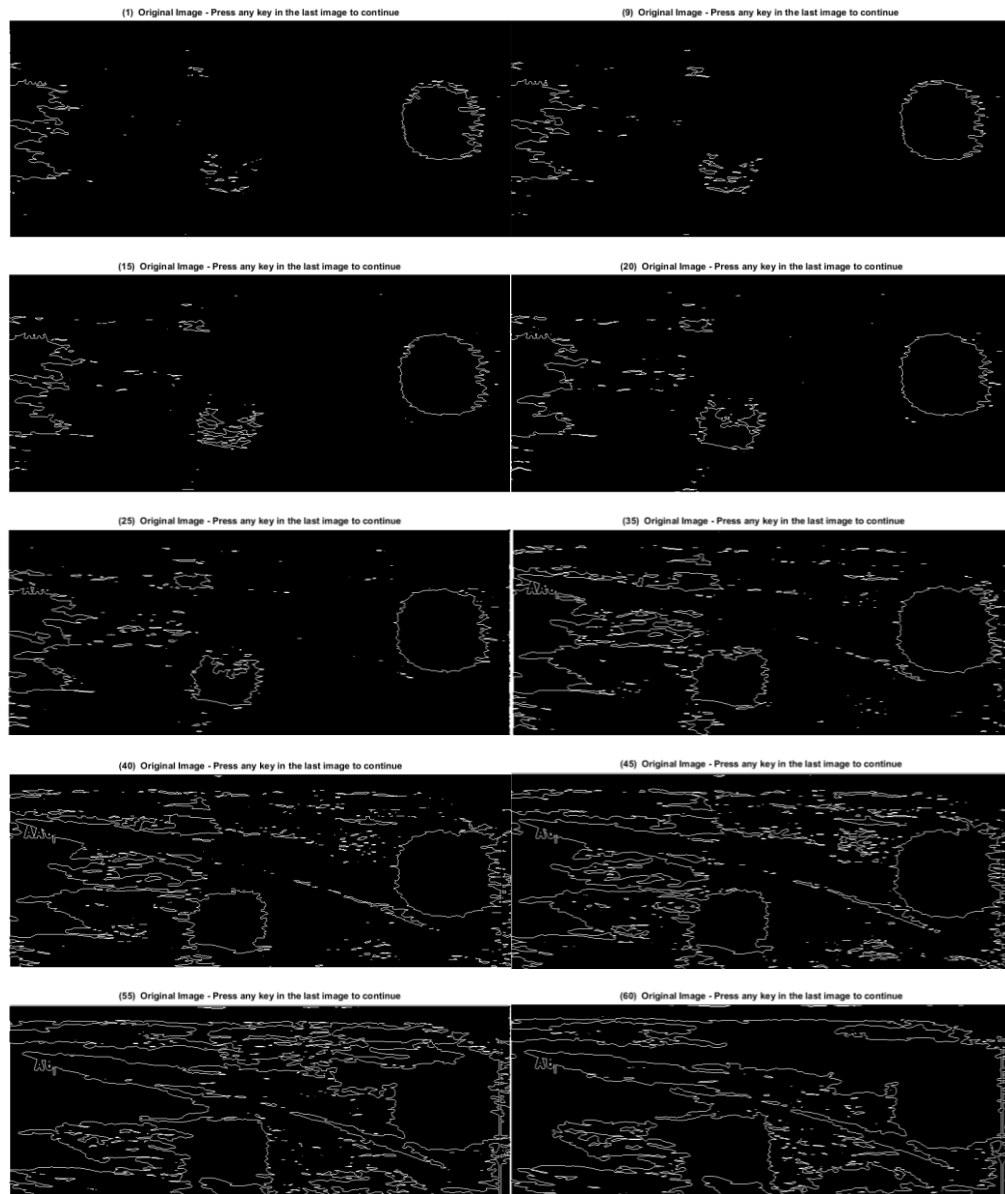


Figure 94 Image thresholding results (different thresholding levels).

*image numbers go with the threshold different level adopted (intermediate levels have been omitted)

- Resulting .mat file data saved at the end of the procedure for every image processed:

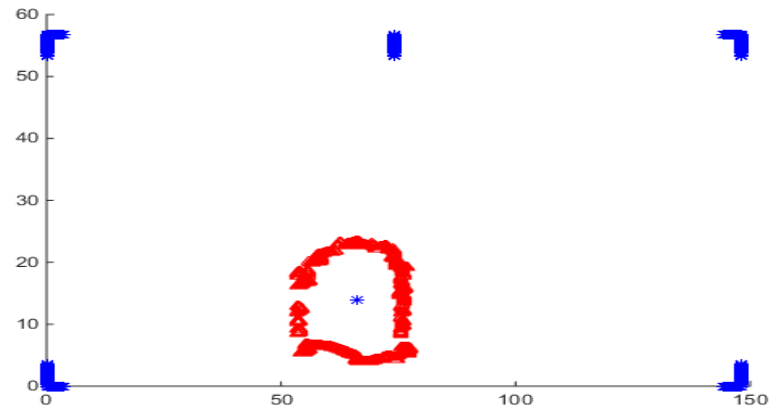


Figure 95 Final coordinates result.

5.7 Edges Points Generator

It has been chosen to divide this section of code from the previous one because in this way it is easier to control the partial results from the first analysis, being able to intervene if some data is not likely.

After having controlled that everything is fine, Edges Generator code can be launched. Edges Points Generator is necessary to correctly process and export the points coordinates of every cross-sectional area edge previously processed by the Edges Points Extraction program.

After importing the processed data from Edges Points Extraction program, the data is firstly checked for holes among the edge points allowing the user to set the angular threshold for the research. If any hole is detected, it is filled with a set of points following the circumference arc interpolated from the cross-sectional area to the two ends of the hole. Once the edges have a continuous perimeter, a filtering is operated exploiting Savitzky-Golay filter to smooth asperities and artefacts deriving from both the imaging equipment and edge extraction program. In the end, once again, the user sets the angular sampling frequency for the points to export to the CAD software.

After that, the program manages itself to provide the points requested, with the addition of the contour frame generate by the Edge Points Extractor, showing the results before asking confirmation for the data export in an Excel file containing the points coordinates of the edge considered.

The program is designed to iterate itself along the number of files the user set at the beginning of the procedure.

5.7.1 The Savitzky–Golay Filter ⁽¹⁰⁴⁾

The Savitzky–Golay filter is a mathematical smoothing method proposed in 1964 by Abraham Savitzky and Marcel J. E. Golay based on the polynomial fitting of subsequent sub-sets of data deriving from a single bigger set of data. This method convolutes these sub-sets of different length (dimension) with a low order polynomial by the method of the linear least squares in order to reduce the noise to the stable main signal. In this way, the Savitzky–Golay filter increases the signal-to-noise ratio of the entire set of digital data points, smoothing the data without greatly distorting the signal.

It's interesting to underline that an analytical solution to the least-squares equations can be found if the data points are equally spaced. This single set of "convolution coefficients" can be applied to all data sub-sets, to give estimates of the smoothed signal, (or derivatives of the smoothed signal) at the central point of each sub-set.

Savitzky and Golay filter has been chosen to smooth the edges spikes and aberrations due to the imaging and edges extraction procedure faults. Due to the quality loss at high magnification, it has been possible to clear this kind of noise along the borders thanks to the use of this filtering technique.

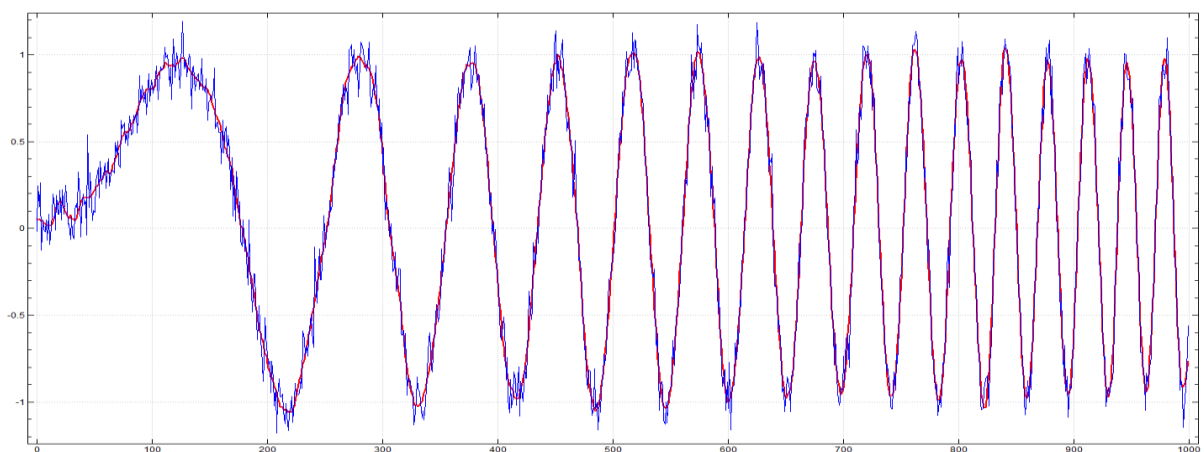


Figure 96 Example of Savitzky-Golay filter applied to a data set.

5.7.2 Principal Commands Used ⁽¹⁰²⁾

The list below present the Image Processing Toolbox™ commands which characterised this program:

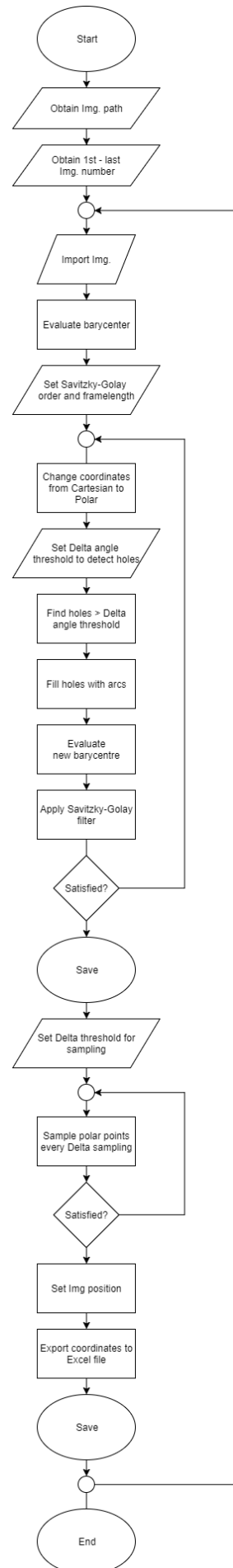
- **“dir(name)”** lists files and folders that match “name”. When “name” is a folder, “dir” lists the contents of that folder. (103)
- **“cart2pol(x,y)”** transforms corresponding elements of the two-dimensional Cartesian coordinate arrays x and y into polar coordinates theta and rho. (105)
- **“pol2cart(theta,rho)”** transforms corresponding elements of the polar coordinate arrays theta and rho to two-dimensional Cartesian, or xy, coordinates.
- **“sgolayfilt(x,order,framelength)”** applies a Savitzky-Golay smoothing filter to the data in vector x. If x is a matrix, sgolayfilt operates on each column. The polynomial order must be less than the framelength and, in turn, the latter must be odd. If “order” = “framelength”-1, the filter produces no smoothing. (106)
- **“xlswrite(filename,A,sheet,xlRange)”** writes to the rectangular array region specified by “xlRange” in the first worksheet of the workbook. Using Excel range syntax, such as 'A1:C3' is possible to set the specified worksheet and range. (103)

5.7.3 Procedures\Algorithms

Just below you can find a simplified algorithm of what the MATLAB code does and how is the basic structure of the program.

The main operations conducted by the program are:

- Start
- Obtain Img. path
- Obtain 1st - last Img. number
- Import Img. .mat file
- Evaluate barycentre
- Set Savitzky-Golay order and framelength
- Change coordinates from Cartesian to Polar
- Set Delta angle threshold to detect holes
- Find holes $>$ Delta angle threshold
- Fill holes with arcs
- Evaluate new barycentre
- Apply Savitzky-Golay filter
- Satisfied?
- Save
- Set Delta threshold for sampling
- Sample polar points every Delta sampling
- Satisfied?
- Set Img position
- Export coordinates to Excel file
- Save
- End



- Save
- End.

The entire MATLAB code can be found in the Appendix.

5.7.4 Edges Points Generator Results

What is obtained from this final program is a list of coordinates, organised in several Excel sheets of a single file, describing the vessel cross-sectional area at each step of the imaging procedure.

These coordinates have been processed to avoid the presence of “holes” on the edges, smoothed to avoid sharp corners or unnatural un-physiologic patterns, and sampled to allow a better modelling by the NURBS tool of the CAD software.

5.7.4.1 Procedure

Principal steps of the procedure the user has to follow during the program running are described below:

1) Input the folder path, selecting the images and entering the reference measures:

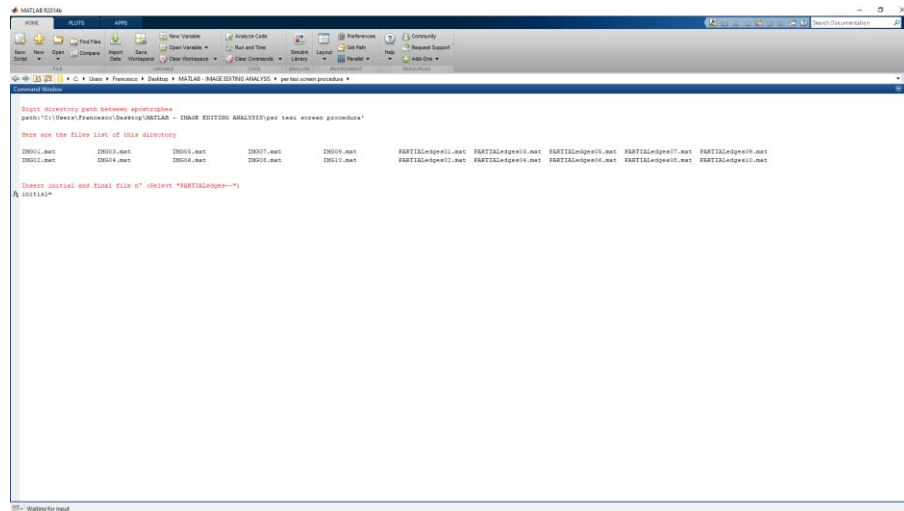


Figure 97 Step 1: images import and selection - reference measure input.

2) Setting Savitzky-Golay Order and frame length:

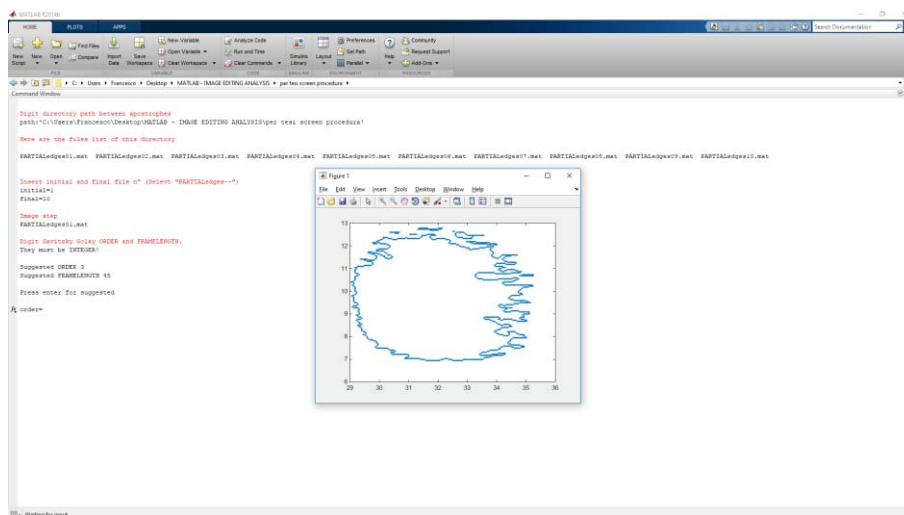


Figure 98 Step 2: Savitzky-Golay filter setup (frame length and order input).

3) Setting the Delta Angle threshold to detect holes:

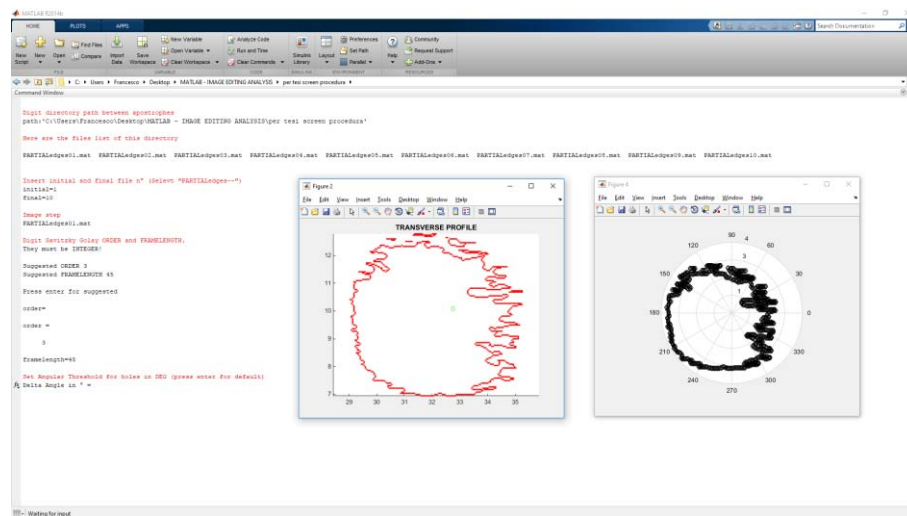


Figure 99 Step 3: setup the holes detector (input the threshold angle).

4) Filling holes:

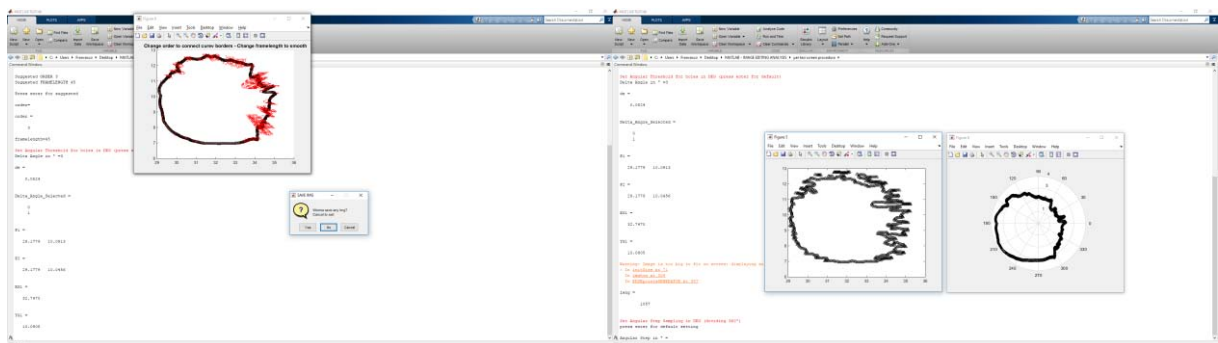


Figure 100 Step 4: holes filling.

5) Setting Delta Angle sampling:

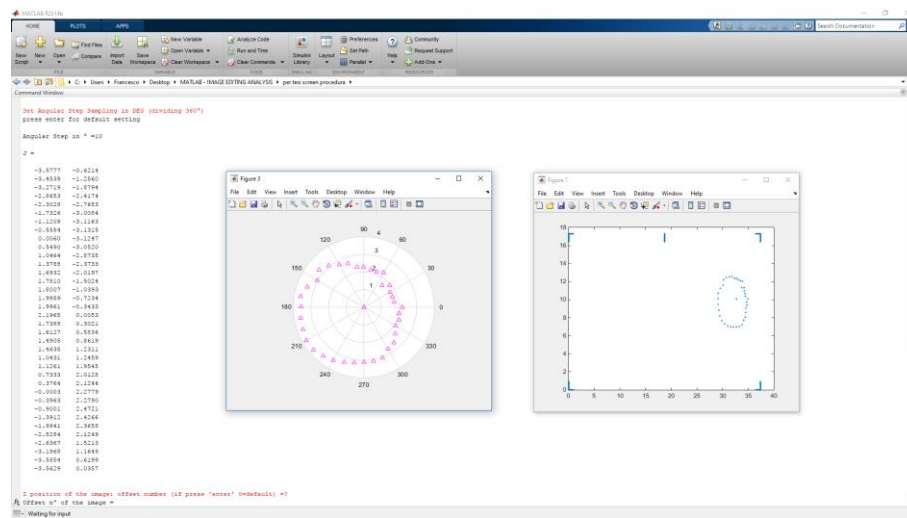


Figure 101 Step 5: setup the sampling angle and exporting the coordinates data.

5.7.4.2 Results

Here below, there can be seen some images processed and edited the program can provide, basing on the different techniques followed:

- Initial image in Cartesian and polar coordinates:

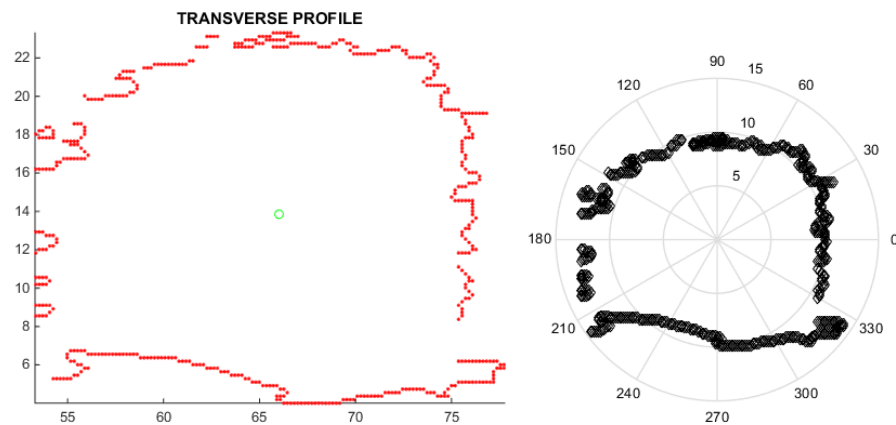


Figure 102 The original points imported and processed in cartesian and polar coordinates.

- Holes filling positions:

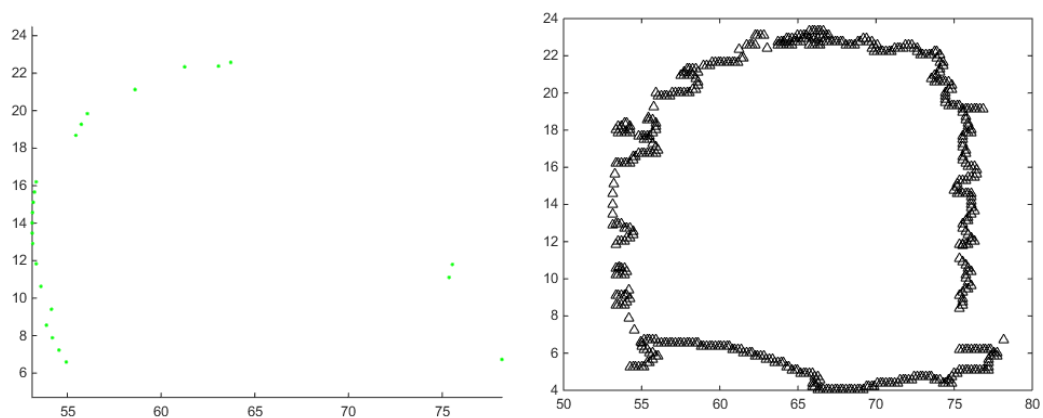


Figure 103 Holes filling positions and resulting image.

- Savitzky-Golay smoothing (Cartesian and polar coordinates):

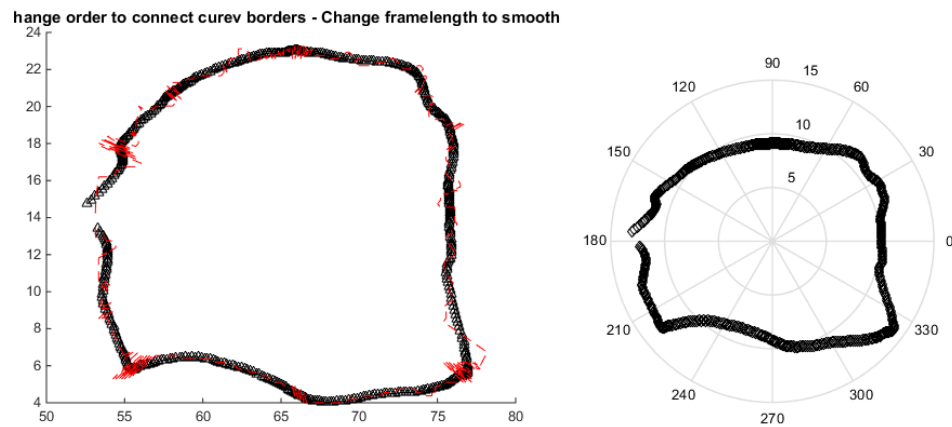


Figure 104 Savitzky-Golay filtered edge profile.

- Sampled points:

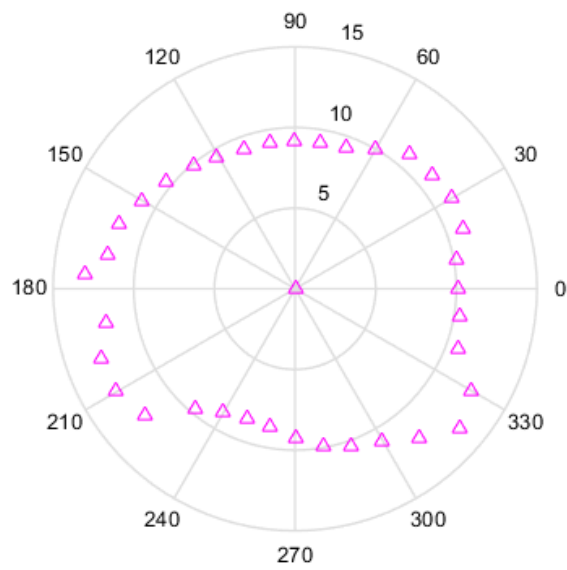


Figure 105 Final sampled points.

- Final results:

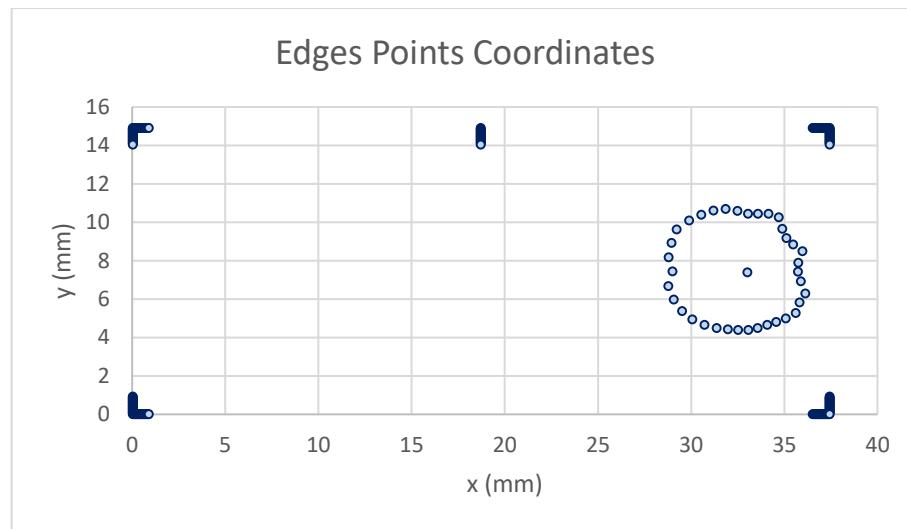


Figure 106 Edges Points Coordinates exported in Excel with the border frame.

- CAD results comparison:

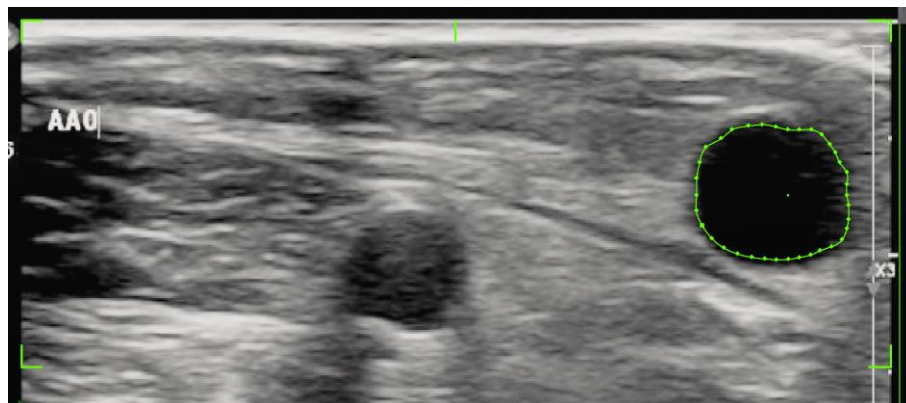


Figure 107 Comparison between the original DICOM image and the CAD imported points.

5.8 Velocity PulseWave Extraction

The need of boundary conditions to setup the simulations can be satisfied from data easily accessible through Ultrasound Colour-Doppler scans, where the blood velocity pulse wave is plotted versus time. Usually, during this procedure by Ultrasound equipment, more than one cycle is captured (usually 5-6 cycles). This is very helpful to have a robust information, allowing the program to extract an average pulse wave, more cleared by uncertainty and errors.

The main issue here is to easily and accurately have access to this kind of information starting from the tools we have.

The strategy found basically encompass what it has been illustrated before: starting from Ultrasound Colour-Doppler images with the velocity pulse wave plotted, the image undergoes through a cropping, a filtering, a conversion and a fitting.

Like in the Edges Points Extraction, the images are loaded by user input, and the measured for scaling from pixel to metric reference. Then the plotted area is cropped, with a subsequent automatic filtering to extract the mean pulse wave line (provided by the Ultrasound equipment computer and coloured in red) from the noisy background of the measurement. The data is extracted, cleared from redundant information and then converted from pixels to velocity vs time dimensions. The different cycles are detected, separated and overlapped to operate the average. Once obtained the averaged cycle, this is fitted by the least square fitting method to obtain a mathematical description of the single representative cycle. Subsequently, the cycle is resampled by the user input, repeated four times and a ramp from zero to the initial sampled velocity is inserted at the very beginning, to avoid velocity discontinuities when the simulation is started. Finally, the resampled, multiplied and ramped velocity pulse wave is exported in an Excel file into arrays of time vs velocity, to be imported into the simulation software for the boundary conditions set up.

The program is designed to iterate itself along the number of files the user set at the beginning of the procedure.

5.8.1 The Least Squares Fitting ⁽¹⁰⁷⁾

In order to have a model of the velocity pulse wave capable of different samplings, the information extracted as coordinates from the velocity vs time graph underwent to a least square fitting. This procedure allowed resampling the data as needed for the subsequent operations (boundary conditions set up) and having a mathematical description of the velocity pulse wave profile.

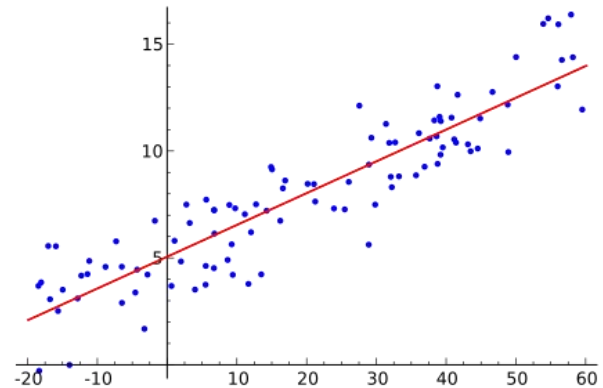


Figure 108 The result of fitting a set of data.

The least-squares method was first published by Adrien-Marie Legendre and is usually credited to Carl Friedrich Gauss (1795), who went beyond Legendre and succeeded in connecting the method of least squares with the principles of probability and to the normal distribution. Following studies into this topic led him to the normal distribution theory invention.

This method is a standard approach to approximate solution of overdetermined systems in the regression analysis (107). The "Least squares" means that the overall solution minimizes the sum of the squares of the residuals made in the results of every single equation.

There are two rather different contexts in which this regression analysis is applied: regression for prediction, and regression for fitting. For our study, the second application has been exploited. In fact, the most important application of this method is in data fitting. The best fit in the least-squares sense minimizes the sum of squared residuals, giving an accurate description of the phenomenon sampled. In standard regression analysis, that leads to the fitting by least squares, there is an implicit assumption that errors in the independent variable are zero or strictly controlled so as to be negligible, otherwise, the simple regression and least squares methods have problems. (108)

Least squares problems fall into two categories: linear or ordinary least squares and non-linear least squares, depending on whether or not the regression function is linear in the unknown parameters that are estimated from the data. Despite the linear least-squares problem, which occurs in statistical regression analysis and it has a closed-form solution, the non-linear problem is usually solved by iterative refinement. Our problem has been solved using a polynomial least squares method, which is a nonlinear modeller of the data, but a linear statistical estimation tool.

The objective consists of adjusting the parameters of a model function to best fit a data set of n points (x_i, y_i) , $i = 1, \dots, n$, where x_i is an independent variable and y_i is a dependent variable. The assumed model function has the form $f(x, \beta)$, where m adjustable parameters are held in the vector β (107). The least squares method finds its optimum when the sum, S , of squared residuals

$$S = \sum_{i=1}^n r_i^2$$

is a minimum, being the residual defined as the difference between the actual value of the dependent variable and the value predicted by the model.

$$r_i = y_i - f(x_i, \beta)$$

The minimum of the sum of squares is found by setting the gradient to zero. Since the model contains m parameters, there are m gradient equations:

$$\frac{\partial S}{\partial \beta_j} = 2 \sum_i r_i \frac{\partial r_i}{\partial \beta_j} = 0$$

and since $r_i = y_i - f(x_i, \beta)$, the gradient equations become

$$-2 \sum_i r_i \frac{\partial f(x_i, \beta)}{\partial \beta_j} = 0$$

The gradient equations apply to all least squares problems, but each particular problem requires its own particular expressions for the model and its partial derivatives.

As said before, in a linear regression model the parameters characterising the models are combined in a linear formulation:

$$f(x, \beta) = \sum_{j=1}^m \beta_j \phi_j(x)$$

where the function Φ_i is a function of x .

Letting:

$$X_{ij} = \frac{\partial f(x_i, \beta)}{\partial \beta_j} = \phi_j(x_i)$$

in case the least square estimate (or estimator, in the context of a random sample), β is given by:

$$\beta = (X^T X)^{-1} X^T y$$

Worth to note that each data point has one residual and both the sum and the mean of the residuals are equal to zero. Moreover, a data point may consist of more than one independent variable, so in the most general case there may be one or more independent variables and one or more dependent variables at each data point.

Exploiting this technique, it is possible to extract a polynomial expression that fit the data given, capable of many applications, from resampling data to modelling a phenomenon similar to the studied one.

5.8.2 Principal Commands Used ⁽¹⁰²⁾

The list below present the Image Processing Toolbox™ commands which characterised this program:

- **“dir(name)”** lists files and folders that match “name”. When “name” is a folder, “dir” lists the contents of that folder. (103)
- **“dicomread(filename)”** reads the image data from the compliant Digital Imaging and Communications in Medicine (DICOM) file “filename”.
- **“imtool”** opens the Image Viewer app in an empty state. The window opened provides some basic tools like measure and point coordinates displayer.
- **“imcrop”** creates an interactive image cropping tool associated with the image displayed in the current figure, called the target image. The Crop Image tool is a moveable, resizable rectangle that you can position over the image and perform the crop operation interactively using the mouse. Then, imcrop returns the cropped image. The Crop Image tool blocks the MATLAB® command line until the operation is completed.
- **“rgb2gray(RGB)”** function converts the truecolor RGB image to the greyscale intensity image by eliminating the hue and saturation information while retaining the luminance. The command can perform this conversion on a GPU.
- **“find(X)”** returns a vector containing the linear indices of each nonzero element in array “X”. If “X” is a vector, then find returns a vector with the same orientation as “X”; if “X” is a multidimensional array, then find returns a column vector of the

linear indices of the result; if “X” contains no nonzero elements or is empty, then find returns an empty array.

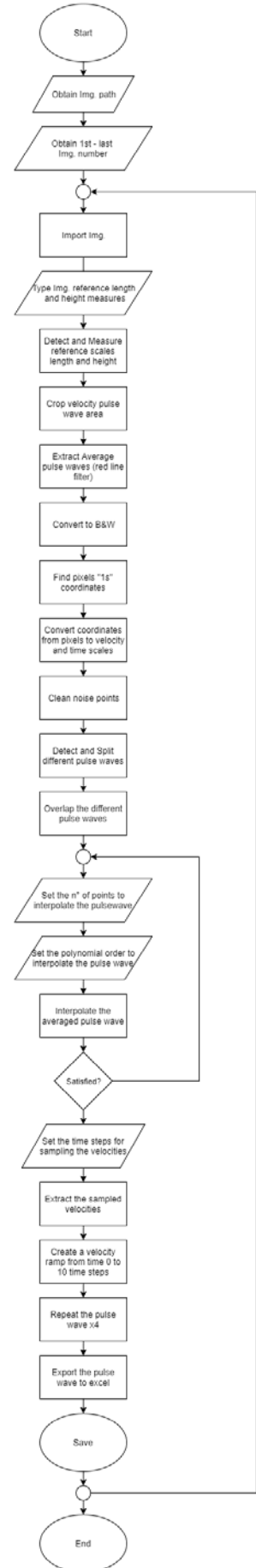
- “**polyfit(x,y,n)**” returns the coefficients for a polynomial $p(x)$ of degree n that is a best fit (in a least-squares sense) for the data in y . The coefficients in p are in descending powers, and the length of p is $n+1$: $y = p_1x^n + p_2x^{n-1} + \dots + p_nx + p_{n+1}$ (109)
- “**polyval(p,x)**” returns the value of a polynomial of degree n evaluated at x . The input argument p is a vector of length $n+1$ whose elements are the coefficients in descending powers of the polynomial to be evaluated: $y = p_1x^n + p_2x^{n-1} + \dots + p_nx + p_{n+1}$. The x can be a matrix or a vector.
- “**linspace(x1,x2,n)**” generates n linearly spaced points. The spacing between the points is $(x2-x1)/(n-1)$. This command is similar to the colon operator, “:”, but gives direct control over the number of points and always includes the endpoints. (110)
- “**xlswrite(filename,A, sheet,xlRange)**” writes to the rectangular array region specified by “xlRange” in the first worksheet of the workbook. Using Excel range syntax, such as ‘A1:C3’ is possible to set the specified worksheet and range. (103)

5.8.3 Procedures\Algorithms

Just below you can find a simplified algorithm of what the MATLAB code does and how is the basic structure of the program.

The main operations conducted by the program are:

- Start
- Obtain Img. path
- Obtain 1st - last Img. number
- Import Img.
- Type Img. reference length and height measures
- Detect and Measure reference scales length and height
- Crop velocity pulse wave area
- Extract Average pulse waves (red line filter)
- Convert to B&W
- Find pixels "1s" coordinates
- Convert coordinates from pixels to velocity and time scales
- Clean noise points
- Detect and Split different pulse waves
- Overlap the different pulse waves
- Set the n° of points to interpolate the pulse wave
- Set the polynomial order to interpolate the pulse wave
- Interpolate the averaged pulse wave
- Satisfied?
- Set the time steps for sampling the velocities
- Extract the sampled velocities
- Create a velocity ramp from time 0 to 10 time steps
- Repeat the pulse wave x4
- Export the pulse wave to excel
- Save
- End



- Extract the sampled velocities
- Create a velocity ramp from time 0 to 10 time steps
- Repeat the pulse wave x4
- Export the pulse wave to excel
- Save
- End.

The entire MATLAB code can be found in the Appendix.

5.8.4 Velocity PulseWave Extraction Results

The result of this program is, like in the other codes, an Excel file with two arrays containing the sampled times and the blood velocities respectively. The fitting operations of the points, extracted from the original image and then converted, it was deliberately left user definable to ensure visual control during the process.

The choice to insert a ramp at the beginning of the data has been made necessary to reduce the instability of the numerical simulation during the first iterations. The repetition of the four-cycle pulsewave has been carried out to ensure correct modelling of the numeric model, significantly improving the quality and validity of the results.

5.8.4.1 Procedure

Principal steps of the procedure the user has to follow during the program running are described below:

- 1) Input the folder path, selecting the images and entering the reference measures:

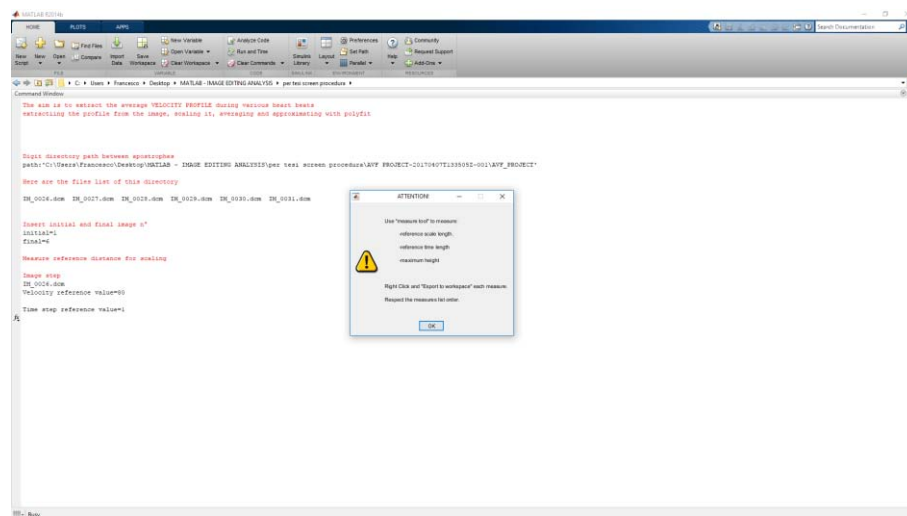


Figure 109 Step 1: images import and selection - reference measure input.

- 2) Measuring the related measures of interest on the real image:

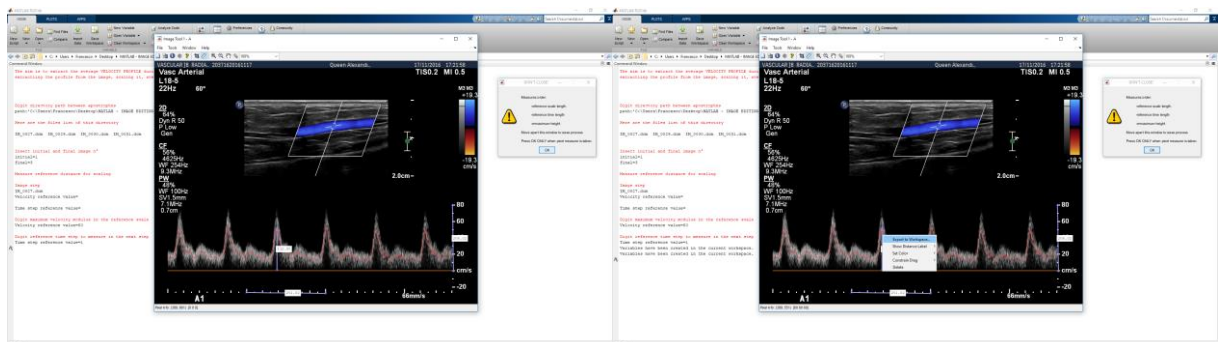


Figure 110 Step 2: image reference measures measurement.

The screenshot displays the Vascular Imaging software interface. The main window shows a B-mode ultrasound image of a vessel lumen. The top panel displays the B-mode image with a color-coded flow overlay. The bottom panel shows a spectral Doppler waveform. The interface includes various parameters and settings on the left and top.

Top Panel (B-mode Image):

- Header:** VASCULAR IS RADIA. 2037420161117 Queen Alexandra. 17/11/2016 17:21:58
- Parameters:** Vaso Arterial, L18-S, 22Hz, 60°
- Color Scale:** MD M3, +19.3, -19.3 cm/s
- Scale Bar:** 2.0cm

Left Panel (Parameters):

- 2D:** 45°, Dyn R 50, P Low, Gen
- CF:** 59%, 48.25Hz, WF 254Hz, 6.5Hz
- PW:** 49%, WF 100Hz, SV1 5mm, 7.1mm, 0.1cm
- Image #:** BR_0027
- Time #:** 208.00
- Time #:** 251.00

Bottom Panel (Spectral Doppler):

- Waveform:** A1
- Scale:** 80, 60, 40, 20, 0, -20 cm/s
- Time Scale:** 0.6mm/s

Bottom Status Bar:

- Peak_velocity = 0.5076

4) Image filtering: extracting the average pulse wave line and eliminating double points, then the conversion from points coordinates to velocity and time dimensions:



- 233 -

5) Detecting and separating different pulse waves:

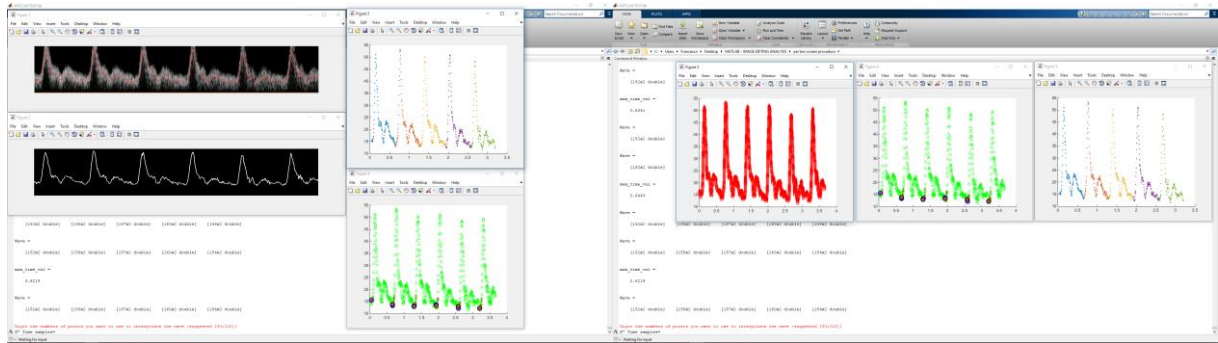


Figure 113 Step 5: splitting the different pulse waves.

6) Overlapping the different pulse waves:

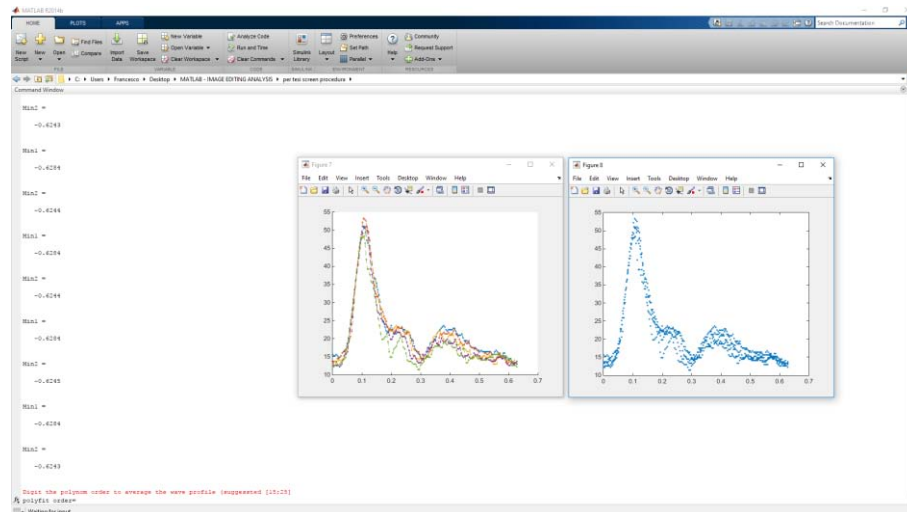


Figure 114 Step 6: overlap of the different pulse waves.

7) Fitting the points with least squares fitting (polynomial order can be varied to evaluate differences and detect the best fitting):

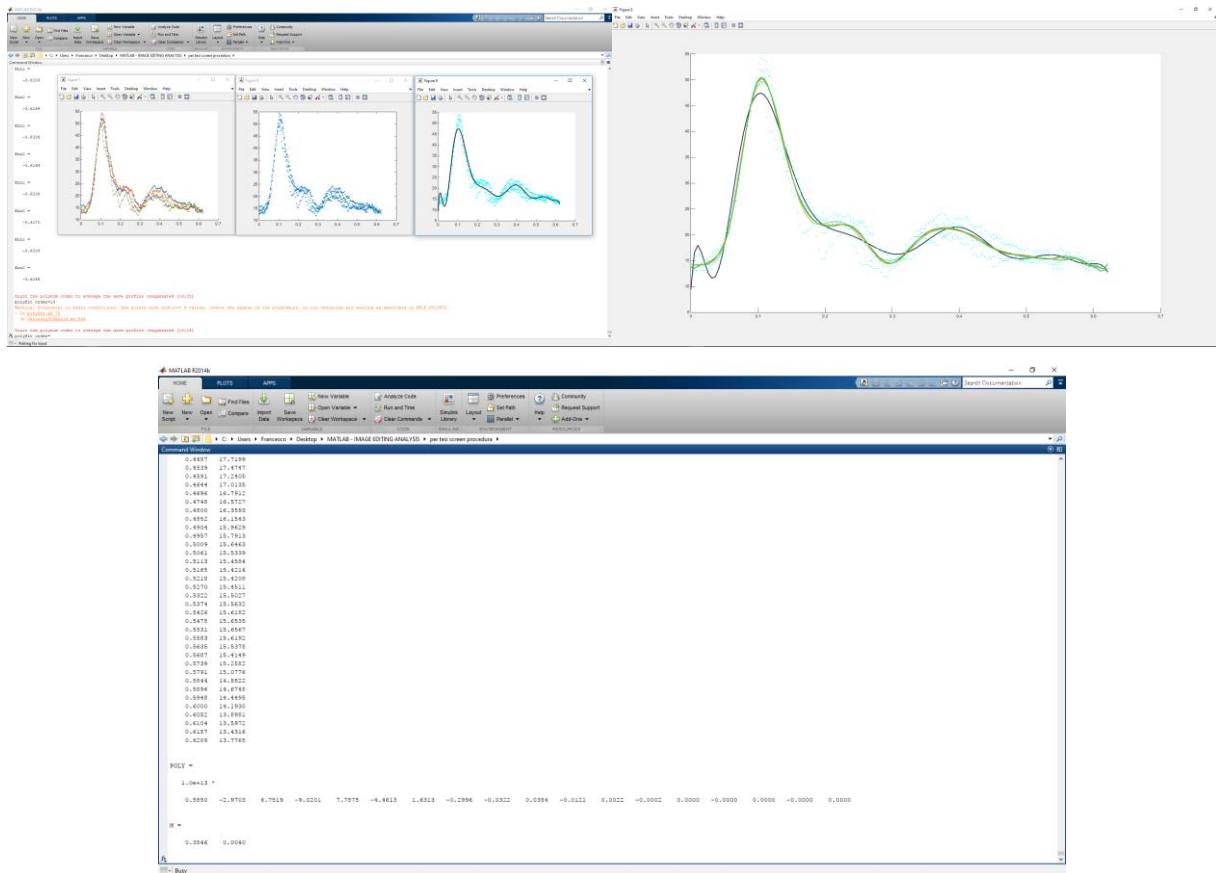


Figure 115 Step 7: pulse wave fitting (different polynomial orders).

The screenshot displays the MATLAB R2016a environment. The main window shows a plot of a signal with three distinct peaks, each reaching a value of approximately 40. The x-axis ranges from 0 to 3, and the y-axis ranges from -10 to 50. The signal starts at 0, rises to the first peak at x ≈ 0.2, falls to a minimum of about 15 at x ≈ 0.5, rises to the second peak at x ≈ 0.8, falls to another minimum of about 15 at x ≈ 1.1, rises to the third peak at x ≈ 1.4, and finally falls to about 15 at x ≈ 1.7. The Command Window on the left contains a list of data points, likely generated from the plot. A small dialog box titled "NEXT (M)" is visible in the bottom right corner, containing a question mark icon and the text "Proceed with read img?".

Command Window:

```

0.1743 16.9723
0.4800 14.3509
0.4802 14.1249
0.4804 13.9429
0.4807 13.7623
0.5009 13.4443
0.5041 13.3339
0.5113 13.4884
0.5149 13.4214
0.5118 13.4508
0.5270 13.4811
0.5302 13.5007
0.5374 13.5482
0.5404 13.4142
0.5470 13.4839
0.5513 13.6047
0.5580 13.4192
0.5609 13.5970
0.5687 13.4149
0.5709 13.2582
0.5781 13.0776
0.5844 14.3522
0.5896 14.4744
0.5940 14.4495
0.6000 14.1303
0.6032 13.8941
0.6104 13.5972
0.6137 13.4324
0.6219 13.1768

```

Poly =

```

1.0e+13 *
0.3860 -0.9708 6.7612i -9.0201i 7.7875i -8.4613i 1.4313i -0.2396i -0.6322i 0.0391i -0.5121i 0.0022i -0.0002i 0.0000i -0.0000i 0.0000i 0.0000i

```

R =

```

0.3866 0.0040

```

R =

```

0.3866 0.0040

```

- 236 -

5.8.4.2 Results

Here below, there can be seen some images processed and edited the program can provide all along the procedure:

- Original image

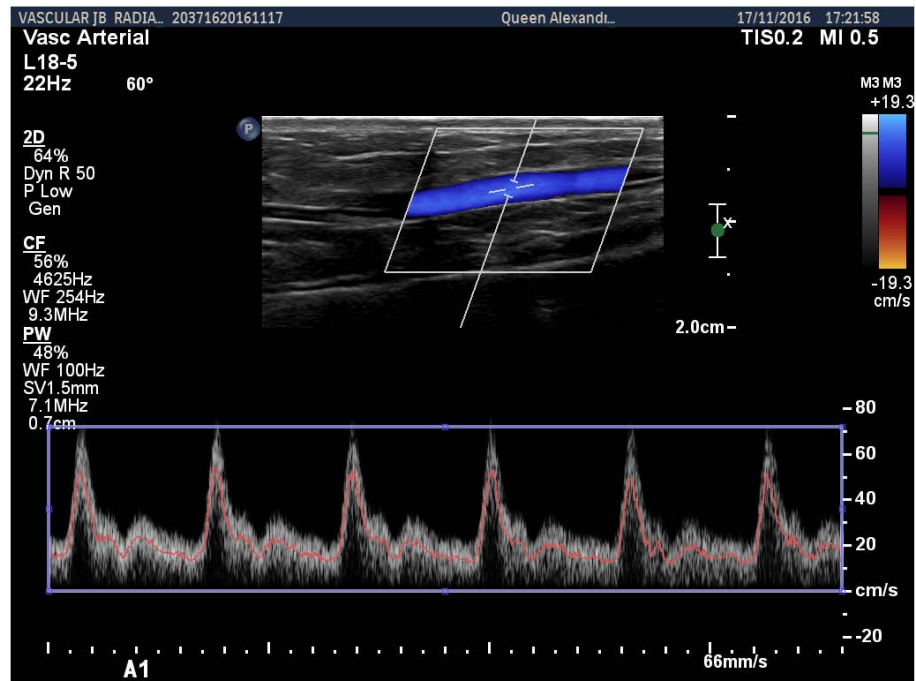


Figure 117 The original imported image.

- Cropped image:

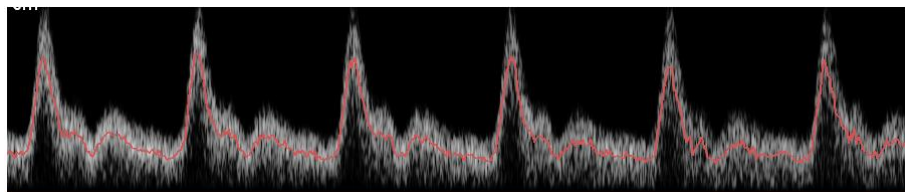


Figure 118 The cropped image of interest.

- Filtered image:

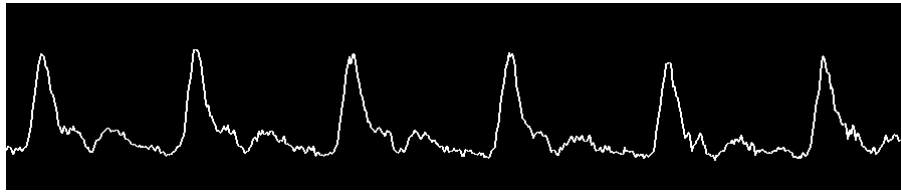


Figure 119 The average velocity pulse wave extracted.

- Points converted in velocity and time dimensions:

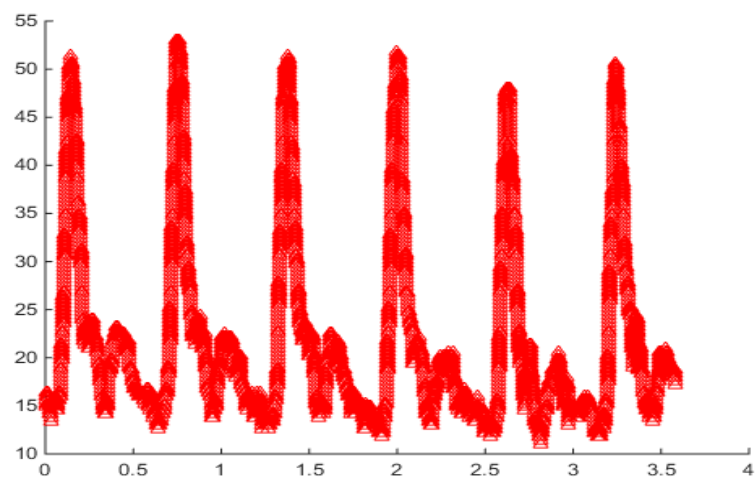


Figure 120 The pulse wave information scaled with the correct metrics.

- Pulse waves detection:

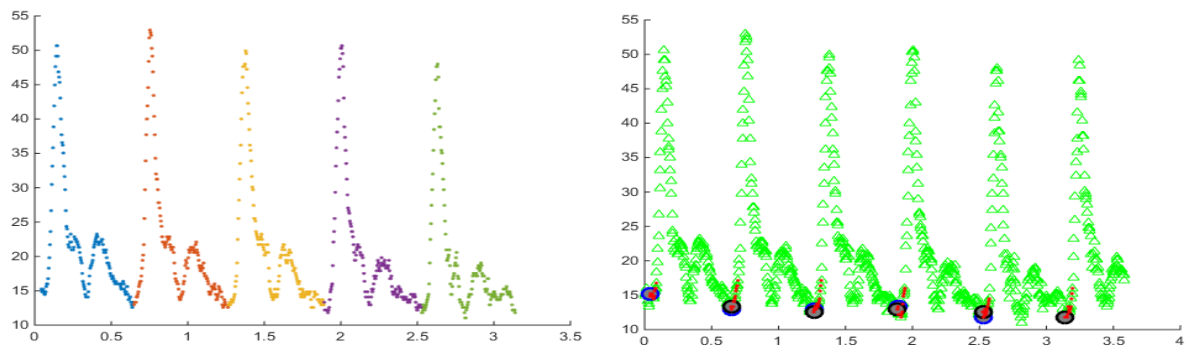


Figure 121 The velocity pulse waves splitting procedure.

- Pulse waves overlap:

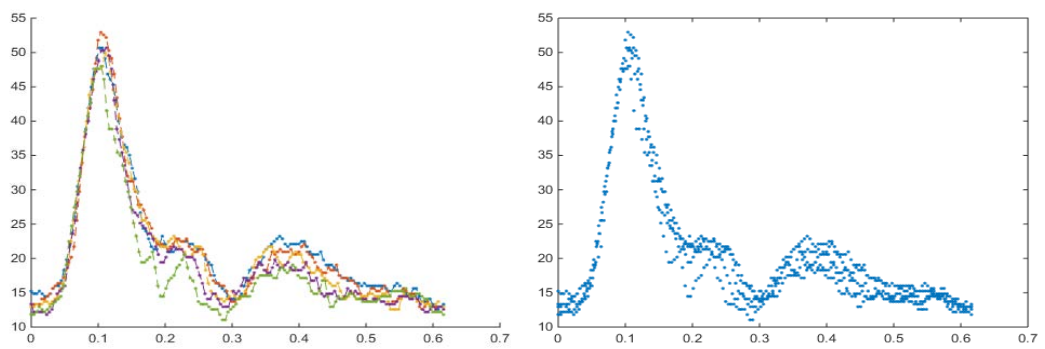


Figure 122 The velocity pulse waves overlapping procedure.

- Pulse waves fitting:

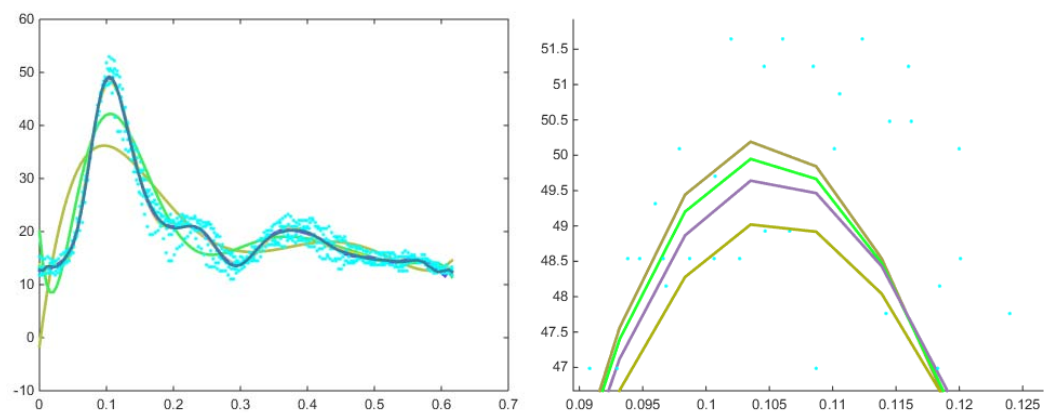


Figure 123 The polynomial fitting results and peak detail.

- Pulse waves export:

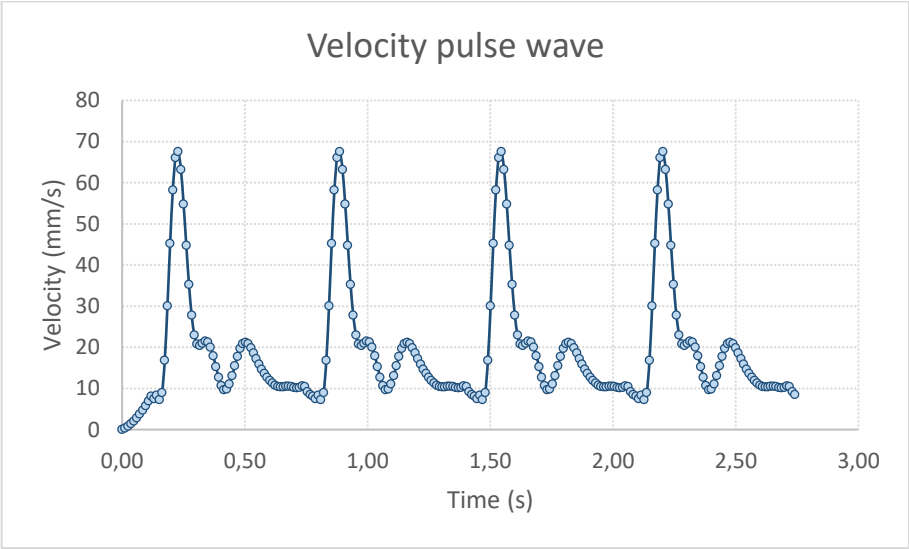


Figure 124 The velocity pulse wave points exported in Excel.

5.9 Uncertainties and Errors

After all the data was processed and extracted, the first errors estimation of the cross-sectional areas and the velocity pulse wave can be done.

Not having a real model of the vessels or a different source to evaluate the pulse wave velocity in time, the only type of analysis that was possible is the uncertainty of the procedure and the comparison with the original data. To operate this validation, Autodesk Inventor® CAD software has been exploited. The main idea is to accurately scale the original images (which have a reference scale) and then overlap the processed images results in order to operate an error analysis.

5.9.1 Procedure and measures uncertainty

Just before the errors estimation, based on the comparison between the results and the original images, an uncertainty analysis has to be done to deepen the causes of uncertainty related to the procedure of cross sectional areas extraction and reconstruction and the results measurements themselves. This permitted to have a better understanding of the errors value, in addition, giving a very interesting indication of where the procedure should be improved to achieve better results.

5.9.1.1 Images Conversion

Using MATLAB DICOMRead program (see the Paragraph 5.10 an the Appendix), all the DICOM scans are opened and, thanks to the graphic interface of the Image Processing

Toolbox™, the images are saved in .png format to be opened outside MATLAB by the CAD software.

Here the only problem that could incur, is the quality loss in the images conversion, but, using the PNG format, this occurrence is reduced at the minimum (and is not valuable).



Figure 125 An original DICOM image before the image processing.

5.9.1.2 Image Import and Scaling

Then, using Inventor software, these images are imported in a sketch, one per each file. The scaling is operated exploiting the reference scale to the side of each image. The scale is measured (usually 3.0 cm), so a 30 mm line is traced and then the image is scaled to permit the two extremities of the reference scale to coincide with the traced line edges.

Here there is the first uncertainty estimation related to the image quality. Every image has a limited quality related to the number of pixels, and every line has a second

uncertainty related to its thickness. Every pixel in all the images has a dimension about 0.08×0.05777 mm after scaling.

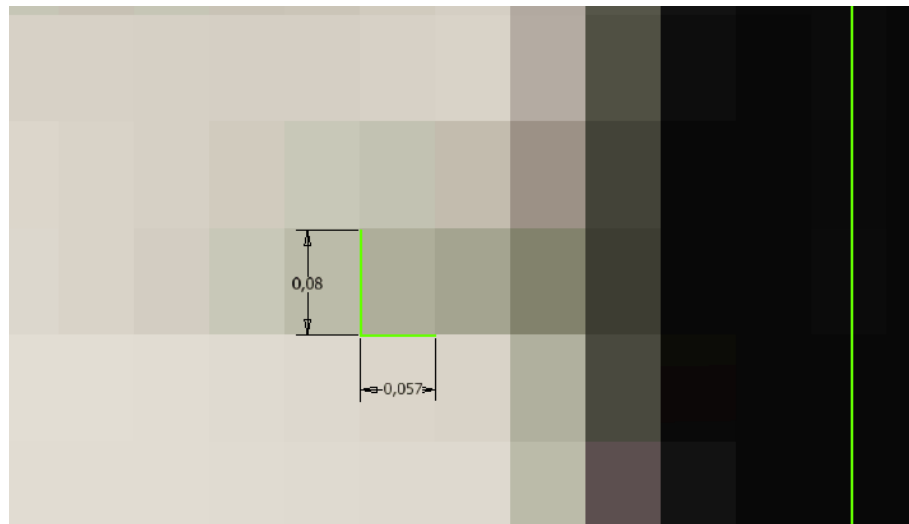


Figure 126 The CAD Pixel measurement after the proper image scaling.

The extreme reference marks have a height of 1 pixel but it is blurred, with two darker borders. So it has been decided to consider 3 pixels the possible clearance in which locate the reference mark, with the half middle pixel as the correspondent position of the real mark.

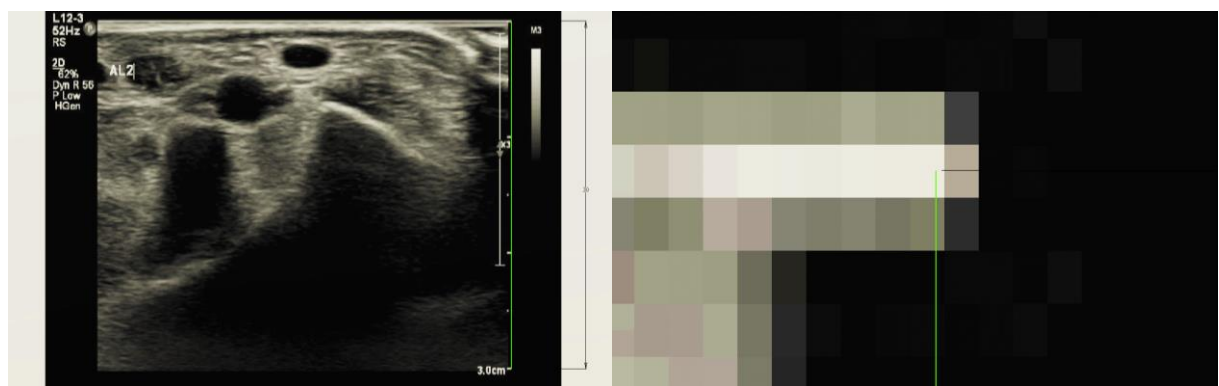


Figure 127 The CAD scaling procedure: exploiting of the scaled reference marks of the original image.

Therefore the uncertainty related to the scaling has been considered to be ± 1.5 pixels in height per each side of the line positioning, so in the end ± 3 pixels in total. This value converted in metric measures, provide an uncertainty of ± 0.24 mm in height and ± 0.171 mm in length (considering the image scaling proportions).

These results are considered remarkably consistent if reported on the entire image measure percentage, providing an uncertainty of the 0.8% and 0.38% respectively.

5.9.1.3 Points Import and Overlap

Then the Excel file with the vessel cross-sectional area are imported in the same sketch and, thanks to the Move command are placed in the correct position on the image. This could be possible thanks to the frame which goes with every cross sectional area processed.

Here the uncertainty is analysed in the same way, because of the blurred edges of the image box. The edge pixels are here only two, and the alignment is operated controlling only one corner of the image. Therefore, the relative uncertainty is only of ± 1 pixel, which corresponds to ± 0.08 mm in height and ± 0.057 mm in length, corresponding to a percent uncertainty respectively of 0.27% and 0.12%.



Figure 128 Example of a CAD scaled image overlap on the extracted edge points.

5.9.1.4 Spline Tracing

Then an interpolant spline is traced along all the cross-sectional area points to model the real vessel edge. The uncertainty of this operation is considered null because of the precision of the software in detecting automatically the exact position of every control point.

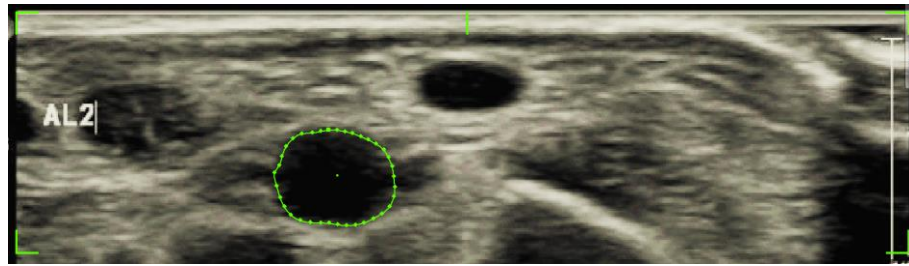


Figure 129 CAD Spline traced using the extracted edge points.

5.9.2 Edges Points Extraction Measured Errors

Not significant errors could be extracted in this phase of the Image Processing procedure, because of the intermediate role of the results obtained. However, the sum of the uncertainties which developed at this stage is considered in the final errors and uncertainty estimation of the Edges Points Generator program.

5.9.3 Edges Points Generator Measured Errors

Large errors in the procedure did not take place. However, evident discrepancies or doubts emerged in the final validation of the results.

The first type of error is related to the poor quality of one Ultrasound scan. In this image, the Image Processing program could not be undertaken because no information could be extracted or noticed even to eyesight. Consequently, the relative cross-sectional area of this step was omitted.

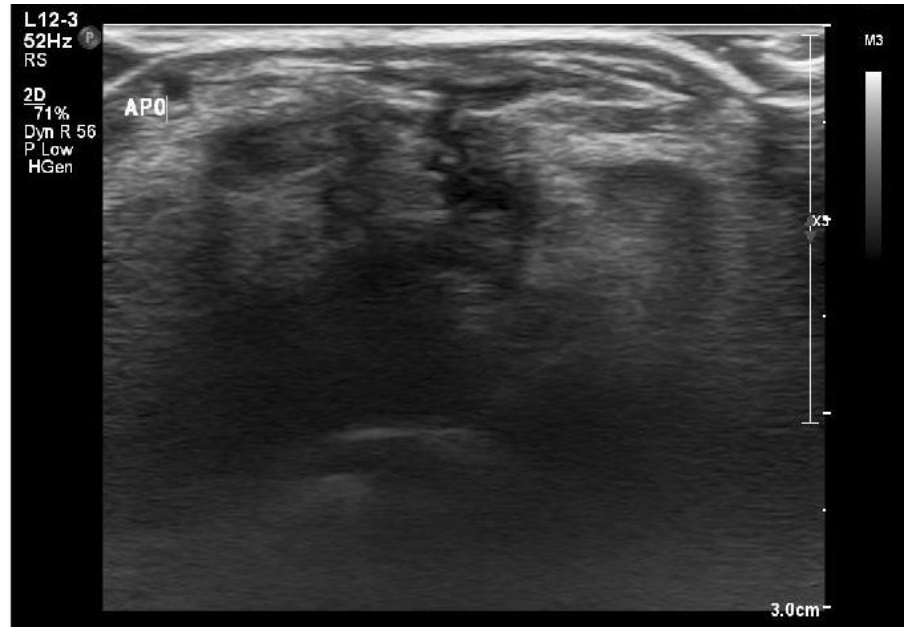


Figure 130 Example of a low-quality Ultrasound scan.

The second type of error encountered is relative the understanding of some Ultrasound artefacts in some images. Here there was some doubt on which would be the real cross-sectional area edge because different borders could be noted. If the inner border, the dark one, is surely part of the inner vessel, there are some doubts regarding the second one.

Asking for some advice to the hospital operators and surgeon, the choice has been to consider the vessel edge the external border present in the scan, being also careful to contrast un-physiological spikes and artefacts present in this occurrence.

The possible errors in these cases have been evaluated very high, of the order of 25% of the total vessel area. Fortunately, the occurrence of this problem was only of five cases on 40 scans.

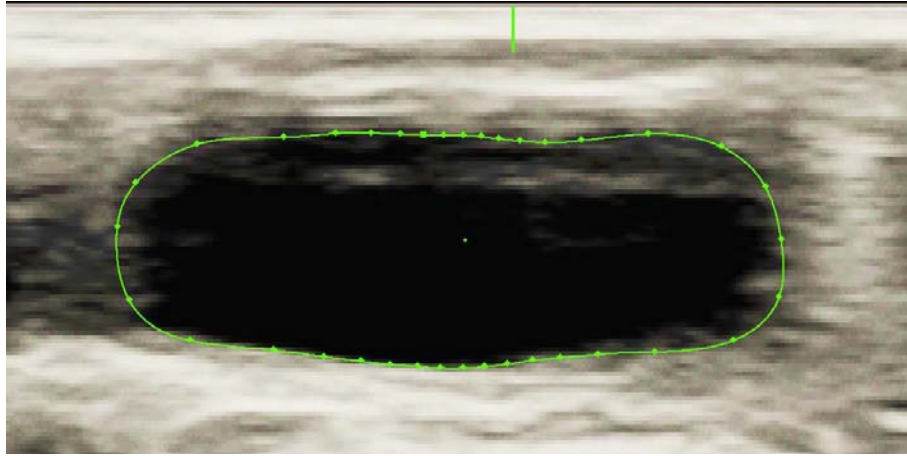


Figure 131 Example of an Ultrasound artefact causing a non-precise edge detection.

5.9.4 Velocity PulseWave Extractor Measured Errors

A similar procedure has been followed for determining the velocity uncertainty. Here however, considering the average between four different pulse waves, there is not a real comparison between the extracted pulsewave and the several real ones, because the first is a representative of an average behaviour of the blood velocity, the second ones are the real ones, each of them singular and different from the others.

For these reasons here, the uncertainty has been considered the sum of the previous uncertainties (max uncertainty 0.8%) with the percent deviation of the four real pulse waves analysed, which is 4.2%, for a total of 5% uncertainty. This value is precisely comparable with the error between the real velocity peaks of the pulse wave and the velocity peaks of the interpolated pulse wave.

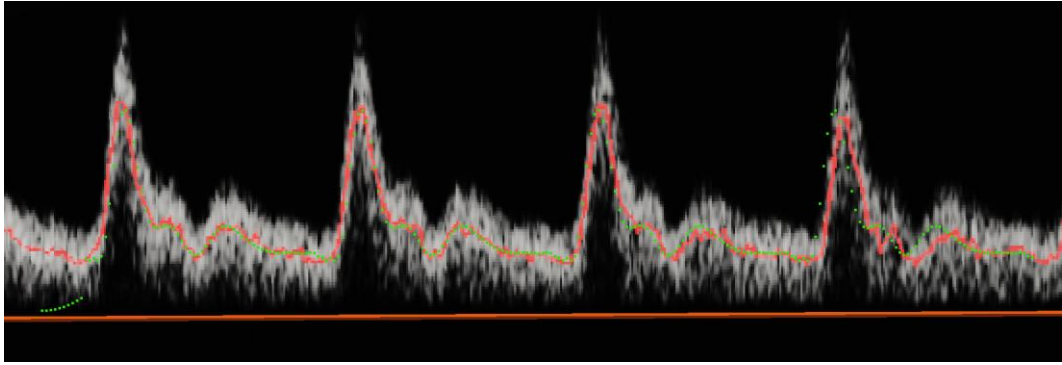


Figure 132 CAD assessment of the extracted velocity pulse wave points overlapped to the original image.

Previous Uncertainty %
0,80
Total Uncertainty %
4,99

Variability					
Variability	Deviation %	Avg. Deviation	Deviation	Avg. Peak	Real Peaks Vel.
4,19	1,40	2,22	0,74	53,02	53,76
	6,59		3,49		49,52
	1,80		0,95		52,06
	6,99		3,70		56,72

Errors				
Interp. Peak Vel.	Difference	Avg. Diff.	Err. %	Avg. Err. %
50,62	3,14	2,95	5,84	5,40
50,62	1,09		2,20	
50,62	1,45		2,78	
50,62	6,10		10,76	

Table 2 Analysis of Velocity peaks variability around the average value.

Due to the averaging of the pulse waves (in magnitude and time), a real error could not be evaluated if not considering the relative deviations. Instead of that, the uncertainty value was considered as leading reference as the accepted variability of the data used.

5.9.5 Errors Measurement

For what regards the cross sectional areas positioning and reconstruction, an error analysis have been possible comparing the results with the original images.

The scaled images are overlapped by the cross sectional areas points, which are positioned controlling the upper left corner of the image (the frame corner must coincide with the image corner). The cross sectional area is reconstructed with a spline through all the cross sectional areas points.

The errors measured are:

- Corner Frame Positioning Error: the error in the right corner frame points position compared to the original image
- Cross sectional area matching error: the error between the cross sectional area reconstructed border and the original cross sectional area of the image

For every image, the error was measured and plotted with the uncertainty (± 1.5 Pixels = ± 0.171 mm) evaluated before. Here the results:

- Corner Frame Positioning Error

The numbers of pixels gap between the image right border and the frame corner were measured in every image and then averaged.



Figure 133 Error related the image cropping during the image processing, scaling and positioning.

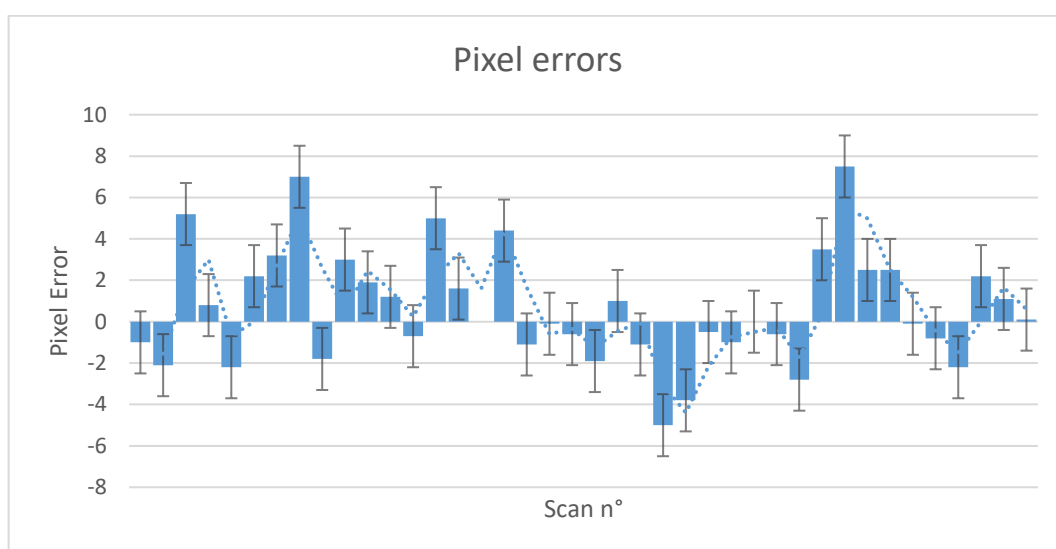


Figure 134 Corner frame position pixels errors for every image processed.

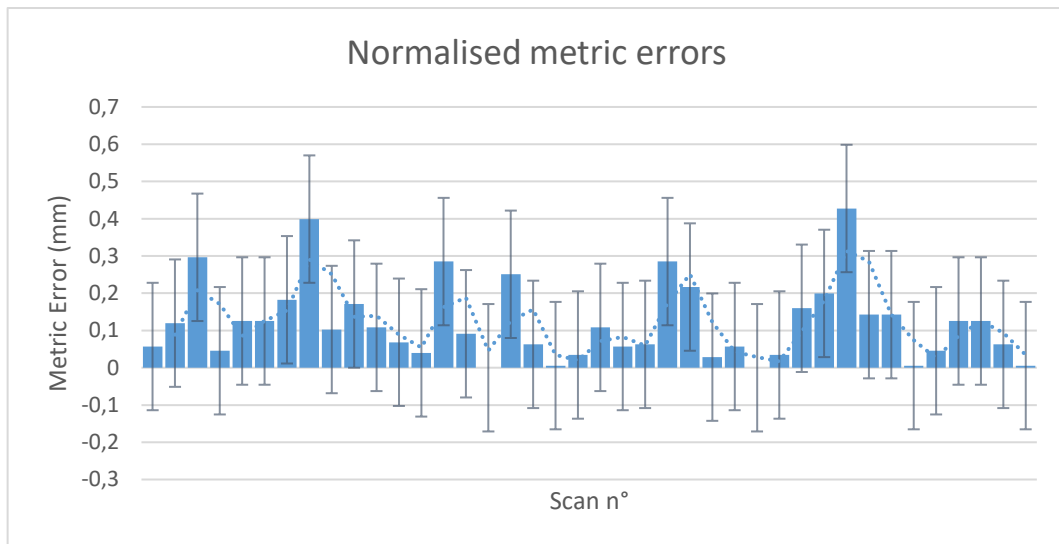


Figure 135 Corner frame position metric errors for every image processed.

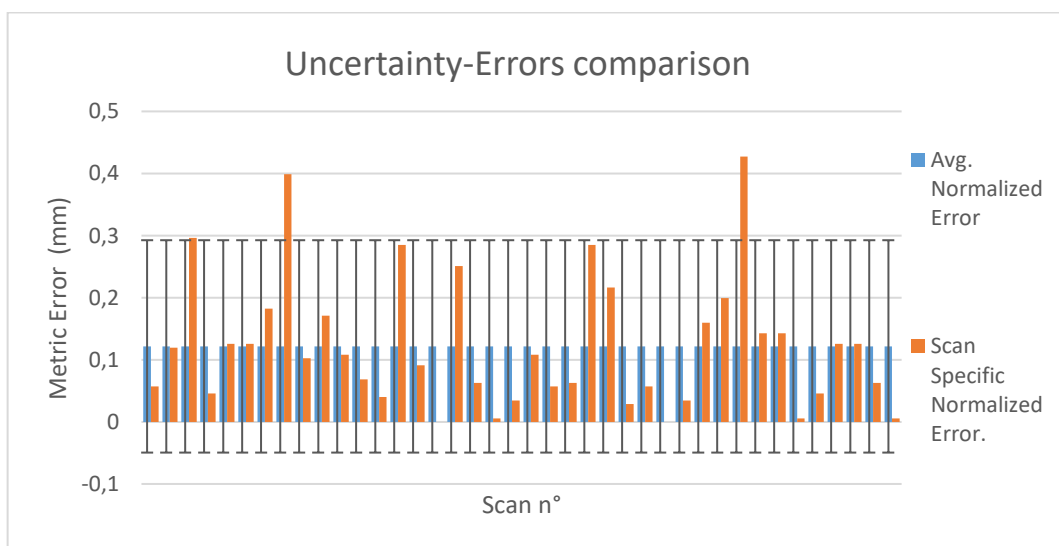


Figure 136 Comparison of the errors measured with the uncertainty evaluated.

The average error has been of 0.12 mm and the relative uncertainty has been of 0.171 mm, with an errors variance of only 0.01. Therefore, the measurements quality has been accurate enough.

- Cross sectional area matching error

At every reconstructed cross sectional area, a line trying to evaluate the discrepancy between the real image cross sectional area edge and the spline. Then this line was measured and averaged.

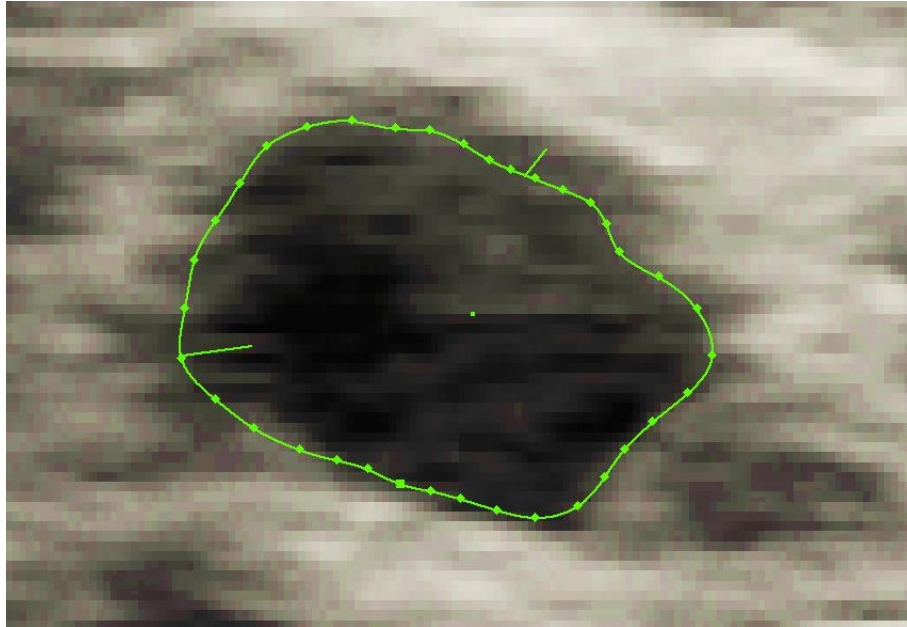


Figure 137 Measurement of the possible maximum error on a blurred vessel cross-sectional image.

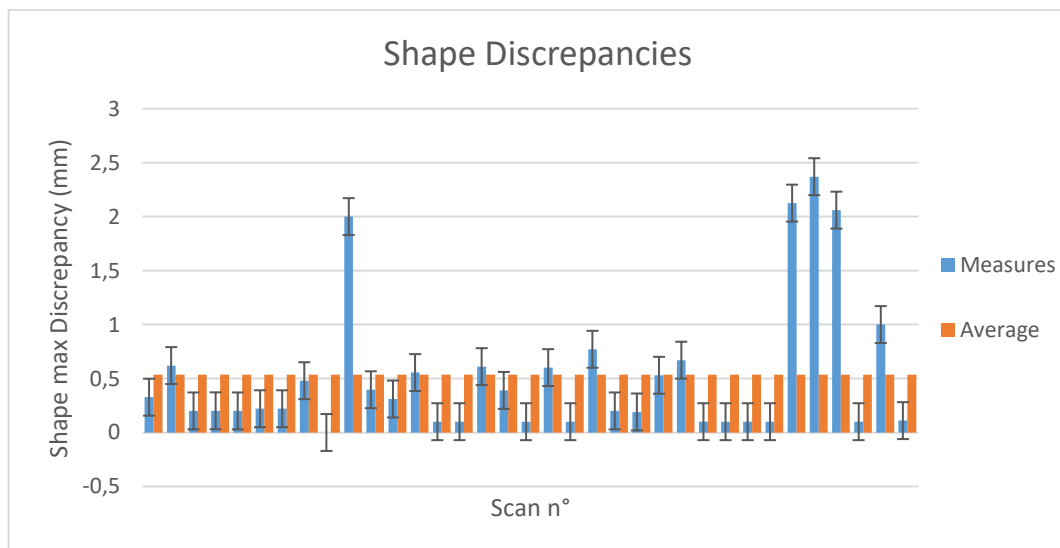
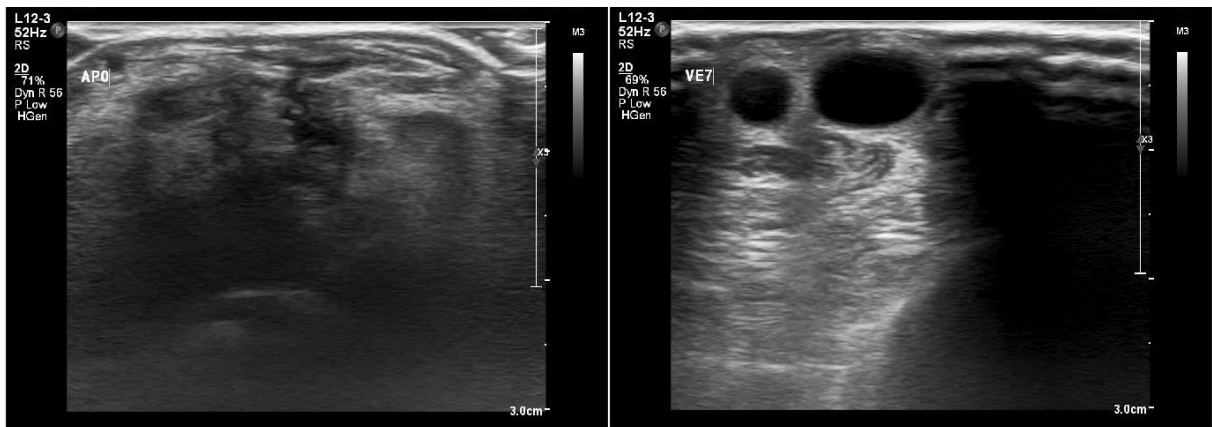


Figure 138 Maximum shape discrepancies measured for all the vessels images.

Here the errors measured are higher, about 0.5 mm average. Worth to note that not all the images suffered from this type of error (as the diagram shows only a few images suffered from a large error) and the ones which suffered the most were the scans with the poorer quality.

However, this strategy was established to considerate the worst-case scenario, taking into account the possible program and user incompetence in detecting the real vessels edges.

In this phase, Ultrasound Imaging scans artefacts and quality played a fundamental role in permitting the best results and the lowest incomprehension, as the two images below illustrate.



5.10 Other Programs

Throughout this work, many ways have been taken to achieve our various purposes. For this reason, many other algorithms have been developed, which have then been integrated into other programs/algorithms or discarded by preferring different solutions.

An example is the Panorama algorithm, to combine the different catches to get a whole route of ships along the area of interest. This program was thought at the beginning of studies when the idea was to undertake a preliminary 2D study of the pathway of the blood vessels. This methodology was designed to ensure continuity throughout the path, with the lack of overlaps due to the 3D development of the various vessels. This main limit has led to the discard of this program as it is incapable of being sufficiently robust in generating significant geometries.

A second developed algorithm is the creator of circumferential arcs. This program has been used to ensure continuity in cross-sectional areas profiles. The sub-program limits generic barycentre centred circumference arcs to the initial and final two points.

Another useful program developed is the “Synchro-times”, designed to synchronise the pulse waves between two different extremities of the blood vessels. Using Ultrasound information about the flow rate and the input speeds being output, known the cross-sectional areas of the inlet and Outlet, the velocity pulse waves and the flow rate, using the principle of mass conservation, it attempts to break off the input and output signals of the speeds to best suit this principle. This program was developed in the light of a validation of the numerical model with reference to the real model. The limits encountered are about the cross-sectional area measurements and the precision in detecting space and time of the flow rate and velocity.

A useful and important service program exploited all along the study has been the “DICOMRead” program. It simply opens the .dcm images stored in a user defined folder. It

helped to revise coding steps, check for results, or even to control Ultrasound scans, enabling a simple conversion through the useful “Save” function of the image window too.

An important and useful code was sketched regarding the determination of the relationship between velocity pulse wave and pressure pulse wave. At the basis of everything, there is the theory of lumped parameters exposed in Chapter 3, paragraph 3. The two, three and four elements Windkessel models were developed to determine the relationship between speed and pressure, referring to the work done by Stergiopoulos et Al. in this regard. (111) All this to achieve the best set up for the CFD simulation and especially for the FSI simulation. Due to the reduced information on the mechanical properties of the vessels, and a vascular recognition algorithm limited to contours and not to the thicknesses, physiological values derived from the literature have been set. It must be admitted that due to the limited time and focus mainly given to the CFD simulation, this program was not developed at best, but remains a good starting point for future developments and studies, especially with regard to FSI simulations.

Knowing the reference dimensions obtained from Ultrasound images, some additional simple programs have been implemented to measure the accuracy of the procedure. Various data has been saved and handed down through the various procedures to ensure this operation. Basically, what has been done has been to evaluate the average, error, and standard deviations between processed and converted MATLAB measurements compared to input values initially entered by the user. The results of these operations are discussed in the next chapter. Because of the possibility in analysing directly the results of the main programs, these codes were discarded, preferring a concrete comparison of the Image Processing results.

The most interesting codes related to the programmes of interest can be found in the Appendix.

6 3D MODELLING⁶

⁶ Eventual references on the chapter or paragraph titles are to be intended to be the main sources of the informations provided on that chapter or paragraph.

6.1 The Case

Modelling the vessels is the first main goal and result of the procedures exposed until now.

In this step, all the information collected by Imaging and Image Processing tools are collected and connected to obtain the final synthesis of the first part of the entire study.

The points that characterize the edges of the blood vessels, obtained after scanning the images, their filtering and analysis, are here placed in their reciprocal positions to recreate the actual pattern of blood vessels themselves.

This has been possible thanks to a reference applied to the patient arm and a precise protocol followed by the hospital operators. The relative position of vessels (and their path through the arm) is achievable thanks to the coordinates where the probe was placed at every scan, provided by the operator itself. Using a 3D template of the arm inspected, reporting to this the position of the grid placed on the real arm, the coordinates transfer has been possible. Repeating the positioning for each cross-sectional area, and then using the 3D tools of the CAD software to reconstruct the solid geometry basing on the path created, the final vessels model was made.

All these passages are very sensitive and it's important since all the mistakes and inconsistencies accumulated in the previous procedures, both in terms of data processing and in terms of the procedure itself, are gathered here and find in this a turning point for obtaining a reliable model.

6.2 Where to Start

From what has been reported at the end of Chapter 3 and in Chapter 4, the engineering issue is the establishment of a procedure reliable, accurate and robust to re-place all the cross-sectional areas collected in the exact relative position, one respect the others.

The starting point, following the protocol described at the end of Chapter 3, are the images collected from Ultrasound imaging and analysed by Matlab to extract the edges of the cross-sectional area. Besides the sole images collected, other information have been provided by the hospital operators inside the images themselves, and with additional documents (as the images of the arm scanned with the references agreed to be placed on patients arm).

Exploiting the additional information provided when the images were collected, and with the help of a CAD software, it was possible to succeed in the reconstruction of the vessels of interest.

6.3 Software

Computer Aided Design (CAD) software has been very helpful at the moment of the model building.

The CAD software choice has been made based on the University licenses availability and the needs of the modelling problem.

6.3.1 Autocad® (112)

AutoCAD® is a computer-aided design (CAD) program developed by U.S. based software company Autodesk and used for 2-D and 3-D design and drafting, and it was one of the first CAD programs for personal computers.



Figure 139 AutoCAD logo.

Today AutoCAD possess a high number of tools for modelling 2D and 3D structures, with numerous interfaces and customizations.

The software native format is DWG (drawing) and has become a standard for 2D drawings. The software supports also Design Web Format (DWF), a format developed by Autodesk for publishing CAD data.

Because of the software formats compatibility capabilities in a large number of different programs and applications, the simple structure of the software itself, and the capability to allow easy and fast drawings starting from scratch, this program has been chosen as support to the modelling operations.

AutoCAD was used to design the grid to be applied to the patients as a reference for the successive model building. The grid was necessary to have the possibility of patching a reference on different positions and different patients in an easy, removable, comfortable and cost effective way, not disturbing the patients and not to incur in several bioethics issues related to the patients care and their annoyance indeed.

For this advantages, and the software license availability, AutoCAD® has been chosen and exploited.

6.3.2 Inventor® (113)

Autodesk Inventor® too is developed by Autodesk and is a computer-aided design application for creating 3D models used in the design, visualization and simulation of products. At Inventor base, there is ShapeManager, Autodesk proprietary geometric modelling kernel.



Figure 140 Inventor logo.

This 3D mechanical solid modelling design software is used in designing 3D mechanical parts, tooling creation enabling users to visualise and simulate products before they are built. This software is provided with a lot of useful tools to test how the product will function in a real-world scenario, as integrated motion simulation and assembly stress analysis.

Autodesk Inventor specific file formats for parts is .ipt, for assemblies is .iam and for drawing views is .dwg, linking directly to AutoCAD.

Inventor provides furthermore, the possibility to export its models in assorted other formats, like IGES, STEP, STL, CATPart, etc.

Thanks to the versatility of this software, the direct compatibility with AutoCAD and the other software employed in this study (simulation software first of all), and the availability of the license for this, Autodesk Inventor has been chosen as a 3D modeller of this study.

6.4 Procedure

Here below is presented the procedure followed to make possible the vessels reconstruction.

6.4.1 The Grid

As illustrated in Chapter 4, to be able to reconstruct the entire vessels model in a precise way, a reference to the patient arm was needed.

This was used to help operators to correctly place the probe along the arm. Exploiting the grid edges and boxes, the probe is easily alignable step by step and, at the same time, it's easier to the operator to provide the exact position along the arm where the scan was taken.

In the same way, the grid resulted useful to help the designer to model the vessels geometry as well as possible, enabling to correctly set the position of the cross-sectional areas relative every scan.



A	1	2	3	4	5	6	7	8	9	10	11
B	1	2	3	4	5	6	7	8	9	10	11
C	1	2	3	4	5	6	7	8	9	10	11
D	1	2	3	4	5	6	7	8	9	10	11
E	1	2	3	4	5	6	7	8	9	10	11
F	1	2	3	4	5	6	7	8	9	10	11
G	1	2	3	4	5	6	7	8	9	10	11
H	1	2	3	4	5	6	7	8	9	10	11
I	1	2	3	4	5	6	7	8	9	10	11
J	1	2	3	4	5	6	7	8	9	10	11
K	1	2	3	4	5	6	7	8	9	10	11
L	1	2	3	4	5	6	7	8	9	10	11
M	1	2	3	4	5	6	7	8	9	10	11
N	1	2	3	4	5	6	7	8	9	10	11
O	1	2	3	4	5	6	7	8	9	10	11
P	1	2	3	4	5	6	7	8	9	10	11
Q	1	2	3	4	5	6	7	8	9	10	11
R	1	2	3	4	5	6	7	8	9	10	11
S	1	2	3	4	5	6	7	8	9	10	11
T	1	2	3	4	5	6	7	8	9	10	11

Figure 141 The grid designed and applied to the patient's forearm.

The grid is characterised by boxes of 1 x 1 cm in size, each containing a reference. The first column contains the alphabetical letters from A to T corresponding to the longitudinal position of the probe along the arm. In the other columns, the numbers 1 through 11 are repeated in each row, which indicates the transverse position of the probe across the arm.

6.4.2 The 3D Model

To create the geometrical 3D model of the vessels using Autodesk Inventor®, the aim is to place and align in the correct order and position every cross-sectional area extracted from the images, and use these as guidelines for the solid shaping. Here below there are the principal steps followed in the final procedure.

6.4.2.1 Import 3D Model of the Arm

A 3D arm template is imported inside Inventor. This template is the basis of all the procedure and acts as reference for the real arm.

The assumption here is that between this arm model and the real arm there are not as many differences. This is done because it is a difficult operation to accurately rebuild each single real arm of every patient, considering the privacy issues related to his annoyance.

So, for practical and privacy reasons a generalised arm template has been chosen as the best solution.

This model specifically had been found in “www.grabcad.com” and represent a reconstruction of a real man body in a mannequin, where only the left hand and forearm has been taken to limit computational costs to the sole area of interest. The physiological characteristics are relative to a 5th percentile adult man.

The original format of the model was STEP, so Inventor did not find any kind of issue to import and reconstruct all the features related to the original model.

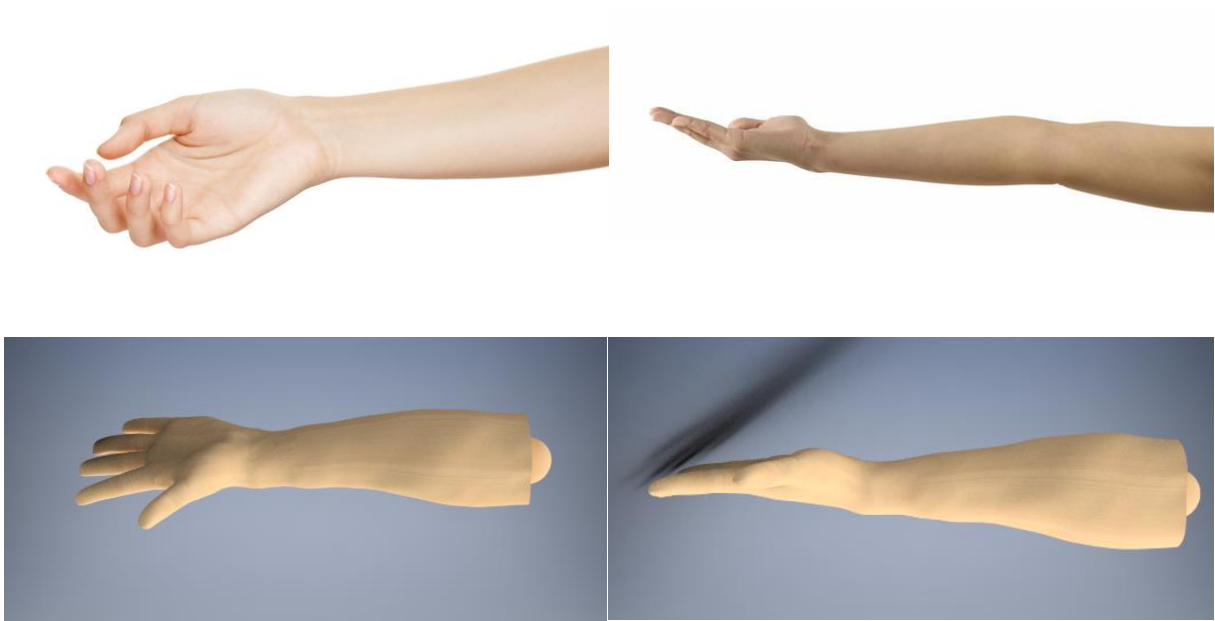


Figure 142 Image of a real forearm and the 3D model of this.

6.4.2.2 Import and Positioning of the Grid

Basing on the photo captured at the time of the Ultrasound scans, it is possible to determine where the grid has been positioned. Considering this photo, an initial sketch is created on a plane orientated so that the same perspective of the arm in the photo is achieved.

To determine the effectiveness of the positioning, the photo is imported and confronted respect the arm. To scale the photo a line 10 cm long has been created and overlapped to 10 grid boxes edges until they perfectly match.

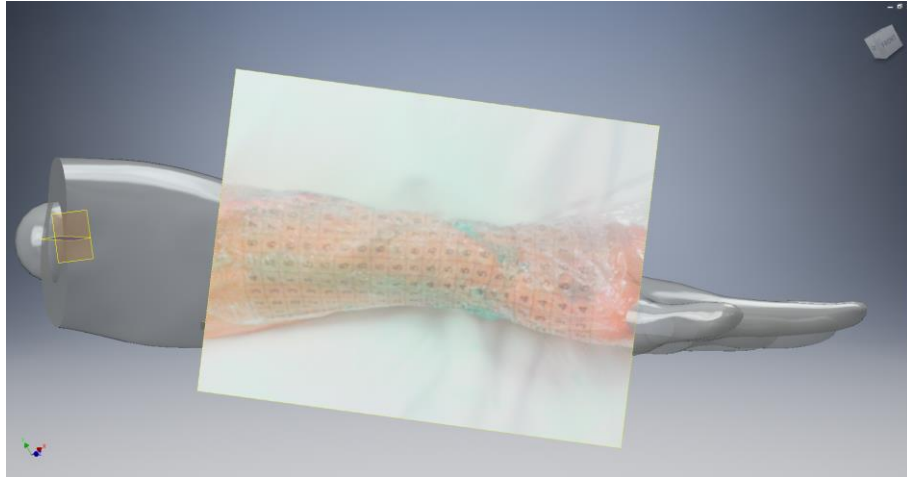


Figure 143 Patient's forearm photo overlapped to the 3Darm.

A sketch surrounding the area of the arm, where the real grid was placed on the real arm, is created. The sketch plane is an offset of the previous one.

Then the .dwg of the grid is imported. Worth to note is that numbers and letters are here no more needed or useful, but they were kept to have some reference. Thereafter the lines have been changed in format to contrast the better. Even the grid placement has been done confronting the photo with the grid sketch. It has been helpful the projection of the latter on the photo itself, exploiting the Move and Rotate affine transformations.

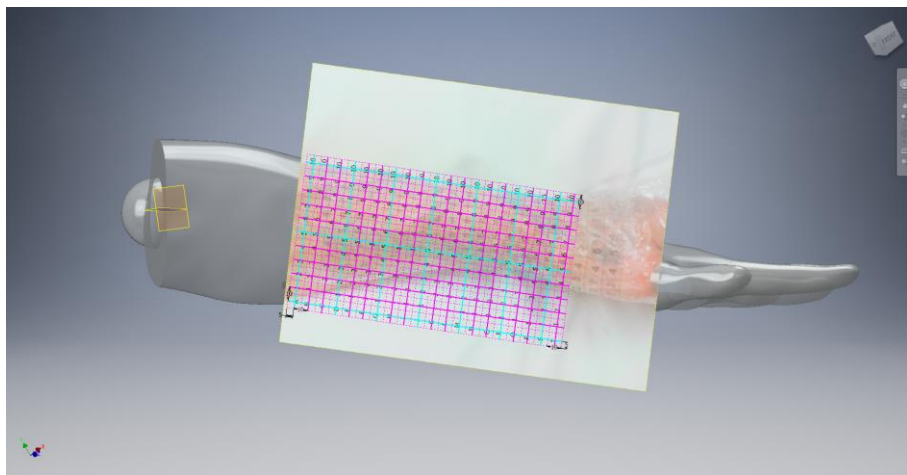


Figure 144 The grid designed on the overlapped image of the patient's forearm.

6.4.2.3 Grid Wrapping - Detection of Reference Points - Creation of Reference Planes

After that, a 3D sketch is set: in this, the entire grid has been projected to the arm with the command Project to Surface, making possible to have the exact reference on the arm surface.

Basing on the information provided by the operators in the scans, every scan location has been tracked down on the projected grid. This could be possible thanks to the coordinates system. At every coordinate intersection, a reference point has been created on the arm surface.

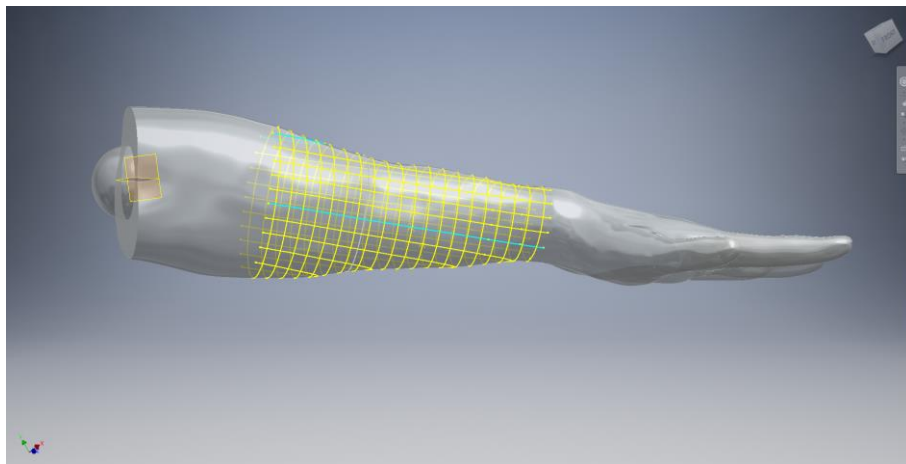


Figure 145 The grid projected on the 3D model of the forearm.



Figure 146 Example of an ultrasound scan, with the labelling providing the location of the scan.

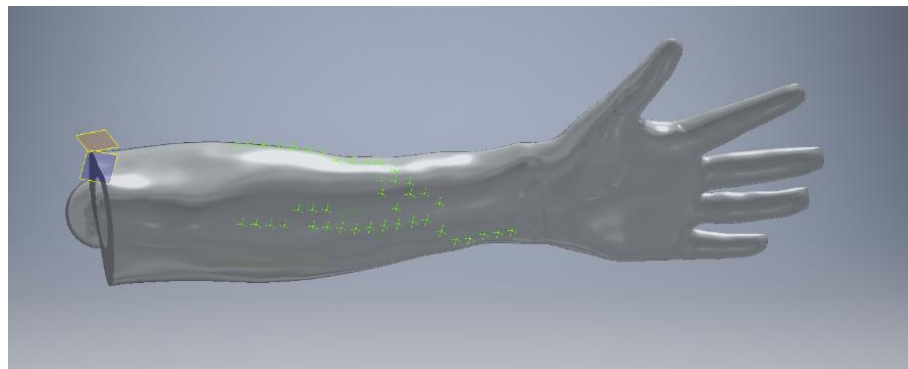


Figure 147 The 3D model traced-back scanning locations.

Exploiting this reference points on the arm surface, cross-sectional planes have been generated perpendicular to the surface. This will be the plane in which the correspondent vessel cross-sectional area will be imported.

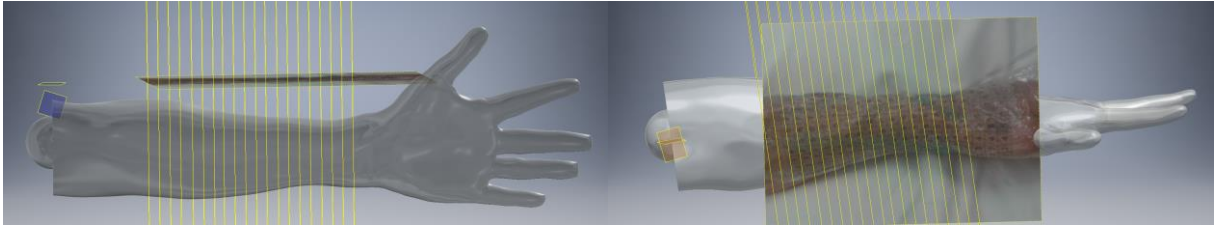


Figure 148 The sketch planes relative to the different scans.

This operation has been repeated for every coordinate, correspondent to every scan done, for both the vein and the artery.

6.4.2.4 Import of Cross-Sectional Areas Edge Points, Positioning and Aligning

In every plane, the relative cross-sectional edges points, gathered by the MATLAB processing in an Excel file, are imported through the Point Import command. These are collected in the single Excel file already ordered in sequence sheet by sheet.

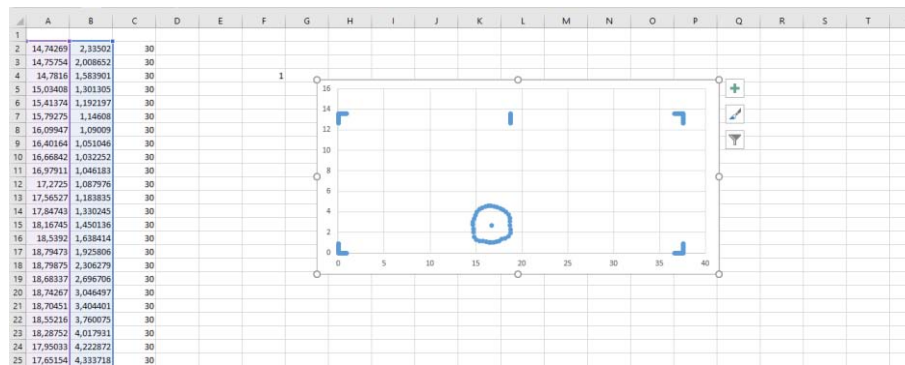


Figure 149 The cross-sectional area points provided by the MATLAB procedure.

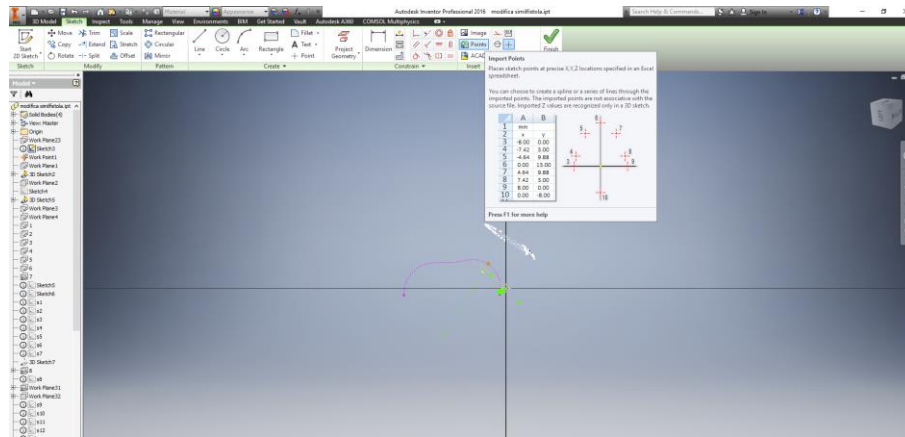


Figure 150 Importing the points coordinates of the cross-sectional area.

After being imported, every set of points is not positioned in the right place. However, thanks to the frame generated by the MATLAB code it is easier to align the contour points through the Rotate and Move affine transformations: the superior frame edge is rotated to be tangent to the arm surface, and the middle column of points has been set coincident with the reference point on the arm surface.

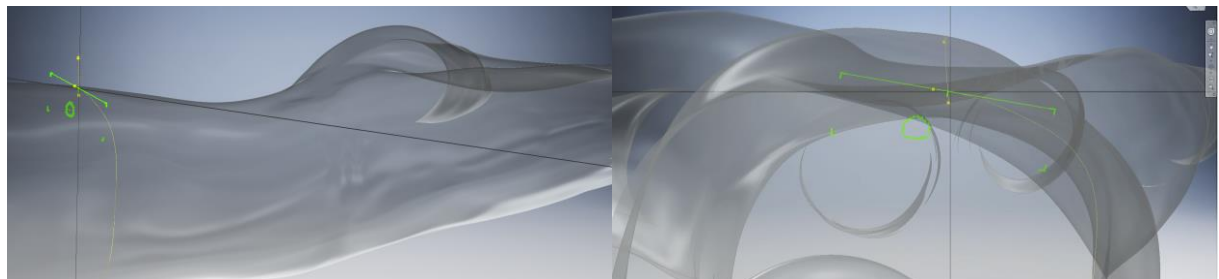


Figure 151 A single cross-sectional area placed in its final position and orientation.

The procedure is repeated for every work plane, correspondent to every cross-sectional area captured, for both the vein and the artery.

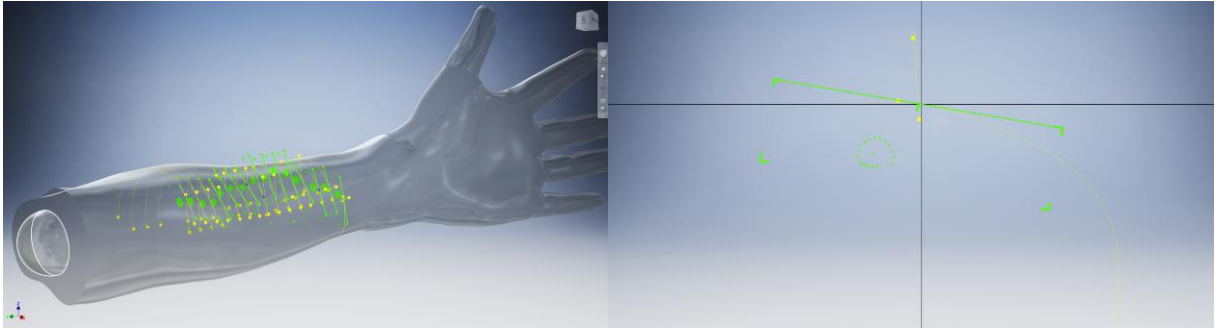


Figure 152 Complete placing of the several cross-sectional areas for one vessel.

6.4.2.5 Cross-Sectional Area Reconstruction

After importing each cross-sectional area points data set, and after having aligned them in the right position, the real cross-sectional area edges have to be re-created.

To do that the tool used in every sketch is the spline command. With this command, a NURBS curve is created selecting all the sampled points which form the edges. Point by point a closed curve is generated.

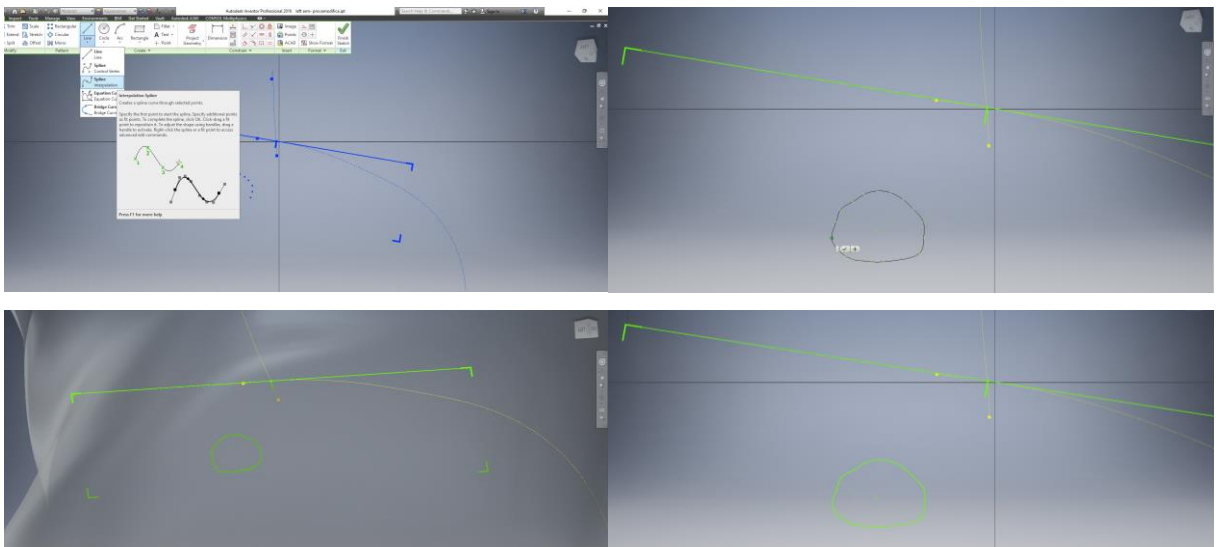


Figure 153 Reconstruction of the cross-sectional area edge through a Spline curve.

6.4.2.5.1 The NURBS Tool⁽¹¹⁴⁾

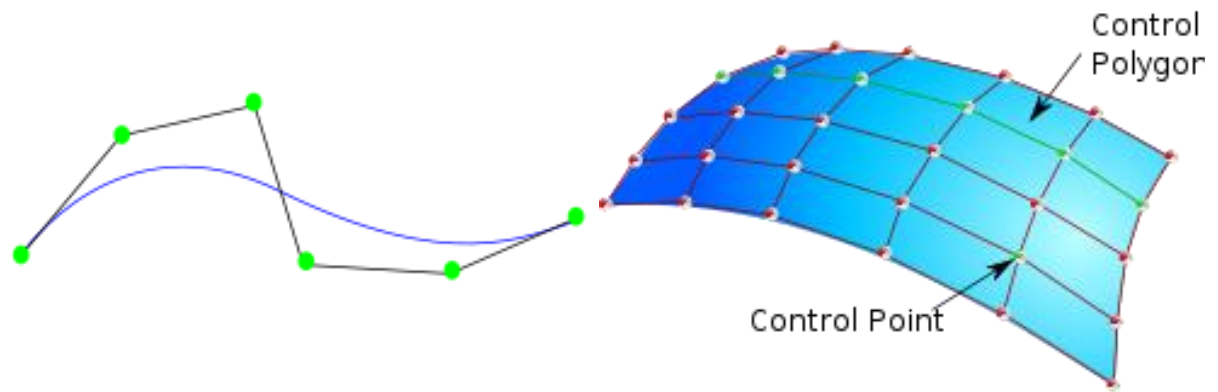


Figure 154 A NURBS curve and surface. (114)

To generate the best objective-matching and adjustable curves, Non-Uniform Rational Basis Spline (NURBS) mathematical model is adopted. NURBS offers great flexibility and precision for handling both analytic and modelled shapes.

NURBS curves and surfaces are useful for a number of reasons:

- They are invariant under affine transformations: rotations and translations can be applied
- They have one common mathematical form for both standard analytical shapes and free-form shapes
- They enable the flexibility to design a large variety of shapes
- They reduce the memory consumption when storing shapes
- They can be evaluated reasonably quickly by numerically stable and accurate algorithms

A NURBS curve is defined by its order, a set of weighted control points, and a knot vector.

The control points are the ones which primarily determine the shape of the curves, being each point of the curve computed by taking a weighted sum of a number of control points. Based on the respective governing parameter, these weights can vary. At the

boundaries, the controlling functions go smoothly to zero, directly depending on the degree of the polynomial.

The fact that every control point influences only restricted intervals, a property called “local support”, is a highly desirable property, allowing the changing of one model part not affecting the entire geometry. Adding more control points a better approximation to a given curve is achievable.

Moreover, NURBS curves also feature a scalar weight for each control point, providing more control over the shape of the curve without unduly raising the number of control points.

The knot vector is a sequence of parameter values that determines where and how the control points affect the NURBS curve. The number of knots is always equal to the number of control points plus curve degree plus one. The knot vector divides the parametric space into the intervals mentioned before, called “knot spans”. Each time the parameter value enters a new knot span, a new control point becomes active, while an old control point is discarded.

Knot vector has an impact on continuity of the resulting curve or its higher derivatives, allowing the creation of corners in an otherwise smooth NURBS curve. Many modelling applications do not make the knots editable or even visible, but more recent versions of NURBS software allow for interactive editing of knot positions.

In the end, the order of a NURBS curve defines the number of nearby control points that influence any given point on the curve. The curve is represented mathematically by a polynomial of degree one less than the order of the curve, with the number of control points greater than or equal to the order of the curve. In practice, cubic curves are the ones most commonly used. Usually, curves of orders higher than fifth are practically never used because of their large calculation times.

The use of spline has been judged a good solution, because keeping hold the control points, allows creating a continuous closed curve with the lowest error in curvature and shape between the two subsequent points.

6.4.2.5.2 Procedure

After selecting the Spline “Interpolation” command, all the edge points describing the cross-sectional area are neatly selected, until returning to the first. Re-selecting the latter, a closed curve is generated, which is the final result of this procedure step.

6.4.2.6 Reconstruction of the solid vessel

Once all the cross-sectional edges curves have been created, it is the time to build the model of the vessel to which every cross-sectional area refers.

To do that, the LOFT tool is exploited.

6.4.2.6.1 The LOFT Tool⁽¹¹⁵⁾

LOFT is the command used to blend multiple profiles or sections and convert them into smooth shapes, creating a 3D solid or surface in the space using several cross sections. A large amount of objects, sub-objects and features are available and editable and with LOFT command.

Using the specific “Curves tab” dialog box it is possible to choose the elements to include in the blend, which can be sketches, edges, or points.

The boundary conditions for end sections and rails are defined and set in the Conditions tab to control the shape of the loft body near its boundary.

To define how different sections are merged together, controlling mapping points, rails, centrelines, and section vertices a Transition tab shows all the adjustable parameters.

LOFT tool is useful to:

- Create a solid feature or new body.
- Generate the shapes, surface models, and then converting them to solid
- Create surfaces and use them to create different shapes, or modify the models

Any number of sections can be added to the Loft dialog box to generate the final shape, after the minimum two required for the basic shape. Then, it is possible to control the resulting profile controlling weights of the sections or adding a rail or a centreline.

For beginning and ending sections, nonplanar or planar faces can be selected to control the 3D model ends. Tangential continuity (G1) or curvature continuity (G2) to adjacent part faces are the most used features.

With the Conditions tab, it is possible to set every boundary condition, controlling the shape and tangency of the loft surface, with the ability to adjust the transition angles (the default is 90 degrees) and the weights of every cross section. An example of the results is provided just below.

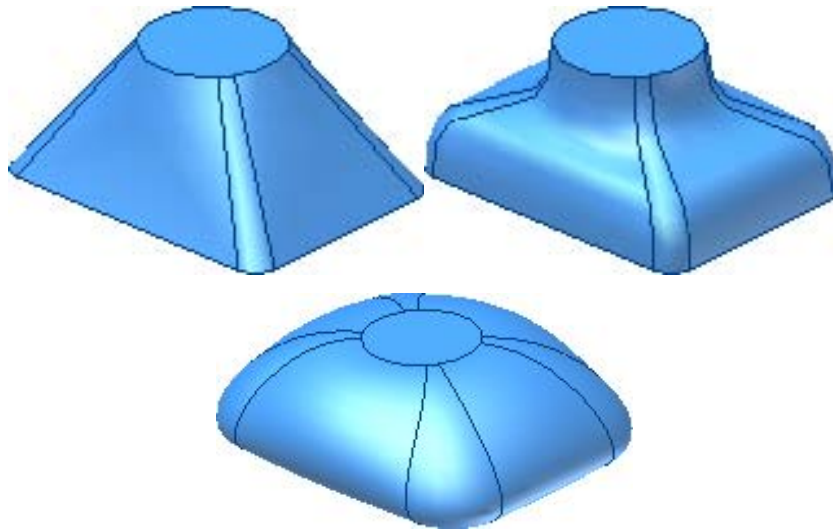


Figure 155 Different weights and transition angles results: 1) No angle or weight factor applied; 2) Both sections with weight factor 10, and a transition angle of 90 degrees; 3) Both sections with weight factor 10, and 180 degrees transition angle. (115)

Rails are 2D or 3D curves used to specify the loft development between sections. Every Rail must intersect each section and must terminate on or beyond the first and last sections to be effective and accepted. However, extending a rail beyond a section is useful to obtain a smooth shape. Rails must be tangent continuous.

It is possible to add different rails to better control the final shape of the entire model.

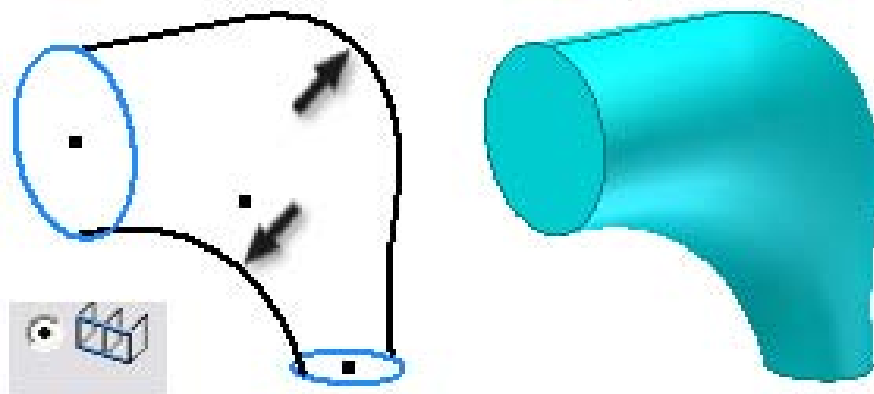


Figure 156 Loft Rails and final result. (115)

A centreline then, is a particular type of rail to which every loft section is considered normal. This causes resulting models similar to those of a sweep path, maintaining a more consistent transition between the cross-sectional areas selected. Centrelines follow the same rules as rails, but they do not need to intersect every section, and only one of them can be added to a Loft part.

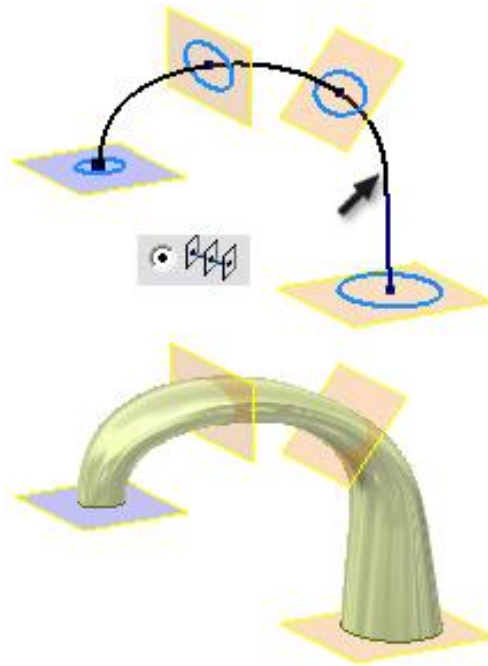


Figure 157 Loft Centreline and the final result. (115)

6.4.2.6.2 Procedure

The procedure followed is:

- 1) Loft command is selected
- 2) On the Curves tab of the Loft dialog box, in sequence, the sections to blend are selected
- 3) Specifying the Solid Output type, a solid feature is created from an open or closed section
- 4) Specifying the Operation:
 - “New Solid”, for the first vessel, the first solid body is created. Each body is an independent collection of features, separate from other bodies. This body can share features with other bodies.
 - “Join”, for the second vessel, the volume created by the lofted feature (first vessel) to another feature or body is added.
- 5) Boundary conditions for sections and rails are selected from the list, specifying angles and weights

At the end, the resulting 3D model is described by the images below.

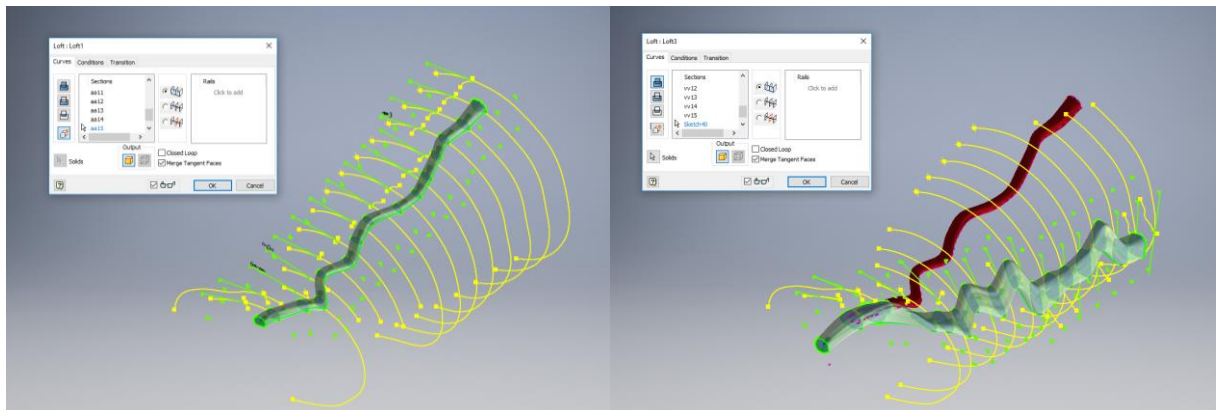


Figure 158 The first vessel lofted (left); the final vessel lofted, joined to the previous(right).

The arm is now showed to give the perception of the relative position of the two vessels respect to the arm and respect to themselves.

A limited part of the vein can be seen sticking out the arm surface, this is motivated by the local curvature of the arm in that position, and by the fact that the AVF itself protrude by the normal arm shape.

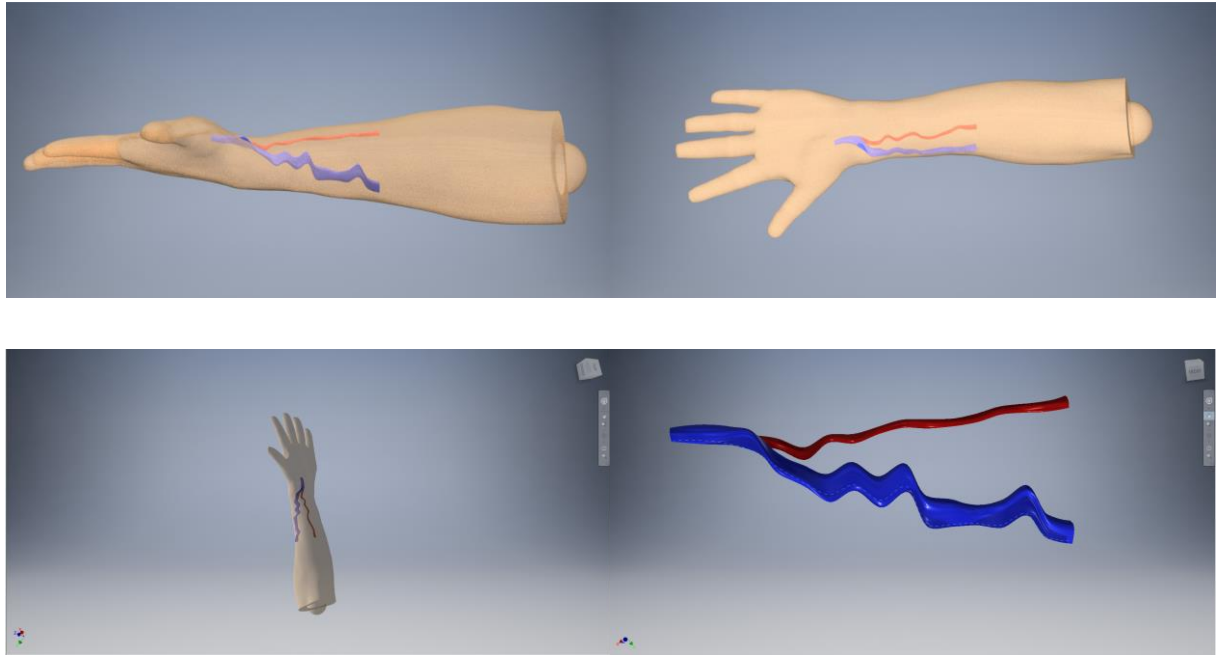


Figure 159 Several rendered views of the 3D modelling results.

6.4.2.7 Exporting to *.Stp File

The final step of the procedure is to save the model created and to export a STEP copy containing only the vessels model. This model will be the one imported into the CFD software to operate all the fluid dynamics studies.

To do that, first of all, the solid model of the arm is suppressed, because not relevant and annoying for the next steps.

Then, from the Inventor main bar, it is selected “Save as” -> “Save a copy as”, and then the STEP format is selected from the formats list.

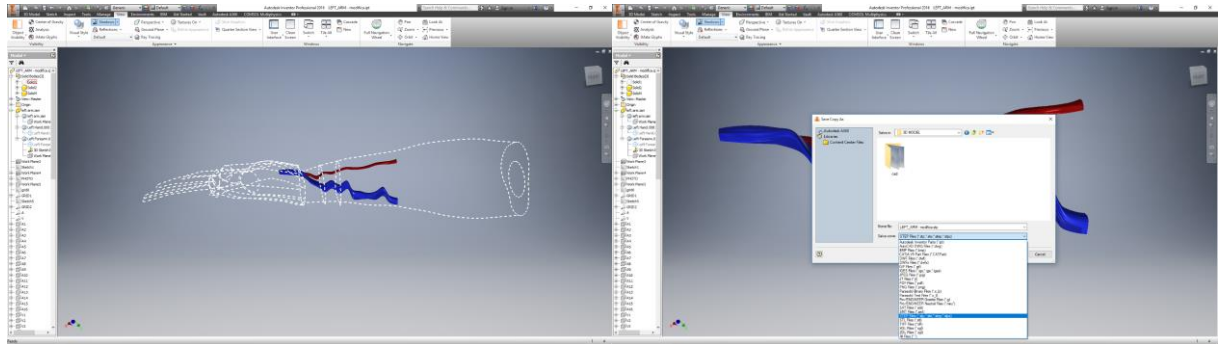


Figure 160 Exporting of the final AVF 3D model.

6.5 Precedents and Possibilities

6.5.1 First Models

The first attempts done to achieve the models desired led to the obtainment of several side models and information. Considering the process and development that led to the imaging, image processing and 3D modelling, different request and procedures have been followed.

From all these data, several models have been obtained which allowed understanding limitations, developing further the procedure, and operating first subsequent simulations.

For example, starting with the idea of obtaining a continuous path for the entire vessels layout, with help of the Panorama code developed in MATLAB to merge the different scans, an early model of one vessel could be built.

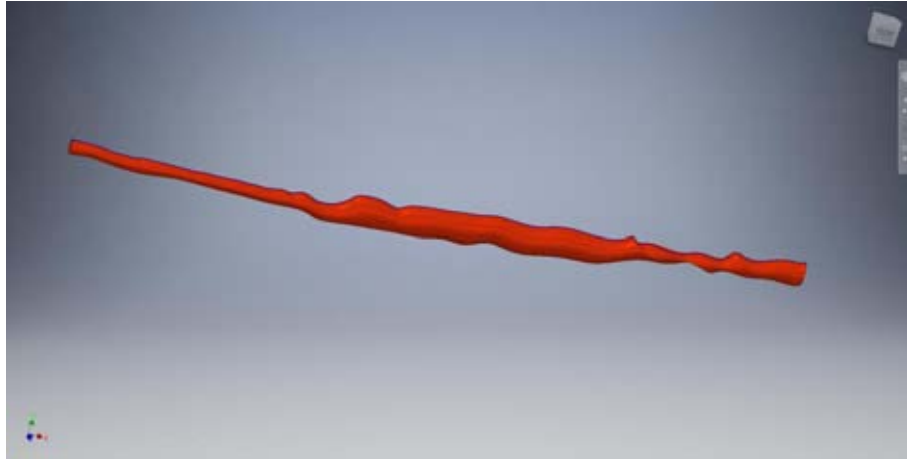


Figure 161 First 3D model of a vein exploiting a longitudinal set of points and the "Rail" feature of the Loft command.

6.5.2 First Real Vessels Procedure

Successively, after new strategies been tested, a complete model of both vein and artery in the area of interest have been possible to build. In this, the procedure was a raw basis of what has been obtained at the end, there was not a grid but a photo of the path followed by the probe and marked with a marker pen.

At this stage, the scans were not operated on a real patient but instead to a voluntary nurse to overcome privacy and bioethical issues.

What it was obtained is a good basic model of the two separated vessels, with some uncertainties about the cross-sectional areas positioning due to the not refined procedure.

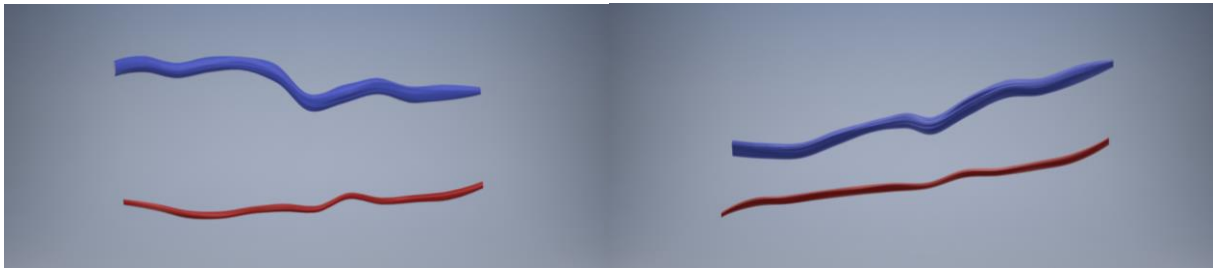


Figure 162 3D model of the two separated vessels exploiting the first raw procedure.

6.5.3 A Virtual Model of AVF Based on Separated Vessels

What is interesting is that this procedure allowed to virtually simulate a fistula establishment starting by vessels data just before the operation. This could help to have an idea of the possible resultant blood flow, besides helping to understand which technique and configuration could be more effective and promising.

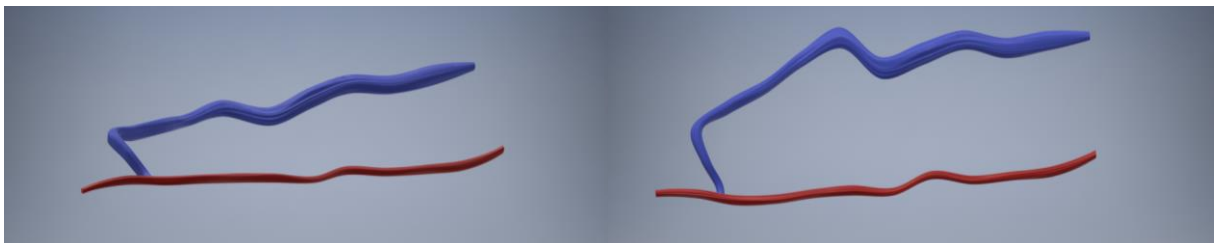


Figure 163 Virtual reconstruction of an AVF 3D model starting from the two separated vessels model.

To do that, the last cross-sectional areas of the vein was accurately moved, and their relative planes were rotated, enough to reach the artery and connect to it. The curvature control of this final part has been possible by a transversal 3D sketch where a 3D spline was built. This curve was designed to mimic in the best way some AVF already established, which form was discussed together with the reference surgeon, to have the complete idea

about the main peculiarities and most important features and shape a good AVF has to comply with.

The results are visible below.

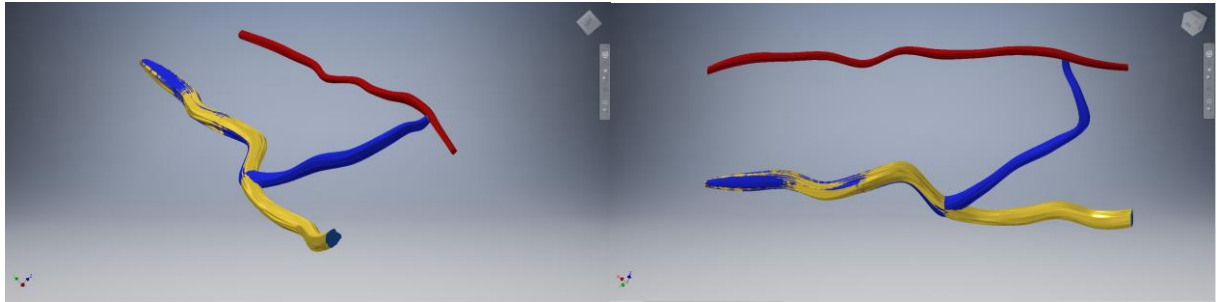


Figure 164 Comparison between the original model of the two separated vessels and the virtual reconstruction of the AVF.

The strategy followed in this modelling, using the vessels cross-sectional areas and relative positions as starting point and then, moving and rotating cross-sectional areas following the angle of incidence which is intended to be studied in a particular configuration, is a very interesting starting point in the study of AVF success prediction and optimization.

The capabilities and results of this procedure, however, are not the main subject of this study although some simulations were operated to investigate the first results achievable.

6.5.4 An Additional Step: Inlets/Outlets Extensions

Regarding the virtual model, another step has been programmed and tested, in order to evaluate the effectiveness of entrance length.

In this step, every inlet/outlet cross-sectional area was extended of 10 cm to avoid entrance/ exit lengths issues of the fluid numerical model. The command used was Extrude, and the cross-sectional area selected was the face already existing of the real inlet/outlet.

Then, as the previous model, a STEP file was exported and simulated.

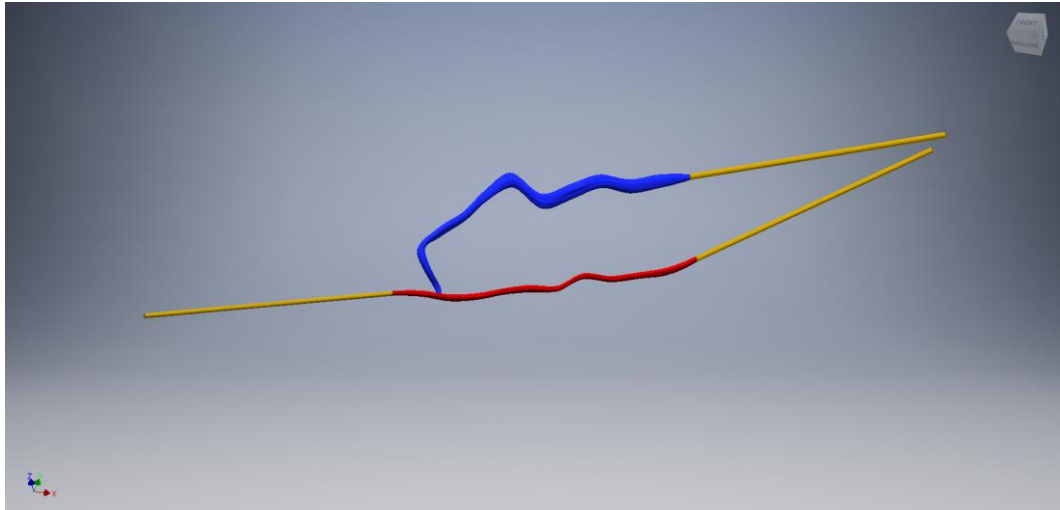


Figure 165 3D model of the inlet/outlet extended AVF.

6.6 Uncertainties and Errors

Errors evaluation in the AVF modelling is quite difficult to achieve without the availability of an MRA 3D scan of the real ArterioVenous Fistula. This is the main limitation of the procedure suggested.

The aim, after establishing this procedure and once well set in, was to compare the 3D models results with their correspondent MRA 3D scans in a number of 3 at least. The intention was to overlap the two different models, the real one and the reconstructed one,

to evaluate the discrepancies between the two. The best way to do that was again through CAD software. This because, thanks to the tools available, it is possible to intersect the two models, being able to evaluate the volumetric difference between the two. Moreover, it is also possible to see where and how there are the major errors, and measure them in terms of distance between surfaces or points.

However, unfortunately, this was not possible to date lacking in this 3D MRA scans.

The only evaluations possible for errors evaluation in this situation are the one relative to uncertainties of measures and procedure, in addition to what already said about errors in cross-sectional areas extraction from imaging in Chapter 5.

Considering the final procedure and model, here there is the uncertainties evaluation on the final model.

6.6.1 Template Arm

Considering the arm template model, it is representing the 5th percentile adult man.

This because generally design limits are based on a range of the user population from the 5th percentile values for critical body dimensions, as an appropriate reference. The use of this range will theoretically provide coverage for 90% of the user population for that dimension.

Respect to this assumption, the main forearm characteristics for a 5th percentile man have been obtained from NASA website, in the Man-systems integration standards topic. (116)

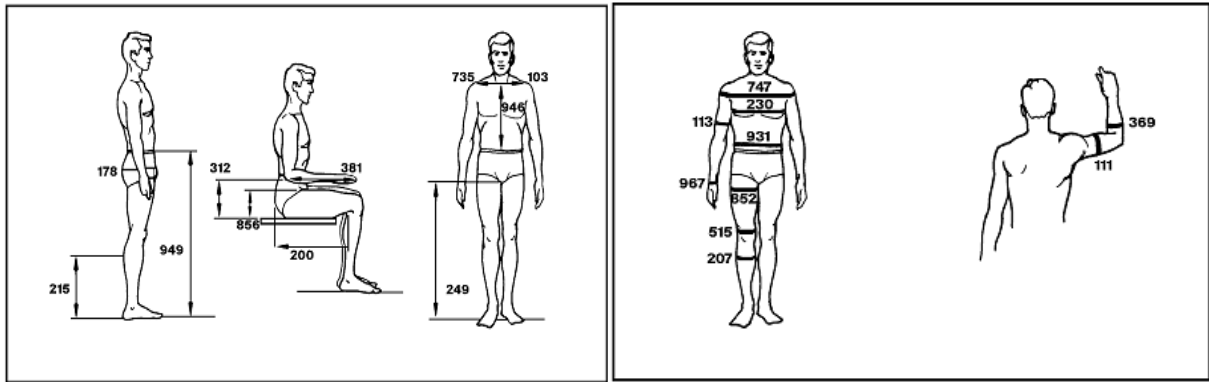


Figure 166 Body Size of the 40-Year-Old American Male for Year 2000 in One Gravity Conditions. (116)

381→ Forearm hand length - 49.5 cm (19.5")

369→ Forearm circumference, relaxed-32.7 cm (12.9")

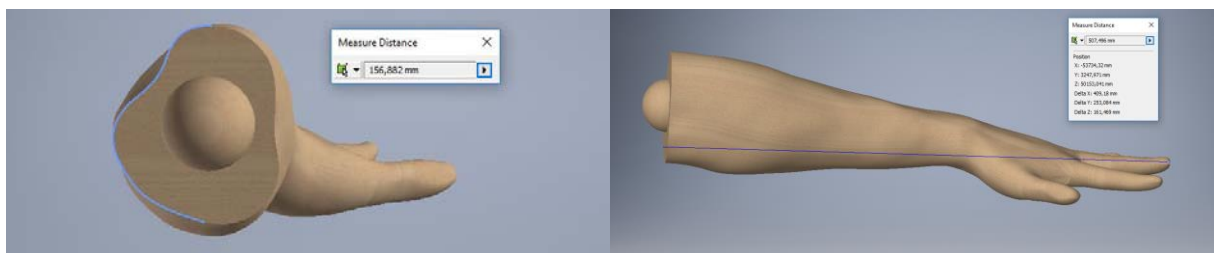


Figure 167 3D model of the forearm correspondent measures.

The difference of the model used and the data from NASA is about the 2,4% in length and 4,5% in the circumference and this is considered the uncertainty on the arm model.

6.6.2 Probe Positioning on the Real Grid

At the very moment of the scanning, there is an inevitable error in the probe positioning on the grid.

To estimate the positioning uncertainty there have been considered three main factors: the probe and grid relative dimensions, the parallax error, the probe slip occurrence during scanning.



Figure 168 The ultrasound linear probe used for the scanning.

The dimensions of the probe used by the hospital are 5x1 cm and the dimension of every grid box are 1x1 cm. When the operator is scanning, the grid is covered by the probe, not being easily visible because of the probe encumbrance. For this reason, it has been considered an uncertainty on the lateral positioning of the probe of half a box. Being the probe 5 cm long, the error is about $0.5/5=10\%$ in lateral positioning. Longitudinal positioning has been considered less affected by this problem due to the comparable dimension of the probe and grid, and the fact that the entire probe length could be a better reference for the good positioning of the latter.

Because of the gel used in the scans then, the probability of the probe slipping while scanning is remarkable. This kind of uncertainty is hardly estimable and, for its characteristics, it has been considered absorbed by the first type of uncertainty.

Because of all these causes, it has been assumed that the error related to the probe positioning and coordinates reading is between 10% and 15% (estimated).

6.6.3 Grid Re-Positioning on the Template Arm

The problem encountered during the virtual grid wrapping is that there have not been possible a precise wrapping and, instead of that, a grid projection has been operated. Because of that, some boxes projected on the arm have been deformed, losing part of their precision.

Helpful it has been the correct grid sketch plane positioning because, thanks of that, the area of the arm exactly parallel to this plane did not suffer from grid distortion.

Considering the coordinate (probe position) with the more arm curvature and farther from the parallel area, the grid dimension has been measured.

The mean longitudinal dimension was of 10,05 mm and the maximum was of 10,118 mm. The longitudinal average error is about 0.5% and the maximum is 1.9%.

The mean lateral dimension was of 10,75 mm and the maximum was of 13.21 mm. The longitudinal average error is about 7.5% and the maximum is 32%. Here important is also the mode, which is 10.4 and its related error is 4%. This can be interpreted saying that there are some spots with big errors, but generally it is limited below the 10%.

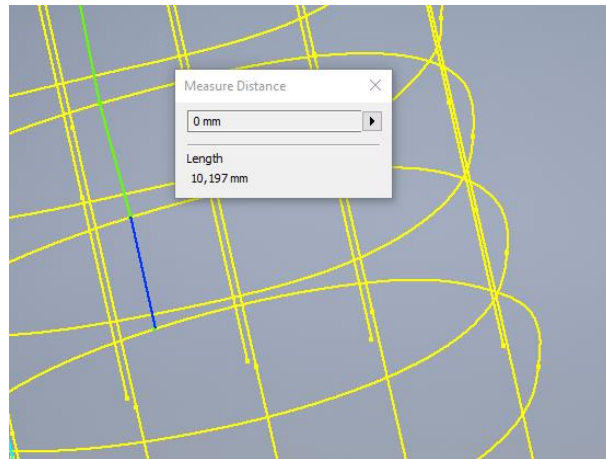


Figure 169 Measuring one side of the projected Grid box.

6.6.4 Cross-Sectional Alignment and Positioning

The error related to the cross sectional alignment and positioning is related to the accuracy the points can be located in the precise position described by the coordinated. The CAD software at this respect is very useful and precise, so the only error that here can be done/evaluated is about the rigidity of the arm model.

This is because, how described in the procedure, the cross-sectional area upper frame border is set to be tangent the arm surface, representing the part of the arm in contact with the probe. In reality, the arm tissues are distensible, so placing the probe, there is full contact. This is not possible with the rigid model of the arm, generating some errors related to the local curvature of the arm. These errors have been estimated to be less important and approximately less than 1% because the curvature of the arm is quite constant and, in any case, it is varying continuously and slowly across the forearm circumference.

So, as described in the end of Chapter 5, the main role here is played by the accuracy of the Image Processing program, which has been evaluated having an uncertainty about

1%, and especially by the Ultrasound scans quality, which provided accidental maximal errors around 25%.

6.7 3D Modelling Results

6.7.1 First Models

The first model obtained was the model of the single vein, considering the longitudinal path of this vessel and not the cross-sectional area. After modelling, it became clear the discrepancies in cross-sectional areas, and the difficulty of processing images and build the 3D model in this way is not a good solution for our purpose, and for this reason it has been discarded.

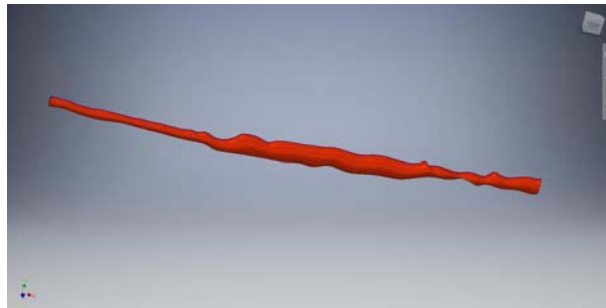


Figure 170 First attempt of modelling a 3D vessel.

Regarding the model of the two separate vessels, the solution undertaken proved to be accurate and easy to operate. Some issues and deficiencies have been detected and then improved with the last procedure, but the model itself is compliant both the position and the shape of the real vessels, according to the surgeon and the related Ultrasound scans.

However, a real engineering comparison based on an MRA 3D scan was not undertaken for bioethical and cost issues.

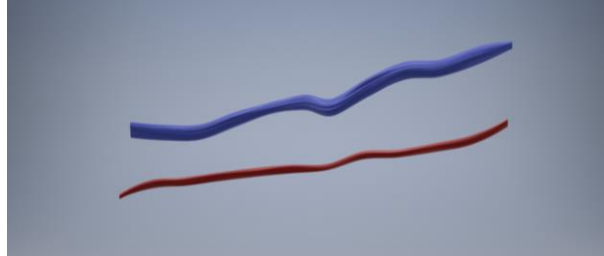


Figure 171 3D model of the two separated vessels.

6.7.2 Virtual Reconstruction of an AVF

The virtual AVF model has proven to be an interesting result for what regards the AVF prediction and optimisation. For what regard the cross-sectional areas the results are good as demonstrated in the previous chapter. For what regards the AVF shape, a lot depends on the designer abilities and knowledge about the problem and the surgical operation. For this reason, the helpful support of the hospital surgeon helped to overcome some details in the AVF shape characterization, receiving a good feedback for what regards the final shape of the virtually reconstructed AVF.

Here the main topic is about what changes to operate to obtain relevant models to study. AVF configurations depend on the patient anatomy and vessels conditions, so they are very various and uncertain. Although, this does not have to discourage because the results in terms of development possibilities and results achievable with this procedure are very high and interesting, considering the simplicity and the costs of the protocol compared to other studies on the same theme.

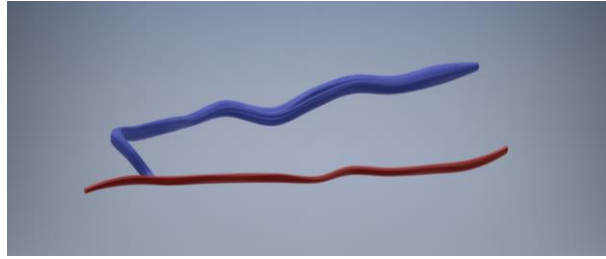


Figure 172 Virtual 3D model of the fistula.

6.7.3 AVF Real Case

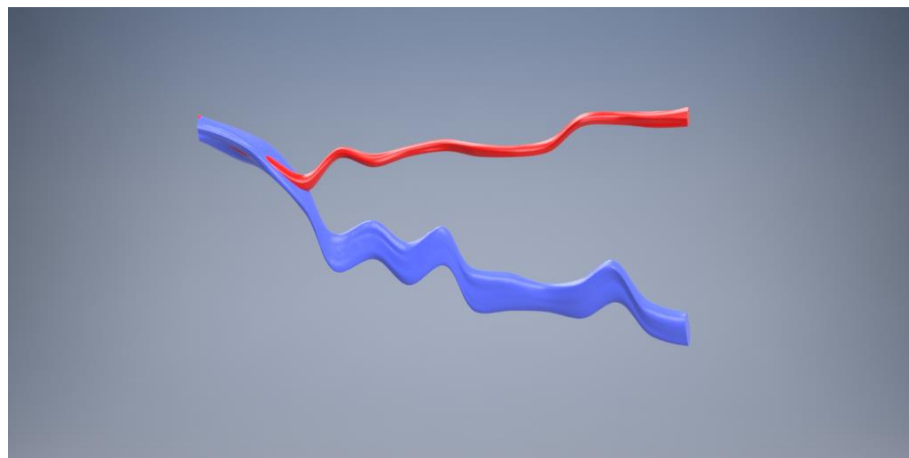
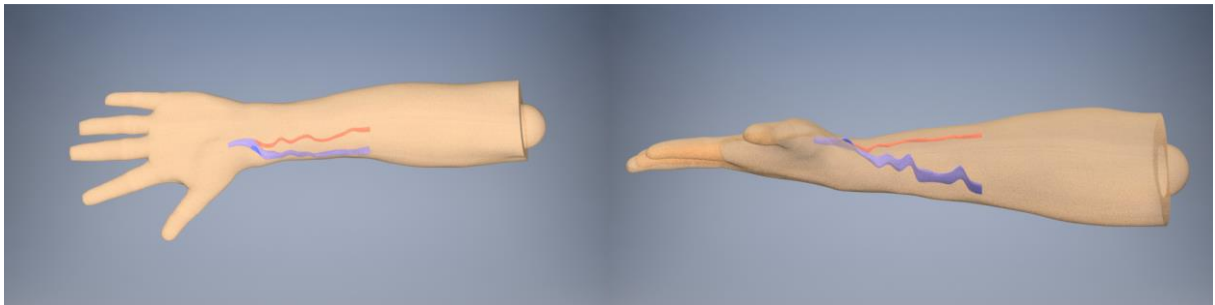


Figure 173 Final 3D model of the fistula.

According to the practise standards in the AVF surgical creation, the surgeon opinion based on its real work and the data at our disposal to date, it can be stated that even with

a certain level of uncertainty, the model provided by the procedure can be considered a good representative of the real AVF geometry.

The vessels cross-sectional areas suffer from low errors, whereas the vessels spatial paths suffer a high quantity of uncertainties and errors, which lead to a relatively poor quality in this aspect. It is important to stress, however, that thanks to the procedure characteristics, even if the absolute accuracy on the vessels path is not so good, the accuracy related to the relative position of the two vessels is better. This is thanks to the fact that the basic references are the same during the vessels reconstruction so that if an error is present, it is common and shared for both the vessels. Anyway, some doubts are still present regarding some particular vessels curves.

Unluckily it has not been possible to evaluate with certainty these errors because the lack of the means to obtain the desired information.

However, from the uncertainty analysis and estimation previously exposed, it is possible in any case to attempt to esteem these uncertainties, resulting in an uncertainty in the relative position of the vessels about the 10% and an uncertainty in the absolute path and position of the single vessel about 25%.

7THE NUMERICAL MODEL⁷

⁷ Eventual references on the chapter or paragraph titles are to be intended to be the main sources of the informations provided on that chapter or paragraph.

Having obtained a 3D model of the ArterioVenous Fistula we want to study, accompanied with sufficient data, a numerical simulation of our case study is now to undertake.

There are copious numerical simulations possible, as shown in Chapter 3, depending on what phenomenon we want to study, the contour environment, the specific situation of the fluid to be studied, and the level of accuracy and complexity it is intended to achieve.

The intention in this chapter is to describe the types of numerical simulations operated, showing the choices done, the purposes intended to achieve, the characteristics and specifications of every operation, finally showing the results obtained.

7.1 The Software: COMSOL Multiphysics (117) (118)

The CFD software choice felt to COMSOL Multiphysics®. The reasons that led to this choice are linked to the software license availability and the properties below described, regarding this software flexibility, user friendliness and power in solving CFD problem of every kind.



Figure 174 COMSOL logo. (117)

COMSOL Multiphysics® is a cross-platform based on finite element analysis, solver and multiphysics simulation software. It allows solving conventional physics-based problems and coupled systems of partial differential equations (PDEs). COMSOL is provided with built-in unified workflow for electrical, mechanical, fluid, and chemical applications. The COMSOL CFD Module is the numerical simulation platform for computational fluid dynamics (CFD) which allows to accurately describe fluid flow in every condition.

With CFD Module, it is possible to study compressible, non-isothermal, Non-Newtonian, multiphase, and porous media flows. The possibility to input the needed equations into the software is a consistent factor to fully control the CFD simulations and results. It is possible to link the CFD Module together with the other modules from the COMSOL® product list, enabling to run multiphysics simulations where fluid flow is not the only important factor.

The CFD Module GUI (Graphic User Interface) grants full access to all steps in the modelling process. It allows setting all the settings of the simulation. The principal controls consist in the creation or import the model geometry, the definition of the fluid properties, the selection the appropriate type of fluid flow, adding sources and sink terms or editing the underlying equations, selecting the mesh elements and controlling the mesh parameters, selecting solvers and tuning them. Every setup window shows the relative equations describing the specific phase of the study presented, allowing a better understanding of the variable playing a role in that step. Easy-to-use physics interfaces provide all the tools to define every step of the study. These interfaces define the conservation of momentum, mass, and energy equations that describe fluid flow, accounting for the contribution from multiphysics couplings to other physics. Moreover, a stabilized form of these equations is formulated, which is exploited by COMSOL to create the finite element discretization for space and the finite differences for time derivatives for stationary or time dependent problems.

Built-in physics interfaces available for the fluid flow characterization are: Single-Phase Flow, Non-Isothermal Flow, Compressible Flow, Two-Phase Flow, Porous Media Flow, Rotating Machinery, Thin-Film Flow, Non-Newtonian Flow, Flow Through Thin Screens, Fluid Flow and Heat Transfer, Reacting Flow. In the Single-Phase Flow, the Navier-Stokes equations which model fluid flow are solved by the CFD Module in multiple variations, to model flows in all velocity regimes. The CFD Module includes Non-Newtonian Flow models like the Carreau and Power-Law models, but also allows to define different equations or bring in external data to describe the viscosity and shear rate of polymer and other non-Newtonian fluids.

In addition to the built-in formulations, it is also possible to define expressions that are arbitrary functions of the modelled variables, and type them into the edit fields to describe material properties or define boundary conditions. The strength of COMSOL is its capability to easily define arbitrary equations of the modelled variables (as averaging, integrating and deriving), allowing for the characterization of fluid flow through using them.

In a further step, there is also the possibility to manipulate the underlying equations in the previously described physics interfaces to modify the description of the flow and to create even more non-standard couplings to other physics interfaces.

Sophisticated descriptions of boundary conditions are also possible for many physics interfaces. Apart from specifying Slip and No Slip boundary conditions, it is also possible to set up walls to simulate Sliding and Moving Wall conditions, as well as walls that are Leaking and, even, Open, where the fluid is assumed to make its own free boundary. For inlets and outlets, a velocity or a velocity profile can be configured along with Pressure, Stresses, or Mass Flow conditions, as well as a Periodic Flow boundary condition that links the outlet flow from one boundary to the inlet of another.

At user disposal, there is also the two-way coupled fluid structure interaction (FSI) formulations. These allow modelling scenarios where the fluid deforms a structure, and where this structure reaction, in turn, influences the fluid flow. All the physics interfaces in the CFD Module can be coupled with any of the other modules in the COMSOL Product Suite to provide the standard platform for applications where computational fluid dynamics need to be considered.

The CAD Import Module or one of the LiveLink™ products enable the user to create the geometry of the part, component, or process to be simulated from a third party CAD software. To reduce small features and artefacts that are not important for the study of the flow, it is also possible to manipulate the geometry. COMSOL Multiphysics supports the ability to create a 2D modelling workspace from 3D geometries, allowing faster

simulations without using the large computational resources that a 3D model would require.

Meshing is often a critical step in modelling computational fluid dynamics in devices or processes. The mesh must be good enough to provide accuracy, but not so fine to drain computational resources. COMSOL Multiphysics provides many different tools to ensure a good mesh for fluid flow simulations. This includes creating unstructured, structured and swept meshes, which ensure flexibility in modelling the geometric domain respecting dimensions and their ratios. To insert structured layers of mesh along boundaries such as walls, boundary layer meshing tool is available in the CFD Module, integrating this layers into surrounding structured or unstructured meshes to become an overall hybrid mesh.

The CFD Module is provided with the most of the linear, nonlinear, time dependent, and parametric solvers found within COMSOL Multiphysics. Direct solvers are present for solving 2D and 3D models, ensuring an easy convergence, and iterative solvers are available for larger or more complex models. Preconditioning and multigrid solvers are useful if there is the need to work in collaboration with other solvers to ensure solutions. Advanced solver functionality and settings are available, and their values can be finely tuned along with most of the other solver settings.

The CFD Module automatically provides results on properties intrinsic to fluid flow, such as flow patterns, pressure losses, forces on objects subjected to flow, temperature distribution. Moreover, a qualitative Post-Processing is possible using tools like surface, streamline, ribbon, arrow as well as animations to display in the most intuitive way any desired variable. All the data from all parameters and variables in the underlying equations and extra terms are easy to extract and be plotted just recalling their function or variable name.

All these properties and characteristics were considered and led to the conclusion that COMSOL Multiphysics should be a good CFD numerical simulation software for our study.

7.2 CFD Simulation of the AVF

The simulation procedure is quite similar for the models before and after the AVF operation. The main aspect is the setting of the boundary conditions and the importing of the CAD geometry and velocities profiles.

About the results, attention is paid to velocity magnitude and distribution (velocity streamlines and arrows/direction), pressure magnitude and distribution, WSS magnitude and distribution, GWSS magnitude and distribution, OSI magnitude and distribution, Reynolds number, Womersley number. Every one of these variables has its own formula to be input into the software, as described in the numerical modelling protocol below.

7.2.1 Pre-Operative Operations

Pre-operative operations undertaken before the real simulations helped to get the best results in the simulations and prevented from time loose and errors.

The first of these operations has been the conversion of the Velocity Pulsewave Excel file to a .txt text file importable to COMSOL. To do so, the commas of the decimals are substituted with periods.

Then a mesh convergence test is made, to evaluate simulations accuracy and computing times.

The mesh size is deliberately left completely controlled by the mesh software, controlling only the Element Size, and setting the sequence type to “Physics-controlled”.

The test undertaken is a time dependent simulation of the AVF model completely identical to the procedure further exposed, with the same final boundary conditions, except for the fact that only two cardiac cycles have been simulated to reduce computational times.

The results are compared basing on the variables of interest of this study:

- Surface Average Velocity at artery outlet
- Line Average WSS along the artery side
- Line Integration WSS along vein side
- Line Integration of WSSG Time Average around anastomosis.

The final comparison led to these results:

- Surface Average Velocity at artery outlet

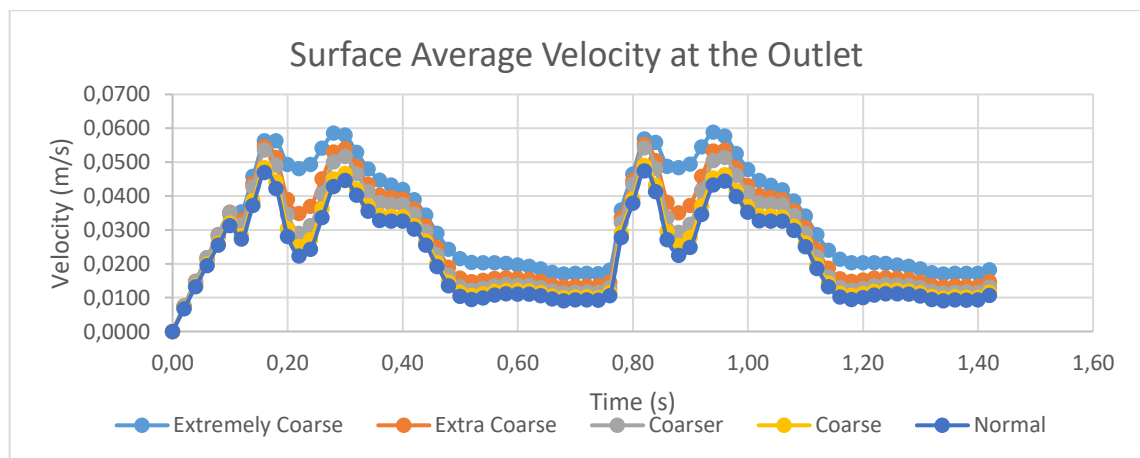


Figure 175 Meshes comparison: Surface Average Velocity at the Outlet.

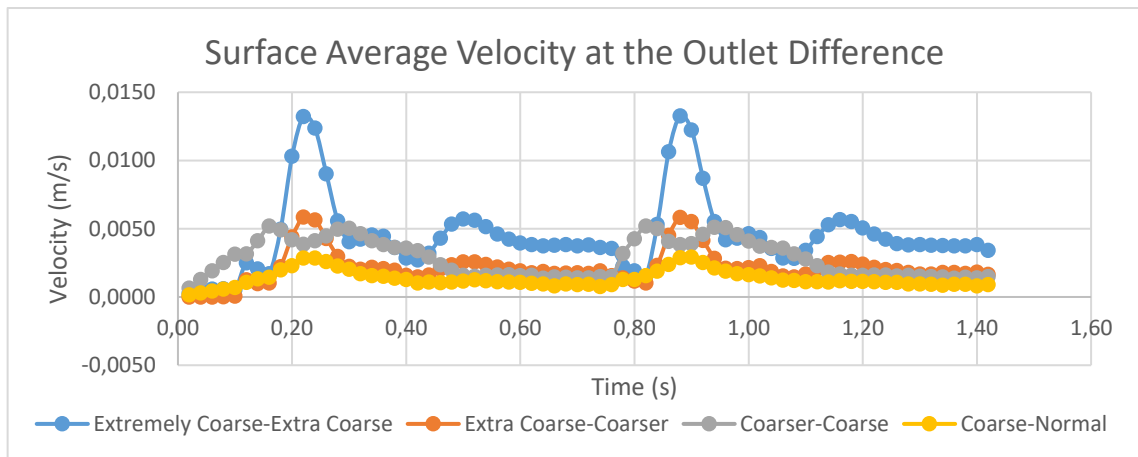


Figure 176 Meshes comparison: Surface Average Velocity at the Outlet Difference.

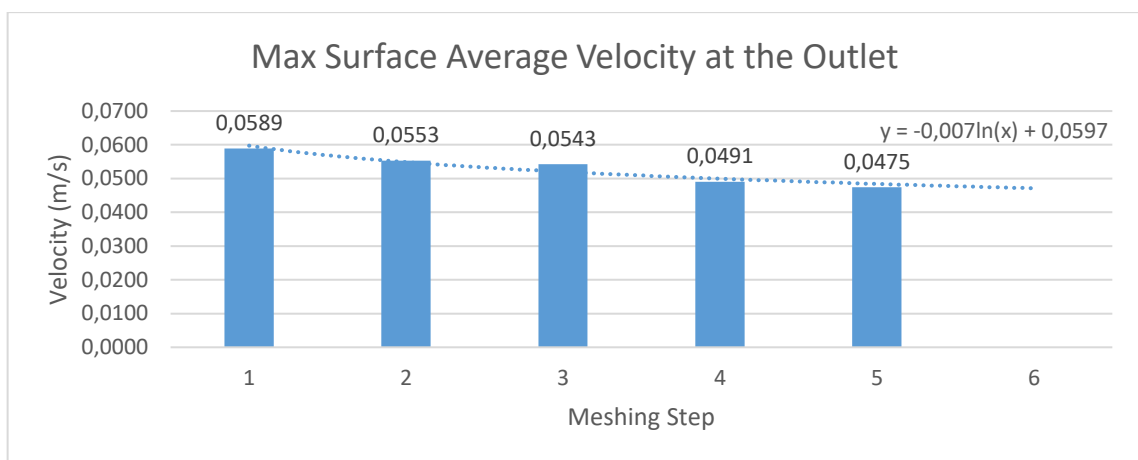


Figure 177 Meshes comparison; Max Surface Average Velocity at the Outlet.

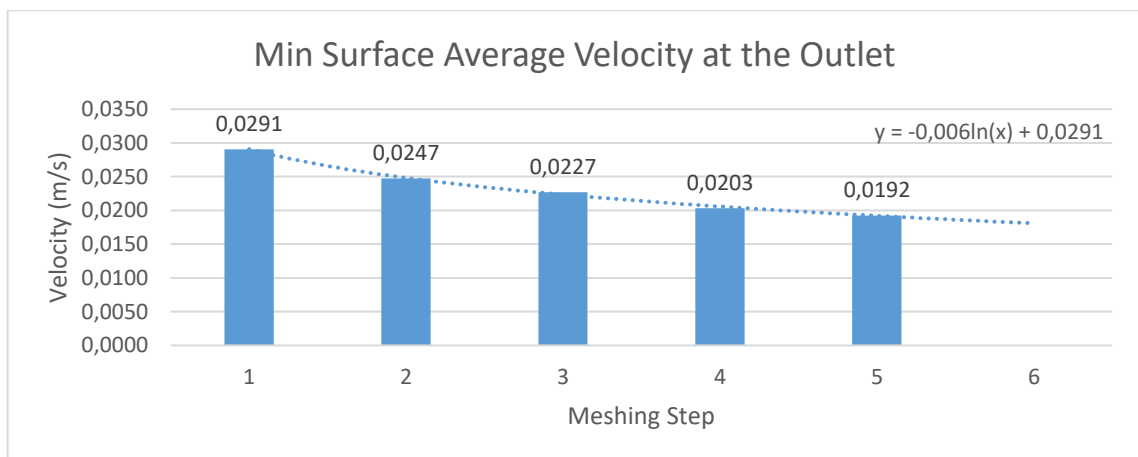


Figure 178 Meshes comparison: Min Surface Average Velocity at the Outlet.

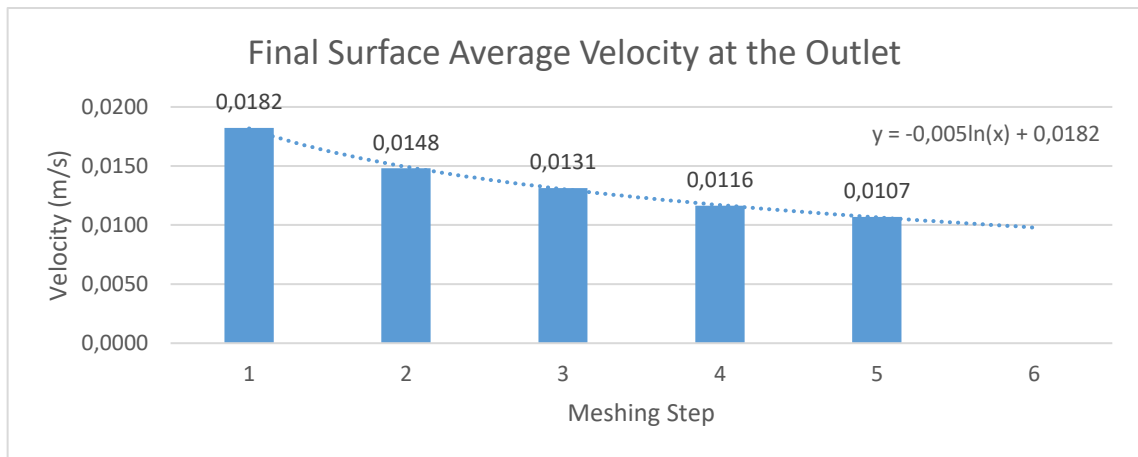


Figure 179 Meshes comparison: Final Surface Average Velocity at the Outlet.

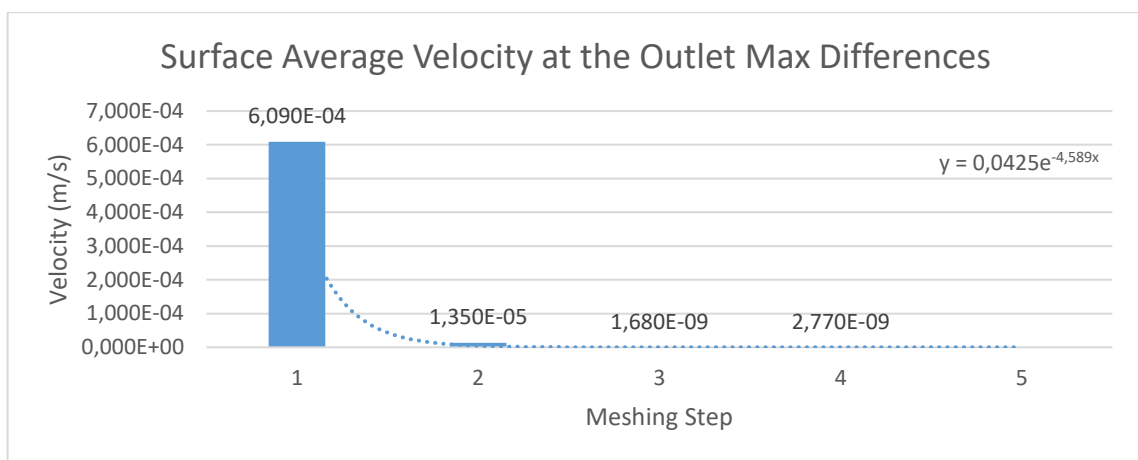


Figure 180 Meshes comparison: Surface Average Velocity at the Outlet Max Differences.

All the different plots of the Surface Average Velocity at artery outlet clearly show the tendency of the meshes to converge. Probably one more Mesh Step could provide a stable convergence; however, the final result with the Normal Mesh is acceptable considering the plots trend.

- Line Average WSS along the artery side

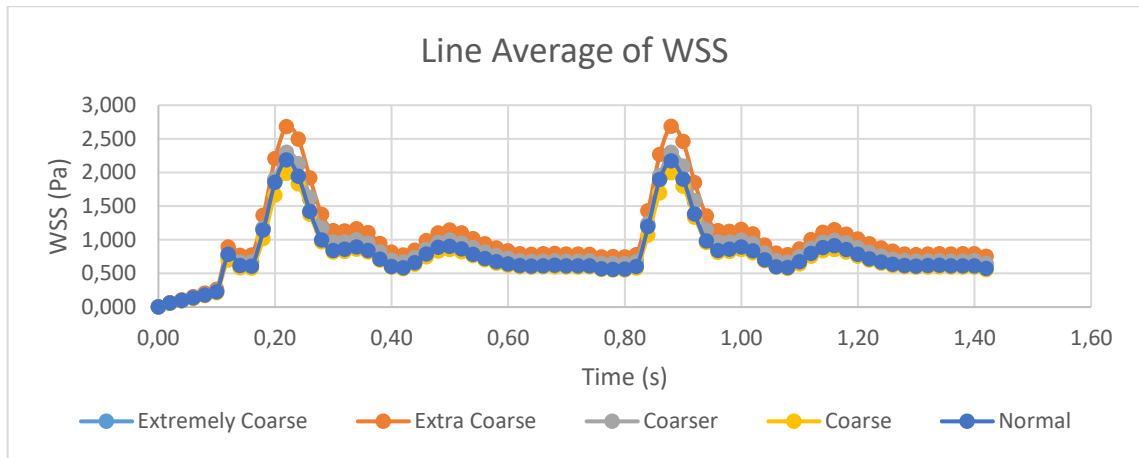


Figure 181 Meshes comparison: Line Average of WSS.

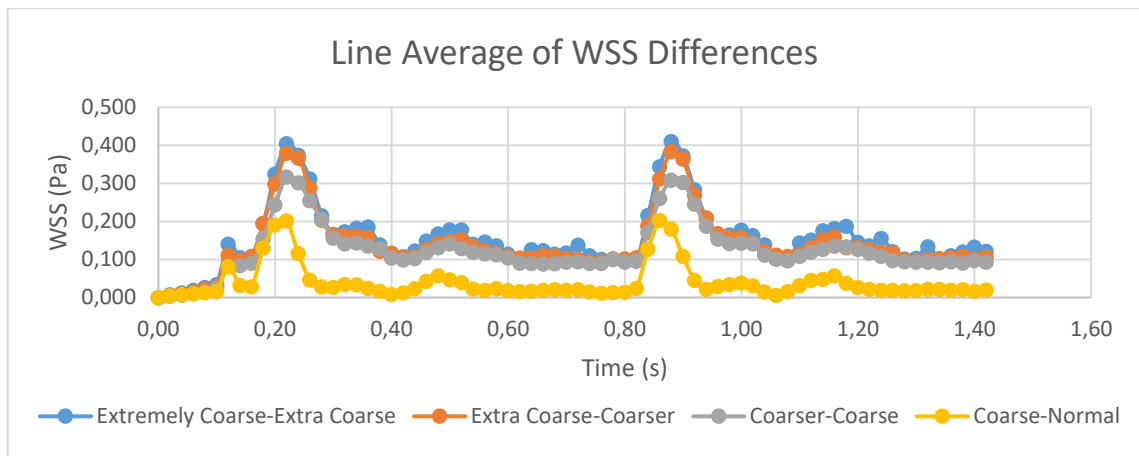


Figure 182 Meshes comparison: Line Average of WSS Differences.

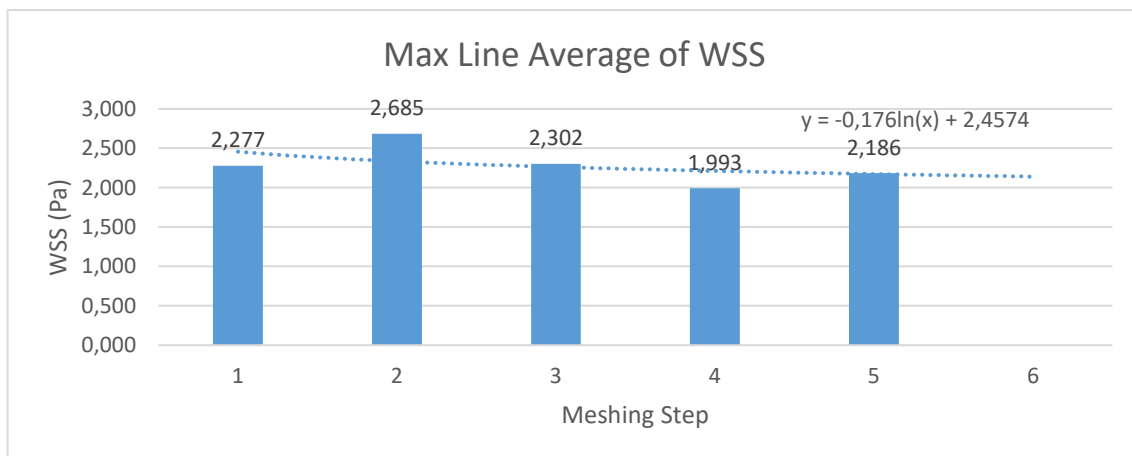


Figure 183 Meshes comparison: Max Line Average of WSS.

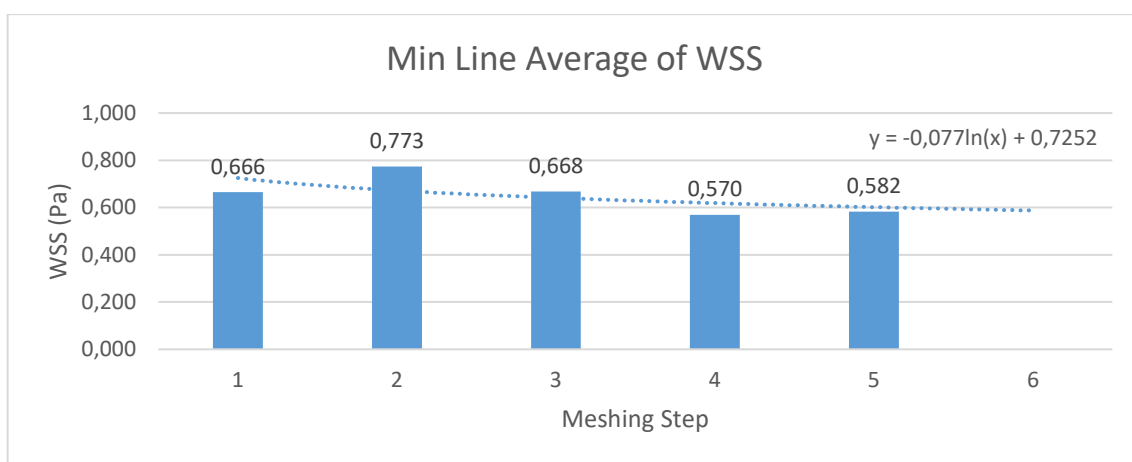


Figure 11 Meshes comparison: Min Line Average of WSS.

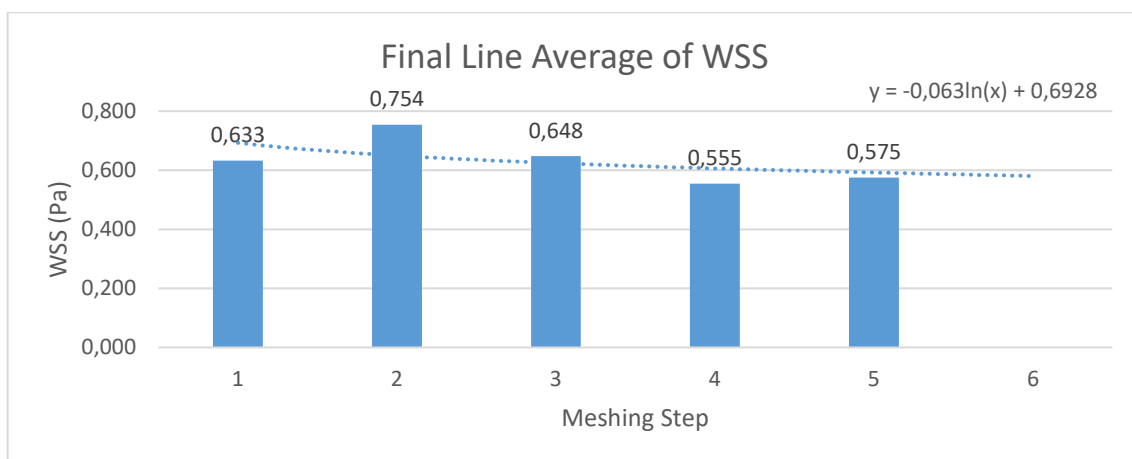


Figure 184 Meshes comparison: Final Line Average of WSS.

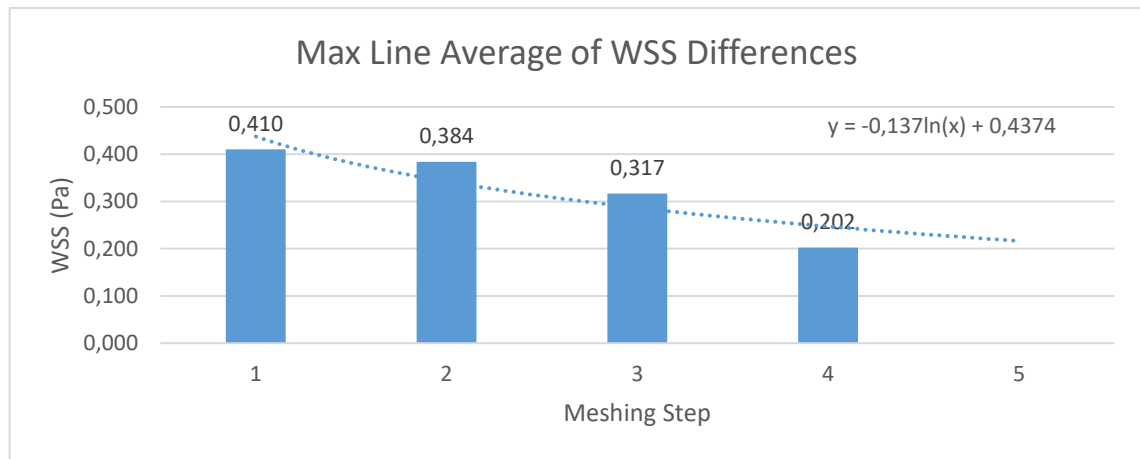


Figure 185 Meshes comparison: Max Line Average of WSS Differences.

In addition, the different plots of the Line Average WSS along the artery side show the same tendency of the meshes to converge, especially considering the Line Average of WSS Differences plot. The plots of Max Line Average of WSS, Min Line Average of WSS and Final Line Average of WSS show a controversial trend difficult to explain, if not with the non-direct sensibility of the meshes on WSS measure along the artery side. The matter here is also the line along with the evaluations have been made. This choice can have very influences on convergence determination, because of the dynamical change of mesh resolution depending on the local geometry complexity.

However, for the same reason why the Line Average of WSS Differences plot was considered, the Max Line Average of WSS Differences is analysed, providing the evidence that comparing the differences on WSS developments of the various meshes the convergence can be appreciated.

- Line Integration WSS along vein side

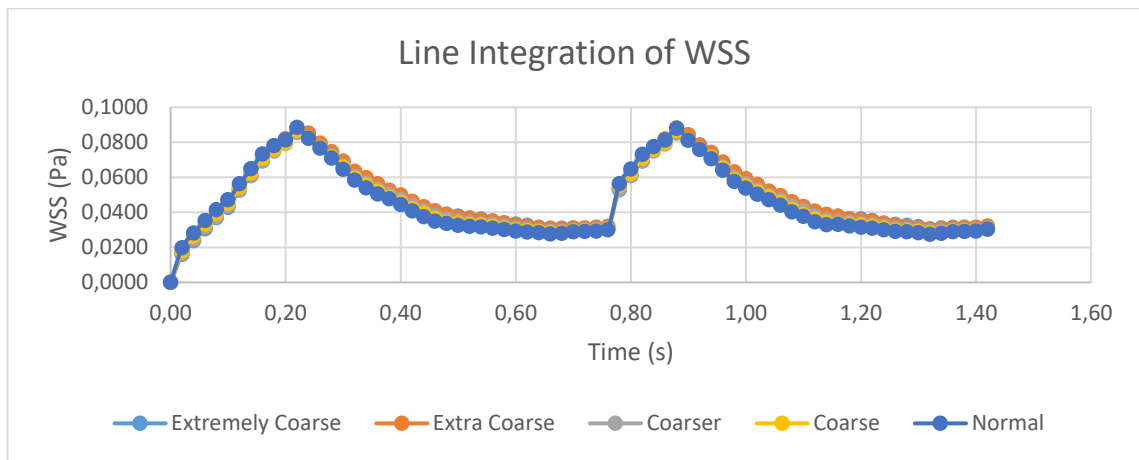


Figure 186 Meshes comparison: Line Integration of WSS.

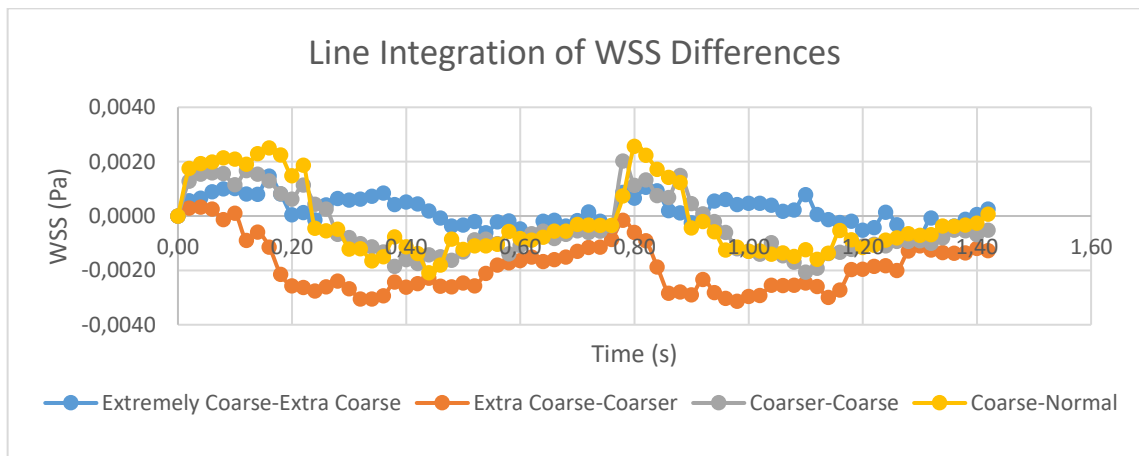


Figure 187 Meshes comparison: Line Integration of WSS Differences.

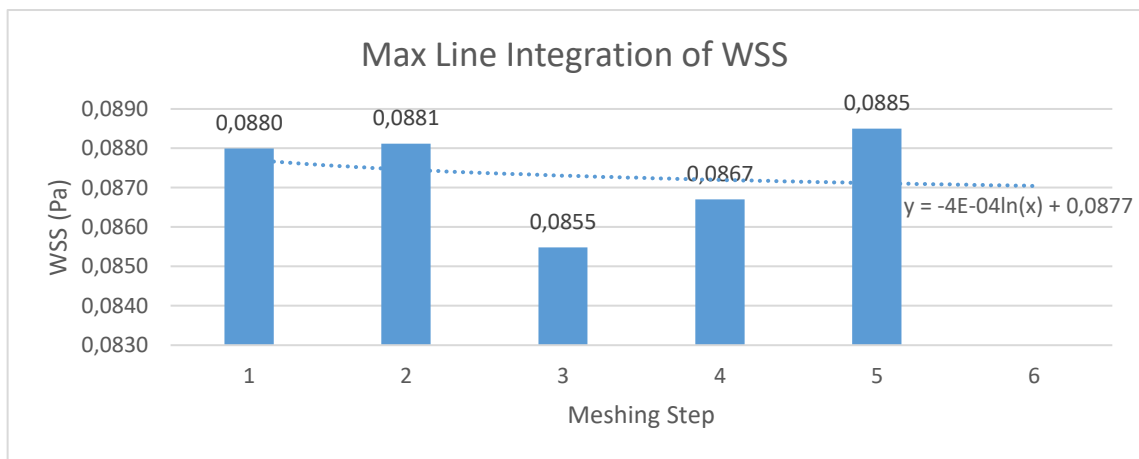


Figure 188 Meshes comparison: Max Line Integration of WSS.

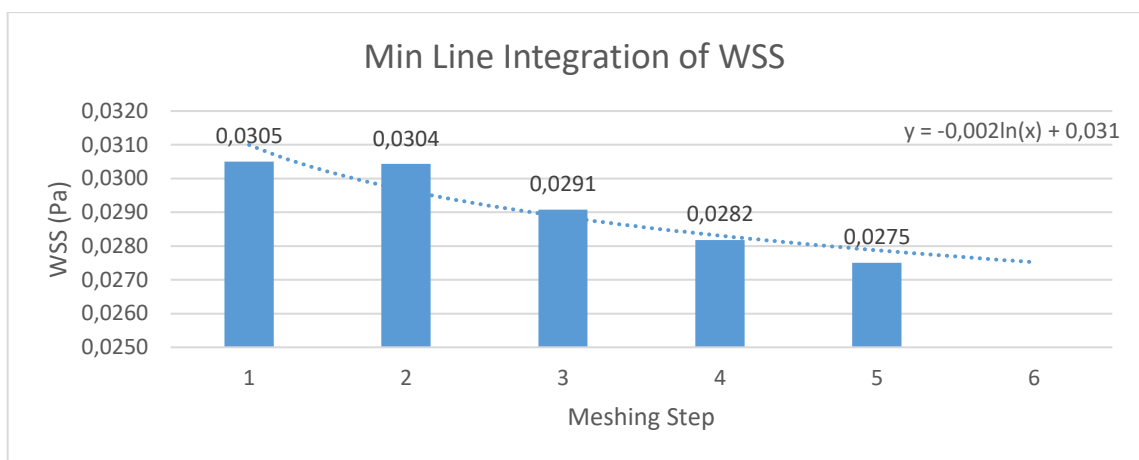


Figure 189 Meshes comparison: Min Line Integration of WSS.

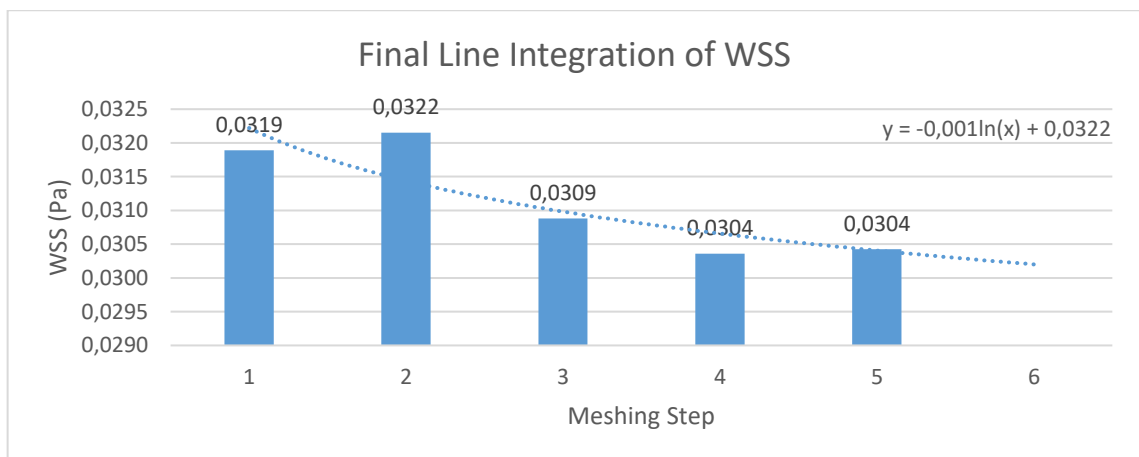


Figure 190 Meshes comparison: Final Line Integration of WSS.

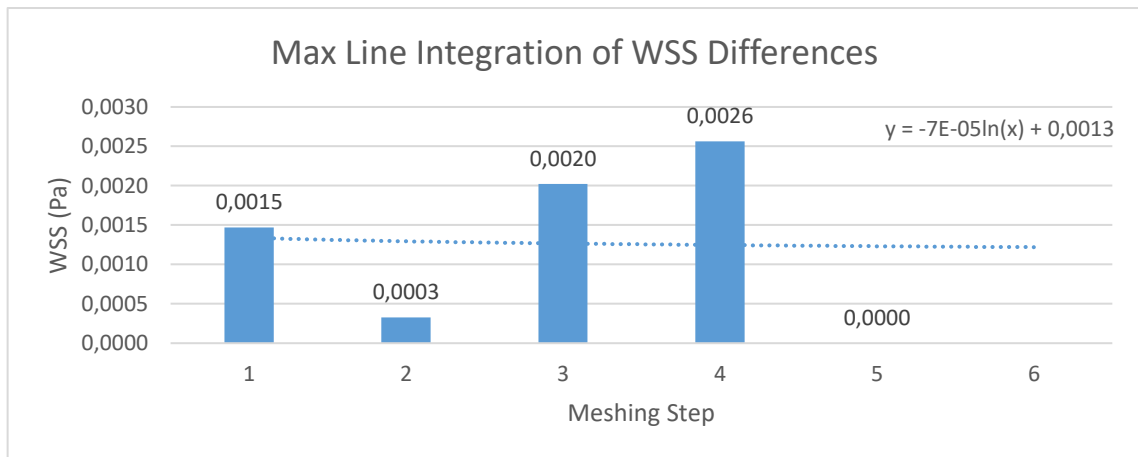


Figure 191 Meshes comparison: Max Line Integration of WSS Differences.

With the Line Integration WSS along vein side plots, the same issues have been found. The motivations should be the same, but here, even the Line Integration of WSS Differences plots do not show some kind of convergence. This suggests paying more attention to the mesh convergence study and a new study topic; anyway, this is not our interest now.

- Line Integration of WSSG Time Average around anastomosis

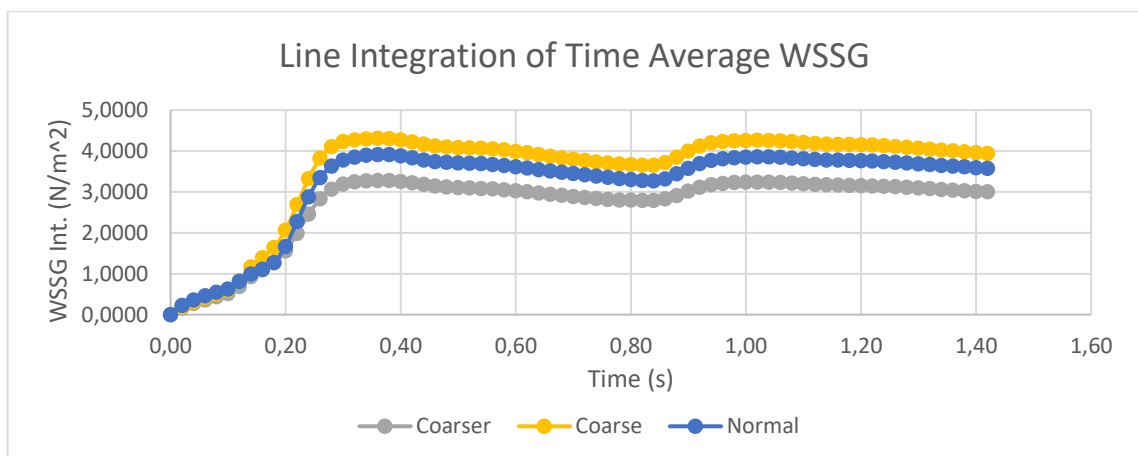


Figure 192 Meshes comparison: Line Integration of Time Average WSSG.

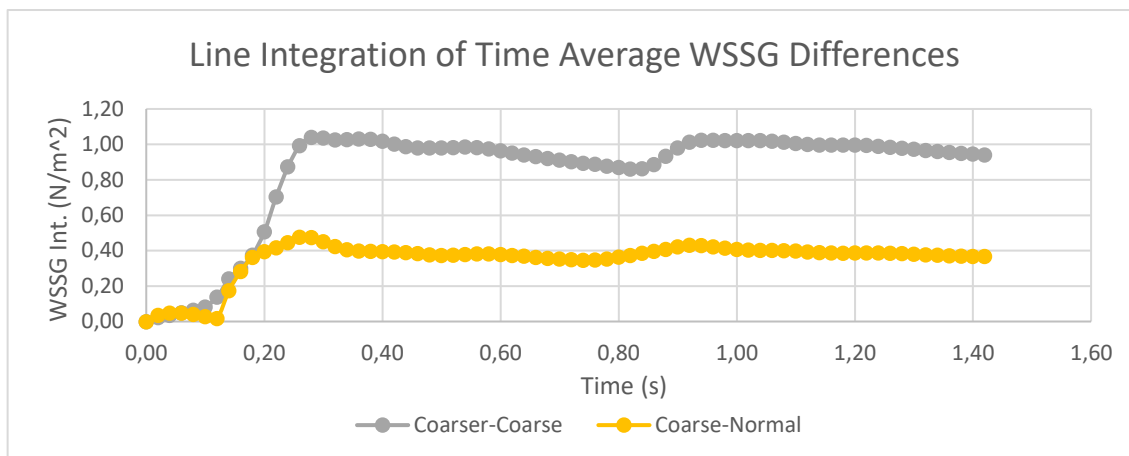


Figure 193 Meshes comparison: Line Integration of Time Average WSSG Differences.

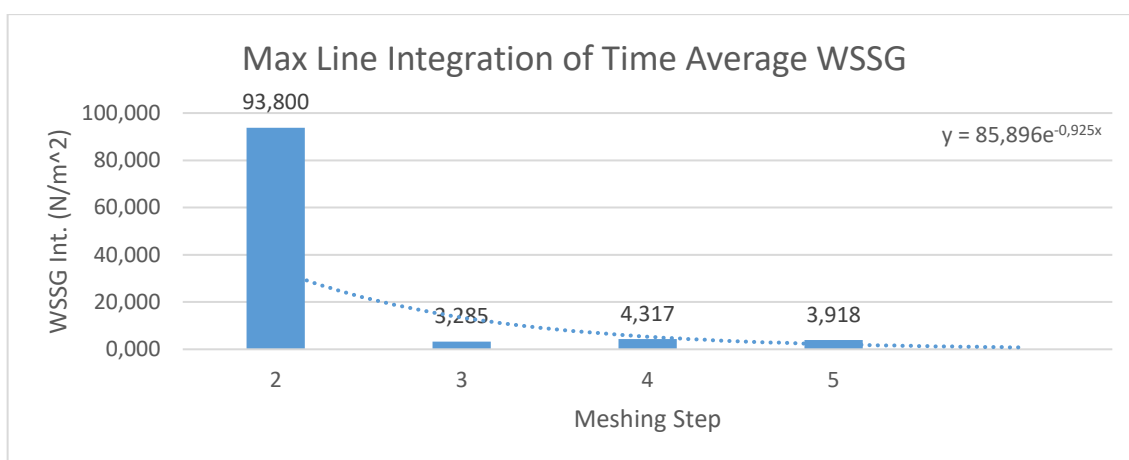


Figure 194 Meshes comparison: Max Line Integration of Time Average WSSG.

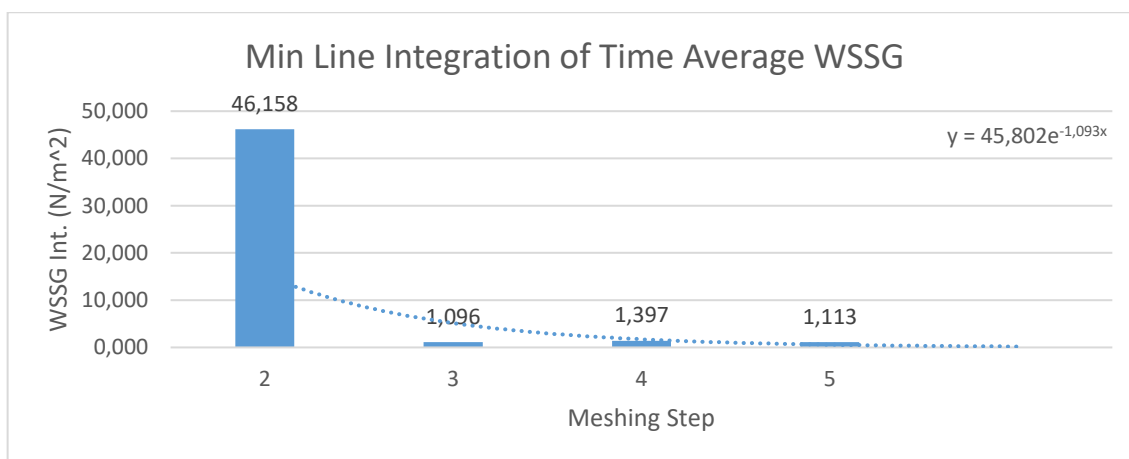


Figure 195 Meshes comparison: Min Line Integration of Time Average WSSG.

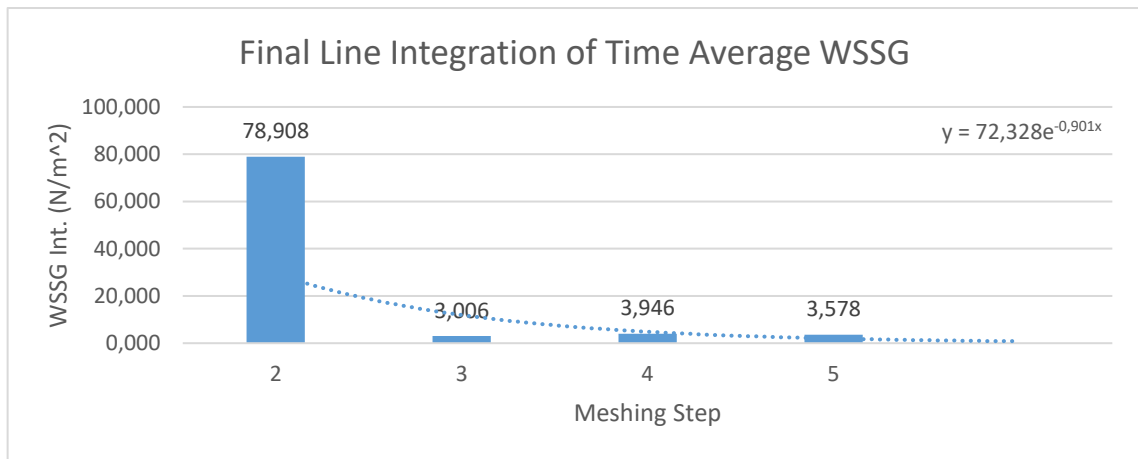


Figure 196 Meshes comparison: Final Line Integration of Time Average WSSG.

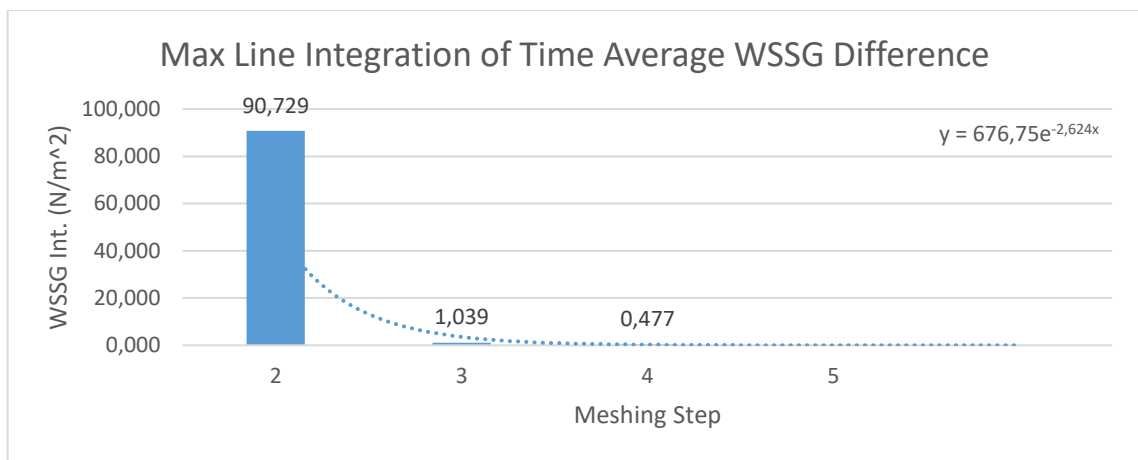


Figure 197 Meshes comparison: Max Line Integration of Time Average WSSG Difference.

Again, in the Line Integration of WSSG Time Average around anastomosis, we found a strong convergence probe, probably due to the effectiveness of this analysis variable choice and the better Mesh refinement on this particular zone.

The first two series of the first two graphs, and the very first series of the bar graphs, have been hidden to appreciate the finer meshes results, being the coarser meshes providing very great values due to the low spatial accuracy.

As we can see, finally, the full Convergence should be considered achieved adding one more refining step. Nevertheless, the computing times did not allow to obtain the related results in an acceptable duration, so the test was dismissed and the convergence check finished at Normal refinement

We chose the Normal Mesh refinement as a compromise between acceptable computing times and good quality results.

The Mesh quality statistics gathered from the software have been considered good.

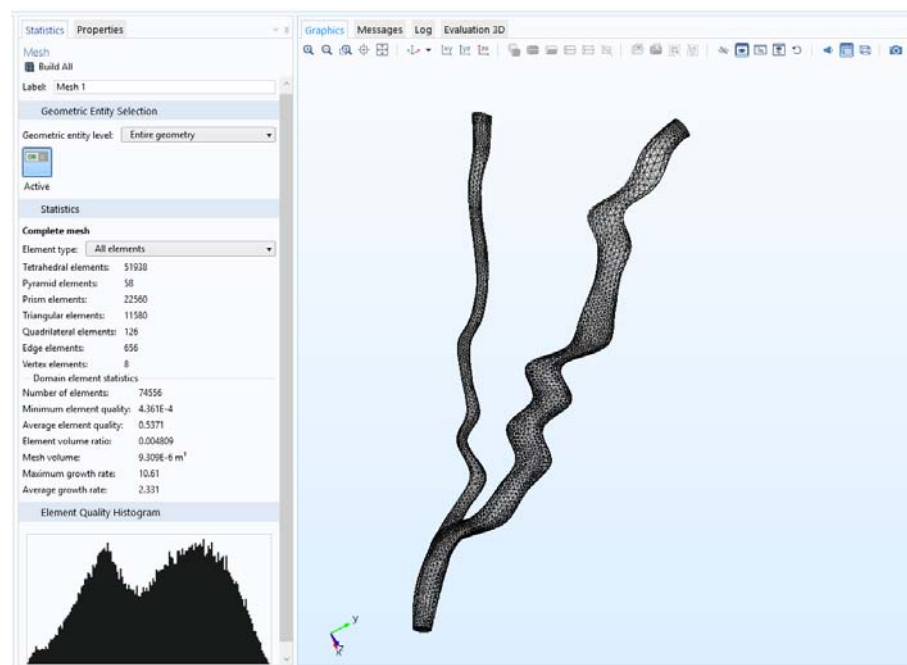


Figure 198 Mesh quality statistics feneralised to all elements.

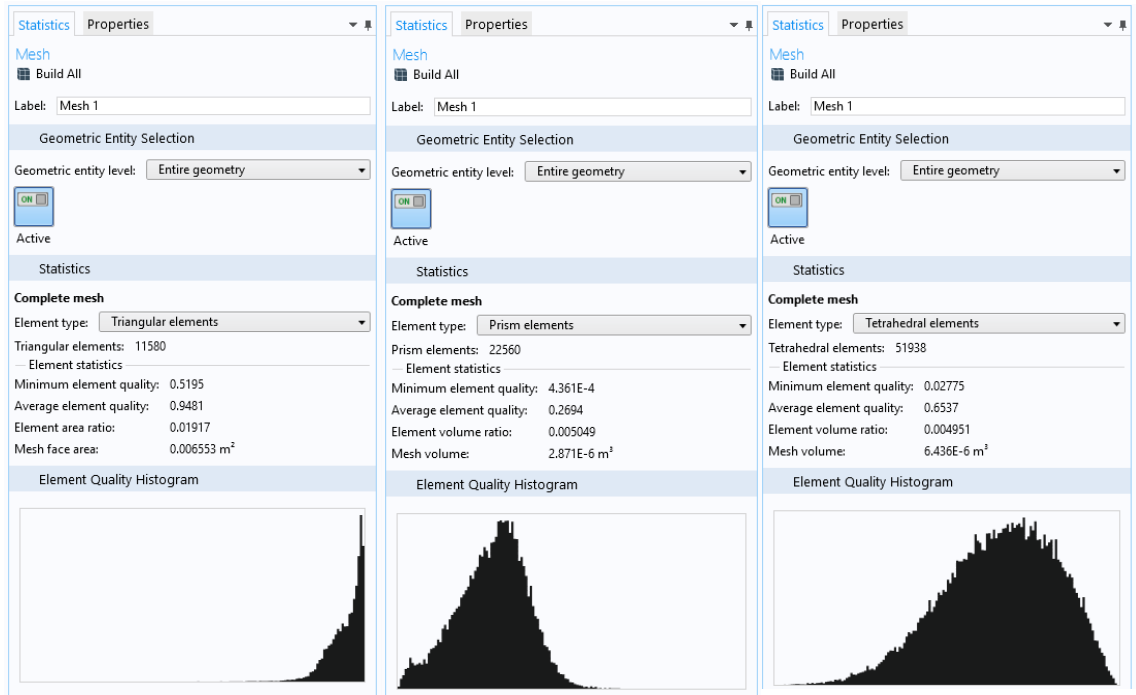


Figure 199 Mesh quality statistics for triangular elements, prism elements and tetrahedral elements.

However, as it is possible to notice, some refinements and correction should be urged in the anastomosis area to improve the results quality.

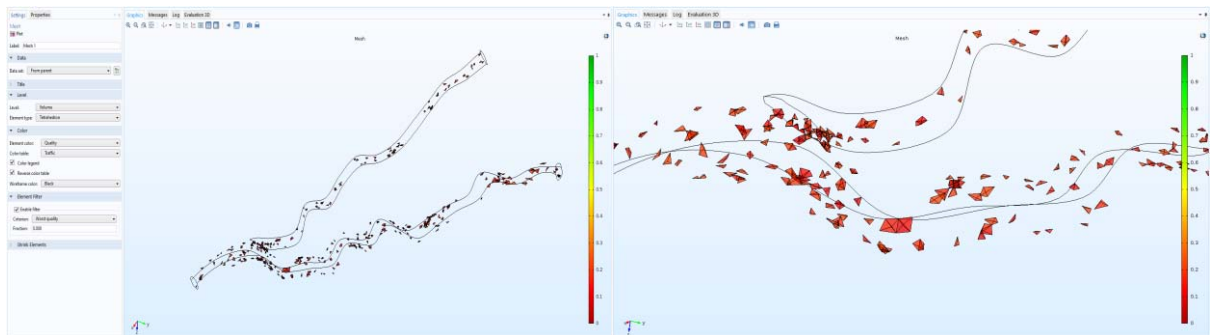


Figure 200 Bad-quality elements location.

It has to be underlined that these bad shaped elements are lower than the 0.8% of the mesh elements.

7.2.2 Pre-Processing

As soon as the program is opened, a 3D “Laminar flow” “Time dependent” simulation is set. Then, we are in the CDF Module main Workspace where the Pre-Processing operations can be undertaken. These starting choices are motivated in Chapter 3, and are due to the relatively low Reynolds number estimation encountered.

7.2.2.1 CAD Import

The 3D model of the AVF is imported as a .stp file. From the “Geometry” drop-down menu is selected Import command, and then from the browse bar the file is selected and imported.

After checking all the geometry, surfaces and lines characterising the AVF model are all present and consistent, the “Build all” command is selected.

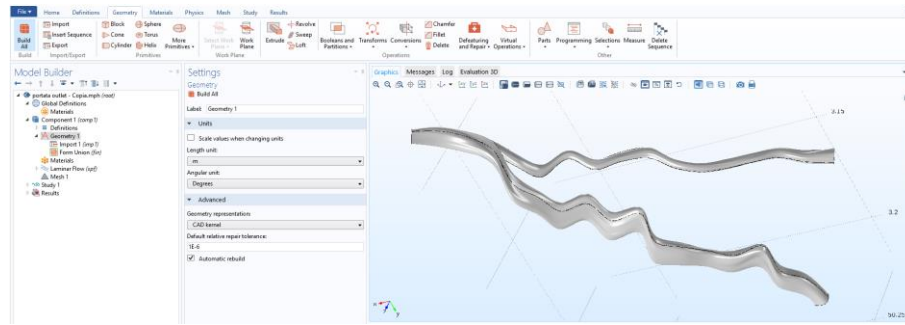


Figure 201 AVF 3D model import.

7.2.2.2 Parameters and Variables Definition

As second step all the Variables necessary for the Post-Processing and all the Parameters needed to the Boundary Conditions setting are compiled.

From the Definitions drop-down menu, respectively “Local Variables” and the Parameters “Functions Interpolation” are selected.

COMSOL provides a good Interface Graphic, which can show all the variables used and available on a CFD simulation and their relative name. If some variable is not defined and can be obtained from the basic ones, thanks to the previous command this variable can be added.

Basic Variables Considered are:

- x-direction velocity: u
- y-direction velocity: v
- z-direction velocity: w
- total velocity: spf.U
- fluid density spf.rho
- fluid viscosity: spf.mu

- Pressure: p
- x-direction stress: $spf.K_stressx$
- y-direction stress: $spf.K_stressy$
- z-direction stress: $spf.K_stressz$
- x-direction stress gradient: $d(spfx.K_stressx,x)$
- y-direction stress gradient: $d(spfx.K_stressy,y)$
- z-direction stress gradient: $d(spfx.K_stressz,z)$

The derived Variables are:

- WSS magnitude and distribution:

$$\sqrt{(spf.K_stressx)^2 + (spf.K_stressy)^2 + (spf.K_stressz)^2}$$

- GWSS magnitude and distribution:

$$\sqrt{(d(spfx.K_stressz,z))^2 + (d(spfx.K_stressy,y))^2 + (d(spfx.K_stressx,x))^2}$$

- OSI magnitude and distribution:

$$0.5 * (1 - (\sqrt{(timeint(0,t,spf.K_stressx))^2 + (timeint(0,t,spf.K_stressy))^2 + (timeint(0,t,spf.K_stressz))^2}) / timeint(0,t,WSS)))$$

- TAWSS magnitude and distribution:

$$timeavg(0,t,\sqrt{(spf.K_stressx)^2 + (spf.K_stressy)^2 + (spf.K_stressz)^2})$$

- RRT magnitude and distribution:

$$\begin{aligned} & ((1 - (1 - ((\text{sqrt}((\text{timeint}(0, t, \text{spf}.K_stressx))^2 \\ & + (\text{timeint}(0, t, \text{spf}.K_stressy))^2 \\ & + (\text{timeint}(0, t, \text{spf}.K_stressz))^2))) \\ & / (\text{timeint}(0, t, \text{sqrt}((\text{spf}.K_stressx)^2 + (\text{spf}.K_stressy)^2 \\ & + (\text{spf}.K_stressz)^2)))))) \\ & * \text{timeavg}(0, t, \text{sqrt}((\text{spf}.K_stressx)^2 + (\text{spf}.K_stressy)^2 \\ & + (\text{spf}.K_stressz)^2)))^2 - 1 \end{aligned}$$

- Reynolds number:

$$\text{spf}.U * \text{spf}.rho * 0.004[m] / \text{spf}.mu$$

0.004 m is the average cross sectional area of the vessels processed.

- Womersley number:

$$\text{spf}.rho * (1/9.42477795 [\text{rad/s}]) * 0.4^2 / (\text{spf}.mu)$$

9.379 rad/s is the average frequency of the pulse waves correspondent to 93 bpm.

For what regards the Parameters, the main data generated in this phase is the pulse wave velocity extracted, interpolated and sampled before. After selecting the “Function – Interpolation” button, the .txt file containing the sampled pulse wave velocity is imported, the time “s” argument is set.

The procedure is repeated for both the artery velocity pulse wave (Inlet) and the vein velocity pulse wave (Outlet) files.

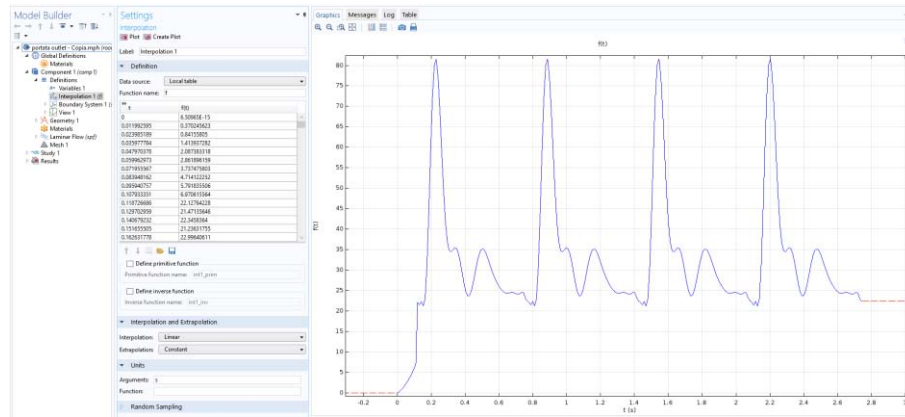


Figure 202 Parameter interpolation of the pulse wave velocity sampled points.

7.2.2.3 Fluid Properties

On the model builder, the “Material” selection is omitted, because all the fluid properties we want to set up can be inserted in the “Fluid Properties” under the “laminar Flow” menu of the model builder.

Here the density of blood is set at 1056 kg/m³, and the viscosity is set to “Non-Newtonian-Carreau Model”, because of the choices exposed in Chapter 3, Paragraph 1.3.

The values for the Carreau model are:

$$\eta_{\infty} = 0.0035 \text{ Pa}\cdot\text{s}$$

$$\eta_0 = 0.056 \text{ Pa}\cdot\text{s}$$

$$\lambda = 3.313 \text{ s}$$

$$n = 0.3568.$$

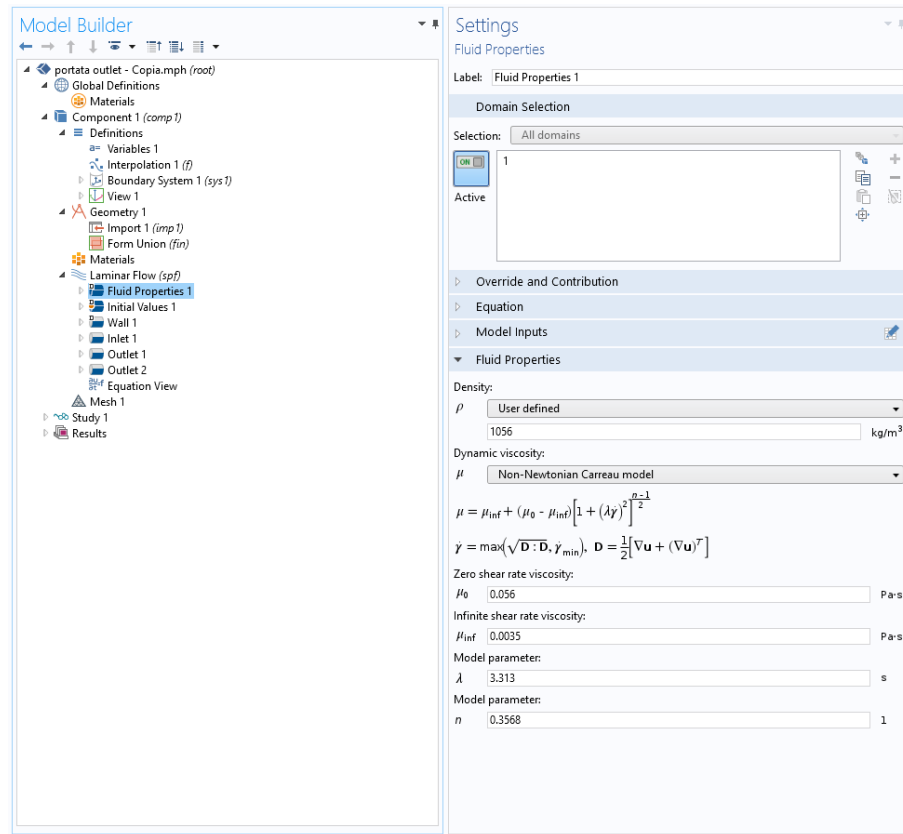


Figure 203 Setup of the Carreau rheological model parameters for blood.

7.2.2.4 Arterial Inlet

Continuing in the “Laminar Flow” setting, an Inlet is added, corresponding to the arterial inflow of the model.

The artery cross-sectional area is selected and then under the “Boundary condition” menu “Laminar Inflow” is chosen, with the “Average velocity” option. This set up try to imitate the real physiological laminar inlet, building a Poiseuille 3D velocity profile with the average velocity set.

The velocity setting is the Parameter $f(t)$ previously defined as the velocity pulse wave sampled (the final time of the velocity pulse wave file is 2.74 s for four pulses).

The Entrance Length has been set to 0.05 m ($L_{laminar} = 0.05 \times Re \cdot D$ with $Re=280$ and $D=0.004$ m) from previous results data. Worth to note is that the inlet extended model of the AVF, to let the entering flow completely develop, has been

studied, but not in the final numerical model, not to alter the results and to reduce computational costs.

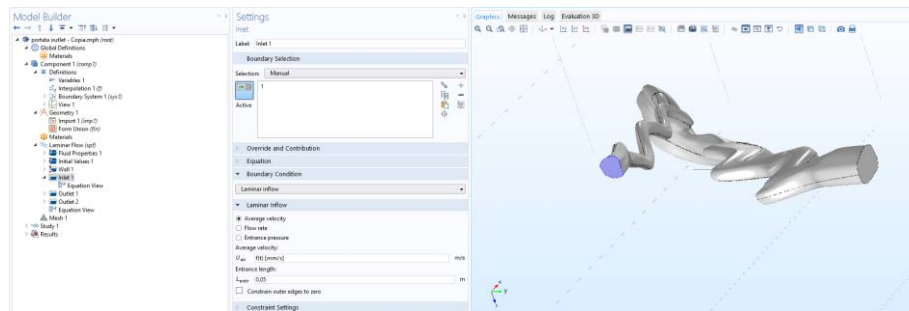


Figure 204 Arterial Inlet boundary condition setup.

7.2.2.5 Venous Outlet

The Venous Outlet incurred in some troubles regarding its large size respect a “standard” vein. For this reason, the setup of this boundary underwent to a change during the study of the simulation process.

In the beginning, a “Laminar Outflow” with the “Average velocity” option was chosen but then, checking the first result, appeared evident that the flow division between the two Outlets resulted too much unbalanced in favour of the vein, providing doubtful results.

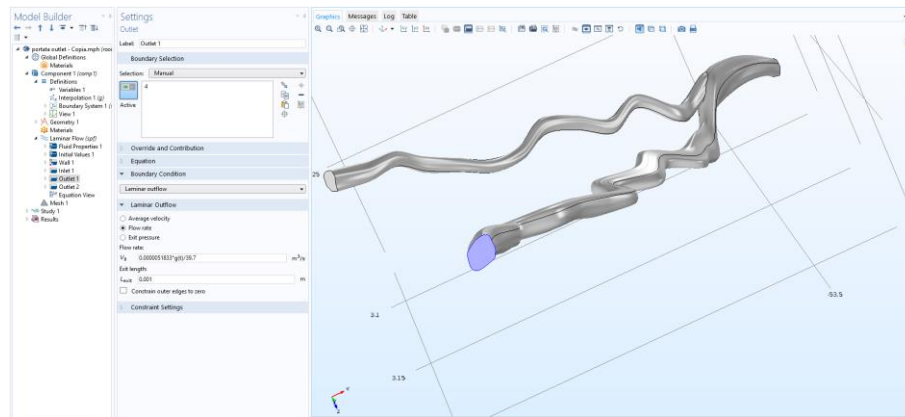


Figure 205 Venous outlet boundary condition setup.



Figure 206 Extraction of the information regarding the blood flow rate.

For these reasons the setup has been changed, so the “Laminar Outflow” option chosen is “Flow rate”, to easily and precisely control the flow rates distributions.

Even so, the velocity pulsewave has been exploited: the flow rate value extracted from the Ultrasound Scans (311 cc/min = 0,000051833 m³/s) has been made time dependent by

scaling it with the normalised outlet velocity pulse wave (the sampling has been divided by the maximum velocity 39.7 mm/s). Exit length was set to 0.001 m.

7.2.2.6 Arterial Outlet

Not being able to correctly predict the pressure pulse wave, and with the awareness that in our CFD case pressure has a secondary role in determining flow distribution, the pressure on the Arterial Outlet is set to a physiological constant value of 80 mmHg (considering the bypass of the fistula this value may be even lower).

Considering the real situation, where distal arterial hand backflow may occur, and for the results seen in the previous simulations, the backflow suppression is disabled.

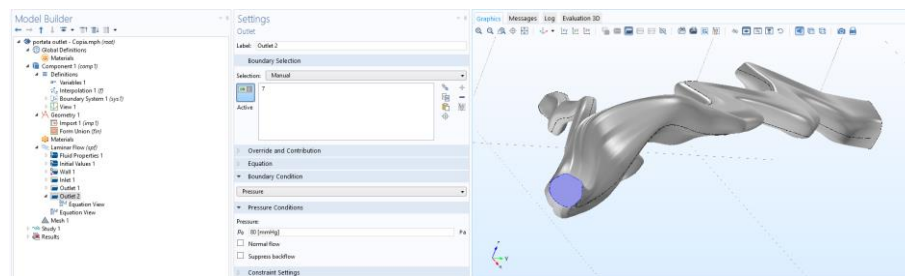


Figure 207 Arterial outlet boundary condition setup.

7.2.2.7 Wall Boundary Conditions

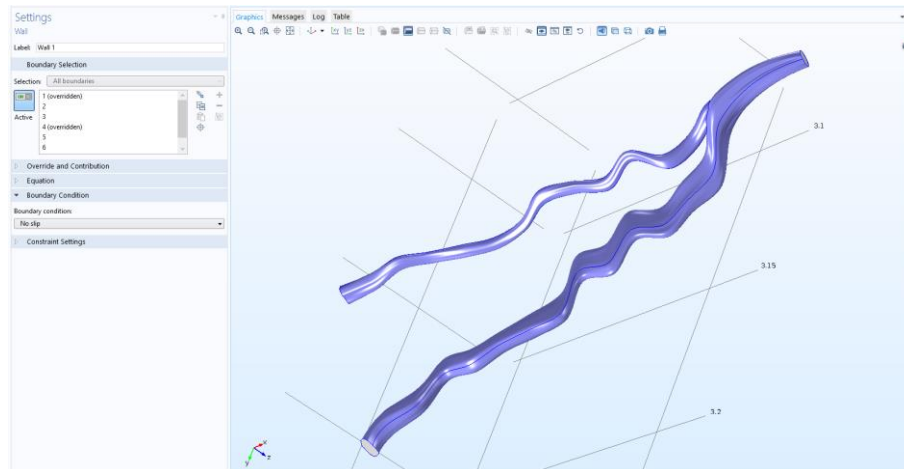


Figure 208 Wall boundary condition setup.

The Wall boundary conditions are set to “No Slip” condition on the surface, as suggested in many related studies. The Wall surfaces automatically update during the other boundary condition setting.

7.2.2.8 Mesh

After the Pre-Operative Mesh convergence test, the mesh has been safely set to “Physics-controlled mesh” and “Normal” element size.

However, if needed, mesh adjustments or refinements can be made easily through the upper menu of the user graphic interface. The choice to accept directly the Mesh tool output was made for several reasons. First the fact that the results themselves are satisfactory, with a total average mesh quality of 54% (surface elements quality 90% -

volume elements quality 55%). The choice to follow an easy and repeatable procedure besides, brings to the choice of the more automated strategy possible.

The convergence results obtained with this automated technique also demonstrated the efficiency and reliability of this choice.

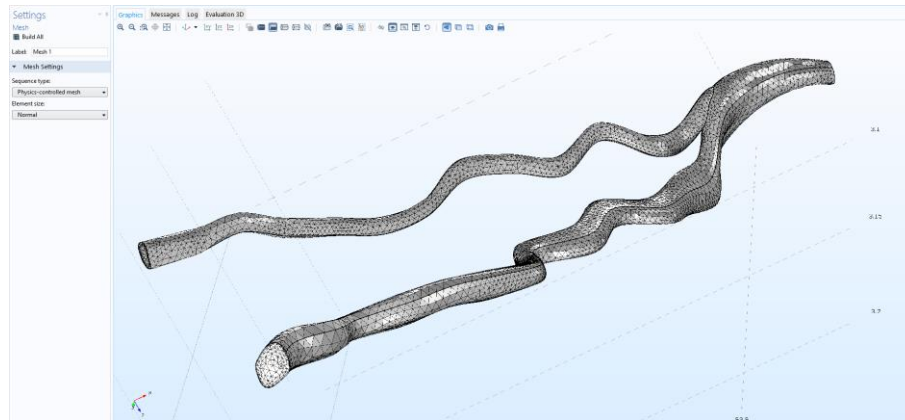


Figure 209 Final Mesh obtained.

The final average element volume size is 0.12 mm^3 , the average element surface size is 0.56 mm^2 and the average element edge size is 0.66 mm .

7.2.3 Simulation

Once the Pre-Processing is all ready, the solution can be obtained, but first, to achieve the best results with the lowest computational cost, the solver set up is refined to our simulation characteristics.

7.2.3.1 Time Steps Definition

The time interval chosen has been set considering the entire time domain of all the four pulse waves and the single pulse wave time. In particular, the solutions are solved at time steps of 0.01 s from 0 to 2.74 s.

This stepping was considered good, being the 0.4% of the total simulated time and the 1.5% of a pulse wave cycle time, for both accuracy and acceptable computing times.

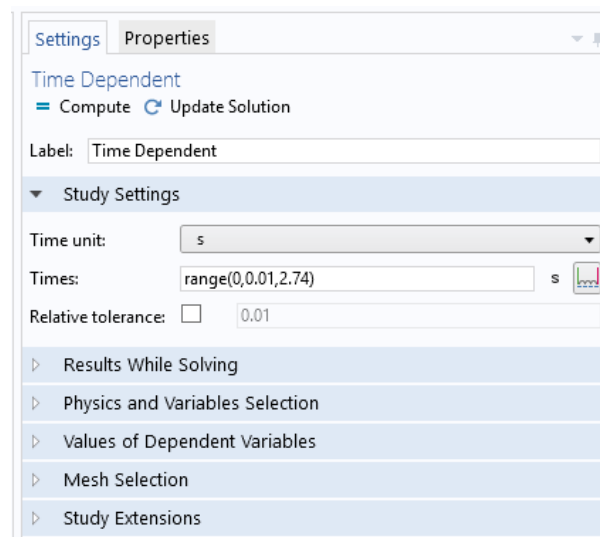


Figure 210 Solver time-steps setup.

7.2.3.2 Solver Set Up

To solve our study, a Direct solver has been chosen, precisely PARDISO. Direct solvers are good for dense matrices and can be made to avoid round-off errors to a large degree. PARDISO is a thread safe, high performance, robust, memory efficient and easy to

use software for solving large sparse symmetric and asymmetric linear systems of equations on shared memory and distributed memory multiprocessors.

The absolute tolerance accepted in the simulation was set to 5×10^{-4} .

The matrix type in PARDISO is set to Non-Symmetric; the coupling is full, set with the Newton method and terminated basing on the tolerance.

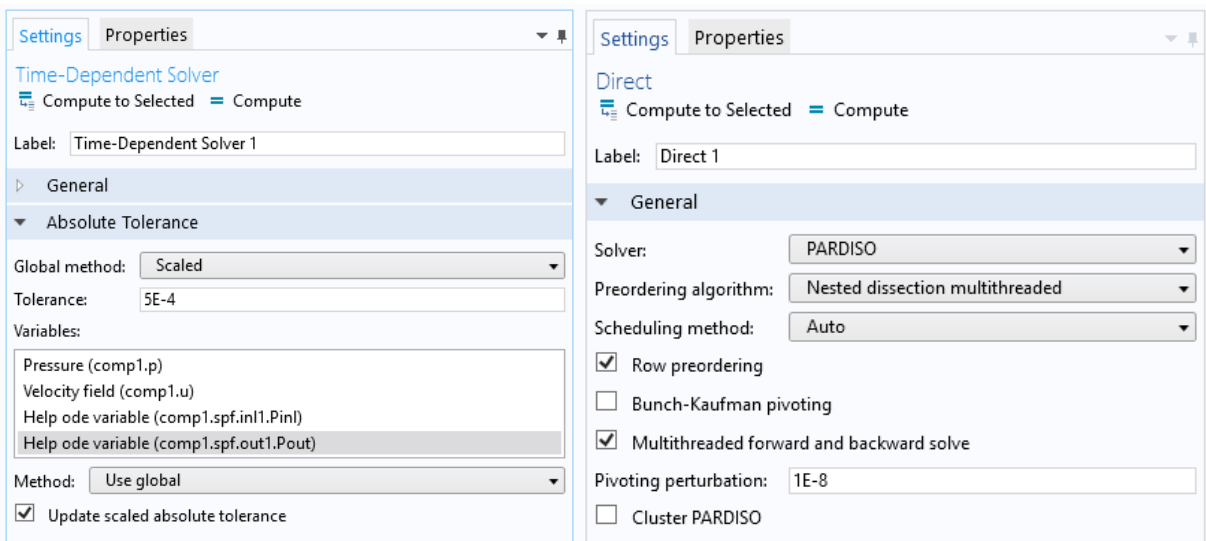


Figure 211 Solver setup.

The final simulation took 1 h 52 min to be solved, with a Reciprocal of the Time Steps plot shown below.

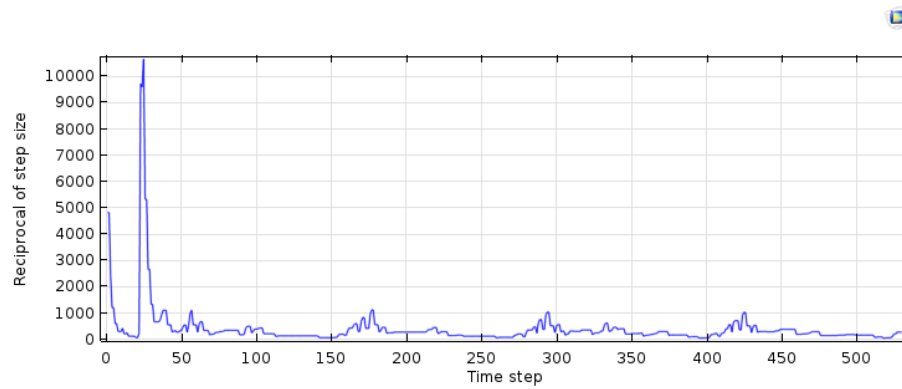


Figure 212 Simulation convergence plot.

Some instabilities should be supposed, considering the Reciprocal of step size trend. The motives could be several, starting with the mesh quality, to the solver set up, passing by the specific case study which has very particular variabilities in shape and time, besides the complex characterization of the fluid rheology. All these complications together may cause problems at the very moment of the solver running.

7.2.4 Post-Processing

Once the solution has been obtained, the results can finally be evaluated. To do that, the Post-Processing graphical tools are exploited in order to get the most useful and clear results.

7.2.4.1 Variables Evaluated

Besides the standard velocity and pressure outputs of the software, the variables described in the Pre-Processing phase are evaluated to get the most information possible from our study.

To do that, 3D Plots are generated.

7.2.4.2 Velocity Field

To the general 3D Plot of the velocity Sections results, a new plot is created with the command “Streamline”, to make more comprehensible the flow path during time. To ease the evaluation of the flow velocity magnitude, the sub-command “Colour Expression”, to colour every streamline with the local flow field velocity.

To correctly set the plot, the “Start point controlled” Positioning option is selected, and an 800 streamlines number is set to deploy from this (NB: it could be less, depending on the resolution desired).

7.2.4.3 Pressure

The Pressure 3D plot has been used to control the simulations results, but it has not been of great interest during the study. For this reason, it has not been modified a lot, but the only change consisted in a plot of the surface pressure instead of the contour lines.

7.2.4.4 WSS – WSSG - TAWSS – OSI - RRT - Reynolds number - Womersley Number

Exploiting the variable definition made in the Pre-Processing phase, it has been easy to check for complex variables as WSS, WSSG, TAWSS, OSI, RRT, Reynolds number and Womersley Number.

As previously, a new 3D Plot is created and a “Surface” plot is selected. Then in the Expression bar, the “WSS” name of the variable was typed to get the Wall Shear Stress distribution plot (NB: the variable name must coincide although an error warning is showed). Alike the WSSG, TAWSS, OSI and RRT follow the same procedure, taking care to type the relative variable name in the Expression bar.

Exploiting the 3D Plot upper control bar, the results changing on time can be shown.

Moreover, to have a more easy and visual effective idea of all the previous results, an animation could be played or exported thanks to the “Animation” tool. Here the study result variable is selected, the time results to display are chosen in the specific menu bar, and an animation of this result can be obtained or exported thanks this same tool. Attention has been paid to the setting of this tool because this procedure is very demanding for the graphic card and the processor. So the lower number of frame and quality sufficient to our purpose has to be set case by case. This operation has been operated to investigate the velocity streamlines too, helping to understand the resulting blood flow paths.

7.3 Validation

Validation amounts to checking if the model itself is adequate for practical purposes. Main steps are:

- *“Verify the code to make sure that the numerical solutions are correct*
- *Compare the results with available experimental data (making a provision for measurement errors) to check if the reality is represented accurately enough*
- *Perform sensitivity analysis and a parametric study to assess the inherent uncertainty due to the insufficient understanding of physical processes*
- *Try using different models, geometry, and initial/boundary conditions*
- *Report the findings, document model limitations and parameter settings.” (119)*

Of all these steps, not all could be affordable or possible. For example, the lack of a real MRA scan caused the impossibility to compare the simulations results with the real situation captured by this technique.

Sensitivity analysis is one of the most interesting operation to undertake in the future, due to the possibility of capturing most influent factors in AVF maturation. Here, however, because of the lack of time and the focus on the development and validation of the entire technique, rather than focusing on the specific application of this technique, it has been chosen to postpone the sensitivity analysis after the validation of the entire procedure through comparison with several MRA comparisons.

What it was done is an accurate check of every simulation setup step, an interesting variation in initial/boundary conditions to appreciate the differences in the results and then, finally, a small report of the results obtained.

Moreover, some comparisons could be possible with some Ultrasound Colour-Doppler Scans specifically demanded to the hospital operators, in which the blood flow magnitude and paths can be recognised.

7.4 Results

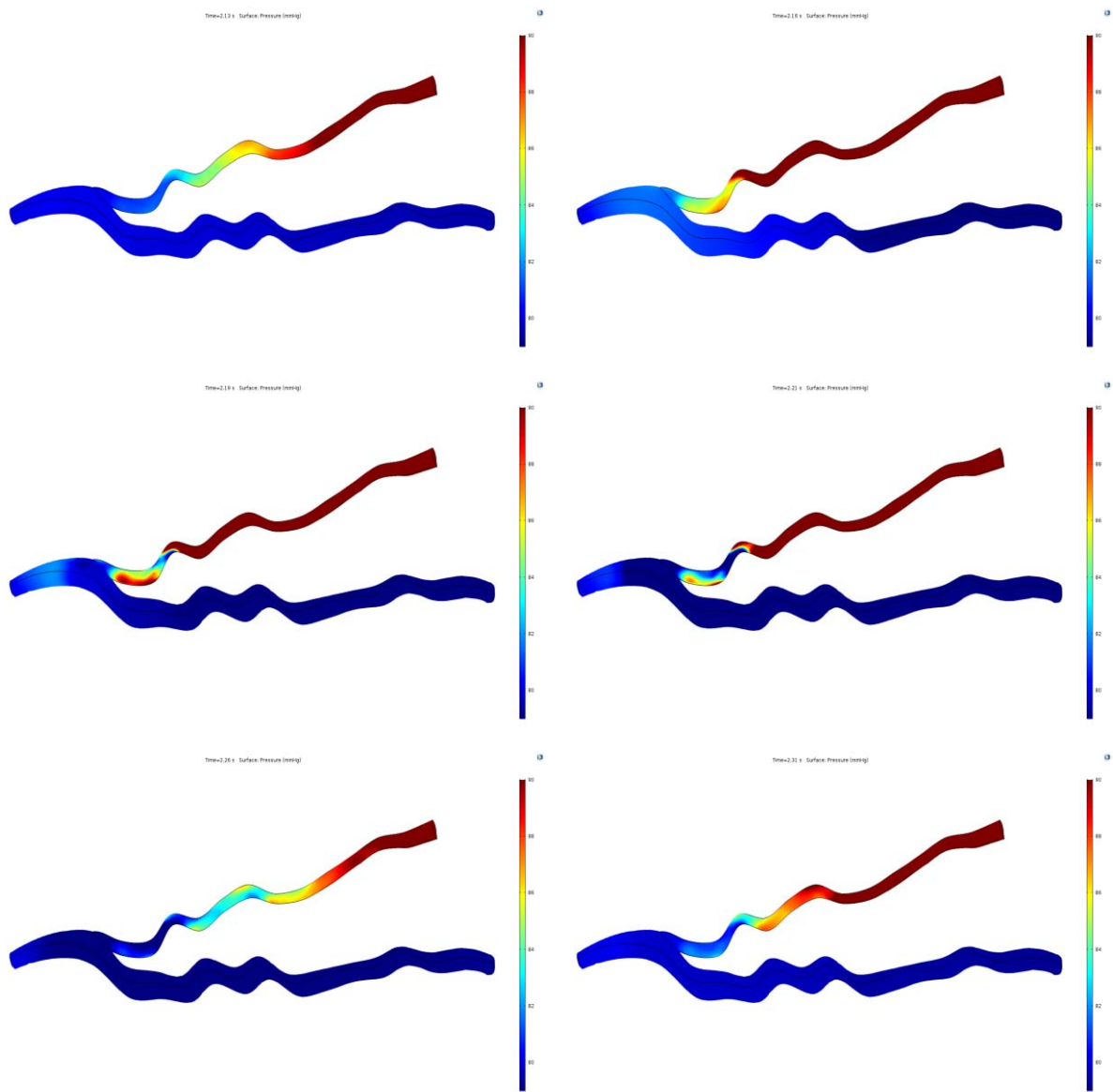
Here below the results of the final simulations can be appreciated. Every parameter has been evaluated over time, being the simulations time dependent. Worth to note that the peak values of every parameter appeared every time at the systolic peak (corresponding to the inlet velocity pulse wave peak), which has been taken as reference and limit for the different results.

For cumulative parameters as TAWSS, OSI and RRT the evaluation has been done considering all the four pulse wave cycles, obtaining a good average result of them.

Every image exposed has been captured from the last of four identical pulse wave cycles, to ensure a good stabilization of the fluid flow during time.

The considered pulse wave starts at 2.10 s, ends at 2.74 s and endure for 0.64 s (corresponding to the 93 BPM cardiac frequency), with the systolic peak at 2.21 s.

7.4.1 Pressure



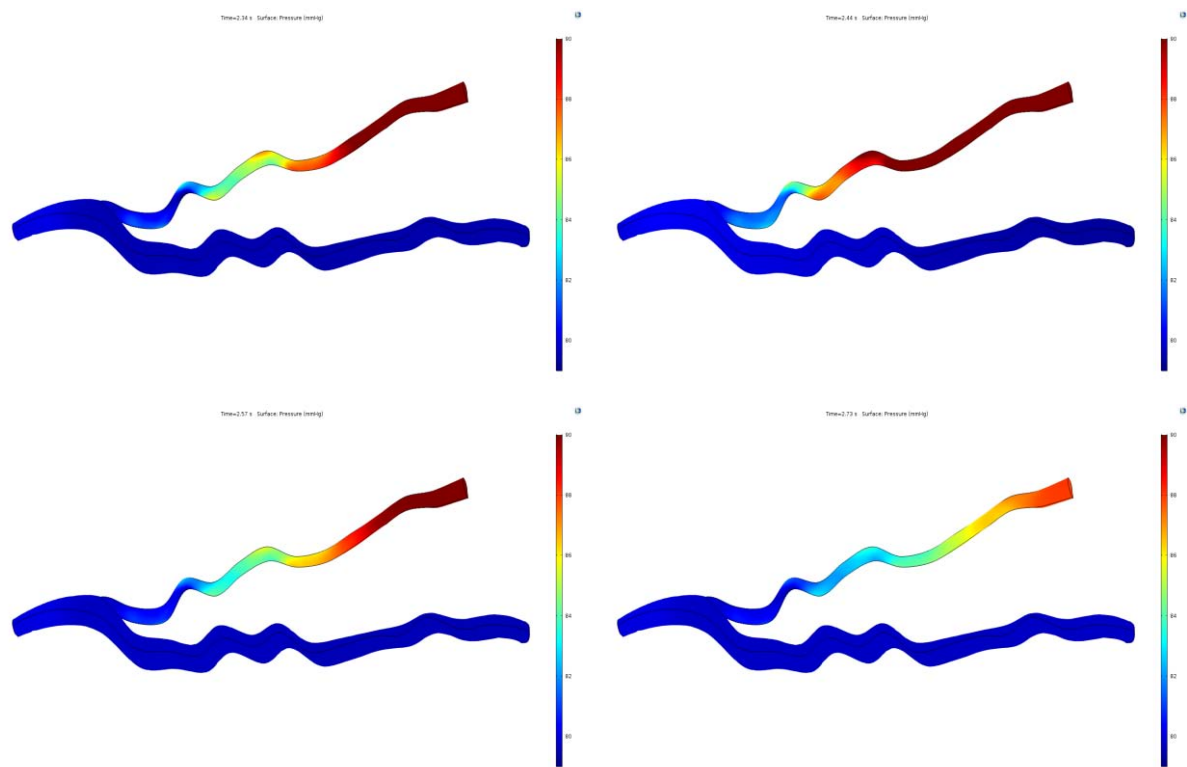


Figure 213 Pressure development by time.

During the cycles, the pressure has been seen varying in a very short range of values around 95 -79 mmHg as expected. These values are very dependent on the Outlet pressure boundary condition, which has been set to 80 mmHg constant.

The distribution along the vessels appears in every case correct, presenting a higher pressure in the artery inlet, an intermediate pressure at the artery outlet, and a lower pressure at the vein outlet.

This was considered reasonable, being the inlet artery the source of both pressure and velocity input and the higher-pressure side of the vascular system. Regarding the output artery, there are fewer data and information to ensure the accuracy of these distributions. Considering how is structured the vascular system of the forearm, with the ulnar and radial arteries in a closed loop by the palmar arch, it is reasonable that

the pressure at the end of the palmar arch could be lower, having drained all the hand before reconnecting to the radial artery.

For the venous output, which is the final part of the vessels structure and the lower pressure side of the vascular system, the pressure has been considered consistent, being the venous system at a very low pressure, even not knowing the exact situation in this zone. Some speculations could be made on the exact Arterial Outlet pressure boundary condition to achieve the most physiological pressure magnitude at the Venous Outlet and Arterial Inlet.

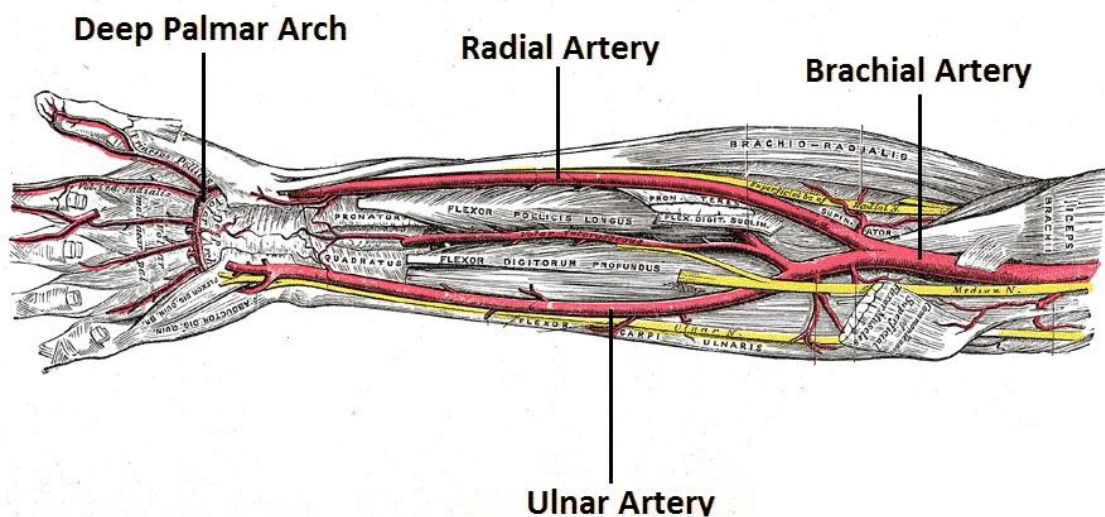


Figure 214 Forearm vascular anatomy.

7.4.2 Reynolds Number

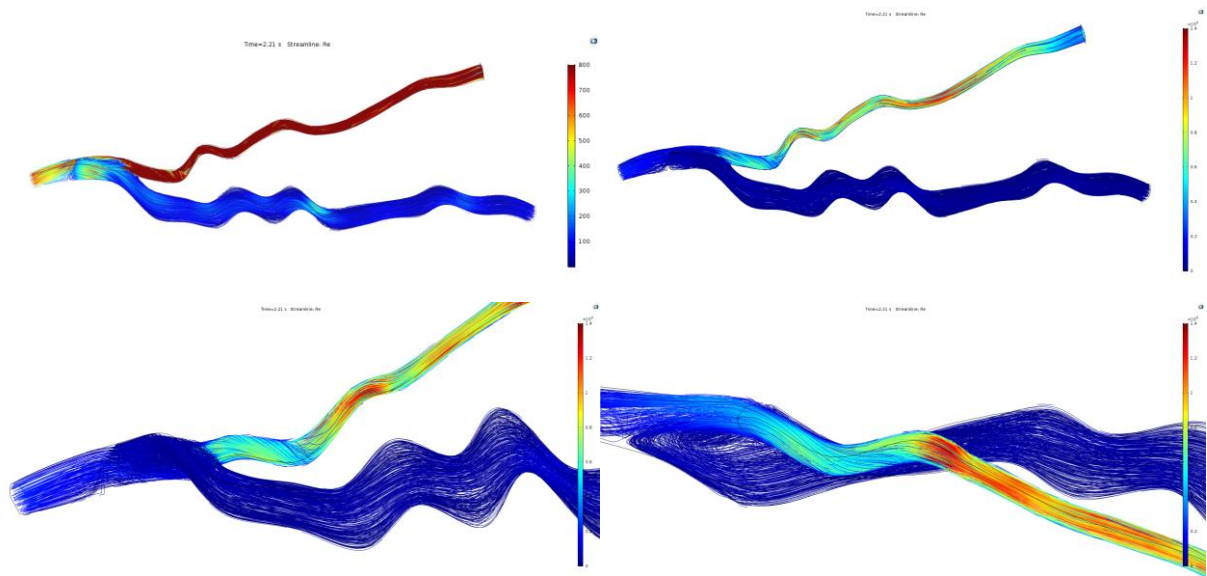


Figure 215 Reynolds number streamlines at the velocity peak.

Considering the previous studies based on simple data, it is possible to notice some discrepancies on the Reynolds Number.

The Reynolds Number predicted at the systolic peak was 965, where in the simulation, depending on the cardiac phase, this value reaches a maximum of 1400 at the same moment. The possibility of unsteady, transitional, or even turbulent flow in this condition could suggest more attention to the selection of the Laminar flow for this study. However, these values are the very maximum values of the systolic peak, where velocity is very high for a very short period if compared to the total cycle time. During the velocity peak turbulence or unsteady flow can even occur, but looking at the results it appears only on the arterial side, where a little less attention could be paid to this factor (it was

demonstrated how principal AVF failures and problems happens for the fluid flow induced stresses on the venous side).

Besides, during all the rest of the cycle, the results are still consistent, with an average Reynolds Number below 1000, and suggest in every case the Laminar Flow choice as the better one.

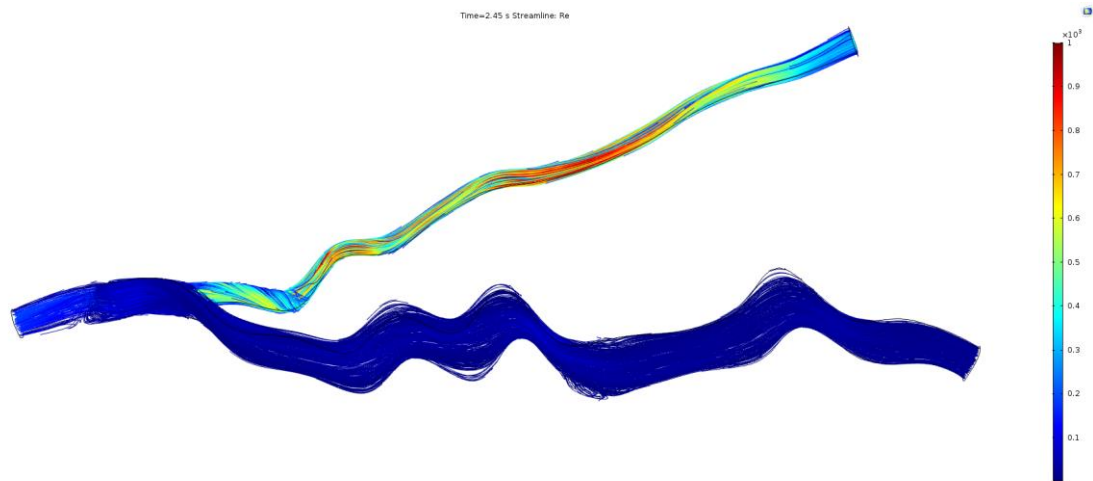
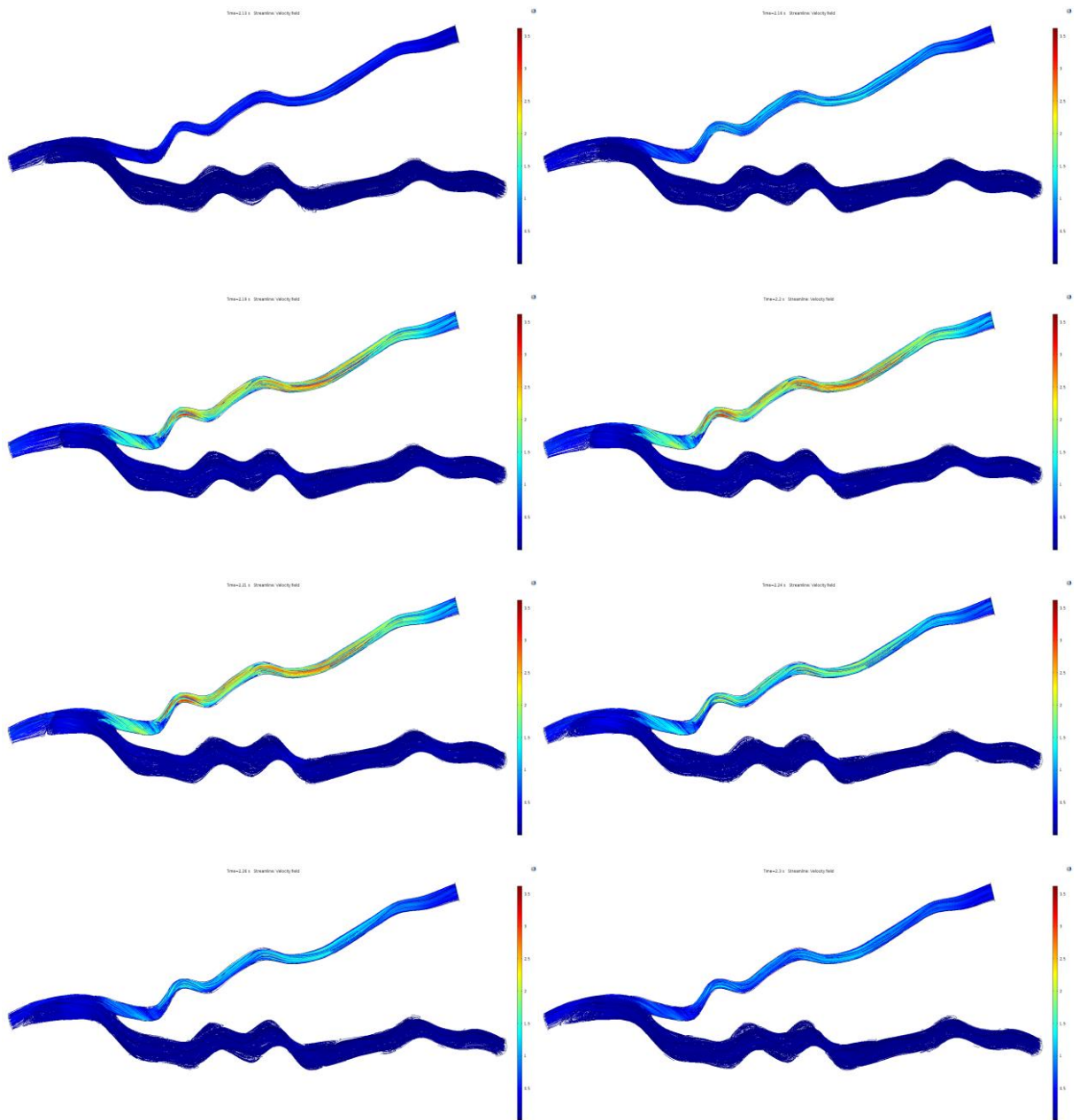


Figure 216 Reynolds number streamlines off the velocity peak.

Therefore, under the flow type studied there has not been any surprise, with the resulted Reynold Number quite close to the predicted one, except for some locations on the arterial side at the very high flow phase of the cardiac cycle.

7.4.3 Velocity Profile

All the below images are referred to velocities in m/s.



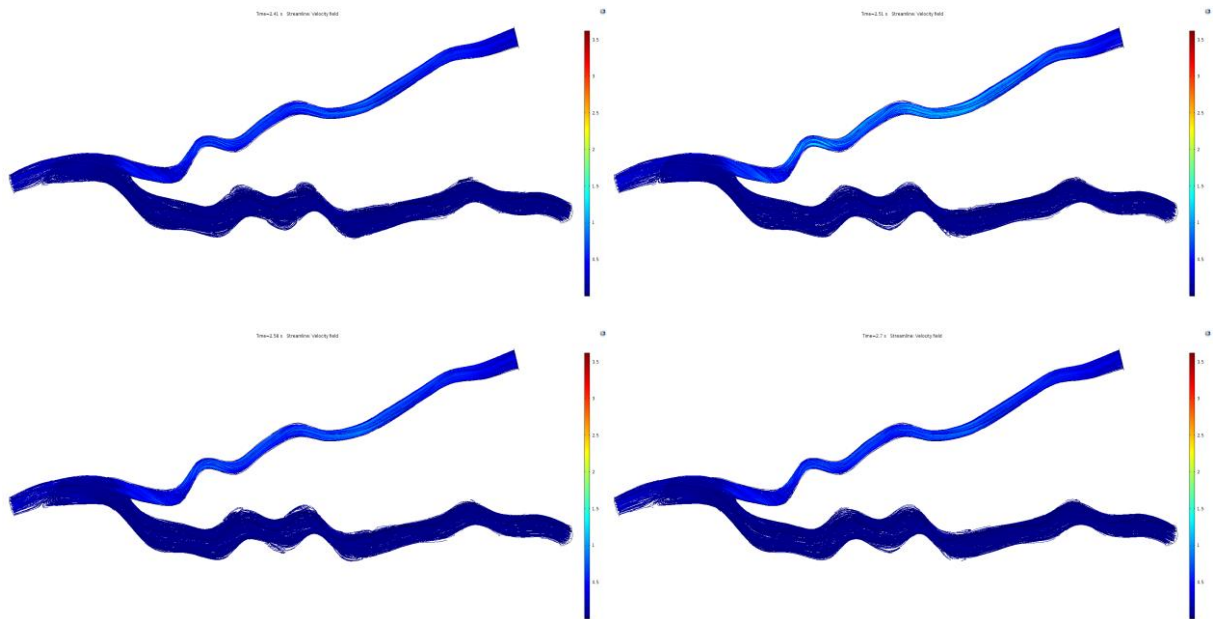


Figure 217 Blood flow velocity streamlines by time.

The velocity profile during one entire cycle has been considered one fundamental parameter to evaluate how blood flow develops during the cardiac cycle, and where instabilities and physiological flow patterns occur along the vessels.

The arterial input presents the highest velocity values all along the cycle, with a velocity peak of 81 cm/s and an average velocity of 32 cm/s. The arterial output velocity peak is 59 cm/s and an average of 24 cm/s. The venous output velocity peak is 10 cm/s and an average of 4 cm/s. Along the entire system, the velocities reach maximum levels above 100 cm/s on the narrowest sides of the artery, with the venous side not exceeding the 25 cm/s.

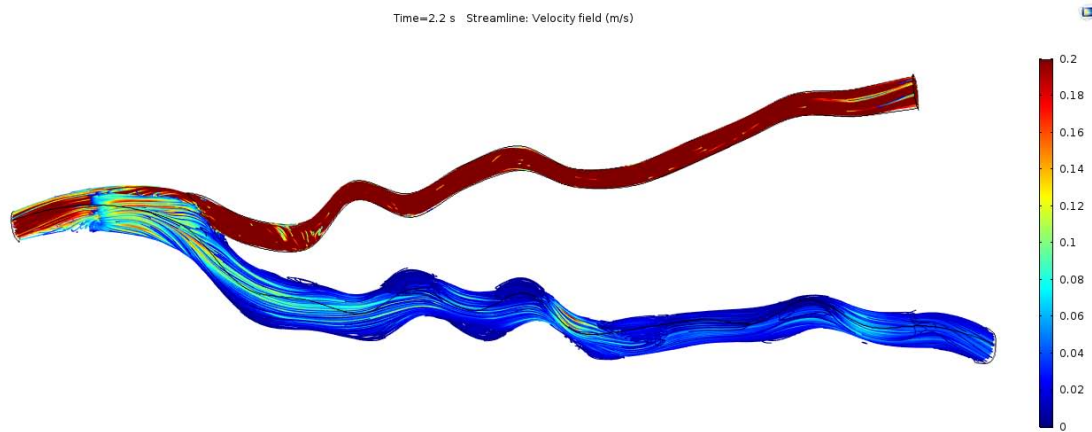
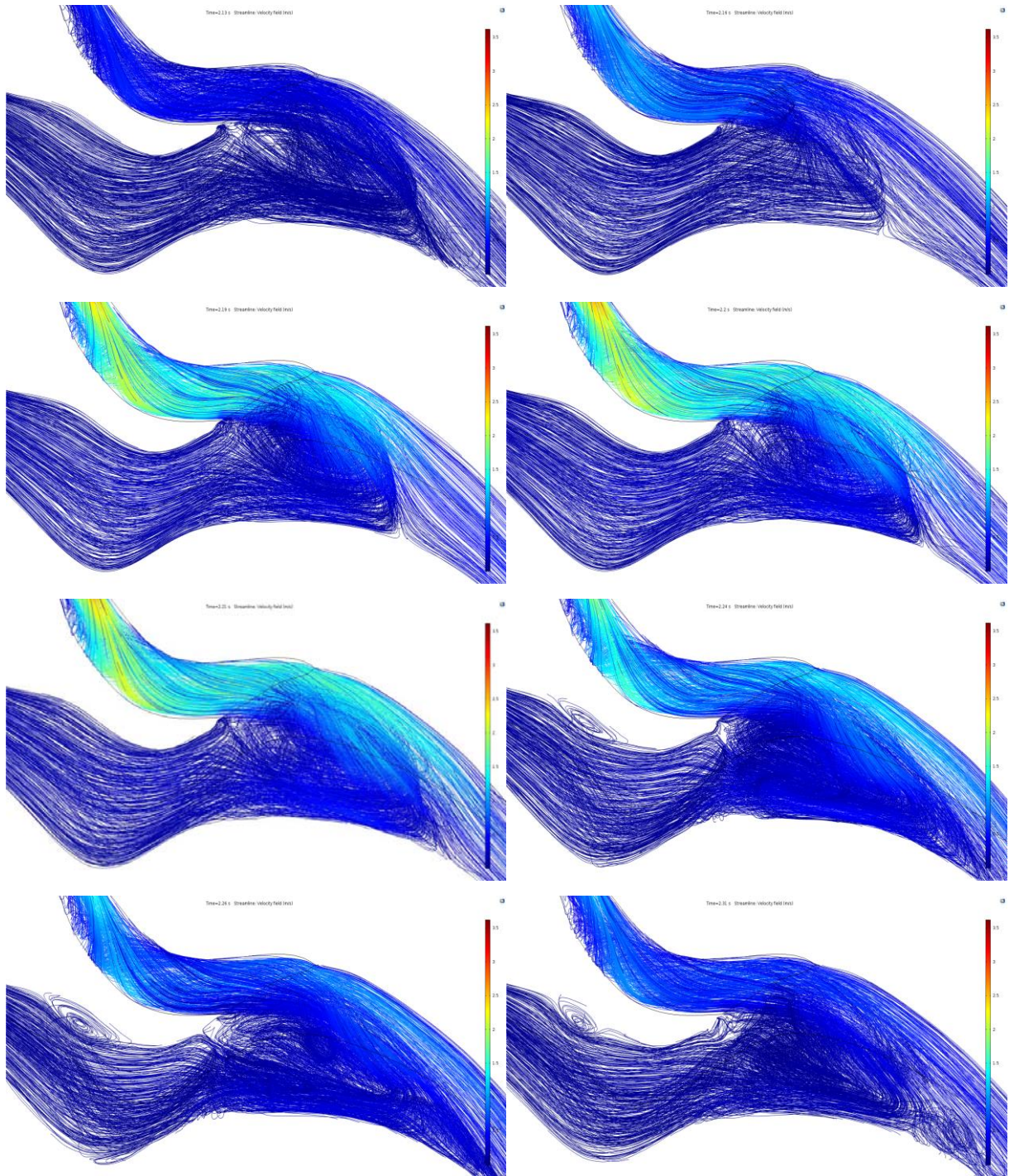


Figure 218 Blood velocity streamlines at the systolic peak with a different colour range.

The image of the entire vessels structure shows the velocities discrepancy between the arterial and the venous side of the AVF, because of the large difference between the vessels cross sectional areas. Another particular that is clear is how veins curvatures play a leading role in affecting the blood flow. It is clearly visible how in the venous swellings blood tends to form vortices and unsteady behaviours during the entire cycle. This behaviour is very influenced by the non-stationarity of the problem, with the blood accelerations, and specially decelerations, causing the detachment of the confined flow of the fluid stream. This is very clear at times 2.41 and 2.51, where recirculation occurs and then disappears.

How we will see, this peculiarity will cause particular effects on the stresses on the veins wall, regarding the magnitude and especially the time variability of these throughout the cardiac phases.



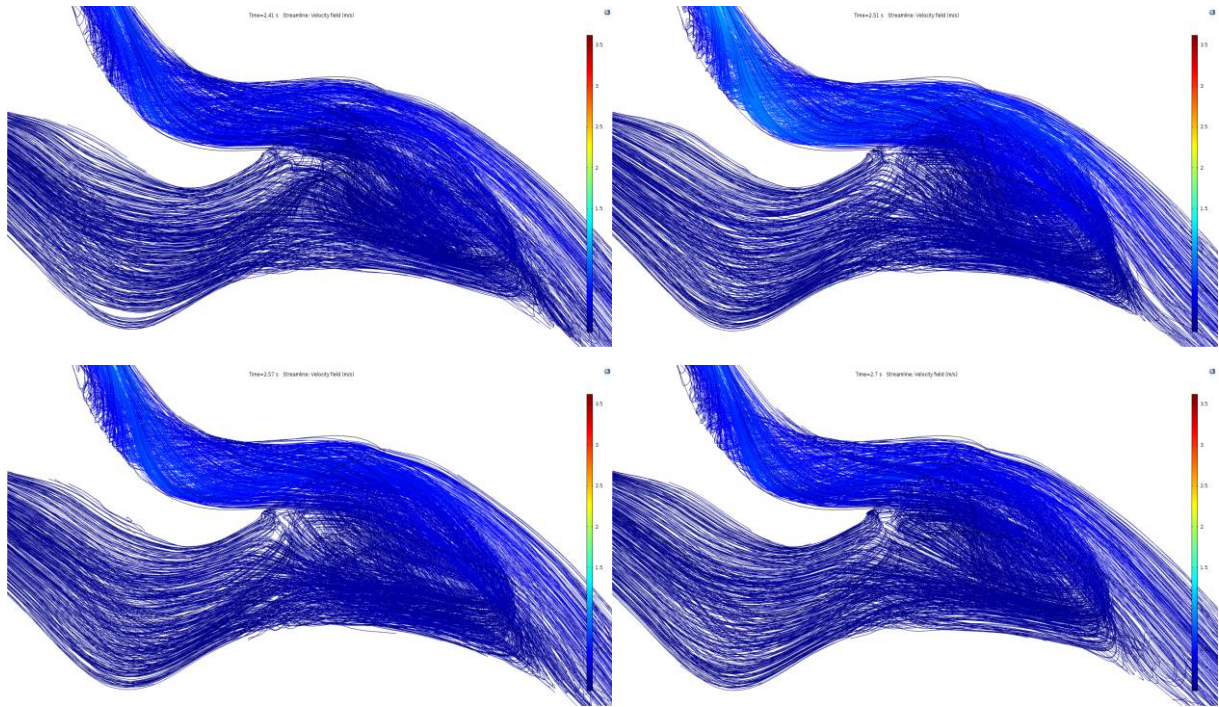


Figure 219 Detail of the velocity streamlines by time at the anastomosis.

Focusing on the anastomosis, it is possible to notice complex flow patterns developing at the systolic peak in this region, meaning that in this particular phase the flow cannot follow a clean path.

This behaviour continues and propagates even after the peak, trying to restore a more stable flow around the anastomosis internal borders. After the peak, the flow deceleration causes detachment of the flow stream right after the internal corner between the vessels, with some traces of recirculation and backflow (clearly visible at time 2.26 s) on both the arterial and venous prosecution of the AVF.

How exposed in Chapter 2, these abrupt changes and non-physiological curvatures are very important to be studied and taken into account, being the geometrical players in AVF maturation success.

The presence of some disturbed flow at the very close region of the anastomosis suggests further studies to verify if the laminar blood flow model is still valid or should be discarded, preferring a turbulent model.

7.4.3.1 *Flow Rate Check*

Starting with the velocity results at the inlet and outlets. A conservation of mass check is operated, to control simulation errors and verify main blood flow direction in the arterial output, which is not controlled by flow rate.

First, the time and spatial average of the velocity at every entrance and exit is computed, then these velocities are combined with their relative cross-sectional area obtained by the CAD software to evaluate the Volumetric Flo Rates.

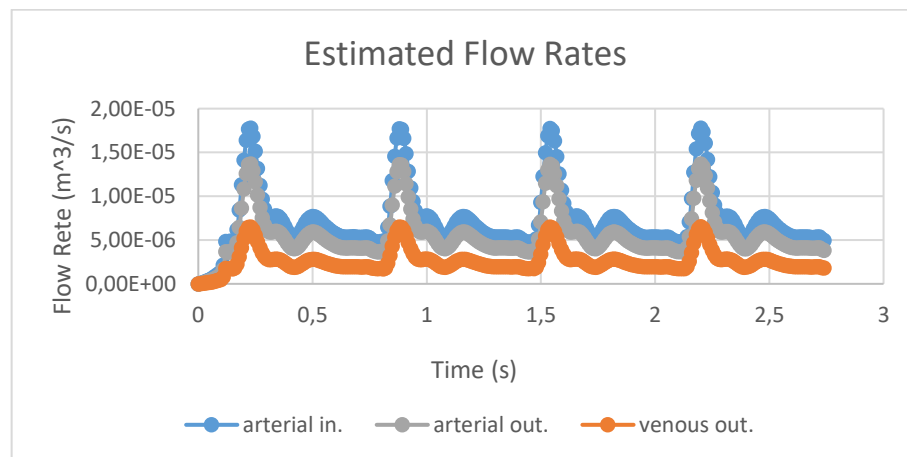


Figure 220 Flow rate check: Estimated Flow Rates from the average velocity and the borders cross-sectional areas.

Then a surface integration of the velocities on the respective entrances/exits is operated exploiting the COMSOL Extended Variables Tools, obtaining the resulting Volumetric Flow Rates.

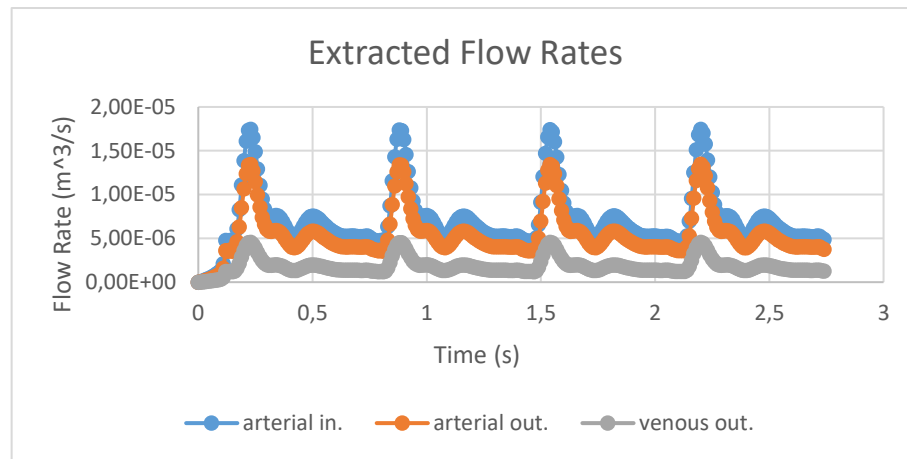


Figure 221 Flow rate check: Extracted Flow Rates from the Comsol Integration tool.

7.4.3.2 Arterial Outlet Flow Direction Evaluation

Thanks to the previous results, it has been possible to evaluate the average flow direction at the arterial outlet. Two cases have been studied: No Backflow, where the arterial inlet flow exits from both the outlets, and Total Backflow, where the arterial outlet acts like a secondary inlet. The related formulas are:

$$A_{in} = A_{out} + V_{out}$$

and

$$A_{in} + A_{out} = V_{out}$$

Subtracting the first terms to the second ones, the average discrepancy in the Mass Conservation equation.

For the estimation with the average velocities we obtain:

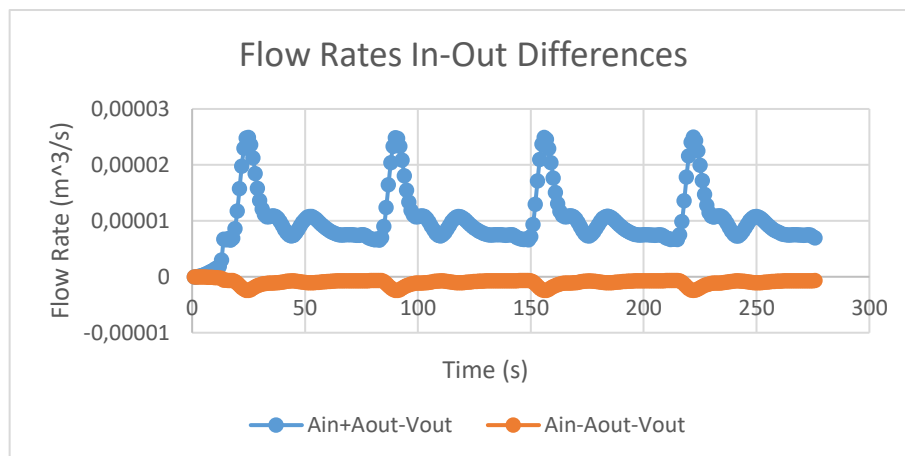


Figure 222 Backflow check: Flow Rates In-Out Differences with the average velocities.

And for the extracted integrals the result is:

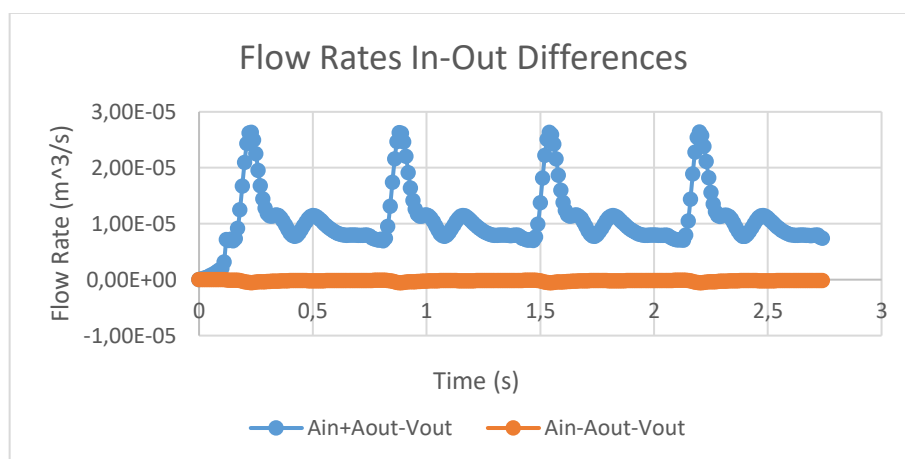


Figure 223 Backflow check: Flow Rates In-Out Differences with the Comsol Integration tool.

The results appear pretty clear, with the Backflow not present in this specific case, being the conservation of mass better respected, with an average error of $2.26 \times 10^{-7} \text{ m}^3/\text{s}$.

7.4.3.3 Discrepancies

To evaluate the discrepancies between the two strategies followed, which in theory should provide the same results, an analysis has been operated on the respective results:

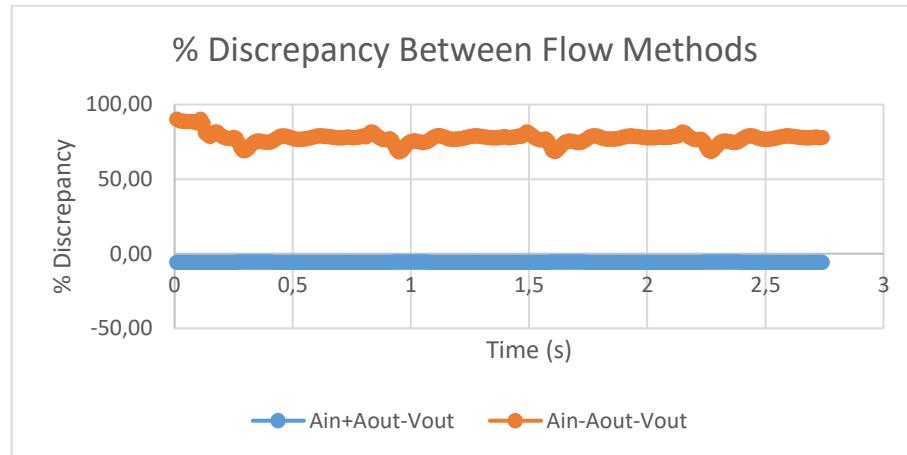


Figure 224 Backflow check: % Discrepancy Between Flow Methods.

It is interesting to see how the integral and average methods present a lower error (5.6%) for the wrong configuration with backflow, and have a very high discrepancy on the right configuration (77%). These results deserve more studies, but the hypothesis is that the errors are higher on the right configuration because of the lower error from the ideal mass conservation, enhancing all the differences between the two methods.

The source of the discrepancies between the two methods instead, have to be attributed to the differences in the evaluation of the cross-sectional areas between the two software, and the consequent techniques used to average the velocities.

7.4.4 Wall Shear Stress

In the next pages, different colour ranges for the most characteristic times of the cardiac cycle are shown to better illustrate the stresses distribution along the artery and the vein and their different magnitudes.

- Colour range 0-5 Pa:

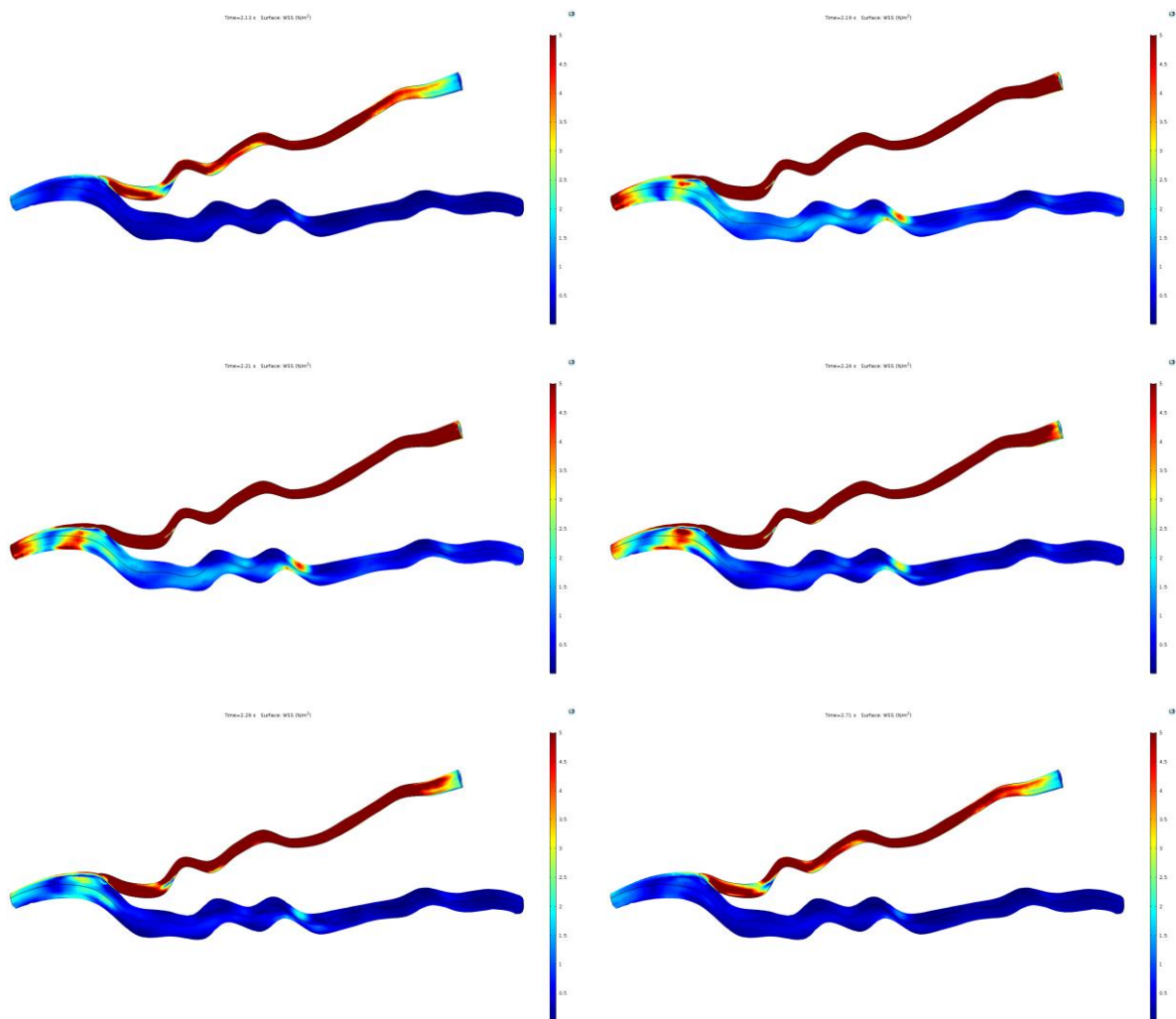


Figure 225 Wall Shear Stress by time with a low colour range by time.

With the lower colour range, it is possible to appreciate how the stresses are distributed on the venous side, which has been pointed as the more sensible to them.

The higher stresses occur at the systolic peak, and the maximums are close to the anastomosis, with a spot on the venous narrowing. The WSS peak values on the venous side are around 6 - 7 Pa. The presence of these relatively high stresses on the two locations detected means that the remodelling in these places should be still to be finished.

The average WSS distribution all along the rest of the vein indicate that here a sufficient vascular remodelling has occurred, bringing the WSS values again into physiological values of 1 - 2 Pa, congruent with the physiological results on this regard cited in Chapter 2.5.3.

Regarding the arterial side, a better analysis is now undertaken.

- Colour range 0-35 Pa:

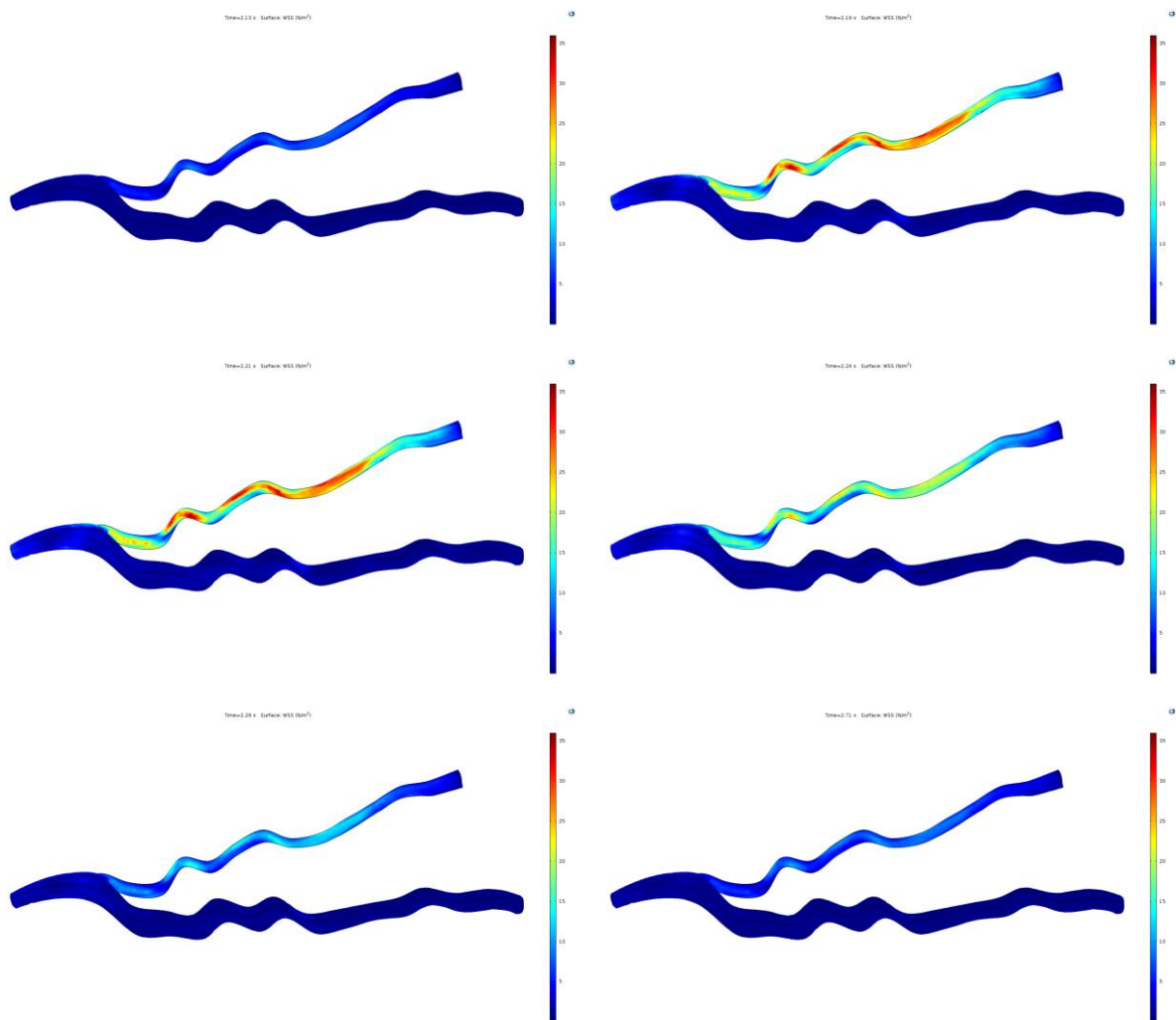


Figure 226 Wall Shear Stress by time with a large colour range.

With this higher colour range, it is possible to appreciate the WSS distribution along the feeding artery.

Here some non-physiological and very high values for the shear stresses are detected.

The higher stresses occur at the systolic peak, in the locations where curves or non-straight paths of the artery occur. In these regions, the WSS reached values above 35 Pa. For the rest of the cardiac cycle, the values are around 20 Pa, for the times just after the peak, and stabilised 10 – 15 Pa for the remaining times.

Even if these values are high for the entire cycle, the most concern has been given to the peak values.

To motivate this, two factors have been detected:

- The higher flow caused by the anastomosis
- The formulation of the numerical model itself, which has rigid walls.

The higher flow naturally involves an increase in the wall stresses, particularly on the narrowest vessels, which is the artery. This increase is caused by the bypass that the AVF operates, with a sensible decrease of the peripheral resistance to the blood flow. Under this aspect plays an important role the vascular remodelling too. It has been exposed in Chapter 2 how arteries are less susceptible to remodelling because of their more structured muscular layers of their section. Therefore, if veins are capable of a sensible enlargement to accomplish to the new flow conditions, this does not happen enough for arteries, leaving them under these non-physiological conditions for a longer period of time.

Not less relevant is the fact that the simulation does not consider the characteristic flexibility of the vessels. The consequences of this detail are that locally, in the very time when the pressure peak of the blood occurs, the vessel enlarges to suit the increased pressure, enabling to lower the velocity peak. To achieve that in the simulations, an FSI simulation should be operated.

It is the writer's belief that the very stresses peaks occurred on the simulation could be significantly softened taking into account these two details.

7.4.5 Wall Shear Stress Gradient

For the same reasons discussed for the WSS, even for the Wall Shear Stress Gradient two colour ranges have been useful to better understand the simulation results.

- Colour range 0-900 N/m³

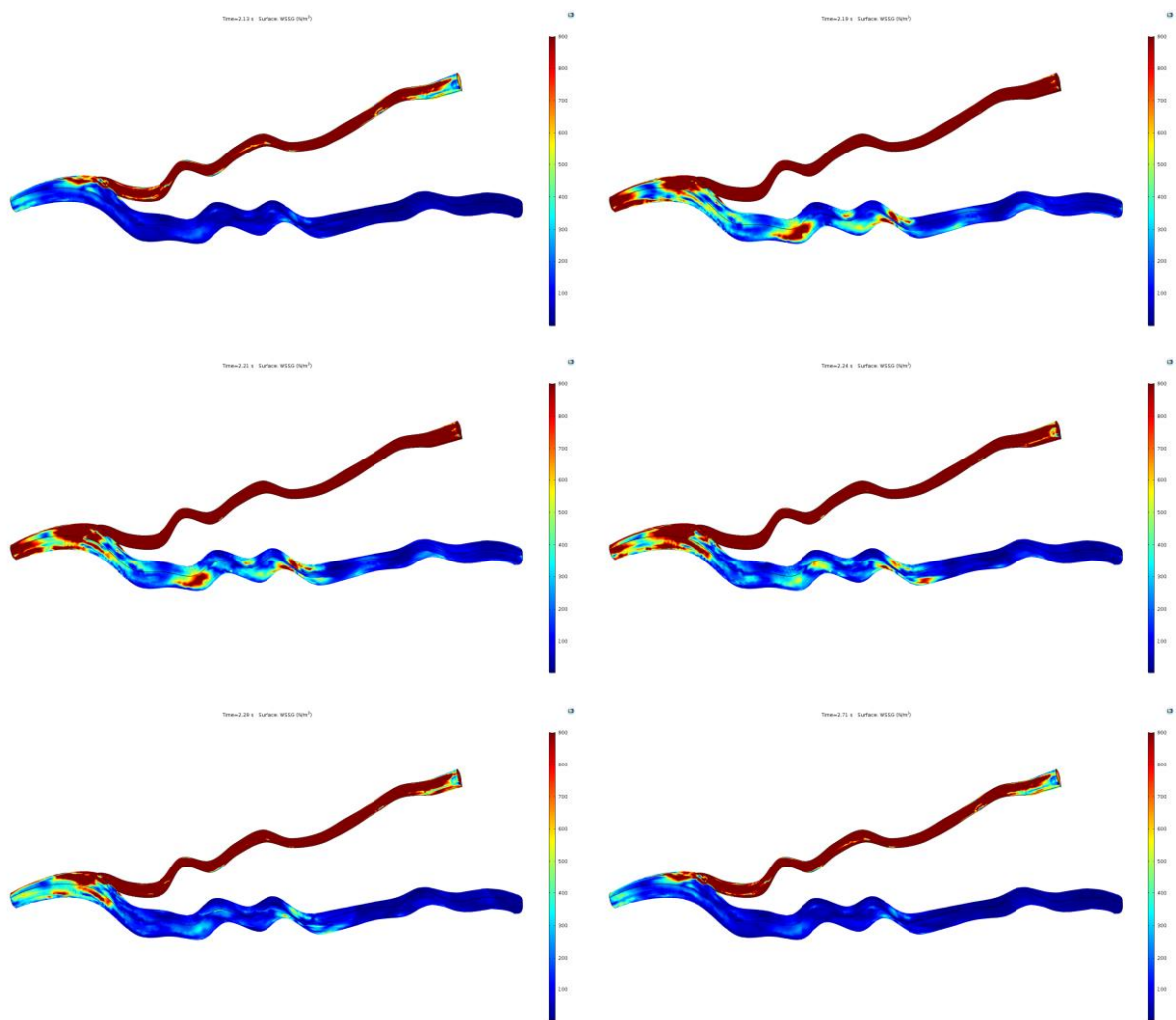


Figure 227 Wall Shear Stress Gradient by time with a low colour range by time.

Looking at the venous side, it is easy to detect the zones where the major spatial changes of the WSS occurs, resulting in the WSSG peaks.

Like discussed before, WSSG in venous segment presents lower values, with systolic peaks locally exceed 1000 N/m^3 .

The anastomosis area is the more inclined to these changes, in addition to some localised spots on the venous narrowings or curvatures.

- Colour range 0-15000 N/m^3

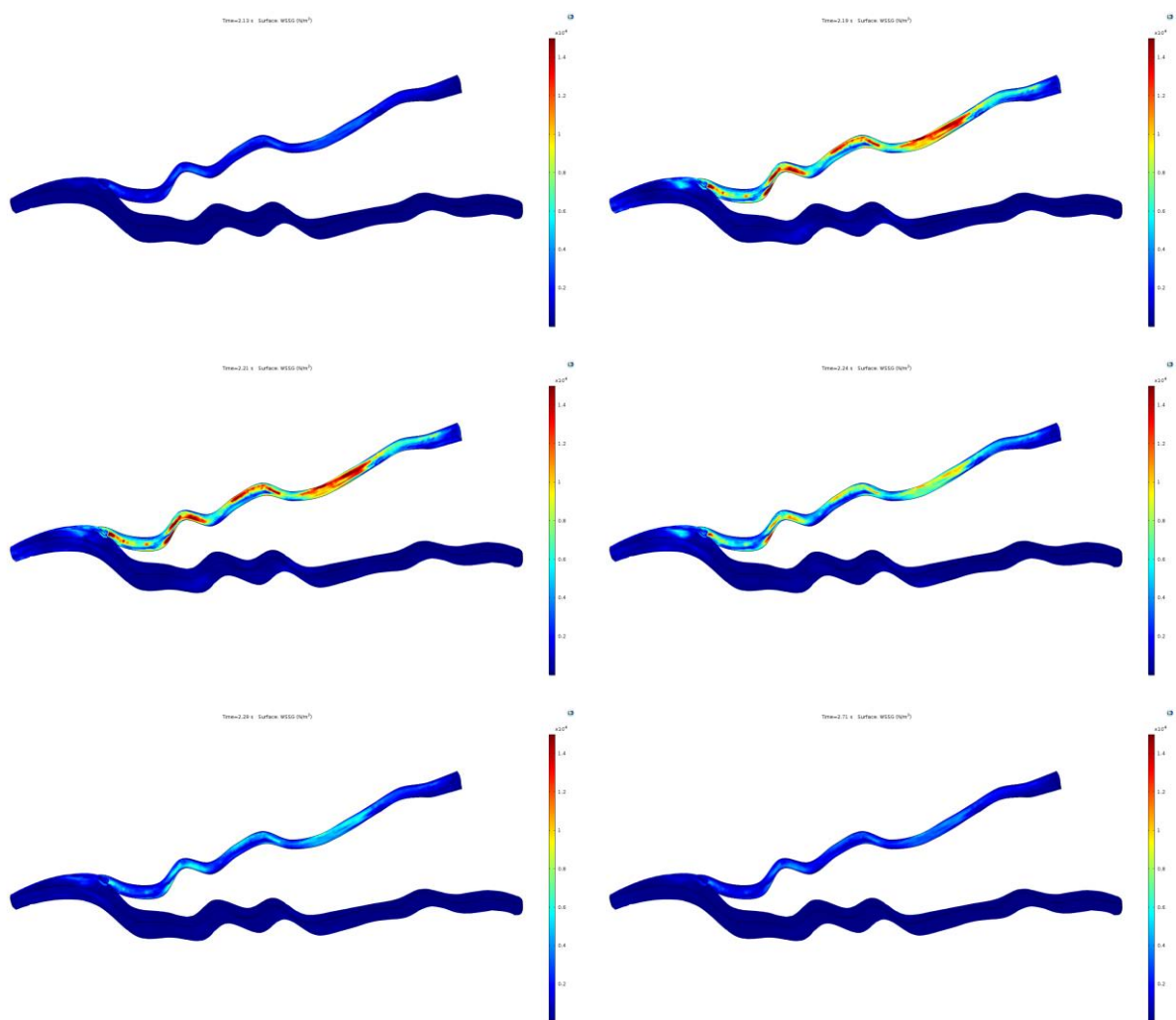


Figure 228 Wall Shear Stress Gradient by time with a large colour range.

The arterial segment presents higher Wall Shear Stress Gradients, about ten times higher than the venous side. The reason of that was attributed to the factors previously discussed for the WSS.

Moreover, here the mesh elements dimensions are believed influent, being the WSSG a spatial derivative of the WSS. The occurrence of elements too large can afflict the accuracy of the WSS evaluation and much more its derivative.

Anyway, Wall Shear Stress Gradient can provide a good indication where to look for to investigate causes of abnormal stresses concentration and variations. In our case, this occurs in the arterial curves and in the inner part of the anastomosis junction.

Similar patterns have been noticed also in the venous tract.

7.4.6 Time Averaged WSS

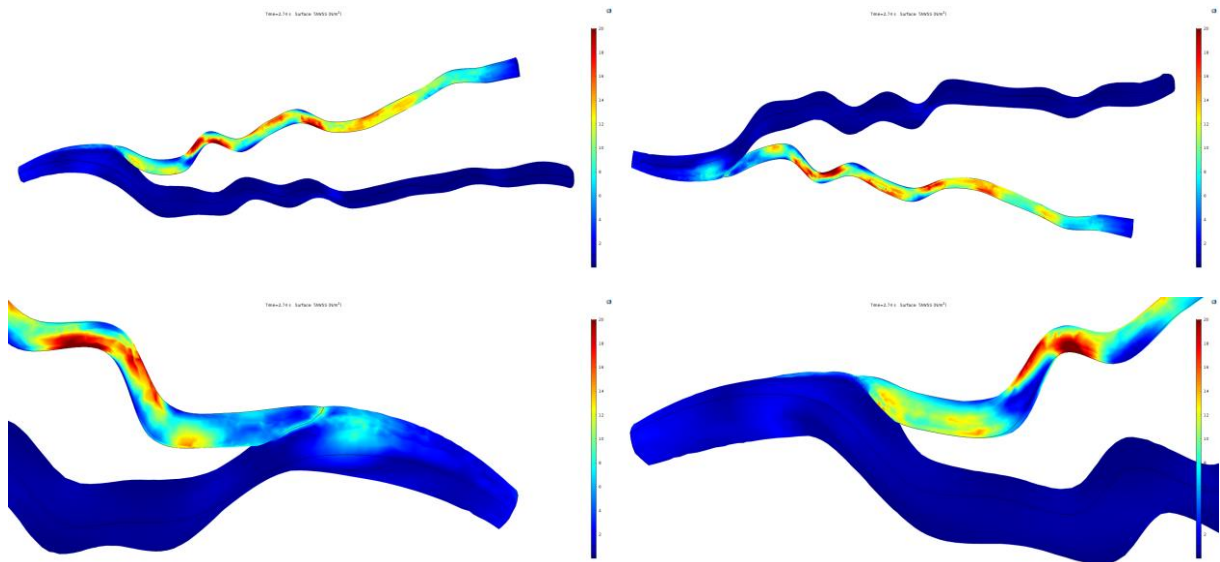


Figure 229 Time Averaged Wall Shear Stress along all the vessels and particular details with a large colour range.

Time Averaged Wall Shear Stress has been reputed the very representant of the stress the vessels walls has to face with, being the average along the all four cardiac cycles of the stresses acting on the boundary layer. That is why the magnitude and position of these results have been deeply taken into account.

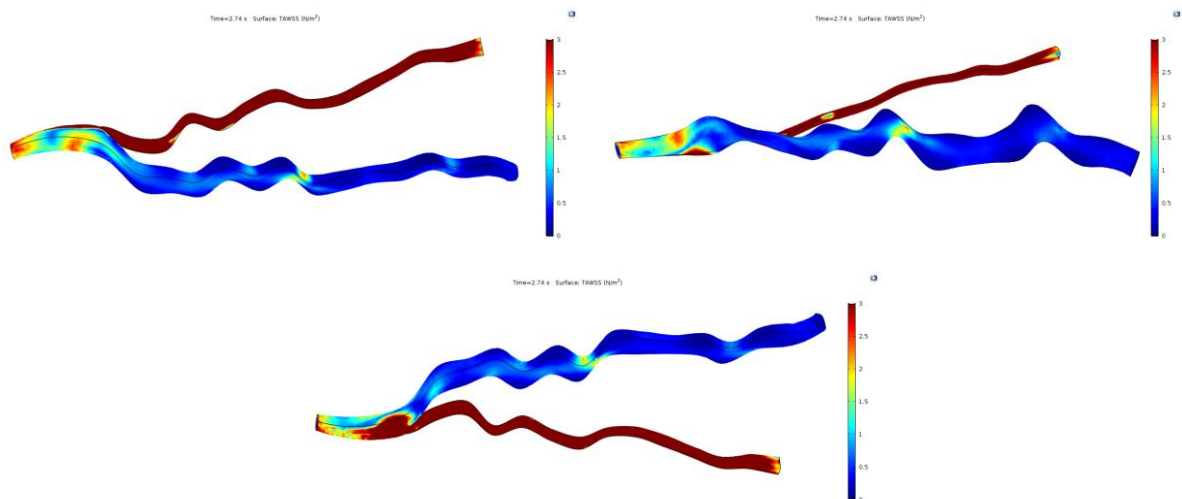


Figure 230 Time Averaged Wall Shear Stress along all the vessels with a low colour range.

Looking specifically at the range of the averaged stresses between 0 and 3 Pa, once again we find that the venous side is pretty stabilised to values under 1.5 Pa.

This is an additional confirmation of what it has already seen, that is an arterial side of the AVF dealing with very high stresses and a venous segment pretty stable to physiological values.

In this case too, the only very exception is at the anastomosis, where the sudden change in flow direction still reflects its effects on the opposite artery-connection-side of the vessels juncture, with stresses reaching the 3.5 Pa which is still high.

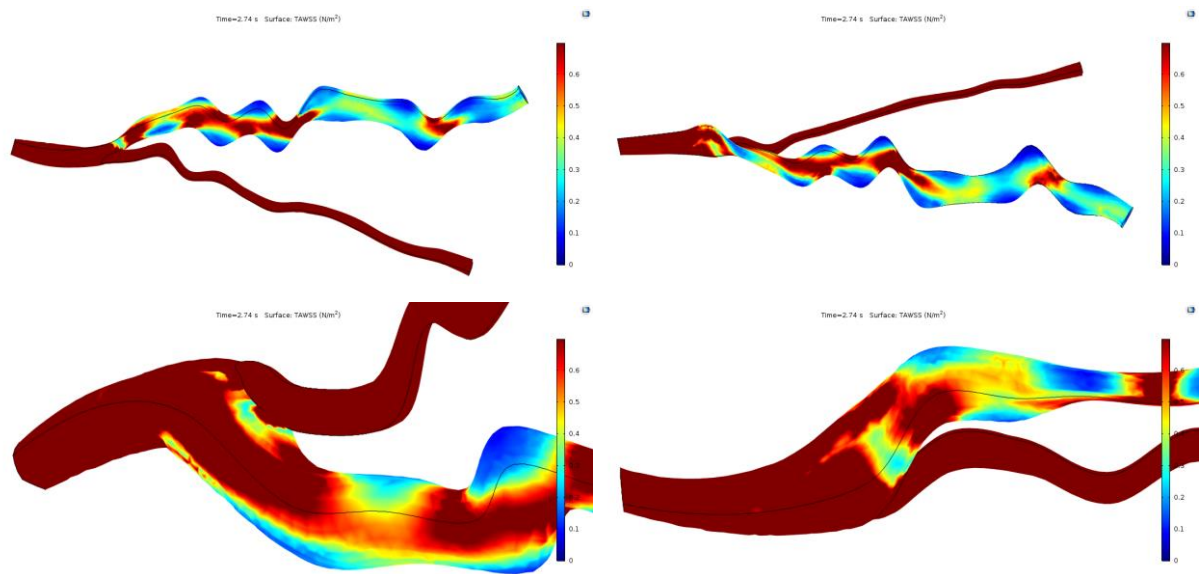


Figure 231 Time Averaged Wall Shear Stress particular details with a low colour range.

Another interesting point of view is about the very low TAWSS zones of the model. In these images, it is possible to appreciate how the regions very close to the anastomosis sharp corner and the vein meanders present a shear stress lower than 0.5 Pa. Such a low stress could be linked to problems related to negative vessels remodelling. However, this aspect will be deepened with the RRT.

TAWSS revealed to be very meaningful, containing in all the information during the heart cycles, enabling to identify the sites more subjected to average high and low stresses and allowing a better and more accurate distinction among them. The consequence of that is a better understanding of the zones more prone to positive vascular remodelling, related to high shear stress, and the zones in danger for intimal hyperplasia, stenoses and, in the end, fistula failure.

7.4.7 Oscillatory Shear Index

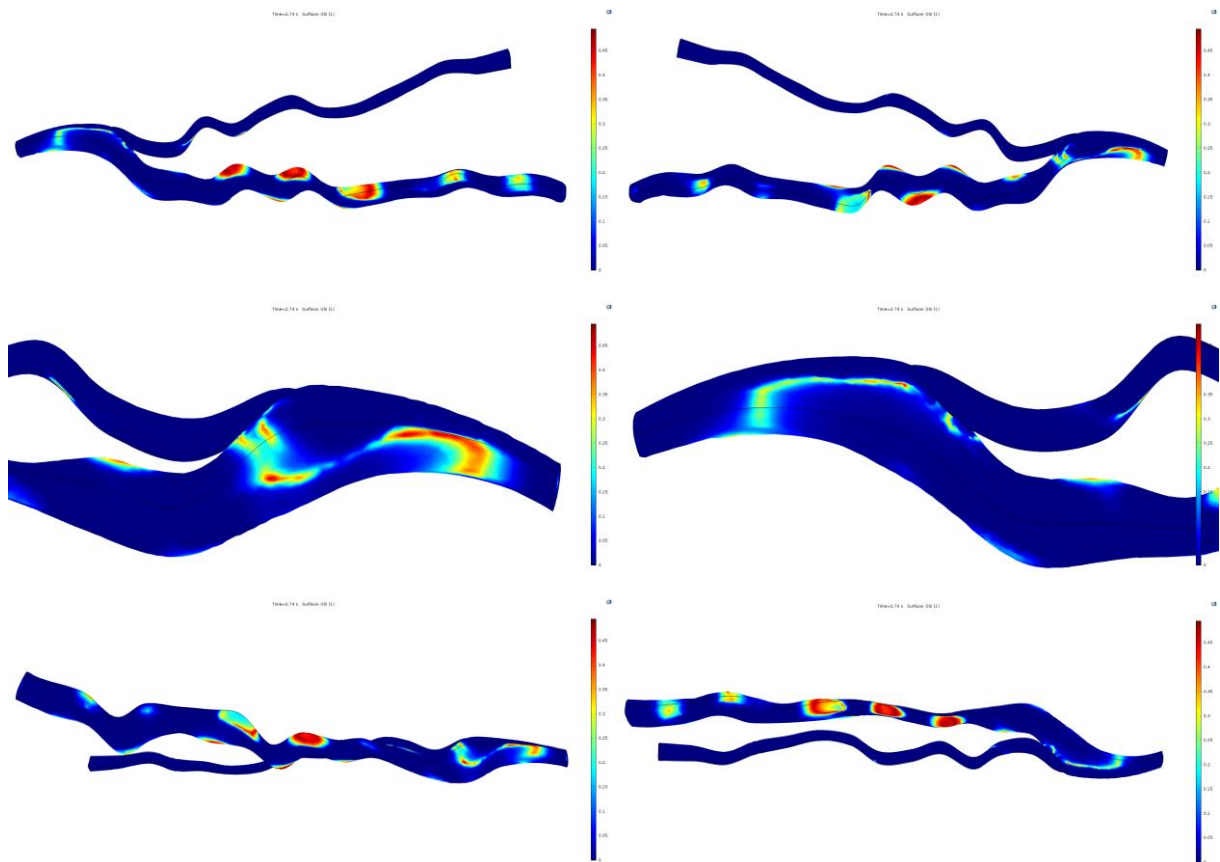


Figure 232 Oscillatory Shear Index along with the vessels and particular details.

Confirmation of what noticed before come also from the Oscillatory Shear Index analysis.

It is easy to observe that the zones with a high OSI can be easily associated with the same where GWSS presents its peaks, and here the blood flow velocity streamlines show the more disturbed behaviour. This occurs at the circumscribed zone around the anastomosis, especially at the venous side and inside the larger curves that develop along the veins proximal from the anastomosis.

The researches done about OSI and exposed on Chapter 3.1.6 explains how these zones are the most critical in studying the maturation and healthiness of an AVF, representing the zones where variable and oscillating flow and stresses occur, leading to negative endothelial remodelling, promoting intimal hyperplasia and low vessel outward remodelling.

It is possible to use OSI and WSSG to point out where the critical points are, enabling to propose new ideas to solve the problems related to these very specific areas.

7.4.8 Relative Residence Time

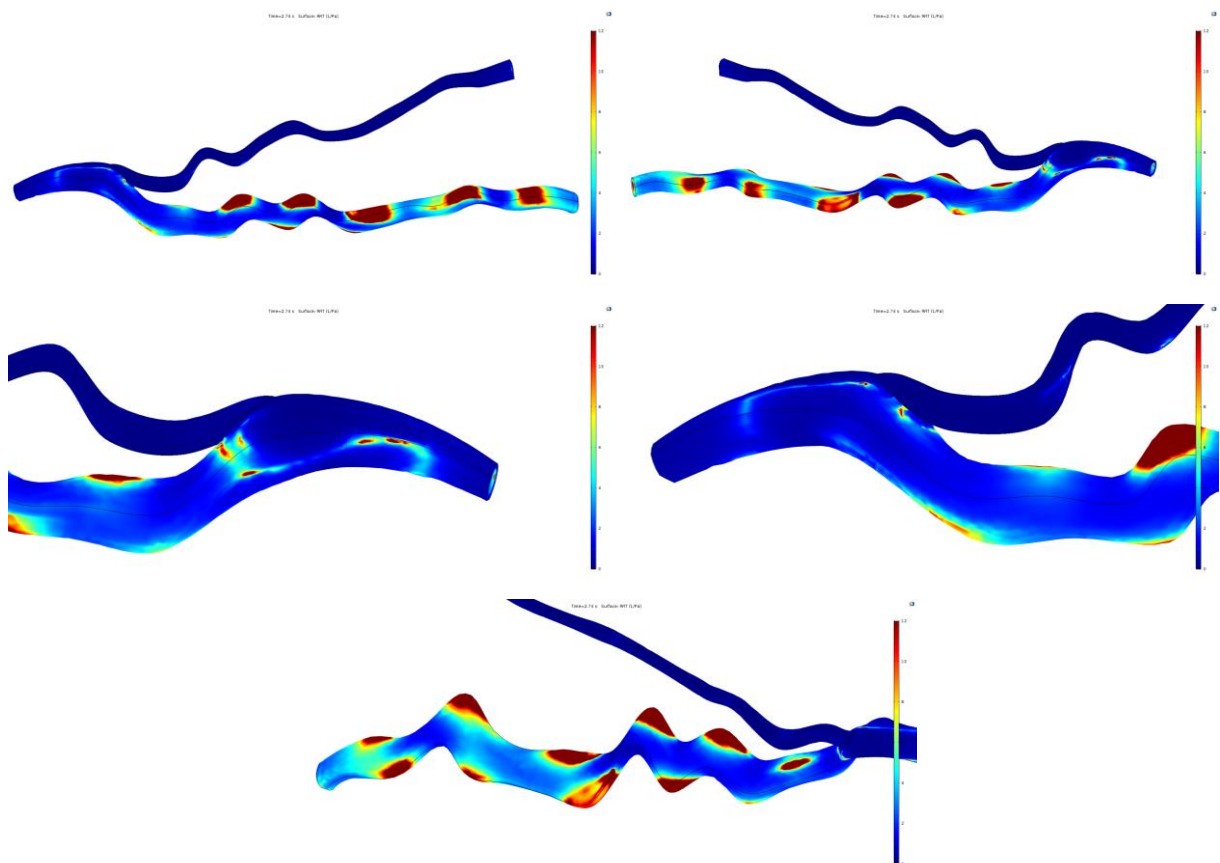


Figure 233 Relative Residence Time along the vessels and particular details.

The location of Relative Residence Time on the vessels walls shows to be consistent with the distribution of OSI and WSSG too but, because of the contribution of both oscillatory and low WSS, RRT patterns results more extended. In this way, RRT is capable to detect a larger portion of the zones of flow reversal and consequent stenosis.

In this way, it is possible to overcome to the insensitiveness of the OSI to the Shear Stress, a property which it has been demonstrated to be primarily influencing the vascular remodelling and the AVF maturation and stabilization.

“This confirms also in the AVF territory that low shear stress per se promotes IH, while the oscillatory shear may exacerbate the development of stenosis.” (38)

Other prominent texts consulted as reference for RRT assessment on its effectiveness and importance are the ones from Soulis et Al. (33) and Lee et Al. (120)

7.5 Precedent Studies

Some of the preliminary studies conducted in the process that leads to the final AVF 3D model CFD analysis have been reputed to be interesting to be exposed. This is because they can illustrate how the situation before the ArterioVenous Fistula establishing is, and what the AVF results could be.

7.5.1 Single Vessel Simulation

First of all the simulation of the 3D models of the singular artery and vein have been undertaken.

The procedure which leads to these result is similar to the one exposed, except that the vein was simulated with the same artery velocities input, to have a primary idea of what conditions the vein should deal with right after the AVF operation. This is the motivation and the cause of the strange non-physiological results just below. The boundary conditions used to run these simulations are different from the previous, being extracted from a sane volunteer, with a normal configuration of the two vessels.

The blood flow velocity:

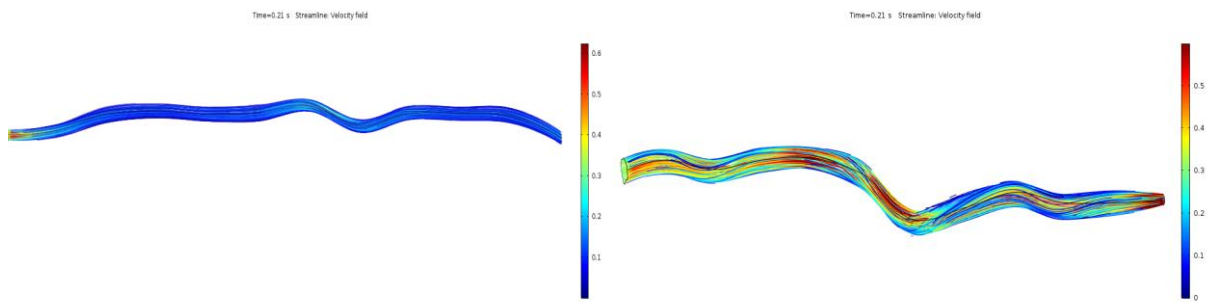


Figure 234 Single vein velocity streamlines at the systolic peak.

The Wall Shear Stress:

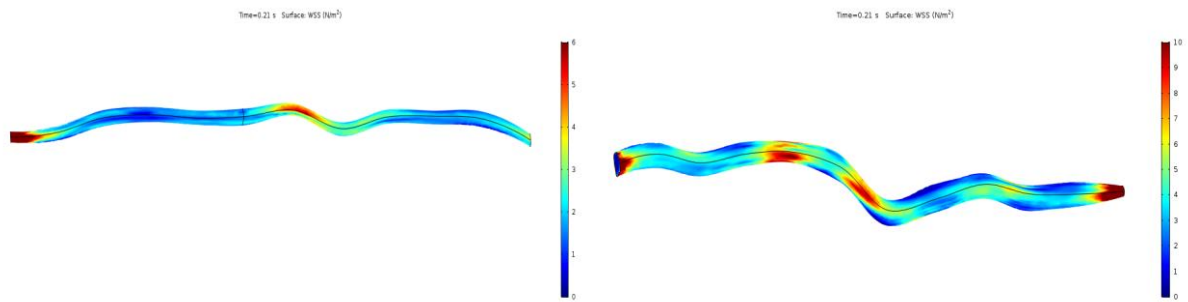


Figure 235 Single vein Wall Shear Stress at the systolic peak.

The Wall Shear Stress Gradient:

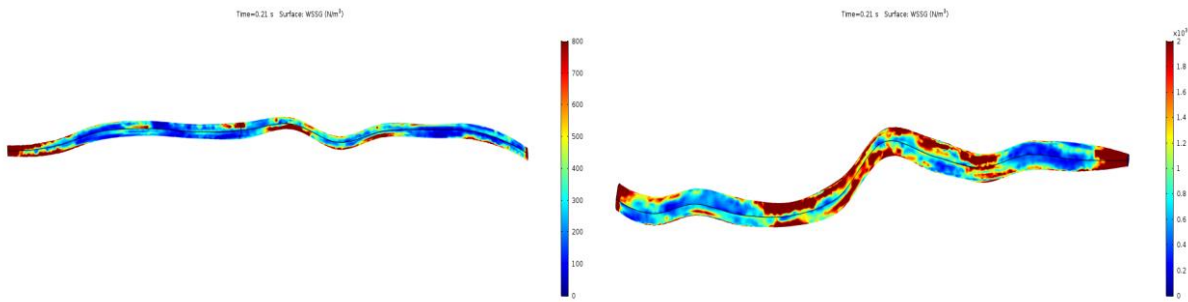


Figure 236 Single vein Wall Shear Stress Gradient at the systolic peak.

The Oscillatory Shear Index:

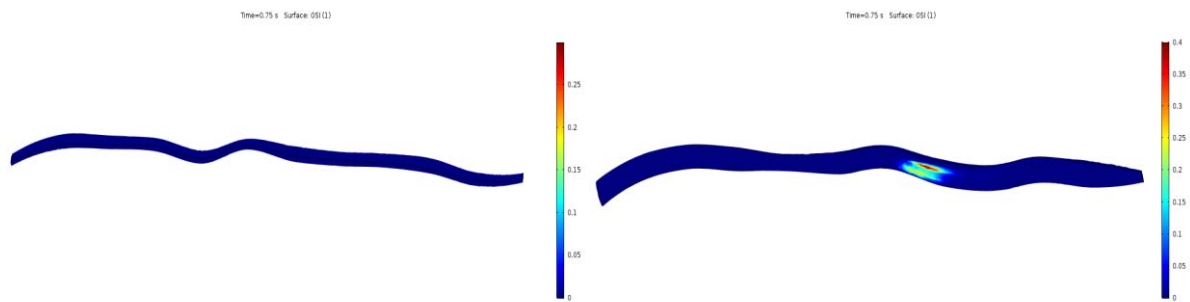


Figure 237 Single vein Oscillatory Shear Index.

7.5.2 Virtual AVF Simulation

Regarding the attempt of predicting the AVF establishment and its behaviour, the attention has been paid to trying to re-create a sensible configuration of the two vessels. Of great help in this phase has been the advice and feedbacks of the surgeon of the hospital.

More models have been tested then to evaluate the need to extend the inlets and outlets to better fit the entrance and exit conditions. This, however, has been resulted not so relevant, if not for a small zone very close to the model ends, and it has been decided to discard this model for the extra computational costs and the complexity related to this solution.

7.5.2.1 Velocity Profile

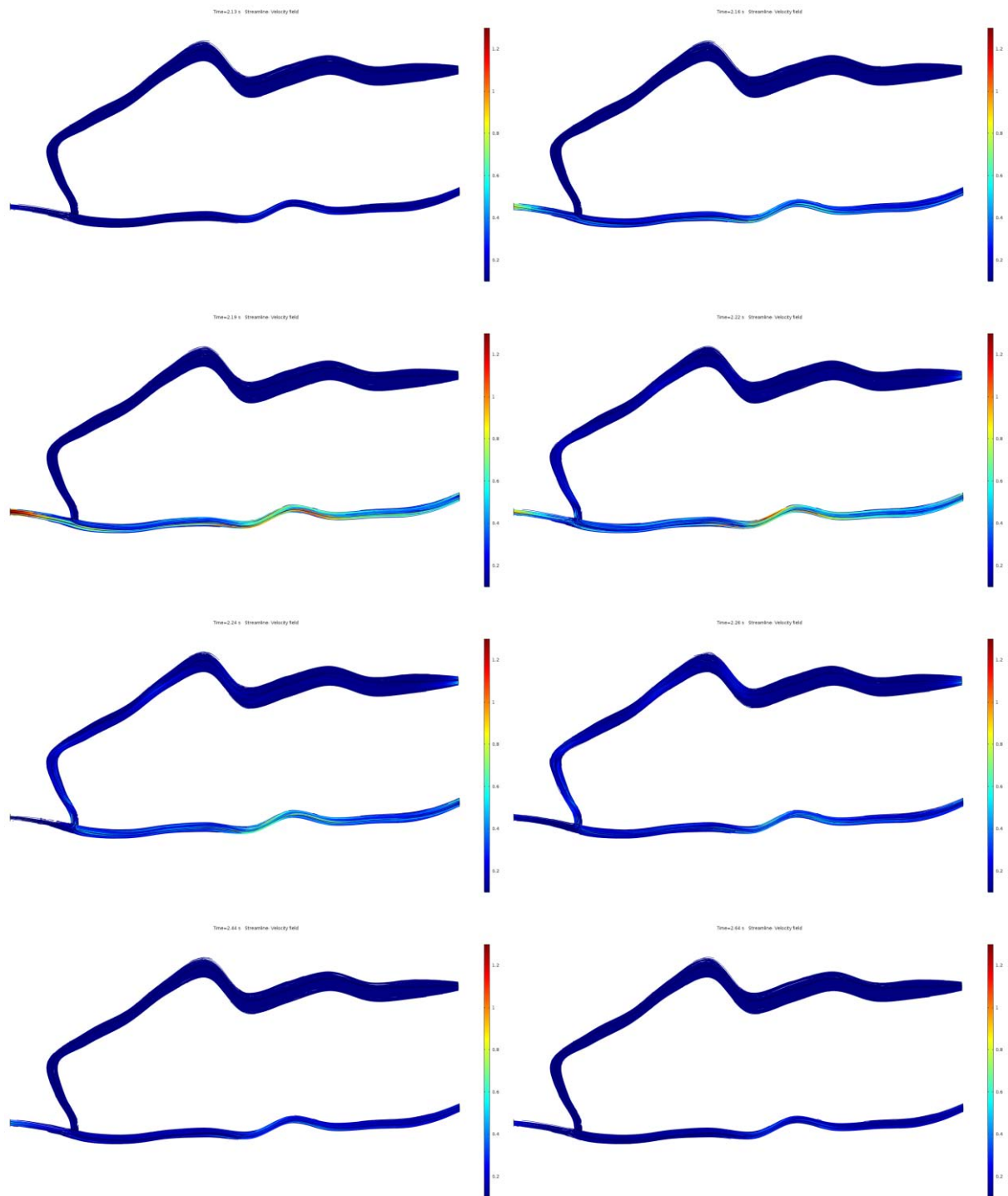
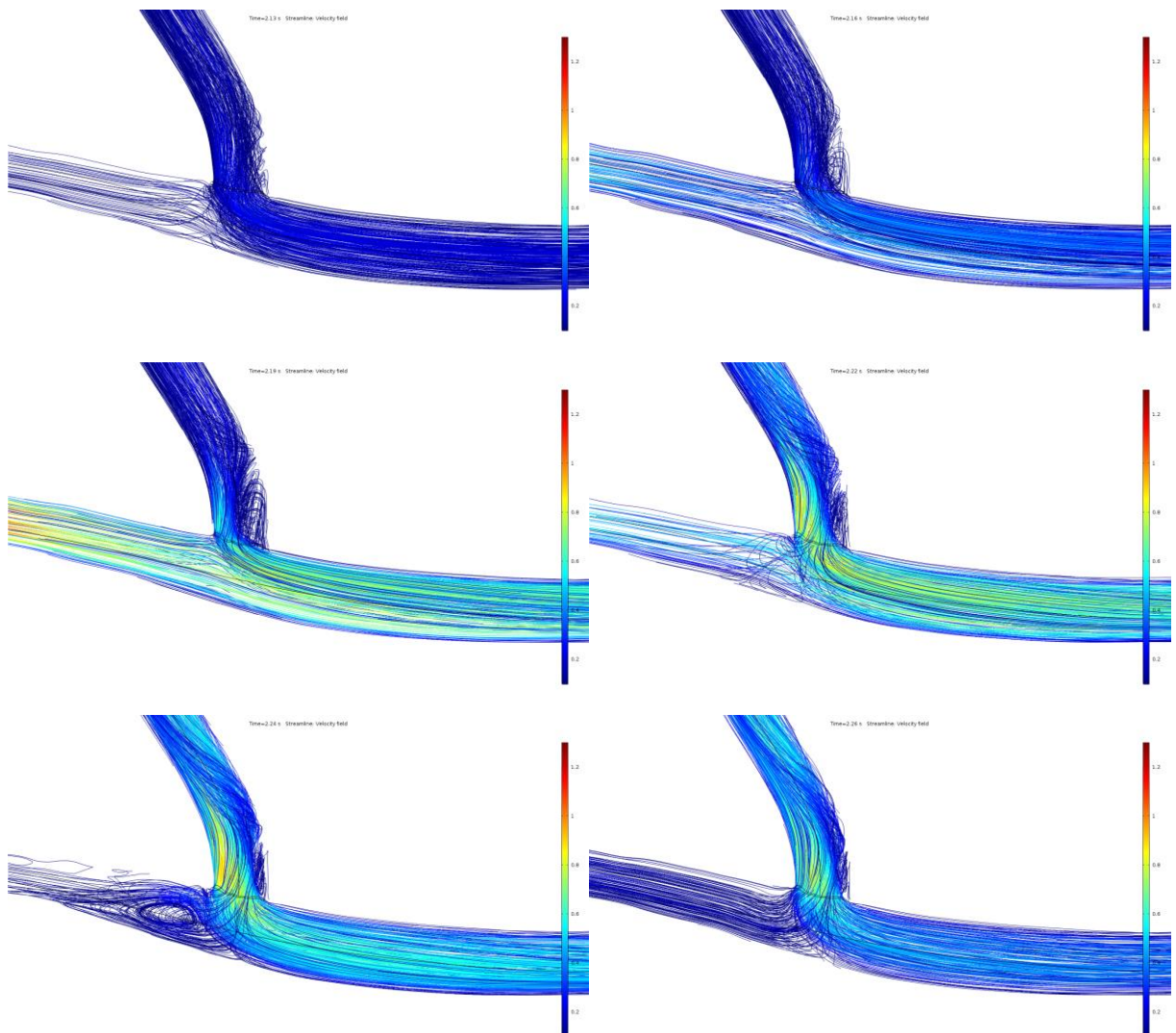


Figure 238 Virtual AVF blood flow velocity streamlines by time.

It is easy to compare these results with the single vessels, but also with the AVF model previously presented.

The velocities are lower all along the system, compared to the real AVF model, but they present the same patterns on the same zones of interest, that are the anastomosis and the venous swelling and curves.



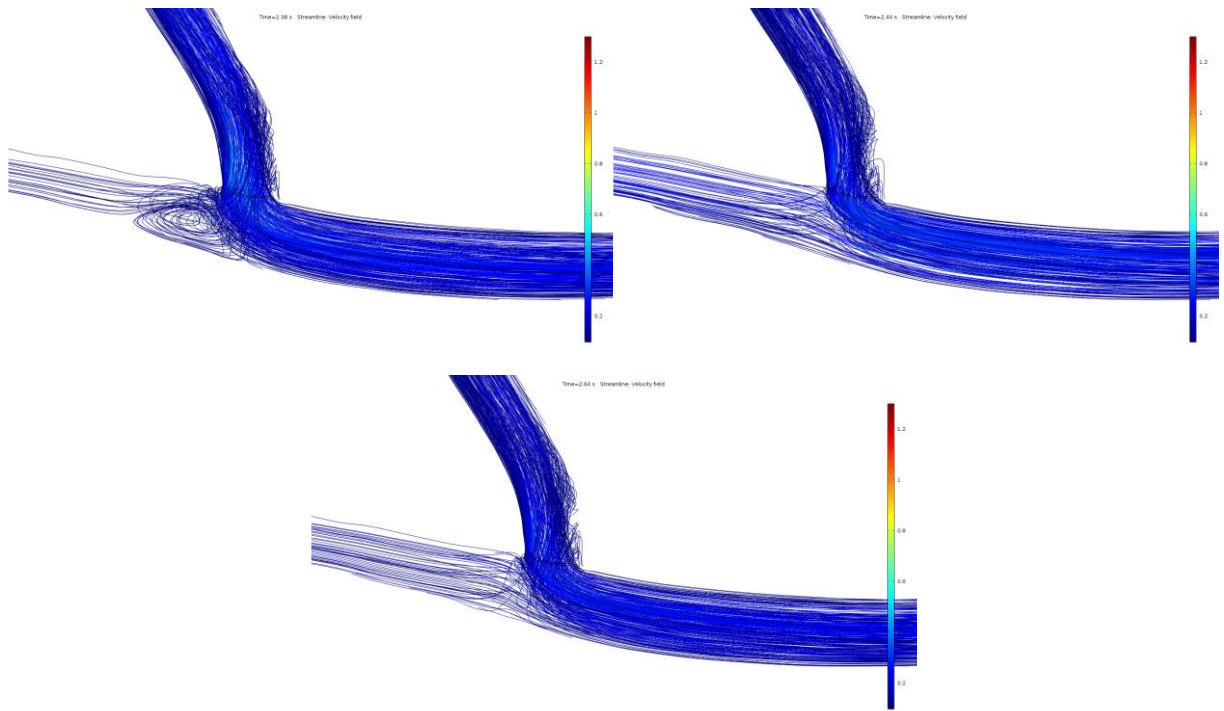


Figure 239 Virtual AVF detail of the velocity streamlines by time at the anastomosis.

At the anastomosis appear the complex patterns presented before: on the arterial side distal to the anastomosis disturbed flow evidently propagate. The venous side close to the internal corner of the anastomosis shows similar patterns discussed before, with a separation zone extending during all the cycle.

7.5.2.2 Reynolds Number

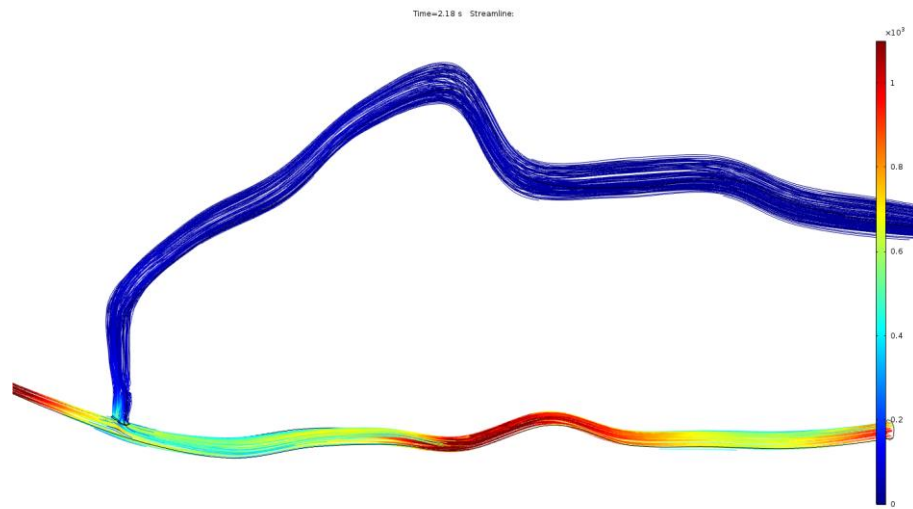


Figure 240 Virtual AVF Reynolds number streamlines at the velocity peak.

The Reynolds Number results appear consistent with the previous results in which, even the boundaries velocities not being the same and the geometry either, the same positions and higher values (around 1000) occurred.

7.5.2.3 Wall Shear Stress

The same situation resulted in the WSS analysis. The higher values are here quite lower respect to the real AVF model, probably because of the different velocities, with peaks of 25 Pa on the arterial side and 4 Pa on the venous starting side of the anastomosis. However, these values are still interesting, because comparable with the previous model in magnitude, but especially in the locations.

It is clear how both the models point out the same hot spots regions.

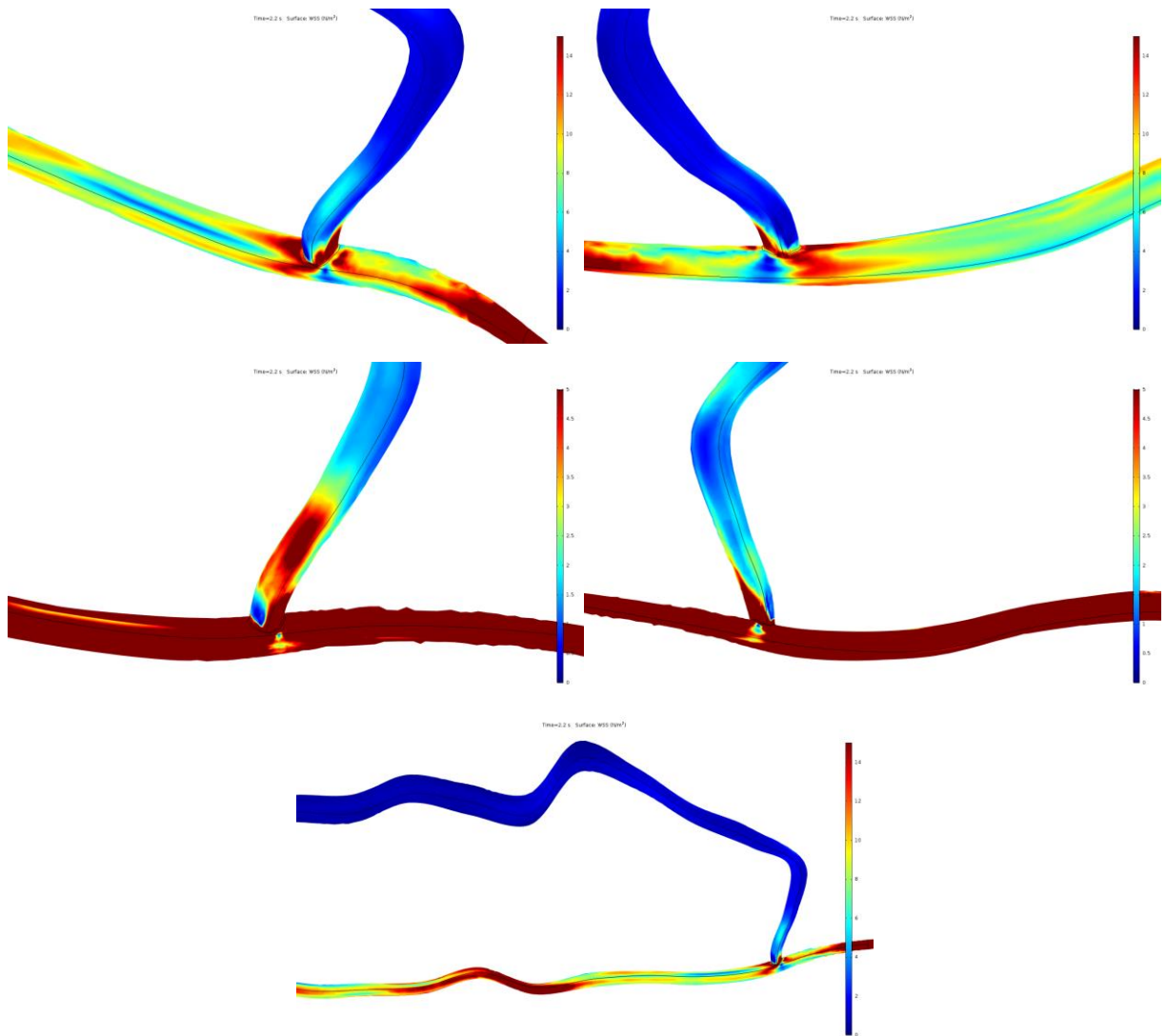


Figure 241 Virtual AVF Wall Shear Stress at the systolic peak.

7.5.2.4 Wall Shear Stress Gradient

The Wall Shear Stress Gradient demonstrates that the zones where the WSS abrupt changes occur are similar to the previous model. The gradient magnitude is lower, and its peaks concentrated around the anastomosis and along the arterial tract.

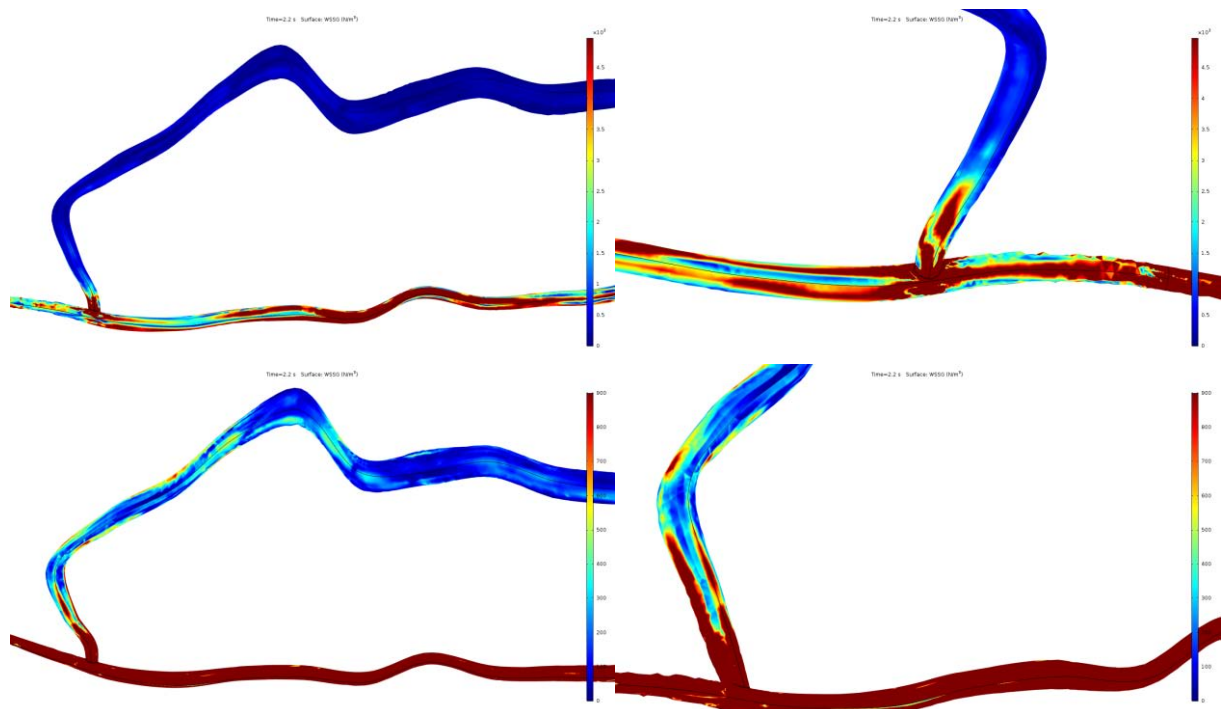


Figure 242 Virtual AVF Wall Shear Stress Gradient at the systolic peak.

7.5.2.5 *Oscillatory Shear Index*

The last speculations are about Oscillatory Shear Index. It results to be less spread respect to the real model. This is probably because of the vessels narrowness, which guides better the blood flow along a principal direction. However, OSI hot spots are still present, and their position, albeit smaller, is coherent with the previous simulation.

The zone around the anastomotic sewing seems the most prone to highly variable shear stresses, especially the zone in front and immediately after it.

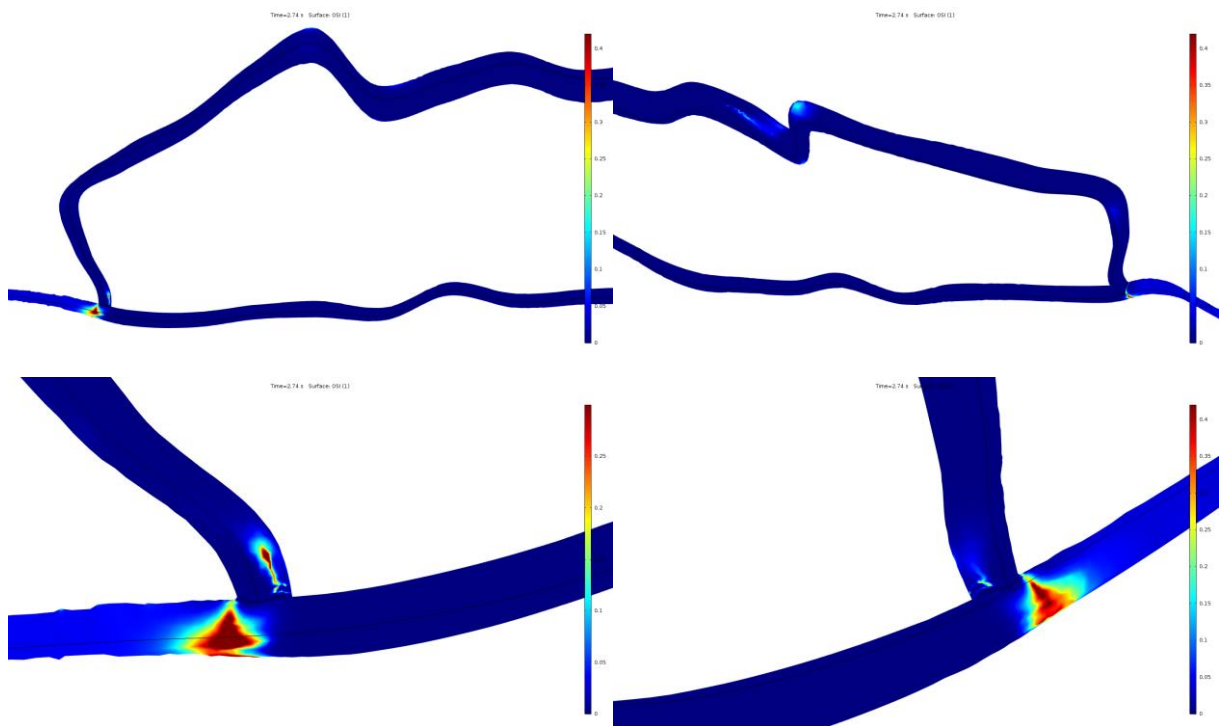


Figure 243 Virtual AVF Oscillatory Shear Index.

7.6 Solutions Errors Evaluation

Unfortunately, an adequate error estimation could not be performed on time to be present in this study. The intention was to compare the 3D model and CFD simulation results with the data obtainable from an MRA scan, which could provide the better and more accurate information about our subject.

Not being able to accomplish this objective because failing to obtain these data, some speculations and parallel comparisons have been done to obviate to that.

First, uncertainties considered were the ones related to the model geometric and temporal discretizations for the numerical simulation, besides the accuracy tolerance set at the moment of the solver set up.

The average mesh size of the mesh is 0.12 mm^3 , the average element is 0.56 mm^2 and the average element is 0.66 mm . The half of these dimensions can be interpreted as the average uncertainty on volume related quantities accuracy, the surface related quantities accuracy and the linear related quantities accuracy. If we consider the average arterial diameter (4 mm) and the uncertainty for every element linear dimension (0.33 mm) we obtain an uncertainty of 8% relative to the vessel diameter and 2.5% relative to the vessel perimeter geometry. It is important to underline that all these estimations have been evaluated very conservative and probably meaningless in the moment when better MRA results are available.

As exposed in Chapter 1.2.2.1, the time steps solutions have been set every 0.01 s , the half of that value 0.005 s could be considered the time-related accuracy uncertainty ($\sim 0.78\%$ related to a single heart cycle of 0.64 s). The absolute tolerance accepted in the simulation was set to 5×10^{-4} which can be considered the results tolerance.

7.6.1 Errors Calculations

The only possible errors estimation that could be possible was to compare the velocity field and its magnitude in the sensible points where Colour-Doppler scans were planned to be taken by the hospital operators. The zones are limited to the anastomosis area, where an average velocity of 48 cm/s was detected by the Colour-Doppler Ultrasound system.

It is possible to appreciate by the scan, how the velocity field undergoes an abrupt change in its direction across the anastomotic area. This is highlighted by the colour change in the central area, where red means a distal direction of blood flow and blue means a proximal direction of blood flow.

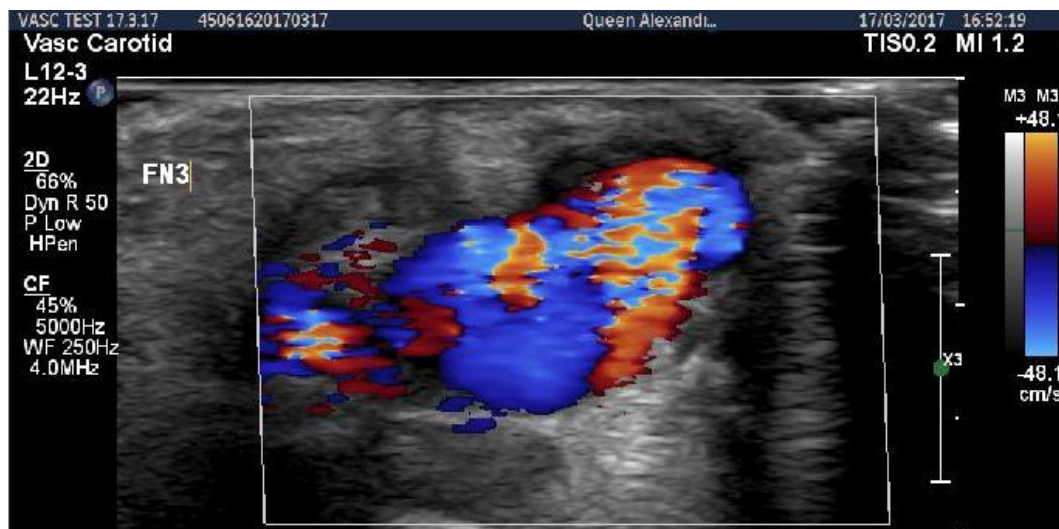


Figure 244 Ultrasound Colour-Doppler scan at the anastomosis to evaluate blood velocity magnitude and patterns.

These very similar patterns have been detected in the simulation too, in the region along with the anastomosis take place. The velocity seems to present the similar patterns, with high velocities

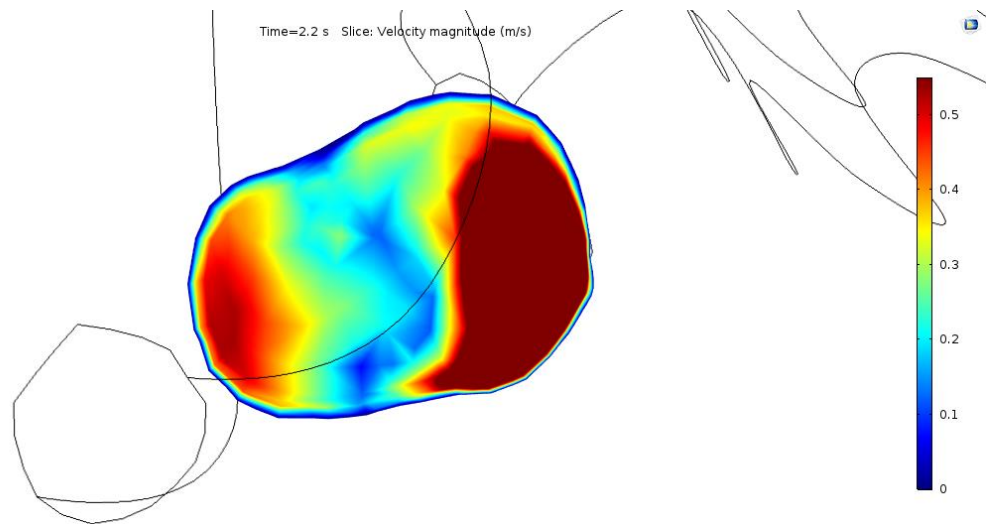


Figure 245 Blood velocity magnitude slice at the anastomosis at the systolic peak.

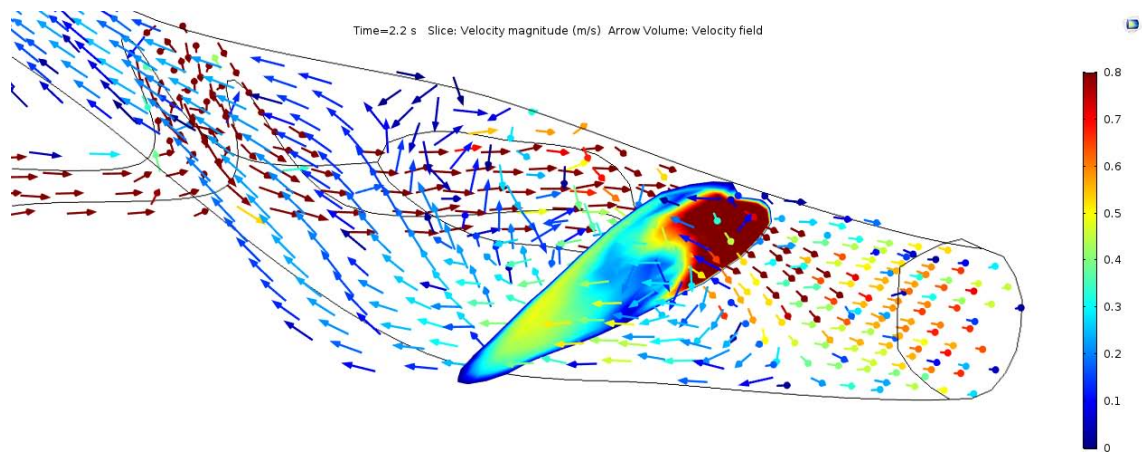
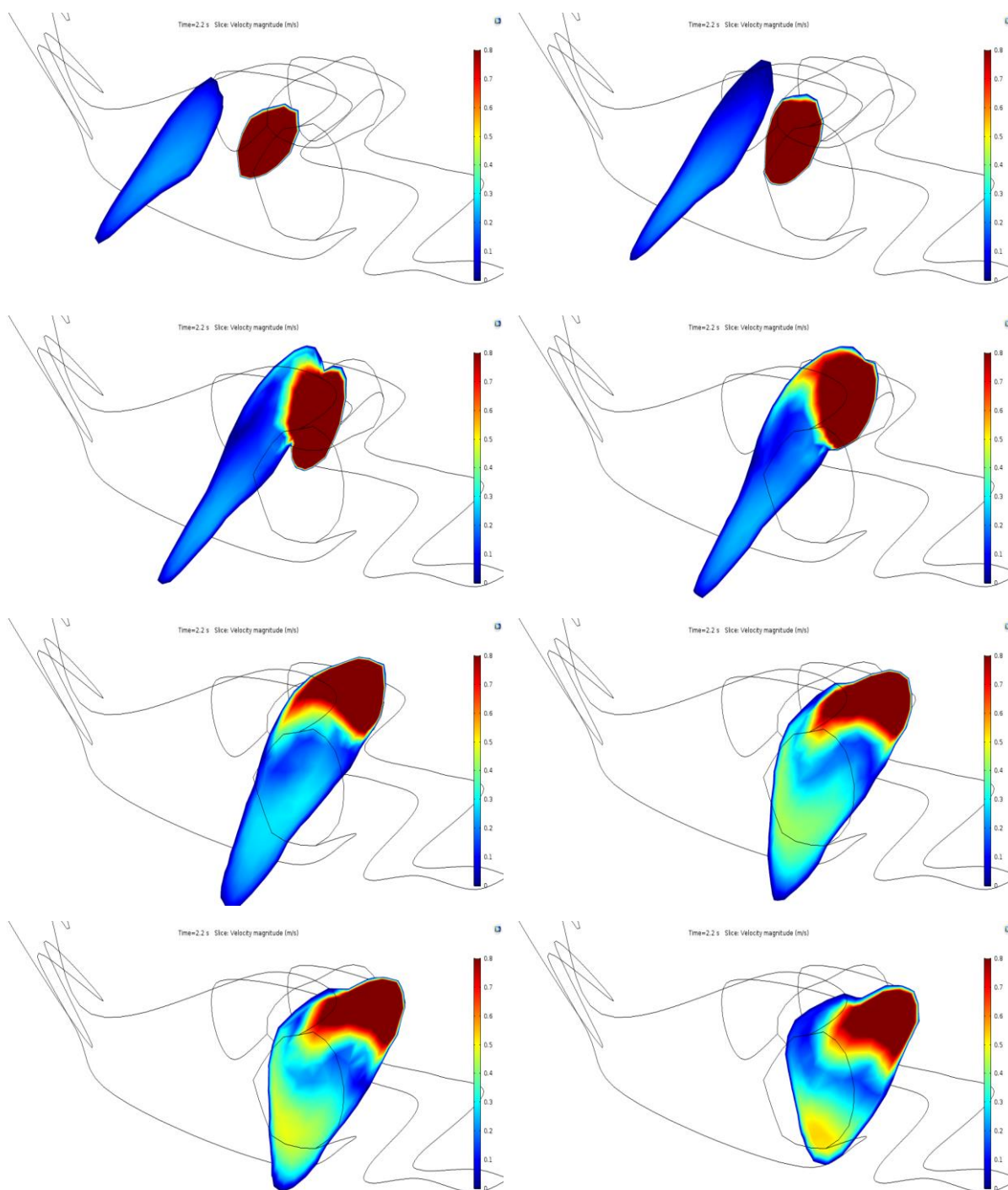


Figure 246 Blood velocity magnitude slice and arrows vectors at the anastomosis at the systolic peak.

It's possible to notice how flow reversal develops starting by the anastomosis and prosecuting all along the vessels connection length.

The spatial sequence of the velocity field is described below.



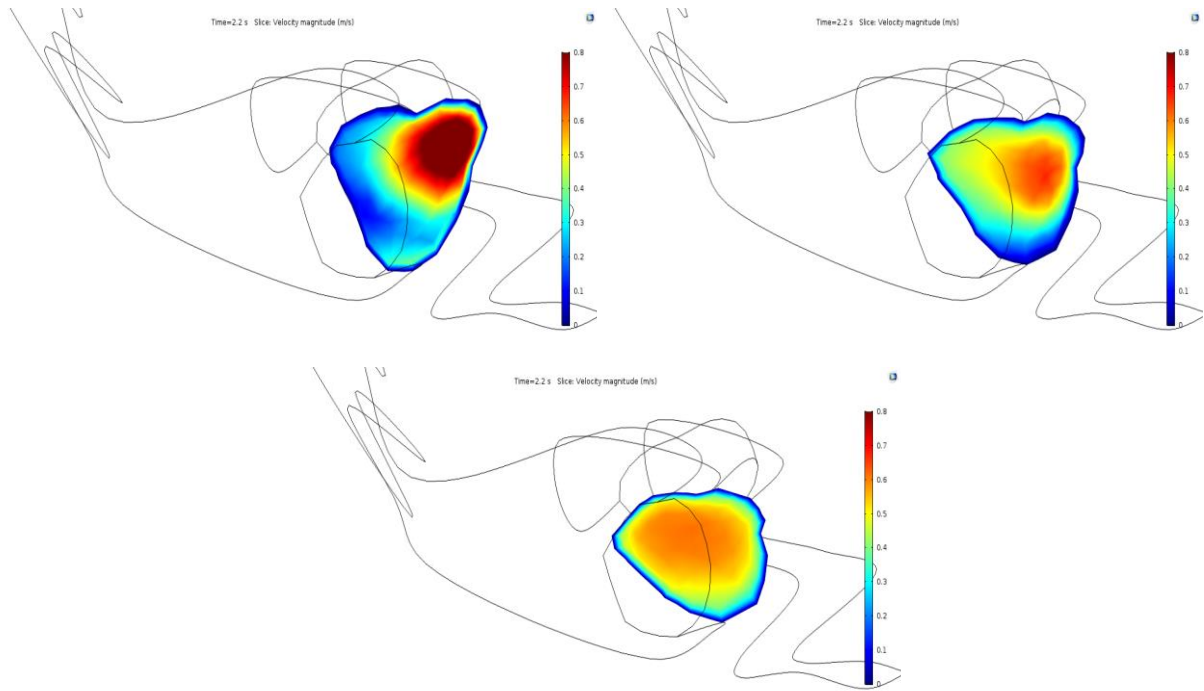


Figure 247 The spatial sequence of the velocity field at the anastomosis site.

From the results exposed, it is clear that the blood flow patterns at the anastomosis are comparable.

For what regards the velocities magnitude, some differences occur: if on the Colour-Doppler scans the average velocity is about 0.5 m/s, in our model the velocities exceed 1 m/s on the arterial side flow, with the reversal venous-oriented velocities comparable to the measurements done.

For what regards the errors here, it is difficult to provide an estimation, because all depends on the accuracy and definition of the Colour-Doppler scan.

In the end, the errors have been evaluated in about 0.02 m/s ($\sim 5\%$) for the flow reversal velocity, with a very large error involving the artery straight-direction velocity, around 0.4 m/s ($\sim 100\%$).

8 DISCUSSION and CONCLUSIONS

Unfortunately, during the study, less data than expected could be analysed and exploited to study and develop the modelling procedure.

To date, only a complete set of scans from a healthy voluntary nurse and only one set of scans of a real patient has been exploited for this study.

This afflicted sensibly the study, in the way of not being able to verify deeply the robustness and accuracy of the procedure and results obtained, besides not being able to detect all the issues and error causes.

However, the uncertainty analysis and errors measurements possible led to a primary assessment of all the works presented, showing all the strengths and weaknesses.

The lack of many data also promoted new ways for study the AVF problem, leading to a promising technique to virtually access and study a patient specific AVF before the real surgical operation, with the possibility to establish a new guideline to AVF prevention studies.

8.1 Ultrasound Imaging & Hospital Protocol

Ultrasound Mode-B and Colour-Doppler scans have demonstrated to be a very useful tool to achieve our objective, even if presented some limitations in the quality and accuracy achievable. The main issue has been the very sensibility of the results on the quality of the scans, linked to the operator ability to obtain very high contrast and high-defined images of the vessels cross sectional areas, not incurring in images artefacts.

The protocol established with the help of the hospital operators has demonstrated to be robust and well feasible, matching all the engineering requests to obtain the best information possible with the lowest hospital, patient and bioethical annoyances.

Possible future developments can include the exploitation of 3D Ultrasound imaging in the vessels detection and reconstruction, even if the possible application of this technique to our specific problem has not been studied enough yet. However, the possibilities related to this techniques are very high, with the interest focused on vessel 3D model reconstruction are very promising.

8.2 Matlab Image Analysis Editing

MATLAB coding has resulted being the fundamental cornerstone of this work, allowing processing Ultrasound Imaging scans, detecting the useful information in them, and convert them into an exploitable format for our purposes.

The Edges Points Extraction program, even not undergoing to a specific uncertainties estimation and errors measurements, demonstrated all its strength in the flexibility and capability to detect and extract from the images the correct cross sectional areas required for the subsequent steps of the study. All the strategies resulted to be useful, but thresholding revealed to be the most important instrument in this phase, enabling to decompose the images preserving the real subject of interest in the best quality possible.

The Edges Points Conversion program presented the results of the first phase of the MATLAB coding work, importing Edges Points Extraction program raw data and processing them to the final result and format desired. Also in this step, the program flexibility and possibility to adapt itself to the very specific needs of the user in terms of edges holes detection and filling, sample points number choice and smoothing possibilities, resulted to be relevant and useful. The final results study revealed the uncertainty of this results to be quite good and reliable, stabilizing around the 1%, and depending on the major part from the image intrinsic quality expressed in pixels density (or their dimensions).

However, the errors measurements done in this regard demonstrated a very high variability. This has been motivated looking at the quality of the scans, depending mostly on the operator skills to provide very precise, stable and defined scans of the area of interest. For the worst case scenario, it has been detected an error up to 25%, worth to note that it has happened only two times, with one more scan where no information could be extracted for the very low quality of the image. Except for this kind of error cause, the general error measure was around the 3%.

For what regards the Velocity Pulswave Extraction program, the final results are pretty similar, with a program which has demonstrated to be very reliant and flexible to provide an accurate pulse wave sample representing an average of several real ones. Here again, its flexibility allows the user to achieve the results desired in a very easy and practical way. The program allowed selecting as many initial pulse waves as desired, fit the average pulse wave with the desired and best grade of the polynomial least squares fitting, and extract a multiple average pulse wave sampled as frequently as desired for the successive steps of the study.

The uncertainty is derived, as for the previous programs, from the intrinsic image quality expressed in pixels density, but here especially from the various pulse waves variability, which demonstrated to be a lot more influent, providing a final uncertainty of 5%, which is acceptable anyway.

The errors measured comparing the average pulse wave to the real ones demonstrated to be comparable and stable around the uncertainty level evaluated.

8.3 3D Model

3D model is the final result of the previous steps procedure, combining their results in order to achieve what is the virtually reconstructed model of the patient specific ArterioVenous Fistula.

3D CAD software has been indispensable to generate this geometrical model, allowing also to import and elaborate the previous data.

The tomographic technique procedure resulted in a good alternative to the standard tomography techniques but compared to these has some limitations in terms of accuracy, nevertheless some real interesting cost advantages.

Most of the uncertainties are related to the arm representativeness of the real arm condition and the transportation of the real reference grid to the virtual one. Due to the lack of a comparing reference on the real geometry (which has hoped to be an MRA scan of the zone of interest), practically all the uncertainties have been estimated on the basis of hypotheses and assumptions based on common sense. Finally, the uncertainty related to the 3D modelling has been estimated to be between 10% and 25% on the worst situations.

The 3D scanning and imaging techniques for the patient-specific arm model reconstruction, could be a good further development possibility to increase the 3D model accuracy.

In the end, we believe that the new procedure and technique established are a good starting point to which rely on for our study, besides having good possibilities in further development, to avoid some of the deficiencies found in this early stage development.

8.4 CFD Simulations

CFD simulations provided good results to understand the flow paths and principal factors controlling AVF maturation.

The results accuracy could not be directly compared to a real 3D description of the real blood flow inside the patient fistula; however, the Ultrasound Colour-Doppler scans came to help, allowing anyhow a first comparison of the results.

WSS, as well as TAWSS, values of the simulations resulted broadly comparable to the results obtained in other studies and researches, both on real and patient-specific simulation of the AVF. Arterial WSS has been seen varying between 0 to 35 Pa, Venous WSS has been seen varying between 0 to 6 Pa.

In the same way, WSSG followed the WSS pattern. Arterial WSSG has been seen varying between 0 to 15000 Pa/m, Venous WSSG has been seen varying between 0 to 900 Pa/m.

It is important to underline how some really high non-physiological (and probably not realistic) stresses values has been noticed on the arterial side. The hypothesis here is that the problem formulation and the basic CFD simulation limitations related the non-flexibility of the walls could remarkably affect the results in this area.

OSI resulted to be consistent with the studies analysed and with the expectations. A good comparison between OSI peaks and WSSG peaks has been noticed.

RRT resulted to be a promising parameter for AVF maturation problems localisation and detection. Including both TAWSS, which is the best indicator of the average stresses which the vessels walls undergo, and OSI, which describes and summarises the time variability of the stresses, it is the candidate to be the best all-embracing parameter to have a very focused, coherent and sensitive response to our main question: in the AVF prone to have any failure?

To that question, we believe that, basing on the simulations results achieved and the theory on blood vessels physio-mechanical behaviour, the answer should be: if in any vessel wall side RRT exceeds the limit value of 10 Pa^{-1} , the risks of AVF problems related to low and oscillatory stresses are consistent. However, we suggest other and deeper studies to verify this statement.

In the end, it can be said that satisfactory, interesting and reality-compliant results are achieved by all this combination of procedures, providing a good base for further development in order to increase accuracy and representativeness of the patient-specific virtual model respect the real one. The results obtained so far can describe the AVF flow-related maturation indicators in an established fistula in a low time and cost effective way.

Furthermore, the efforts made at the very beginning of this study led also to an interesting side road, which is AVF maturation prediction and experimentation, based on original patient-specific vessels virtual manipulation, in order to simulate a real AVF establishment before the real surgical operation to be done.

The power and possibilities of this procedure are very high and can lead to a new era in AVF study and prediction, with different solutions studied before the real AVF establishment in order to achieve the most providing configuration.

8.5 FSI Simulations

As mentioned before, CFD simulations demonstrated to have some limitations in perfectly mimic the blood behaviour in real vessels. The main reason of that is that vessels distensibility has been considered a great influencer of blood flow, in the way of smoothing the pressure signal originating from the heart and allowing a bigger amount of blood flow to slide through the vessels with a smaller velocity.

FSI simulations appear to be the very step further in patient-specific ArterioVenous Fistula failure analysis, being able to consider both the major subjects physical and physiological behaviours.

Unfortunately, this type of simulations also present some disadvantages, related to the problem increased complexity. Because of that, FSI simulations are very sensitive to every even small boundary condition change, requiring very accurate data to set up the problem and provide coherent results. This kind of data is nowadays missing to us (especially for what regards the pressure and velocity/flow rate pulse waves synchronisation at the extremities of the studied model) leading to propose this solution only as development of this study.

8.6 General Conclusions

The final and general conclusion of all this work is that the patient-specific procedure established, based on the Ultrasound 3D segmentation imaging technique, Image Processing through MATLAB coding, 3D model reconstruction and CFD simulation, to study and evaluate an AVF establishment and maturation demonstrated promising results both in terms of accuracy and ability to provide sensible and significant results. Furthermore, the possibilities of development in every area are still very high, being this study at the very beginning, leaving encouraging expectations. The author's belief is that the primary focus of the next improvements should be in relation to the whole process robustness and the accuracy of the singular steps, which with the data available demonstrated some discrepancies and flaws.

9 APPENDIX

9.1 Matlab Codes

9.1.1 DicomREAD

```
clear

close all

clc

fprintf(2,'Digit directory path between apostrophes\n');

path = input('path:');

% correct=('"path"');

% addpath(path);    %or use  cd('...');

DIR=dir([path, '\*.dcm']);                                %dir([FolderName, '\*.dcm']);

fprintf(2,'Here are the files list of this directory\n');

dir([path, '\*.dcm'])                                     %dir([FolderName, '\*.dcm']);

fprintf(2,'Insert initial and final image n°\n');

a = input('initial=');

b =input('final=');

for n=a:b

    c='\';
```



```

pp=DIR(n).name;

index=[path c pp];

A=dicomread(index);

figure()

% imtool(A)

imshow(A)

str=sprintf(pp);

title(str)

%

% rr = warndlg(sprintf(' -image window scale\n \n      -figure diameter \n \n\n \n
Right Click and "Esport to workspace" each measure.\n \n Respect the measures list
order.\n \n Press OK ONLY when pixel measure is taken. '), '      DON" T CLOSE!');

% drawnow % Necessary to print the message

% waitfor(rr);

%

% imtool close all

%

% dim=25*distance1/distance

clear distance distance1

end

```

9.1.2 Edge Extraction: “EDGEpointsEXTRACTION”

```
clear
```

```
close all
```

```
clc
```

```
fprintf(2,'The aim is to choose the best perimeter filtered image, save it, \n');
```

```
fprintf(2,'and use POINTSconverter.m or SavitzkyGolay.m program to extract the final  
profile for CAD\n');
```

```
fprintf(2,'      \n');
```

```
fprintf(2,'      \n');
```

```
fprintf(2,'      \n');
```

```
disp(' ')
```

```
fprintf(2,'Digit directory path between apostrophes\n');
```

```
path = input('path:');
```

```
disp(' ')
```

```
DIR=dir([path, '*.dcm']);                                %directory choice
```

```
fprintf(2,'Here are the files list of this directory\n');
```

```
dir([path, '*.dcm'])
```

```
disp(' ')
```

```
fprintf(2,'Insert initial and final image n°\n');
```

```

a = input('initial=');

b =input('final=');

while a<1 || b<1 || b<a

    a=[];

    b=[];

    a = input('initial=');

    b =input('final=');

end

for n=a:b                                % start cycle for different images

    cont=1;                             % initial posizion for image matrix

    disp(' ')

    fprintf(2,'Measure reference distance for scaling \n');

    c='\';

    Nimg=DIR(n).name;

    index=[path c Nimg];

    A=dicomread(index);                  % read image

    disp(' ')

    fprintf(2,'Image step \n');

    disp(Nimg)

```

```

g = warndlg(sprintf(' Type measured distance in cm provided in the image.\n \nThen
press any key to close. '), '          ATTENTION!');

drawnow % Necessary to print the message

waitfor(g);

figure()

imshow(A)

title('Press any key when you read the measure')

w = waitforbuttonpress;

if w == 1

    close all %permit user to have time to read

end

dist=input('Measured distance=');

while size(dist)==[0,0]

    dist=[];

    disp(' ')

    fprintf(2,'Type measured distance in cm provided in the image \n');

    dist=input('Measured distance=');

end

% Construct a questdlg with three options

choice = questdlg('Is it ok?', 'CHECK' , 'Yes');

```

```

% Handle response

switch choice

    case 'Yes'

    case 'No'

        dist=input('Measured distance=');

    case 'Cancel'

        figure()

        imshow(A)

        title('Press any key when you read the measure')

        w = waitforbuttonpress;

        if w == 1

            close all                                %permit user to have time to read

        end

        dist=input('Measured distance=');

    end

    rr = warndlg(sprintf(' Use "measure tool" to measure:\n \n          -reference scale
length.\n \n          -image window length\n \n          -height between up image border and
lower vessel edge\n \n\n \n Right Click and "Esport to workspace" each measure.\n \n
Respect the measures list order.\n \n '), '          ATTENTION!');

    drawnow    % Necessary to print the message

    waitfor(rr);

```

```

measures=0;

while measures==0

    imtool(A)

    f = warndlg(sprintf(' Measures order:\n\n      -reference scale length.\n\n      -
image window length\n\n      -vessel edge/upper border height \n\n Move apart this
window to ease process\n\n Press OK ONLY when pixel measure is taken. '), '
DON''T CLOSE!');

    drawnow % Necessary to print the message

    waitfor(f);

    imtool close all

    % Construct a questdlg with three options

    choice = questdlg('Is it ok?', 'CHECK' , 'Yes');

    % Handle response

    switch choice

        case 'Yes'

            measures=1;

            imtool close all

        case 'No'

            imtool close all

            measures=0;

        case 'Cancel'

```

```

        imtool close all

        misure=0;

    end

end

disp(' ')

distance

Pix_Length=distance1

Pix_Height=distance2

scale=(dist)/(distance)                %scale factor

Lower_Edge_Height=Pix_Height*scale

Window_Length=Pix_Length*scale

SCALE=[scale,Window_Length,Lower_Edge_Height,dist];

disp(' ')

l = warndlg(sprintf(' Crop the shape of interest. \n \n Mantain the total length and
height of the image. '), '                ATTENTION!!');

drawnow    % Necessary to print the message

waitfor(l);

B=imcrop(A);                %crop image to edit: mantain al the area
scanned by the instrument to make simplier the scaling

close all

```

```

% Construct a questdlg with three options

choice = questdlg('Is it ok?', 'CHECK' , 'Yes');

% Handle response

switch choice

    case 'Yes'

        close all

    case 'No'

        clear B

        B=imcrop(A);

    case 'Cancel'

        close all

end

close all

Y = im2double(B);

if size(Y,3)==3;

    r=Y(:,1);                                % Remove all red components from every
pixel.

    g=Y(:,2);                                % Remove all green components from every
pixel.

    b=Y(:,3);                                % Remove all blue components from every
pixel.

```



```

figure()

imshow(r)

title('choose R --> type [1]')

figure()

imshow(g)

title('choose G --> type [2]')

figure()

imshow(b)

title('choose B --> type [3]')

fprintf(2,'Insert color level you wanna edit [r-g-b]\n');

disp('r=1');

disp('g=2');

disp('b=3');

color = input('color=');

if color==1

    Z=r;

else if color==2

    Z=g;

else if color==3

```

```

        Z=b;

        else disp('insert a correct value');

    end

end

end

else Z=Y;

end

figure()

imshow(Z)

% size(Z)

title('\color{red} The image which is going to edit is:', 'fontsize', 20);

lv=graythresh(B);

IM=im2bw(B,lv);

%figure()

%imshow(IM)

%title('\color{red}graythresh&im2bw', 'fontsize', 20)

binaryImage = imfill(IM, 'holes');

figure()

imshow(binaryImage)

```

```

title('\color{red}(1) Graythresh&im2bw filled','fontsize',20)

BW = bwperim(binaryImage);

figure()

imshow(BW)

title('\color{red}(2) Graythresh&im2bw perimeter','fontsize',20)

BWx1 = gpuArray(IM); % try to extract main features(remove
filled images//extract skell of path)

BWx2 = bwmorph(BWx1,'remove');

figure

imshow(BWx2)

title('\color{red}(3) Bwmorph remove','fontsize',20)

BWx3 = bwmorph(BWx1,'skel',Inf);

figure

imshow(BWx3)

title('\color{red}(4) Bwmorph skel','fontsize',20)

% Construct a questdlg with three options

choice = questdlg('Are you satisfied?', 'CHECK' , 'No');

% Handle response

switch choice

case 'Yes'

```

```

        answ=1;

    case 'No'

        answ=0;

    case 'Cancel'

        answ=0;

    end

    if answ==0

        % Construct a questdlg with three options

        choice = questdlg('Wanna save any img?', 'SAVE IMG'    , 'No');

        % Handle response

        switch choice

            case 'Yes'

                sav=1;

            case 'No'

                sav=0;

            case 'Cancel'

                sav=0;

        end

        if sav==1

```

```

fig=1;

while fig~=0

    disp('Insert Figure number (when finished digit 0)');

    fig = input('Figure n°');

    if fig~=0

        if fig==1

            IMG(:,:,cont)=binaryImage;

            cont=cont+1;

        else if fig==2

            IMG(:,:,cont)=BW;

            cont=cont+1;

        else if fig==3

            IMG(:,:,cont)=BWx2;

            cont=cont+1;

        else if fig==4

            IMG(:,:,cont)=BWx3;

            cont=cont+1;

        end

    end

end

```

```

        end

    end

end

end

end

close all

figure()

imshow(Y)

figure()

imshow(Z)

originalImage=B;                                % first editing with original
image

lv=graythresh(B);

IM=im2bw(B,lv);

%figure()

%imshow(IM)

%title('\color{red}graythresh&im2bw filter','fontsize',20)

IM = imfill(IM, 'holes');

figure()

imshow(IM)

```

```

title('\color{red} Graythresh&im2bw holes fill','fontsize',20)

BW = bwperim(IM);

figure()

imshow(BW)

title('\color{red} Graythresh&im2bw perimeter','fontsize',20)

% Construct a questdlg with three options

choice = questdlg('Wanna proceed with Sobel filtering?', 'SOBEL' , 'No');

% Handle response

switch choice

    case 'Yes'

        sobl=1;

    case 'No'

        sobl=0;

    case 'Cancel'

        sobl=0;

end

if sobl==1                                % sobel filtering

    Mx=[-1 -2 -1;0 0 0;1 2 1];

    C=double(B);

```

```

[r,c]=size(C);

OUT=zeros(r-3,c-3);

for i=1:(r-3)

    for j=1:(c-3)

        Csqr=C(i:(i+2),j:(j+2));

        OUT(i,j)=sum(sum(Mx.*Csqr));

    end

end

%figure()

Gx=(OUT);

%imshow(Gx)

My=[-1 0 1;-2 0 2;-1 0 1];

OUT=zeros(r-3,c-3);

for i=1:(r-3)

    for j=1:(c-3)

        Csqr=C(i:(i+2),j:(j+2));

        OUT(i,j)=sum(sum(My.*Csqr));

    end

end

```



```

%figure()

Gy=(OUT);

%imshow(Gy)

G= sqrt(Gx.^2+Gy.^2);

%figure()

%imshow(G)

P=uint8(G);

if size(Y,3)==3;                                % if image is RGB the 3 graylevels form a
3xcolums image -> check to keep right dimension

    [Sr,Sc]=size(G);

    inP=1+(2/3)*Sc;                                % RGB-> 3xcolums -> divided by 3 ->
only 1 column discrepance between sobel and original

    finP=Sc;

    P=P(:,inP:finP);

    [ri,ci]=size(P);                                % Image dimensions adjust after Sobel
elaboration

    ir=ri+1;

    ic=ci+1;

    P(ri+1:ri+3,:)=0;

    P(:,ci+1)=0;                                % Addenda of zeros rows and colums to
adjust image dimensions

```

```

else                                     % BW-> difference in 3 rows and 3 columns

    [ri,ci]=size(P);                     % Image dimensions adjust after Sobel
elaboration

    ir=ri+1;

    ic=ci+1;

    P(ri+1:ri+3,:)=0;

    P(:,ci+1:ci+3)=0;                     % Addenda of zeros rows and columns to
adjust image dimensions

end

figure()

imshow(P)

title('\color{red}Sobel filtered image', 'FontSize', 20)

originalImage=P;                         % Thresholding with Sobel filtered
image

lv=graythresh(P);

IM=im2bw(P,lv);

figure()

imshow(IM)

title('\color{red}(1) Graythresh&im2bw filter on Sobel','fontsize',20)

lv1=[];

while size(lv1)=[0 0]

```

```

disp(' ')

fprintf(2,'Insert threshold levels n° for Sobel filtered image elaboration.\n');

lv1 = input('Levels for Sobel thresholding=');

end

BufferS(:,1)=IM; % Image (1) of Sobel Buffer = threshold
on original image P (as reference)

for i=1:lv1

    T=i;

    thresholdValue = T;

    binaryImage = originalImage < thresholdValue; % Bright objects will be chosen
    if you use >.

    % Do a "hole fill"

    binaryImage = imfill(binaryImage, 'holes');

    figure()

    imshow(binaryImage)

    Is=2*i-1+1;

    step=['(',num2str(Is),')'];

    tit=[step,' Binaryimage Sobel'];

    title(tit)

    BufferS(:,Is)=binaryImage; % Image (2*i-1+1) of Sobel Buffer

```

```

neg = imcomplement(binaryImage);

%      figure()

%      imshow(neg)

%      title('binaryimage negative')

BW = bwperim(binaryImage);

figure()

imshow(BW)

Iss=2*i+1;

step=['(',num2str(Iss),')'];

tit=[step,' Sobel with threshold - Press any key in the last image to continue'];

title(tit)

BufferS(:,Iss)=BW;                                % Image (2*i+1) of Sobel Buffer

end

end

w = waitforbuttonpress;

if w == 1                                           %permit user to have time to read

end

% Construct a questdlg with three options

choice = questdlg('Wanna proceed with the original img?', 'ORIGINAL' , 'Yes');

```

```

% Handle response

switch choice

    case 'Yes'

        orig=1;

    case 'No'

        orig=0;

    case 'Cancel'

        orig=1;

end

if orig==1

    % Construct a questdlg with three options

    choice = questdlg('Wanna save any img?', 'SAVE IMG' , 'No');

    % Handle response

    switch choice

        case 'Yes'

            sav=1;

        case 'No'

            sav=0;

        case 'Cancel'

```

```

        sav=0;

end

if sav==1

    fig=1;

    while fig~=0

        disp('Insert Figure number (when finished digit 0)');

        fig = input('Figure n°');

        if fig~=0

            IMG(:, :, cont)=BufferS(:, :, fig);

            cont=cont+1;

        end

    end

end

end

close all

figure()

imshow(Y)

title('Colours original image')

figure()

imshow(Z)

```

```

title('Gray levels original image - Digit the n° of threshold levels to run')

TT=size(B);

OO=size(TT);

if OO(1,2)==3                                % select always a grayscale image

    UU=rgb2gray(B);

    originalImage=UU;

else

    originalImage=B;

end

BufferO(:,,1)=logical(originalImage);

lv2=[];

while size(lv2)=[0 0]

    disp(' ')

    fprintf(2,'Insert threshold levels n° for original image elaboration\n');    %
    Thresholding with original image                                           %

    lv2 = input('Levels original thresholding =');

end

for j=1:lv2

    T=j;

    thresholdValue = T;

```

binaryImage = originalImage < thresholdValue; % Bright objects will be chosen
if you use >.

% Do a "hole fill"

binaryImage=uint32(binaryImage);

binaryImage = imfill(binaryImage, 'holes');

%figure()

%imshow(binaryImage)

BW = bwperim(binaryImage);

figure()

imshow(BW)

step=['(',num2str(j),')'];

tit=[step, ' Original Image - Press any key in the last image to continue'];

title(tit)

BufferO(:,j)=logical(BW); % Image (j) of Original Buffer

end

w = waitforbuttonpress; %permit user to have time to read

if w == 1

end

else

% Construct a questdlg with three options


```

choice = questdlg('Wanna save any img?', 'SAVE IMG' , 'Yes');

% Handle response

switch choice

    case 'Yes'

        sav=1;

    case 'No'

        sav=0;

    case 'Cancel'

        sav=0;

end

if sav==1

    fig=1;

    while fig~=0

        disp('Insert Figure number (when finished digit 0)');

        fig = input('Figure n°');

        if fig~=0

            IMG(:,:,cont)=BufferS(:,:,fig);

            cont=cont+1;

        end

    end

```

```

        end

    end

end

end

% Construct a questdlg with three options

choice = questdlg('Wanna save any img?', 'SAVE IMG'    , 'Yes');

% Handle response

switch choice

    case 'Yes'

        sav=1;

    case 'No'

        sav=0;

    case 'Cancel'

        sav=0;

end

if sav==1

    fig=1;

    while fig~=0

        disp('Insert Figure number (when finished digit 0)');

```

```

fig = input('Figure n°');

if fig~=0

    IMG(:,:,cont)=BufferO(:,:,fig);

    cont=cont+1;

end

end

end

close all

clc

close all

num=sprintf('%02d', n);

name=['IMG',num];

save(name, 'IMG','SCALE');

%%%%%%%%%%%%%%%%%%%%%%%%%%%%%%%%%%%%%%%%%%%%%%%%%%%%%%%%%%%%%%%%%%%%%%%%
%%%%%%%%%%%%%%%%%%%%%%%%%%%%%%%%%%%%%%%%%%%%%%%%%%%%%%%%%%%%%%%%%%%%%%%%

[x,y,z]=size(IMG);

figure()

subplot(1,z,1)

imshow(IMG(:,:,1))

```

```

title(' IMAGE#1')

if z>1

    for q=2:z

        subplot(1,z,q)

        imshow(IMG(:,:,q))

        step=num2str(q);

        tit=[' IMAGE #', step];

        title(tit)

    end

end

disp(' ')

disp(' ')

if z==1

    Z=IMG(:,:,1);

else

    fprintf(2,'Choose the image to use\n');

    img = input('Image #=' );

    Z=IMG(:,:,img);

end

```

```

%cleaning image

clean=0;

while clean==0

    disp(' ')

    w = warndlg(sprintf(' Select areas to clean the image. \n \n Press [1] when satisfied.
'), '    ATTENTION!');

    drawnow    % Necessary to print the message

    waitfor(w);

    figure()

    imshow(Z)

    title('Starting Image')

    P=Z;

    [hmax,lmax]=size(P);

    figure()

    subplot(2,2,1)

    imshow(B)

    title('Original')

    %clean the borders

    P(1:5,:)=0;

    P(end-5:end,:)=0;

```

```

P(:,1:5)=0;

P(:,end-5:end)=0;

subplot(2,2,2)

imshow(P)

title('B&W')

subplot(2,2,3)

imshow(P)

title('cleaned borders')

satisf=0;

repeat=0;

P_in=P;

while satisf==0

    figure

    imshow(B)

    title('Original')

    figure()

    imshow(P)

    title('Select area to PRESERVE')

    rect=getrect;          %select area to clean

```

```

x1min=double(rect(1,1));

y1min=double(rect(1,2));

l1=double(rect(1,3));      %coordinates

h1=double(rect(1,4));

x1max=x1min+l1+1;

y1max=y1min+h1;

P(1:y1min,1:lmax) =0;      %clean all noise points

P(1:hmax,1:x1min) =0;

P(1:hmax,x1max:lmax) =0;

P(y1max:hmax,1:lmax) =0;

figure()

imshow(P)

title('Partial Result - Cancel to restart')

% Construct a questdlg with three options

choice = questdlg('Are you satisfied?', 'CONTINUE'      , 'No');

% Handle response

switch choice

    case 'Yes'

        satisf=1;

```

```

        clean=1;

    case 'No'

        satisf=0;

        clean=1;

        P=P_in;

    case 'Cancel'

        clear rect P

        satisf=1;

        clean=0;

    end

end

close all

satisf=0;

while satisf==0

    figure

    imshow(B)

    title('Original')

    figure()

    imshow(P)

```



```

title('Select area to CLEAN')

rect=getrect;          %select area to clean

xmin=double(rect(1,1));

ymin=double(rect(1,2));

l=double(rect(1,3));    %coordinates

h=double(rect(1,4));

xmax=xmin+l+1;

ymax=ymin+h;

if xmin<1              %respect of boundaries

    xmin=1;

end

if ymin<1

    ymin=1;

end

if xmax>lmax

    xmax=lmax;

end

if ymax>hmax

    ymax=hmax;

```

```

end

P(ymin:ymax,xmin:xmax) =0;                                %clean all noise points

figure()

imshow(P)

title('Partial Result - Cancel to restart')

% Construct a questdlg with three options

choice = questdlg('Are you satisfied?', 'CONTINUE'      , 'No');

% Handle response

switch choice

    case 'Yes'

        satisf=1;

        clean=1;

    case 'No'

        satisf=0;

        clean=1;

    case 'Cancel'

        clear rect P

        satisf=1;

        clean=0;

```

```

    end

    close all

end

close all

end

[hmax,lmax]=size(P);                                % create image frame

F=zeros(hmax,lmax);

F(1,1:20)=1;

F(1,end-20:end)=1;

F(1:20,1)=1;

F(end-20:end,1)=1;

F(end,1:20)=1;

F(end,end-20:end)=1;

F(1:20,end)=1;

F(end-20:end,end)=1;

middle=lmax/2;

middle=round(middle);

F(1:20,middle)=1;

% Find white pixels position

```

```

[Zrow,Zcolumn]=find(P>0);

lr=hmax;

Lower_Edge_Points_Height=max(Zrow); % Pixel height--
>error calculation

SCALE=[SCALE,Lower_Edge_Points_Height];

Zrow=lr-Zrow; % y axis inversion (from image pixel
coordinate to cartesian ones)

Zrow=10*Zrow*scale; % heigth scaling between pixel heigth
and real image heigth

Zcolumn=10*Zcolumn.*scale; % heigth scaling between pixel
lenght and real image lenght

COORD=[Zcolumn Zrow];

N=length(Zrow);

%Calcuate Barycenter

XG = 0;

YG = 0;

for i=1:N

    XG = XG + Zcolumn(i);

    YG = YG + Zrow(i);

end

XG = XG / N;

```

```

YG = YG / N;

% final framework

[Zr1,Zc1]=find(F>0);

Zr1=lr-Zr1;

Zr1=10*Zr1.*scale;

Zc1=10*Zc1.*scale;

ADD=[Zc1,Zr1;XG,YG];

figure()

hold on

plot(ADD(:,1),ADD(:,2),'b*')

plot(Z(:,1),Z(:,2),'y.')

plot(P(:,1),P(:,2),'g+')

plot(Zc1,Zr1,'*b');

plot(Zcolumn,Zrow,'r^');

hold off

%save

num=sprintf('%02i',n);

num=char(num);

name=['PARTIALedges',num];

```

```

save(name, 'COORD','ADD','SCALE'); % salva COORDINATE e cornice come ADD

M=[scale]

filename = 'CoarseEDGE_Points.xlsx';

sheet = Nimg(1:end-4);

ColRow='A2';

xlswrite(filename,COORD,sheet,ColRow)

xlswrite(filename,M,sheet,'F4')

Zrow=0;

Zcolumn=0;

% Construct a questdlg with three options

choice = questdlg('Proceed with next img?', 'NEXT IMG' , 'Yes');

% Handle response

switch choice

    case 'Yes'

        quest=1;

    case 'No'

        quest=0;

    case 'Cancel'

end
end

```

```

if quest==1

    clear distance distance1 distance2 BufferS BufferO IMG SCALE scale N M F P Zrow
Zcolumn          % To permit the new cycle to use the same variables

    close all

else

    close all

    break  %%%%%%%%% to exit if i don't want to continue

end

end

```

9.1.3 Points Conversion: "EDGEpointsGENERATOR"

```
clear all
```

```
close all
```

```
clc
```

```
disp(' ')
```

```
fprintf(2,'Digit directory path between apostrophes\n');
```

```
path = input('path:');
```

```
disp(' ')
```

```
DIR=dir([path, '\*.mat']);
```

```
fprintf(2,'Here are the files list of this directory\n');
```

```
dir([path, '\*.mat'])
```

```
disp(' ')
```

```
fprintf(2,'Insert initial and final file n° (Selevt "PARTIALedges--")\n');
```

```
a = input('initial=');
```

```
b =input('final=');
```

```
while a<1 || b<1 || b<a
```

```
    a=[];
```

```
    b=[];
```

```
    a = input('initial=');
```



```

    b =input('final=');

end

for n=a:b

    c='\';

    Nimg=DIR(n).name;

    index=[path c Nimg];

    load(index);

    disp(' ')

    fprintf(2,'Image step \n');

    disp(Nimg)

    %COORDINATES=VARIABLE

    FINAL_RESULT=length(COORD(:,1));

    XX=COORD(:,1);

    YY=COORD(:,2);

    %Calcuate Barycenter

    XG = 0;

    YG = 0;

    for i=1:FINAL_RESULT

        XG = XG + XX(i);

```

```

    YG = YG + YY(i);

end

XG = XG / FINAL_RESULT;

YG = YG / FINAL_RESULT;

figure

plot(COORD(:,1),COORD(:,2),'.')

satisf=0;

while satisf==0                                %Savitzky Golay points filtering

    disp(' ')

    fprintf(2,'Digit Savitzky Golay ORDER and FRAMELENGTH. \n');

    disp('They must be INTEGER!')

    disp(' ')

    disp('Suggested ORDER 3')

    disp('Suggested FRAMELENGTH 45')

    disp(' ')

    disp('Press enter for suggested ')

    disp(' ')

    order=input('order=');

    if size(order)==[0,0]

```

```

        order=3

    end

    framelength=input('framelength=');

    if size(framelength)==[0,0]

        framelength=45

    end

    while order<1||framelength<=order | mod(framelength,2)==0

        order=[];

        framelength=[];

        order=input('order=');

        framelength=input('framelength=');

    end

    clear Xn Yn DTE X_LEFT Y_LEFT X_RIGHT Y_RIGHT X_TREATED Y_TREATED X Y TOT
NewTOT INIZ TE R

    FINAL_RESULT = length(XX);

    figure

    hold on

    plot(XX,YY,'r.')

    axis equal

    title('TRANSVERSE PROFILE')

```

```

plot(XG, YG,'go')

hold off

%polar switch

for h=1:FINAL_RESULT                                %coordinates respect to
barycenter to switch in polar respect G

    Xn(h,:)=XX(h)-XG;

    Yn(h,:)=YY(h)-YG;

end

[TE,R]=cart2pol(Xn,Yn);

%    R=ones(N,1);

%    TE=atan2(Yn,Xn)

figure()

plot(TE,R,'kd')

figure()

polar(TE,R,'kd')

INIZ=[XX,YY,TE,R];                                % XX YY are the absolute coordinates

TOT=sortrows(INIZ,3);

TE_b=TOT(:,3);

D_TE(1,1)=TE_b(FINAL_RESULT)-TE_b(1);

for h=2:FINAL_RESULT

```

```

    D_TE(h,1)=TE_b(h)-TE_b(h-1);

end

TOT=[TOT,D_TE];

[ff,~]=size(TOT);

% set delta threshold_1

disp(' ')

fprintf(2,'Set Angular Threshold for holes in DEG (press enter for default)\n');

delta = input('Delta Angle in ° =');

if size(delta)==[0,0]

    de=0.03

else

    de=delta*pi/180

end

thr=TOT(:,5)>de;

for i=1:5

    NewTOT(:,i)=TOT(:,i).*thr;

end

Pos=find(NewTOT(:,5)~=0);

Prec=Pos-1;

```

```

Delta_Angle_Selected=[Prec;Pos]

[j,~]=size(Delta_Angle_Selected);

if Delta_Angle_Selected(1,1)==0

    Delta_Angle_Selected(1,1)=ff;

    Delta_Angle_Selected((1+(j/2)),1)=1;

end

for i=1:j

    posi=Delta_Angle_Selected(i);

    TOT2(i,:)=TOT(posi,:);

end

step=j/2;

Sampled_Coordinates=TOT;

figure()

for i=1:step

    P0=[XG,YG];

    P1=TOT2(i,1:2)

    P2=TOT2((i+step),1:2)

    v1 = P1-P0;

    v2 = P2-P0;

```

```

c = det([v1;v2]); % "cross product" of v1 and v2

Angle = 180*atan2(abs(c),dot(v1,v2))/pi;

Points_Number = 0.5*Angle; % The number of points in
the arc

a = linspace(0,atan2(abs(c),dot(v1,v2)),Points_Number); % Angle range

v3 = [0,-c;c,0]*v1'; % v3 lies in plane of v1 and v2 and is
orthog. to v1

Circle_Fill = v1'*cos(a)+((norm(v1')/norm(v3))*v3)*sin(a); % Arc, center
at (0,0)

Circle_Fill=Circle_Fill';

Circle_Fill(:,1)=Circle_Fill(:,1)+XG;
Circle_Fill(:,2)=Circle_Fill(:,2)+YG;

hold on

plot(Circle_Fill(:,1),Circle_Fill(:,2),'g.') % Plot arc, centered at
P0

axis equal

Circle_Fill(:,3:5)=0;

Sampled_Coordinates=[Sampled_Coordinates;Circle_Fill];

clear v

end

hold off

```

```

[nl,~]=size(Sampled_Coordinates);

XG1=mean(Sampled_Coordinates(:,1))                % Re-calculate
polar coordinates (New Barycenter)

                                %[maybe isn't necessary, but should be usefull]

YG1=mean(Sampled_Coordinates(:,2))

for i=1:nl

    Xn1=Sampled_Coordinates(:,1)-XG1;

    Yn1=Sampled_Coordinates(:,2)-YG1;

end

[newTE,newR]=cart2pol(Xn1,Yn1);

POLAR=[Sampled_Coordinates(:,1),Sampled_Coordinates(:,2),newTE,newR];

POLAR=sortrows(POLAR,3);

TE_b=POLAR(:,3);

D_TE(1,1)=TE_b(nl)+TE_b(1);

for h=2:nl

    D_TE(h,1)=TE_b(h)-TE_b(h-1);

end

POLAR=[POLAR,D_TE];

[ff,~]=size(TOT);

figure()

```



```

plot(POLAR(:,1),POLAR(:,2),'^k')

X=POLAR(:,1);

Y=POLAR(:,2);

% Savitzky Golay filtering

SG = sgolayfilt([X Y],order,framelength);

figure

hold on

plot(SG(:,1),SG(:,2),'-^k')

plot(X,Y,'--r')

title('Change order to connect curev borders - Change framelength to smooth')

filter=SG;

% Construct a questdlg with three options

choice = questdlg({'Wanna save any img?','Cancel to exit'}, 'SAVE IMG' , 'No');

% Handle response

switch choice

case 'Yes'

    satisf=1;

case 'No'

    satisf=0;

```

```

    case 'Cancel'

        satisf=3;

    end

    if satisf==0

        % Construct a questdlg with three options

        choice = questdlg('Wanna save original points [Y]? (N) to continue)', 'SAVE IMG'
        , 'No');

        % Handle response

        switch choice

            case 'Yes'

                orig=1;

            case 'No'

                orig=0;

            case 'Cancel'

                orig=0;

        end

        if orig==1

            filter=[X,Y];

            old=filter;

            satisf=1;

```

```

else

    satisf=0;

end

else

    old=filter;

end

figure()

imshow(filter)

plot(filter, '*')

clear X_DOWN Y_DOWN X_UP Y_UP X_LEFT Y_LEFT X_RIGHT Y_RIGHT X_LEFT
Y_LEFT X_RIGHT Y_RIGHT X_TREATED Y_TREATED TOT D_TE

end

%%%%%%%%%%%%%%%%%%%%%%%%%%%%%%%%%%%%%%%%%%%%%%%%%%%%%%%%%%%%%%%%%%%%%%%%
%%%%%%%%%%%%%%%%%%%%%%%%%%%%%%%%%%%%%%%%%%%%%%%%%%%%%%%%%%%%%%%%%%%%%%%%

leng=length(X)

% POINTS SAMPLING

%polar switch

for h=1:leng                                %coordinates respect to barycenter to
switch in polar respect G

    XN2(h,:)=filter(h,1)-XG1;

```

```

    YN2(h,:)=filter(h,2)-YG1;

end

[TE2,R2]=cart2pol(XN2,YN2);

figure()

polar(TE2,R2,'kd')

BUFF_initial=[filter(:,1),filter(:,2),TE2,R2];           % XX YY are the
absolute coordinates

BUF=sortrows(BUFF_initial,3);

% set delta threshold_2

disp(' ')

fprintf(2,'Set Angular Step Sampling in DEG (dividing 360°)\n');

disp('press enter for default setting')

disp(' ')

cntrl=0;

while cntrl==0 | Step>60

    Step = input('Angular Step in ° =');

    if size(Step)==[0,0]

        Step=10

    end

    beta=360/Step;

```

```

    cntrl=isequal(fix(beta),beta);

end

Angle=Step*pi/180;

SAMPLED=[];

for t=1:(360/Step)    %da -pi a +pi devo cambiare

    AnglePos=Angle*t-pi;

    Dalfa=BUF(:,3);

    Dalfa=abs(Dalfa-AnglePos);

    minDalfa=min(Dalfa);

    reach=(Dalfa==minDalfa);

    pTE=BUF(:,3).*reach;

    pR=BUF(:,4).*reach;

    SAMPLED=[SAMPLED; pTE pR];

end

figure

polar(SAMPLED(:,1),SAMPLED(:,2),'^m')

% Construct a questdlg with three options

choice = questdlg('Are you satisfied','CHECK' , 'No');

% Handle response

```

```

switch choice

    case 'Yes'

        sat=1;

    case 'No'

        sat=0;

    case 'Cancel'

        sat=0;

end

if sat==1

    Tefin=SAMPLED(:,1);

    Rfin=SAMPLED(:,2);

    [xfin,yfin]=pol2cart(Tefin,Rfin);

    J=[xfin,yfin];

    J(any(J==0,2),:)=[]

    figure

    hold on

    plot(xfin,yfin,'^g')

    xfin=J(:,1)+XG1;

    yfin=J(:,2)+YG1;

```

```

plot(xfin,yfin,'*b')

xxfin=[xfin;XG1];

yyfin=[yfin;YG1];

plot(xxfin,yyfin,'.r')

hold off

%    figure

%

%    hold on

%    plot(xfin,yfin,'^g')

%

%    xfin=xfin+XG1;

%    yfin=yfin+YG1;

%

%

%    plot(xfin,yfin,'.r')

%    hold off

end

%%%%%%%%%%%%%%%%%%%%%%%%%%%%%%%%%%%%%%%%%%%%%%%%%%%%%%%%%%%%%%%%%%%%%%%%%%%%%%
%%%%%%%%%%%%%%%%%%%%%%%%%%%%%%%%%%%%%%%%%%%%%%%%%%%%%%%%%%%%%%%%%%%%%%%%%%%%%%

Sampled_Coordinates=[xfin,yfin;ADD];

```

```

figure

plot(Sampled_Coordinates(:,1),Sampled_Coordinates(:,2),'.')

if satisf==1

    %XYZ image positioning

    disp(' ')

    fprintf(2,'Z position of the image: offset number (if press "enter" 0=default) =?\n');
% Z positioning

    Pos=input('Offset n° of the image =');

    [Npoints,~]=size(Sampled_Coordinates);

    if size(Pos)==[0,0]

        Zpos=zeros(Npoints,1);

    else if Pos==1

        Zpos=ones(Npoints,1)*10;

    else

        unity=ones(Npoints,1);

        Zpos=unity.*Pos*10;

    end

end

FINAL_RESULT=[Sampled_Coordinates Zpos];

M=[1] %SCALE//ERROR INFO

```



```

filename = 'FINAL EDGES_Coordinates.xlsx';

sheet = Nimg(1:end-4);                                %%% ATTENZIONE!!!! PERCHE???

ColRow='A2';

xlswrite(filename,FINAL_RESULT,sheet,ColRow)

xlswrite(filename,M,sheet,'F4')

Zriga=0;

Zcolonna=0;

clear clear FINAL_RESULT Xn Yn D_TE F X Y TOT NewTOT INIZ TE R STEP thr V filter
SG TE2 R2 J xfin yfin xxfin yyfin BUFF TEfin Rfin XN2 YN2

close all

clc

else

break

end

end

close all

clear

clc

```

9.1.4 Velocity Profile Generation: “PulseWaveExtractor”

```
clear
```

```
close all
```

```
clc
```

```
fprintf(2,'The aim is to extract the average VELOCITY PROFILE during various heart beats\n');
```

```
fprintf(2,'extractiing the profile from the image, scaling it, averaging and approximating with polyfit\n');
```

```
fprintf(2,'      \n');
```

```
fprintf(2,'      \n');
```

```
fprintf(2,'      \n');
```

```
disp(' ')
```

```
fprintf(2,'Digit directory path between apostrophes\n');
```

```
path = input('path:');
```

```
disp(' ')
```

```
DIR=dir([path, '\*.dcm']); %directory choice
```

```
fprintf(2,'Here are the files list of this directory\n');
```

```
dir([path, '\*.dcm'])
```

```
disp(' ')
```

```

fprintf(2,'Insert initial and final image n°\n');

a = input('initial=');

b =input('final=');

while a<1 || b<1 || b<a

    a=[];

    b=[];

    a = input('initial=');

    b =input('final=');

end

for n=a:b                                % start cycle for different images

    cont=1;                              % initial posizion for image matrix

    disp(' ')

    fprintf(2,'Measure reference distance for scaling \n');

    c='\';

    pp=DIR(n).name;

    index=[path c pp];

    A=dicomread(index);                  % read image

    disp(' ')

    fprintf(2,'Image step \n');

```

```

disp(pp)

g = warndlg(sprintf(' Digit reference VELOCITY and TIME STEP provided from the
image.\n \nThen press any key to close. '), '          ATTENTION!');

drawnow                                % Necessary to print the message

waitfor(g);

figure()

imshow(A)

title('Press any key when you read the measure')

w = waitforbuttonpress;

if w == 1

    close all                          %permit user to have time to read

end

dist=input('Velocity reference value=');

disp(' ')

dist2=input('Time step reference value=');

while size(dist)==[0,0] | size(dist2)==[0,0]

    dist=[];

    dist2=[];

    disp(' ')

    fprintf(2,'Digit maximum velocity modulus in the reference scale \n');

```

```

dist=input('Velocity reference value=');

disp(' ')

fprintf(2,'Digit reference time step to measure in the next step \n');

dist2=input('Time step reference value=');

end

% Construct a questdlg with three options

choice = questdlg('Is it ok?', 'CHECK' , 'Yes');

                                % Handle response

switch choice

    case 'Yes'

    case 'No'

        dist=input('Velocity reference value=');

        disp(' ')

        dist2=input('Time step reference value=');

    case 'Cancel'

        figure()

        imshow(A)

        title('Press any key when you read the measure')

        w = waitforbuttonpress;

```

```

if w == 1

    close all                                %permit user to have time to read

end

dist=input('Velocity reference value=');

disp(' ')

dist2=input('Time step reference value=');

end

rr = warndlg(sprintf(' Use "measure tool" to measure:\n \n          -reference scale
length.\n \n          -reference time length\n \n          -maximum height\n \n\n \n Right
Click and "Esport to workspace" each measure.\n \n Respect the measures list order.\n
\n '), '          ATTENTION!');

drawnow                                    % Necessary to print the message

waitfor(rr);

measures=0;

while measures==0

    imtool(A)

    f = warndlg(sprintf(' Measures order:\n \n          -reference scale length.\n \n          -
reference time length\n \n          -mmaximum height \n \n Move apart this window to
ease process\n \n Press OK ONLY when pixel measure is taken. '), '          DON''T
CLOSE!');

    drawnow                                    % Necessary to print the message

    waitfor(f);

```

```

imtool close all

% Construct a questdlg with three options

choice = questdlg('Is it ok?', 'CHECK' , 'Yes');

                                % Handle response

switch choice

    case 'Yes'

        measures=1;

        imtool close all

    case 'No'

        imtool close all

        measures=0;

    case 'Cancel'

        imtool close all

        misure=0;

end

end

disp(' ')

Velocity_Step=distance

disp(' ')

```

```

Time_Step=distance1

disp(' ')

%Scale Factors

Vel_scale=(dist)/(Velocity_Step);

Time_scale=(dist2)/(Time_Step);

disp(' ')

Peak_velocity=distance2*Vel_scale

SCALE=[Vel_scale,Time_scale,Time_Step,Peak_velocity];

disp(' ')

l = warndlg(sprintf(' Crop the shape of interest. \n \n Mantain the total length and
height of the image. '), '          ATTENTION!!');

drawnow    % Necessary to print the message

waitfor(l);

B=imcrop(A);                                %crop image to edit: mantain al the area
scanned by the instrument to make simplier the scaling

close all

% Construct a questdlg with three options

choice = questdlg('Is it ok?', 'CHECK'    , 'Yes');

                                % Handle response

switch choice

```



```

case 'Yes'

    close all

case 'No'

    clear B

    B=imcrop(A);

case 'Cancel'

    close all

end

close all

% extract average velocity line

imshow(B);

[D1,D2,D3]=size(B);

C = zeros(D1,D2,D3);

for i=1:D1

    for j=1:D2

        if B(i,j,1)>200 && B(i,j,2)<200 %&& B(i,j,3)<200

            C(i,j,1)=B(i,j,1);

            C(i,j,2)=B(i,j,2);

            C(i,j,3)=B(i,j,3);

        end

    end

end

```

```

        end

    end

end

figure

imshow(C)

% Find white pixels position

C=rgb2gray(C);

[Zrow,Zcolumn]=find(C>0);

lr=D1;

Zrow=lr-Zrow;                                %y axis inversion (from image pixel
coordinate to cartesian ones)

Zrow=Zrow*Vel_scale;                          % heigth scaling between pixel heigth
and real image heigth--->velocity scaling

Zcolumn=Zcolumn.*Time_scale;                  % heigth scaling between pixel
lenght and real image lenght---->time scaling

Profile=[Zcolumn Zrow];

Profile=sortrows(Profile,2);

Profile=sortrows(Profile,1);

N=length(Zrow);

figure()

hold on

```

```

plot(Zcolumn,Zrow,'r^');

hold off

%%%%%%%%%%%%%%%%%%%%%%%%%%%%%%%%%%%%%%%%%%%%%%%%%%%%%%%%%%%%%%%%%%%%%%%%
%%%%%%%%%%%%%%%%%%%%%%%%%%%%%%%%%%%%%%%%%%%%%%%%%%%%%%%%%%%%%%%%%%%%%%%%

Max=max(Profile(:,2));

C= unique(Profile(:,1));

[C_size,~]=size(C);

New_points=[];

for j=1:C_size                %clear multiple points taking the middle one

    pos=find(C(j)==Profile(:,1));

    [~,p]=size(pos);

    if mod(p,2)==0

        loc=p/2;

    else

        loc=(p+1)/2

    end

    New_points=[New_points;Profile((pos(loc)),:)];

    clear pos

end

OLD=Profile;

```

```

clear Profile

Profile=New_points;

Points_vect=20    % experimental values to evaluate velocity gradient at the beginning
of the pulsewave

Delta_value=20

Profile=sortrows(Profile,1);

Diff=[];

Pos=[];

ref=[];

for i=1:(length(Profile(:,1))-Points_vect)

    Diff(i)=abs(Profile(i,2)-Profile((i+Points_vect),2));

    if Diff(i)>Delta_value

        Pos=[Pos;i];

    end

end

ll=length(Pos);

CLEARED=Profile(Pos,:);

for j=1:ll

    if CLEARED(j,2)>(Max-35)

        CLEARED(j,:)=0;

```

```

    end

end

CLEARED = CLEARED(any(CLEARED,2),:);           %clear zeros rows

L=length(CLEARED(:,1));

for y=2:L-1

    Delta_t(y)=abs(CLEARED(y,1)-CLEARED(y-1,1));

end

Delta_t(1)=abs(CLEARED(1,1)-CLEARED(L,1));

Step=find(Delta_t>0.3)

Pulse_end=Step;

Pulse_start=Step+1;

Wave_n=length(Step)

for k=1:Wave_n

    Many_pos_start(k)=find(Profile==(CLEARED(Pulse_start(k),1)));

    STEP(:,k)=0;

end

Many_pos_end=Many_pos_start-1;

Many_pos_end=Many_pos_end(2:end)

Many_pos_start=Many_pos_start(1:end-1)

```

```

figure()

hold on

plot(Profile(:,1),Profile(:,2),'^g')

plot(Profile(Many_pos_start,1),Profile(Many_pos_start,2),'ob','LineWidth',2,'MarkerSize'
,10,'MarkerFaceColor',[0.5,0.5,0.5])

plot(Profile(Many_pos_end,1),Profile(Many_pos_end,2),'ok','LineWidth',2,'MarkerSize',1
0,'MarkerFaceColor',[0.5,0.5,0.5])

plot(CLEARED(:,1),CLEARED(:,2),'r.')

hold off

for k=1:Wave_n-1

    Time_Delta(k)=abs(Profile(Many_pos_end(k),1)-Profile(Many_pos_start(k),1));

end

Average_Time=mean(Time_Delta);

for k=1:Wave_n-1                                % split waves

    Wave(k)={Profile(Many_pos_start(k):Many_pos_end(k),:)};

end

figure

for k=1:Wave_n-1

x=[];

Y=[];

```

```

x=Wave{1,k}(:,1);

Y=Wave{1,k}(:,2);

hold on

plot(x,Y,'.')

end

hold off

for j=1:Wave_n-1                                % normalized wave + scaling

    Wave{1,j}(:,1)=Wave{1,j}(:,1)-Wave{1,j}(1,1)    %all waves starting from
zero

    max_time_val=max(Wave{1,j}(:,1))

    Wave{1,j}(:,1)=Wave{1,j}(:,1)/max_time_val*Average_Time

end

%%%%%%%%%%%%%% --Mean

chk=0;

while chk==0

    disp(' ')

    fprintf(2,'Digit the numbers of points you want to use to interpolate the wave (suggested
[80;200]) \n');

    Samples_n=input('N° Time samples=');

    if size(Samples_n)==[0,0] | Samples_n<15

```

```

    chk=0;

else

    chk=1;

end

end

Time_step=Average_Time/Samples_n

Mean=[0,0];

for ww=1:Samples_n                                %extract the average mean from waves

    TIME=Time_step*ww;

    for ff=1:Wave_n-1

        Delta=Wave{1,ff}(:,1)-TIME;

        Min_delta=sortrows(Delta,1);

        Min1=Min_delta(1)

        Min2=Min_delta(2)

        pos_1=(Delta==Min1);

        pos_2=(Delta==Min2);

        Y_single(ff)=(Wave{1,ff}(pos_1,2)+((Wave{1,ff}(pos_1,2)-
Wave{1,ff}(pos_2,2)))*Min1/(Min1+Min2)));

    end

Y_mean=mean(Y_single);

```



```

    Mean=[Mean;TIME,Y_mean];

end

figure

plot(Mean(:,1),Mean(:,2),'.r')

title('mean')

figure

for k=1:Wave_n-1

x=[];

Y=[];

x=Wave{1,k}(:,1);

Y=Wave{1,k}(:,2);

hold on

plot(x,Y,'--.')

end

hold off

New_x=[];

New_y=[];

for k=1:Wave_n-1

New_x=[New_x;Wave{1,k}(:,1)];

```

```

New_y=[New_y;Wave{1,k}(:,2)];

end

figure

plot(New_x,New_y, '.')

satisf=0;

figure

while satisf==0

    disp(' ')

    fprintf(2,'Digit the polynom order to average the wave profile (sugessted [15;25] \n');

    order=input('polyfit order=');

    if size(order)==[0,0]

        order=12;

    end

    fact=polyfit(New_x,New_y,order);

    Sampled_Time=linspace(0,Average_Time,Samples_n);           %Sampling at equal
    time length usin Samples_n points

    Y_interp=polyval(fact,Sampled_Time);

    hold on

    plot(New_x,New_y, 'c')

    plot(Sampled_Time,Y_interp,'color',rand(1,3),'LineWidth',2)

```

```
%axis([0 3.2 0 60])
```

```
hold off
```

```
% Construct a questdlg with three options
```

```
choice = questdlg('Are you satisfied?', 'CHECK' , 'No');
```

```
% Handle response
```

```
switch choice
```

```
    case 'Yes'
```

```
        satisf=1;
```

```
    case 'No'
```

```
        satisf=0;
```

```
    case 'Cancel'
```

```
end
```

```
end
```

```
hold off
```

```
ORIGINAL=Profile;
```

```
OVERLAPPED=[New_x,New_y]
```

```
INTERP=[Sampled_Time,Y_interp']
```

```
% VELOCITY RAMP creation
```

```
x_ramp=[0;6*Time_step;20*Time_step];           % initial parabolic time points where  
to evaluate the ramp function
```

```

y_ramp=[0;2;INTERP(1,2)];          % initial parabolic velocity points where to
evaluate the ramp function

fact_ramp=polyfit(x_ramp,y_ramp,2);    %parabolic fitting

time_ramp=linspace(0,(10*Time_step),10);    %time spacing for the ramp profile

ramp_val=polyval(fact_ramp,time_ramp);    %parabolic evaluation

% figure

% plot(time_ramp,ramp_val,'-*')

RAMP=[time_ramp;ramp_val]';

%%%%%%%%%%%%%%%%%%%%%%%%%%%%%%%%%%%%%%%%%%%%%%%%%%%%%%%%%%%%%%%%%%%%%%%%%%%%%%
%%%%%%%%%%%%%%%%%%%%%%%%%%%%%%%%%%%%%%%%%%%%%%%%%%%%%%%%%%%%%%%%%%%%%%%%%%%%%%

% MULTIPLYING PULSE WAVES

MOD1=INTERP;

MOD1(:,1)=MOD1(:,1)+(11*Time_step);

MOD2=MOD1;

MOD2(:,1)=MOD2(:,1)+INTERP(end,1)+Time_step;

MOD3=MOD2;

MOD3(:,1)=MOD3(:,1)+INTERP(end,1)+Time_step;

MOD4=MOD3;

MOD4(:,1)=MOD4(:,1)+INTERP(end,1)+Time_step;

PULSE=[RAMP;MOD1;MOD2;MOD3;MOD4];

```

```

figure()

plot(PULSE(:,1),PULSE(:,2),'-b')

%%%%%%%%%%%%%%%%%%%%%%%%%%%%%%%%%%%%%%%%%%%%%%%%%%%%%%%%%%%%%%%%%%%%%%%%%%%%%%
%%%%%%%%%%%%%%%%%%%%%%%%%%%%%%%%%%%%%%%%%%%%%%%%%%%%%%%%%%%%%%%%%%%%%%%%%%%%%%

% saving results

POLY=[fact]

num=sprintf('%02i',n);

num=char(num);

name=['VELOCITY',num];

save(name, 'ORIGINAL','INTERP','POLY','OVERLAPPED','SCALE');           %
salva COORDINATE

M=[Vel_scale,Time_scale]

filename = 'CoarsePulseWaveOVERLAPPED_points.xlsx';

sheet = n;

ColRow='A2';

xlswrite(filename,OVERLAPPED,sheet,ColRow)

xlswrite(filename,M,sheet,'L4')

M=[Vel_scale,Time_scale]

filename = 'CoarsePulseWaveINTERPOLED.xlsx';

sheet = n;

```

```

ColRow='A2';

xlswrite(filename,PULSE,sheet,ColRow)

xlswrite(filename,M,sheet,'L4')

Zrow=0;

Zcolumn=0;

% Construct a questdlg with three options

choice = questdlg('Proceed with next img?', 'NEXT IMG'      , 'Yes');

% Handle response

switch choice

    case 'Yes'

        quest=1;

    case 'No'

        quest=0;

    case 'Cancel'

end

if quest==1

    clear distance distance1 distance2 Profile CLEARED WAVEORIGINAL POLY INTERP
OVERLAPPED SCALE scale N M p Zrow Zcolumn Step STEP Pulse_start Pulse_end x y Y
Y_interp fact                % To permit the new cycle to use the same variables

    close all

```

else

close all

break

%%%%%%%%%% to exit if i don't want to continue

end

end

10 Bibliography & References

1. Atherton, John C. Role of the kidney in acid–base balance. *Anaesthesia & Intensive Care Medicine*. s.l. : Anaesthesia & Intensive Care Medicine, June 2015. Vol. 16, 6.
2. Kidney. *Wikipedia*. [Online] <https://en.wikipedia.org/wiki/Kidney>.
3. Chronic Kidney Disease (CKD). *NATIONAL INSTITUTE OF DIABETES AND DIGESTIVE AND KIDNEY DISEASES*. [Online] <https://www.niddk.nih.gov/health-information/kidney-disease/chronic-kidney-disease-ckd>.
4. What is Dialysis and Chronic Kidney Disease? *The Dialysis Patients Citizens (DPC) Education Center*. [Online] <http://www.dpcedcenter.org/what-dialysis-and-chronic-kidney-disease>.
5. Kidney Transplant. *The Dialysis Patients Citizens (DPC) Education Center*. [Online] <http://www.dpcedcenter.org/classroom/kidney-transplant>.
6. Dialysis. *Wikipedia*. [Online] <https://en.wikipedia.org/wiki/Dialysis>.
7. Dialysis. *Medicinenet*. [Online] <http://www.medicinenet.com/dialysis/page2.htm>.
8. DIALYSIS. *National Kidney Foundation*. [Online] <https://www.kidney.org/atoz/content/dialysisinfo>.
9. Home Dialysis. *Renal Medicine Associates*. [Online] <http://renalmed.com/home-dialysis/>.

10. Hemodialysis. *Wikipedia*. [Online] <https://en.wikipedia.org/wiki/Hemodialysis>.
11. In-Center Hemodialysis. *The Dialysis Patients Citizens (DPC) Education Center*. [Online] <http://www.dpcedcenter.org/classroom/center-hemodialysis>.
12. Home Hemodialysis. *The Dialysis Patients Citizens (DPC) Education Center*. [Online] <http://www.dpcedcenter.org/home-hemodialysis>.
13. Vascular Access for Hemodialysis. *National Institute of Diabetes and Digestive and Kidney Diseases*. [Online] <https://www.niddk.nih.gov/health-information/kidney-disease/kidney-failure/hemodialysis/vascular-access>.
14. *Arteriovenous access failure: more than just intimal hyperplasia?* Tonia C. Rothuizen, ChunYu Wong, Paul H.A. Quax, Anton Jan van Zonneveld, Ton J. Rabelink, Joris I. Rotmans. 5, s.l. : Nephrology Dialysis Transplantation, March 2013, Vol. 28.
15. Brachio-basilic Fistula vs. Brachio-cephalic Fistula. *Laminate medical technologies*. [Online] <http://www.laminatemedical.com/brachio-basilic-fistula-vs-brachio-cephalic-fistula/>.
16. Which type of AV fistula is best for dialysis patients? *Laminate Medical Technologies*. [Online] <http://www.laminatemedical.com/type-av-fistula-best-dialysis-patients/>.
17. *The Arteriovenous Fistula*. Klaus Konner, Barbara Nonnast-Daniel, Eberhard Ritz. 6, s.l. : Journal of the American Society of Nephrology, June 2003, Vol. 14. 0000069219.88168.39.
18. *No-touch technique for radiocephalic arteriovenous fistula – surgical technique and preliminary results*. Tal M. Hörer, Per Skoog, Robin Quell, Kristofer F. Nilsson, Thomas Larzon, Domingos R. Souza. 1, s.l. : The Journal of Vascular Access, 2016, Vol. 17. 26391584.
19. *A prospective study of end-to-side vs. side-to-side arteriovenous fistulas for haemodialysis*. K. R. Wedgwood. s.l. : BJS, August 1984.

20. *The Role of Shear Stress in Arteriovenous Fistula Maturation and Failure: A Systematic Review*. Leonard D. Browne, Khalid Bashar, Philip Griffin, Eamon G. Kavanagh, Stewart R. Walsh, Michael T. Walsh. s.l. : PLOS ONE, December 30, 2015.
21. *Low-pressure environment and remodelling of the forearm vein in Brescia-Cimino haemodialysis access*. Corpataux JM, Haesler E, Silacci P, Ris HB, Hayoz D. 2002 Jun. 12032197.
22. *Effects of Disturbed Flow on Vascular Endothelium: Pathophysiological Basis and Clinical Perspectives*. Jeng-Jiann Chiu, Shu Chien. 1, s.l. : HHS Public Access, 2011, Vol. 91. 1522-1210.
23. *Carotid bifurcation atherosclerosis. Quantitative correlation of plaque localization with flow velocity profiles and wall shear stress*. Zarins CK, Giddens DP, Bharadvaj BK, Sottiurai VS, Mabon RF, Glagov S. 4, s.l. : Circulation Research, Oct 1983 , Vol. 53. 6627609.
24. *Biology of arteriovenous fistula failure*. Prabir Roy-Chaudhury, Lawrence M. Spergel. s.l. : JNEPHROL, March 2007. 17514619.
25. *Most Important Chronic Complications of Arteriovenous Fistulas for Hemodialysis*. Stolic, Radojica. s.l. : Medical Principles and Practice, November 2012. 23128647.
26. *Arteriovenous Access Failure, Stenosis, and Thrombosis*. Jennifer M. MacRae, Christine Dipchand, Matthew Oliver, Louise Moist, Charmaine Lok, Edward Clark, Swapnil Hiremath, Joanne Kappel, Mercedeh Kiaii, Rick Luscombe, Lisa M. Miller. s.l. : Canadian Journal of Kidney Health and Disease, Sept. 2016. PMC5332078.
27. *3D Quantification of Wall Shear Stress and Oscillatory Shear Index Using a Finite-Element Method in 3D CINE PC-MRI Data of the Thoracic Aorta*. Sotelo J, Urbina J, Valverde I, Tejos C, Irarrazaval P, Andia ME, Uribe S, Hurtado DE. 6, s.l. : IEEE Transactions on Medical Imaging, January 2016, Vol. 35. 26780787.

28. *Effects of disturbed flow on vascular endothelium: pathophysiological basis and clinical perspectives.* Chiu JJ, Chien S. 2011 Jan. PMC3844671.
29. *Hemodynamic Shear Stress and Endothelial Dysfunction in Hemodialysis Access.* Michelle K. Fitts, Daniel B. Pike, Kasey Anderson, Yan-Ting Shiu. 2014 May. PMC4189833.
30. *The Role of Shear Stress in Arteriovenous Fistula Maturation and Failure: A Systematic Review.* Leonard D. Browne, Khalid Bashar, Philip Griffin, Eamon G. Kavanagh, Stewart R. Walsh, Michael T. Walsh. s.l. : Plos One, December 30, 2015.
31. *High wall shear stress and spatial gradients in vascular pathology: a review.* Dolan JM, Kolega J, Meng H. 2013 Jul. PMC3638073 .
32. *Complex Hemodynamics at the Apex of an Arterial Bifurcation Induces Vascular Remodeling Resembling Cerebral Aneurysm Initiation .* Hui Meng, Zhijie Wang, Yiemeng Hoi, Ling Gao, Eleni Metaxa, Daniel D. Swartz, John Kolega. 2007 May . PMC2714768.
33. *Relative residence time and oscillatory shear index of non-Newtonian flow models in aorta.* Johannes V. Soulis, Olga P. Lampri, Dimitrios K. Fytanidis, George D. Giannoglou. s.l. : IEEE - International Workshop on Biomedical Engineering, Oct. 2011. 978-1-4577-0554-0.
34. *A Review on Computational Fluid Dynamics Modelling in Human Thoracic Aorta.* A. D. Caballero, S. Laín. s.l. : BMES, April 2013. 1869-408X.
35. Krishnan B. Chandran, Stanley E. Rittgers, Ajit P. Yoganathan. *Biofluid Mechanics: The Human Circulation, Second Edition.* s.l. : CRC Press , 2012. 9781439845165.
36. *Numerical and experimental study of blood flow through a patient-specific arteriovenous fistula used for hemodialysis.* Kharboutly Z., Deplano V., Bertrand E., Legallais C. 2, s.l. : Medical Engineering & Physics, March 2010, Vol. 32. 19962337 .

37. *Hemodynamic shear stress and its role in atherosclerosis*. Malek A.M., Alper S.L., Izumo S. s.l. : JAMA, December 1999. 10591386.
38. *Disturbed flow in radial-cephalic arteriovenous fistulae for haemodialysis: low and oscillating shear stress locates the sites of stenosis*. Ene-Iordache B, Remuzzi A. 1, s.l. : Nephrology Dialysis Transplantation, Jan 2012, Vol. 27. 21771751.
39. Blood. *Wikipedia*. [Online] <https://en.wikipedia.org/wiki/Blood>.
40. Ayyaswamy, Portonovo S. Introduction to Biofluid Mechanics. [aut. libro] Ira M. Cohen and David R. Dowling Pijush K. Kundu. *Fluid Mechanics 5ed*. s.l. : Academic Press, Sept 2011.
41. *Blood Flow*. Grobelnik, Barbara. University in Ljubljana : s.n., January 2008.
42. Whitmore, R L. *Rheology of the circulation*. s.l. : Pergamon Press , 1968. 9780080035321.
43. Pijush K. Kundu, Ira M. Cohen and David R. Dowling. *Fluid.Mechanics 5ed*. s.l. : Academic Press, September 2011. 978-0-12-382100-3.
44. Fåhræus–Lindqvist effect. *Wikipedia*. [Online] https://en.wikipedia.org/wiki/F%C3%A5hr%C3%A6us%E2%80%93Lindqvist_effect.
45. *Pulsatile Non-Newtonian Laminar Blood Flows through Arterial Double Stenoses*. Mir Golam Rabby, Sumaia Parveen Shupti, Md. Mamun Molla. s.l. : Journal of Fluids, 2014. 757902.
46. Owens, Anne M. RobertsonAdélia SequeiraRobert G. Rheological models for blood. [aut. libro] Alfio Quarteroni, Alessandro Veneziani Luca Formaggia. *Cardiovascular Mathematics*. s.l. : Springer, 2009.
47. *Numerical simulation of blood pulsatile flow in a stenosed carotid artery using different rheological model*. Razavi A., Shirani E., Sadeghi M.R. s.l. : Journal of Biomechanics, June 2011. 21696742.

48. *Non-Newtonian blood flow in human right coronary arteries: Steady state simulations*. Johnston B.M., Johnston PR, Corney S., Kilpatrick D. 5, s.l. : Journal of Biomechanics, May 2004, Vol. 37. 15047000.
49. *Non-Newtonian Rheology in Blood Circulation*. Sochi, Taha. s.l. : arXiv, Jun 2014. 1306.2067.
50. *Computation Of Blood Flows Accounting For Red-Blood Cell Aggregation/Fragmentation*. A.S. Kane, Y. Bourgault, A. Iolov, R.G.Owens, A. Fortin. s.l. : Dept. of Mathematics and Statistics University of Ottawa .
51. *Computation of the Coefficients of the Power law model for Whole Blood and Their Correlation with Blood Parameters*. Mohamed A. Elblbesy, Abdelrahman T. Hereba. 2, s.l. : Canadian Center of Science and Education , 2016 , Vol. 8. 1916-9639.
52. Wikipedia. *Reynolds number*. [Online]
https://en.wikipedia.org/wiki/Reynolds_number.
53. Falkovich, Gregory. *Fluid Mechanics*. Israel : Cambridge University Press, 2011. 9780511794353.
54. —. *Fluid Mechanics A Short Course for Physicists*. s.l. : Cambridge University Press, 2011. 9780511794353.
55. Entrance Length. *Wikipedia*. [Online]
https://en.wikipedia.org/wiki/Entrance_length.
56. Wikipedia. *Womersley number*. [Online]
https://en.wikipedia.org/wiki/Womersley_number.
57. *Wall shear stress in backward-facing step flow of a red blood cell suspension*. Gijsen F.J.H., F.N. Vosse, and J.D. Janssen,. 4,5, s.l. : Biorheology, 1998, Vol. 35.

58. *A numerical study of the effect of catheter angle on the blood flow characteristics in a graft during hemodialysis.* Hong Sun Ryou, Soyeon Kim, Kyoungchul Ro. 1, s.l. : Korea-Australia Rheology Journal, February 2013, Vol. 25.
59. *Computational fluid dynamics of a vascular access case for hemodialysis.* Giuseppe Remuzzi, Bogdan Ene-Iordache. 3, s.l. : Journal of Biomechanical Engineering, July 2001, Vol. 123.
60. *Carreau fluid model for blood flow through a tapered artery with a stenosis.* Noreen SherAkbar, S.Nadeemb. 44, s.l. : Ain Shams Engineering Journal, July 2014, Vol. 5.
61. *Analysis of the Casson and Carreau-Yasuda non-Newtonian blood models in steady and oscillatory flows using the lattice Boltzmann method.* Joshua Boyd, James M. Buick, Simon Greenc). 9, s.l. : Physics of Fluids, July 2007, Vol. 19.
62. Boundless. Blood Vessel Structure. *Boundless Anatomy and Physiology/Cardiovascular System: Blood Vessels.* s.l. : Boundless.
63. Tunica Intima. *Wikipedia.* [Online] https://en.wikipedia.org/wiki/Tunica_intima.
64. Cardiovascular System. *University of Oklahoma Health Science Center.* [Online] <http://www.ouhsc.edu/histology/text%20sections/cardiovascular.html>.
65. Magnetic Resonance Imaging. *Wikipedia.* [Online] https://en.wikipedia.org/wiki/Magnetic_resonance_imaging.
66. How are MRI and MRA scans different? *Two Views.* [Online] <http://www.two-views.com/mri-imaging/difference-MRA-scan.html#sthash.vvOz4N63.Gzxtj7G.dpbs>.
67. Medical Ultrasound. *Wikipedia.* [Online] https://en.wikipedia.org/wiki/Medical_ultrasound.
68. *Model of Aortic Blood Flow Using the Windkessel Effect.* MarianneCatanho, MriduSinha, VarshaVijayan. s.l. : BENG 221 - Mathematical Methods in Bioengineering, October 2012.

69. Lee Waite, Jerry Fine. *Applied Biofluid Mechanics*. s.l. : McGraw-Hill, 2007. 9780071472173.
70. *A pulse wave propagation model to support decision-making in vascular access planning in the clinic*. Huberts W1, Bode AS, Kroon W, Planken RN, Tordoir JH, van de Vosse FN, Bosboom EM. 2, s.l. : Medical Engineering & Physics, 2012 Mar, Vol. 34. 21840239 .
71. Computational fluid dynamics. *Wikipedia*. [Online]
https://en.wikipedia.org/wiki/Computational_fluid_dynamics.
72. Computational fluid dynamics for chemical reactor design. *World of Chemicals*. [Online] <http://www.worldofchemicals.com/11/chemistry-articles/computational-fluid-dynamics-for-chemical-reactor-design.html>.
73. Dmitri, KuzminInstitute. Introduction to Computational Fluid Dynamics. s.l. : Applied Mathematics - University of Dortmund.
74. Fluid Structure Interaction. *Comsol*. [Online]
<https://www.comsol.com/multiphysics/fluid-structure-interaction>.
75. *A fully-coupled fluid-structure interaction simulation of cerebral aneurysms*. Y. Bazilevs, M.-C. Hsu, Y. Zhang, W. Wang, X. Liang, T. Kvamsdal, R. Brekken, J. G. Isaksen. 1, s.l. : Computational Mechanics, June 2010, Vol. 46.
76. *Fluid Structure Interaction: Fundamentals and Application - A Review*. Jainish Topiwala, Gaurav Mistry, Sandip Patel, Pratik Umrigar. 1, s.l. : IJRMET, Oct 2016, Vol. 6. 2249-5762.
77. Luca Bertagna, Marta D'Elia, Mauro Perego, and Alessandro Veneziani. Data Assimilation in Cardiovascular Fluid–Structure Interaction Problems: An Introduction . [aut. libro] Giovanni P. Galdi, Šárka Nečasová Tomáš Bodnár. *Fluid-Structure Interaction and Biomedical Applications* . s.l. : Birkhäuser, 2014.

78. Ultrasound. *Wikipedia*. [Online] <https://en.wikipedia.org/wiki/Ultrasound>.
79. Medical Ultrasound. *Wikipedia*. [Online]
https://en.wikipedia.org/wiki/Medical_ultrasound.
80. Abigail Thrush, Tim Hartshorne. *Peripheral Vascular Ultrasound How, Why and When - Second Edition*. s.l. : Elsevier, 2005. 0443072833.
81. *Application of Ultrasound in Medicine*. Aladin Carovac, Fahrudin Smajlovic, Dzelaludin Junuzovic. s.l. : PubMed Central, 2011 Sep. PMC3564184.
82. *Value of Preoperative Sonographic Vascular Evaluation of Haemodialysis Access in Upperlimb*. Aishwarya K.C., M.G Srinath, Sanjay C Desai, Ashok Kumar A, Chandrashekar AR, Gowtham Gowda A.G. s.l. : Journal of Clinical and Diagnostic Research, 2014 Dec. PMC4316311.
83. Image Analysis. *Wikipedia*. [Online] https://en.wikipedia.org/wiki/Image_analysis.
84. *Digital Image Processing Technology based on MATLAB*. Saadia Hassan Abdalla, Saif Eldin Fattoh Osman. 3, s.l. : International Journal of Advanced Research in Computer Science, June 2016, Vol. 7. 0976-5697.
85. Cross. <http://ilwis.itc.utwente.nl>. [Online]
http://ilwis.itc.utwente.nl/wiki/index.php/Operations:_Cross.
86. DICOM. *Wikipedia*. [Online] <https://en.wikipedia.org/wiki/DICOM>.
87. Rabus, Dr. Hella. math. [Online] <https://www.math.hu-berlin.de/~ccafm/teachingAdvanced/Tutorials/matlab.php>.
88. tutorialspoint. MATLAB - Overview. *tutorialspoint*. [Online]
https://www.tutorialspoint.com/matlab/matlab_overview.htm.
89. cimss.ssec.wisc. whatismatlab. <http://cimss.ssec.wisc.edu>. [Online]
<http://cimss.ssec.wisc.edu/wxwise/class/aos340/spr00/whatismatlab.htm>.

90. Image Processing. *mathworks*. [Online]
<https://it.mathworks.com/help/images/index.html>.
91. features. *mathworks*. [Online]
<https://www.mathworks.com/products/image/features.html>.
92. Hough transform. *Wikipedia*. [Online]
https://en.wikipedia.org/wiki/Hough_transform.
93. Sobel Operator. *Wikipedia*. [Online] https://en.wikipedia.org/wiki/Sobel_operator.
94. Otsu's method. *Wikipedia*. [Online]
https://en.wikipedia.org/wiki/Otsu%27s_method.
95. Image Processing Toolbox Functions. *mathworks*. [Online]
<https://it.mathworks.com/help/images/functionlist.html>.
96. mathworks. *dir*. [Online]
https://it.mathworks.com/help/matlab/ref/dir.html?searchHighlight=dir&s_tid=doc_srchtile.
97. xlswrite. *mathworks*. [Online]
<https://www.mathworks.com/help/matlab/ref/xlswrite.html>.
98. Savitzky-Golay filter. *Wikipedia*. [Online]
https://en.wikipedia.org/wiki/Savitzky%E2%80%93Golay_filter.
99. cart2pol. *mathworks*. [Online]
<https://www.mathworks.com/help/matlab/ref/cart2pol.html>.
100. sgolayfilt. *mathworks*. [Online]
https://it.mathworks.com/help/signal/ref/sgolayfilt.html?s_tid=doc_ta.
101. Least Squares. *Wikipedia*. [Online] https://en.wikipedia.org/wiki/Least_squares.

102. least-square. *Slideshare*. [Online]

<https://www.slideshare.net/somyabagai/method-of-least-square>.

103. polyfit. *mathworks*. [Online]

https://it.mathworks.com/help/matlab/ref/polyfit.html?searchHighlight=polyfit&s_tid=doc_srchtile.

104. linspace. *mathworks*. [Online]

https://it.mathworks.com/help/matlab/ref/linspace.html?s_tid=doc_ta.

105. *Total arterial inertance as the fourth element of the windkessel model*. Stergiopoulos N., Westerhof B.E., Westerhof N. 1, s.l. : American Journal of Physiology, 1999 Jan, Vol. 276 . 9887020.

106. AutoCAD. *Wikipedia*. [Online] <https://en.wikipedia.org/wiki/AutoCAD>.

107. Autodesk Inventor. *Wikipedia*. [Online]

https://en.wikipedia.org/wiki/Autodesk_Inventor.

108. Non-uniform rational B-spline. *Wikipedia*. [Online]

https://en.wikipedia.org/wiki/Non-uniform_rational_B-spline.

109. Autodesk. Loft feature. *Autodesk*. [Online] Loft feature.

<https://knowledge.autodesk.com/support/inventor-lt/learn-explore/caas/CloudHelp/cloudhelp/2014/ENU/InventorLT/files/GUID-4AA1C20A-B5AE-428A-B0EE-857209FFF353-htm.html>.

110. Man-system integration standard . *NASA* . [Online]

<https://msis.jsc.nasa.gov/sections/section03.htm>.

111. Comsol. COMSOL Multiphysics. *Comsol*. [Online] <https://www.comsol.com/comsol-multiphysics>.

112. COMSOL Multiphysics. *Wikipedia*. [Online]

https://en.wikipedia.org/wiki/COMSOL_Multiphysics.

113. Dmitri, Kuzmin. Introduction to Computational Fluid Dynamics. Institute of Applied Mathematics - University of Dortmund : s.n.
114. —. "Introduction to Computational Fluid Dynamics" . Institute of Applied Mathematics - University of Dortmund : s.n.
115. *Relative residence time and oscillatory shear index of non-Newtonian flow models in aorta*. Johannes V. Soulis, Olga P. Lampri, Dimitrios K. Fytanidis, George D. Giannoglou. s.l. : IEEE, Oct. 2011.
116. *Disturbed flow in radial-cephalic arteriovenous fistulae for haemodialysis: low and oscillating shear stress locates the sites of stenosis*. Ene-Iordache B, Remuzzi A. 2012 Jan. 21771751 .
117. *Blood Flow* . Grobelnik, Barbara. University in Ljubljana : s.n., January 2008.
118. *A numerical study of the effect of catheter angle on the blood flow characteristics in a graft during hemodialysis*. Hong Sun Ryou, Soyeon Kim, Kyoungchul Ro. s.l. : Springer, March 2013, Vol. Korea-Australia Rheology Journal. 1226-119X.
119. *Fluid Structure Interaction: Fundamentals*. Jainish Topiwala, Gaurav Mistry, Sandip Patel, Pratik Umrigar. May - Oct 2016, Vol. IJRMET. 2249-5762.
120. wikipedia. Image Analysis. <https://en.wikipedia.org>. [Online] https://en.wikipedia.org/wiki/Image_analysis.
121. canada, natural resources. <http://www.nrcan.gc.ca>. [Online] <http://www.nrcan.gc.ca/node/9303>.
122. algonquincollege. <http://www7.algonquincollege.com>. [Online] <http://www7.algonquincollege.com/onlineresources/fsg/doc/characteristics-of-an-accessible-document.pdf>.
123. westnile. <http://westnile.ca.gov>. [Online] http://westnile.ca.gov/special/category_a/?page=Chapter8.htm.

124. wikipedia. DICOM. <https://en.wikipedia.org>. [Online]
<https://en.wikipedia.org/wiki/DICOM>.
125. ifasystems. www.ifasystems.com. [Online]
http://www.ifasystems.com/index.php?option=com_content&view=article&id=45&Itemid=53.
126. santesoft. <http://www.santesoft.com/win/sante-dicom-editor-3d/howto/network.html>. www.santesoft.com. [Online]
<http://www.santesoft.com/win/sante-dicom-editor-3d/howto/network.html>.
127. tutorialspoint. www.tutorialspoint.com. [Online]
https://www.tutorialspoint.com/matlab/matlab_overview.htm.
128. mathworks. Image Processing. [Online]
<https://it.mathworks.com/help/images/index.html>.
129. —. features. www.mathworks.com. [Online]
<https://www.mathworks.com/products/image/features.html>.
130. quora. www.quora.com. [Online] <https://www.quora.com/Image-Processing-Can-someone-explain-what-exactly-does-Hough-transform-do>.
131. wikipedia. Sobel Operator. <https://en.wikipedia.org>. [Online]
https://en.wikipedia.org/wiki/Sobel_operator.
132. mathworks. <https://it.mathworks.com>. [Online]
<https://it.mathworks.com/help/images/functionlist.html>.
133. —. dir. [Online]
https://it.mathworks.com/help/matlab/ref/dir.html?searchHighlight=dir&s_tid=doc_searchtitle.

134. —. [Online]

https://it.mathworks.com/help/images/ref/dicomread.html?searchHighlight=dicomread&s_tid=doc_srchttitle.

135. —. [Online]

https://it.mathworks.com/help/images/ref/imtool.html?searchHighlight=imtool&s_tid=doc_srchttitle.

136. —. xlswrite. *www.mathworks.com*. [Online]

<https://www.mathworks.com/help/matlab/ref/xlswrite.html>.

137. wikipedia. Savitzky-Golay filter. [Online]

https://en.wikipedia.org/wiki/Savitzky%E2%80%93Golay_filter.

138. mathworks. cart2pol. *www.mathworks.com*. [Online]

<https://www.mathworks.com/help/matlab/ref/cart2pol.html>.

139. Least Squares. *https://en.wikipedia.org*. [Online]

https://en.wikipedia.org/wiki/Least_squares.

140. least-square. *www.slideshare.net*. [Online]

<https://www.slideshare.net/somyabagai/method-of-least-square>.

141. Least_squares. *www.cs.mcgill.ca*. [Online] https://www.cs.mcgill.ca/~rwest/link-suggestion/wpcd_2008-09_augmented/wp/l/Least_squares.htm.

142. *A pulse wave propagation model to support decision-making in vascular access planning in the clinic*. W. Huberts, A.S. Bode, W. Kroon, R.N. Plankend, J.H.M. Tordoir, F.N. van de Vosse, E.M.H. Bosboom. Eindhoven University of Technology : s.n., Jul. 2011.

143. *Model of Aortic Blood Flow Using the Windkessel Effect*. Marianne Catanho, Mridu Sinha, Varsha Vijayan. s.l. : University of California San Diego, Oct. 2012, Vol. BENG 221 - Mathematical Methods in Bioengineering.

144. *Application of Ultrasound in Medicine*. Aladin Carovac, Fahrudin Smajlovic, Dzelaludin Junuzovic. s.l. : PubMed Central®, 2011 Sep. PMC3564184.
145. *Colour Doppler ultrasound in dialysis access*. Patrick Wiese, Barbara Nonnast-Daniel. s.l. : Nephrology Dialysis Transplantation, June 2004, Vol. Volume 19, Issue 8.
146. What is Dialysis and Chronic Kidney Disease? *DPC Education Center*. [Online] <http://www.dpcedcenter.org/what-dialysis-and-chronic-kidney-disease>.
147. Chronic Kidney Disease. *Renalus Center for Kidney Care*. [Online] <https://renalus.com/treatment-services/consultation-diagnostics/chronic-kidney-disease/>.
148. Dialysis. *RxList*. [Online] <http://www.rxlist.com/dialysis/page2.htm>.
149. *Disturbed flow in a patient-specific arteriovenous fistula for hemodialysis: Multidirectional and reciprocating near-wall flow patterns*. Bogdan Ene-Iordache, Cristina Semperboni, Gabriele Dubini, Andrea Remuzzi. 10, s.l. : Journal of Biomechanics, April 2015, Vol. 48. 25920898.
150. *1D modeling of blood flow in networks : numerical computing and applications*. Wang, Xiaofei. s.l. : HAL, May 2015. tel-01149085.
151. *A sensitivity analysis of a personalized pulse wave propagation model for arteriovenous fistula surgery. Part A: Identification of most influential model parameters*. Huberts W., de Jonge C., van der Linden W.P., Inda M.A., Tordoir J.H., van de Vosse F.N., Bosboom E.M. 6, s.l. : Medical Engineering & Physics, 2013 Jun, Vol. 35. 22964062 .
152. Lumped Element Model. *Wikipedia*. [Online] https://en.wikipedia.org/wiki/Lumped_element_model.

153. *Model of Aortic Blood Flow Using the Windkessel Effect*. Marianne Catanho, Mridu Sinha, Varsha Vijayan. s.l. : University of California San Diego, Oct. 2012, Vol. BENG 221 - Mathematical Methods in Bioengineering.
154. *Computational fluid-structure interaction: methods and application to cerebral aneurysms*. Yuri Bazilevs, M.-C. Hsu, J. Benson, S. Sankaran, A. L. Marsden. 1, s.l. : Computational Mechanics, December 2009, Vol. 45.
155. *Computational simulation of aortic aneurysm using FSI method: Influence of blood viscosity on aneurismal dynamic behaviors*. Xiaohong Wang, Xiaoyang Li. 9, s.l. : Computers in Biology and Medicine, June 2011, Vol. 41.
156. *Fluid-structure interaction simulation of aortic blood flow*. Paolo Crosetto, Philippe Reymond, Simone Deparis, Dimitrios Kontaxakis, Nikolaos Stergiopoulos, Alfio Quarteroni. s.l. : Computers & Fluids, December 2010.
157. *Fluid structure interaction in abdominal aortic aneurysms effects of asymmetry and wall thickness*. Scotti CM1, Shkolnik AD, Muluk SC, Finol EA. s.l. : BioMedical Engineering OnLine, 2005 Nov.
158. *Influence of microcalcifications on vulnerable plaque mechanics using FSI modeling*. Bluestein D., Alemu Y., Avrahami I., Gharib M., Dumont K., Ricotta J.J., Einav S. 5, s.l. : Journal of Biomechanics, Vol. 41.
159. *Unsteady blood flow and mass transfer of a human left coronary artery bifurcation: FSI vs. CFD*. M. Malvè, A. García, J. Ohayon, M.A. Martínez. s.l. : International Communications in Heat and Mass Transfer, April 2012.